# EFFECTIVENESS OF GEOCELL REINFORCED RECLAIMED ASPHALT PAVEMENT BASE LAYER FOR FLEXIBLE PAVEMENT SYSTEM OVER EXPANSIVE SUBGRADES

A Dissertation

by

MD ASHRAFUZZAMAN KHAN

Submitted to the Graduate and Professional School of
Texas A&M University
in partial fulfillment of the requirements for the degree of

DOCTOR OF PHILOSOPHY

| | |
|---|---|
| Chair of Committee, | Anand J. Puppala |
| Committee Members, | Robert Lytton |
| | Charles Aubeny |
| | Zofia Rybkowski |
| Head of Department, | Zachary Grasley |

December 2021

Major Subject: Civil Engineering

# ABSTRACT

The transportation agencies must allocate a significant annual budget to rehabilitate low to high volume roads constructed over expansive subgrades. This type of subgrade soil undergoes substantial changes in volume due to the seasonal fluctuation of moisture levels, which will lead to pavement distress, including rutting, heaving, or/and longitudinal cracking. On the other hand, utilizing the large volume of reclaimed asphalt pavement (RAP) aggregates as a part of the pavement base layer has been a big challenge for researchers due to its poor mechanical properties. The traditional subgrade treatment procedures with full-depth reclamation are cost-intensive and time-consuming. Therefore, the transportation industry looks for an economical and sustainable alternative to address both these issues. This research study aims to assess the potential benefits of a three-dimensional confinement system, commercially known as “geocell,” to improve the performance of RAP materials and provide consistent support to the flexible pavement structure constructed over expansive subgrades.

This dissertation focused on contributing to the field of pavement geotechnics in two ways: first, to evaluate the performance of the geocell reinforced RAP-base (GRRB) layers to improve the performance of the flexible pavement constructed over expansive subgrade soil; and second, to develop a design methodology for such pavements based on field observations, cost and sustainability assessments.

Several test sections were constructed over an existing farm-to-market road, FM 1807, which suffered from distresses induced by the underlying expansive subgrade.

These test sections were designed and constructed with different geocell-RAP infill materials, instrumented with sensors including Shape Array Accelerometers (SAAs) and Earth Pressure Cells. The structural capacities of the pavement sections were further evaluated by performing nondestructive field tests, including Falling Weight Deflectometer (FWD) and Automated Plate Load Test (APLT).

In addition to the field testing, numerical modeling analyses were performed to understand the contributions from the geocell bases and determine the future load-carrying capacity based on compressive strain acting on the subgrade soil. The expected design life of the geocell-reinforced pavement was calibrated with the field monitored data, and these results are used to develop flexible pavement design on expansive soils by utilizing a GRRB layer. The economic and sustainability aspects of flexible pavements with GRRBs are further verified with Life-Cycle Cost Analysis (LCCA) and sustainability analysis. It is believed that this research study will provide future practical guidelines for the construction and design of flexible pavements with GRRBs over expansive subgrades.

# ACKNOWLEDGEMENTS

First and foremost, I would like to express my sincere gratitude to my supervisor, Dr. Anand J. Puppala. I am deeply grateful for his continuous guidance and support throughout my Ph.D. study. I also would like to thank Dr. Robert Lytton, Dr. Charles Aubeny, and Dr. Zofia Rybkowski for their practical advice and comments throughout this research.

I want to thank all my colleagues who supported me throughout my research, especially during the construction of the field test section, including Dr. Shi He, Dr. Puneet Bhaskar, Dr. Burak Boluk. I want to express my special thanks to Nripojyoti Biswas, Dr. Surya Sarat Chandra Congress, Dr. Sayantan Chakroborty, Dr. Jasaswee Das, and Dr. Aritra Banerjee for their unconditional support and help.

I would like to thank all my friends in Arlington, Texas, who supported me from the beginning of my Ph.D. study. I would also like to thank my friends and colleagues in College Station who always helped me during the difficult pandemic time. I am grateful to Dr. Anwarul Mustafa, who inspired me to choose civil engineering as my major.

I would like to thank my parents, Md Wahiduzzamanand and Afsana Begum, for their unconditional love and support throughout my study. I would also like to thank my younger sister Ayesha Khatun and my younger brother Md Ashaduzzaman for their mental support throughout my research. Finally, I would like to acknowledge my beloved wife, Umme Zakira, who motivated me and supported me throughout the journey of my Ph.D. study.

# CONTRIBUTORS AND FUNDING SOURCES

## Contributors

This work was supervised by a dissertation committee consisting of Professor Dr. Anand J. Puppala, Dr. Robert Lytton, and Dr. Charles Aubeny of the Department of Civil Engineering, and Professor Zofia Rybkowski of the Department of Construction Science.

The work conducted for the dissertation was completed by the student independently.

## Funding Sources

This research was funded by the Fort Worth District of the Texas Department of Transportation (Grant Number 02-9XXIA005) and the NSF Industry-University Cooperative Research Center's (I/UCRC) Center for Integration of Composites into Infrastructure (CICI) located at TAMU (Award Number 2017796). Graduate study was also partially supported by a fellowship from Texas A&M University.

Its contents are solely the responsibility of the authors and do not necessarily represent the official views of the funding agencies.

# TABLE OF CONTENTS

Page

## LIST OF FIGURES

# LIST OF TABLES

Page

# CHAPTER I

# INTRODUCTION

## 1.1 Problem Statement

Flexible pavements constructed over expansive subgrades suffer from severe distresses, leading to an annual damage cost of more than a billion dollars (Christopher et al., 2006). Transportation agencies are looking for sustainable solutions to mitigate this global problem. According to Texas Transportation Plan 2040, the Texas Department of Transportation (TxDOT) will require $547 billion in state and federal funding through 2040 to keep the various transportation modes in a “good state of repair” (Lowry & Costello, 2016).

One of the largest shares of the transportation infrastructure in Texas is the Farm to Market (FM) roads, which is the most extensive secondary highway system. TxDOT has to allocate and spend a significant amount of the annual budget to rehabilitate the FM roads constructed over expansive subgrades (Das et al., 2019a; Lowry & Costello, 2016). This type of subgrade soil undergoes substantial changes in its volume due to the seasonal moisture content fluctuations, which leads to several types of pavement distresses, including rutting, heaving, and longitudinal cracking. The traditional soil stabilization techniques, i.e., lime, fly ash, cement, and other chemical additives, are not sustainable as the utilization of chemicals has an adverse effect on the environment (Sambodh, 2017). Instead of stabilizing the subgrade soil, stiffening the base layer can be a potential solution as it could provide uniform support, which will restrict the differential movement of the soil underneath. The base layer is generally constructed with natural aggregate, which is 94.4% by weight of the total material used in the pavement (Sullivan, 2006).

According to Federal Highway Administration (FHWA), there is a need of 700 million tons of aggregates every year for the pavement industry (FHWA-HRT-11-006). To prevent the declination of natural resources, the FHWA recommended that the reclaimed material should get first consideration while selecting the material for the pavement system. Potential cost savings could be 30% if 50% RAP materials are used to construct the base and subbase layers (Hoppe et al., 2015). The maximum percentage of RAP was limited to 50% due to its poor mechanical properties. Thus, both state and federal agencies are looking for some economic and sustainable solutions that could maximize the utilization of reclaimed material and provide uniform support for the roads constructed over problematic expansive soil.

The two-dimensional (2-D) planar geosynthetic system, i.e., geogrid, geotextile, is widely used to reinforce the base layer of flexible pavements. In most cases, the planar geosynthetics products are used at the interface of the base and subgrade material. The tensile force developed within the planar geosynthetic layers helps to restrict the local movement of the base aggregate material close to the interface; however, this mechanism will not be helpful to restrict the overall lateral movement of the low-quality reclaimed materials (Dash et al., 2019). A three-dimensional confinement system, i.e., geocell, is required to restrict the lateral movement of such material.

Geocell is a honeycomb-shaped structure, generally made from the sheets of high-density polyethylene (HDPE) materials, and this helps to "restrict the lateral movement" of the infill material and provide a "mattress effect". The restriction of lateral movement due to geocell can be beneficial to control the permanent deformation or rutting of the RAP material, which will eventually improve the stiffness of the base layer. The "mattress effect" can help to distribute the traffic load over a wider area on top of the layer beneath it, which will ultimately increase the overall load-bearing capacity of the pavement foundations system. The differential movements on top of the pavement surface due to the seasonal fluctuation of the expansive soil can be restricted with such confining system. However, the lack of information available about the geocell-reinforced flexible pavement hinders the designer/pavement engineers from providing design solutions with geocell.

## 1.2 Motivation of the Research Study

The benefit of using geocell is well established from the laboratory study; however, very little information is available regarding the utilization of geocell-reinforced RAP base (GRRB) layer in the field, in particular over expansive subgrade conditions. Highway agencies, including TxDOT, acknowledged that the application of geocell can improve the performance of the base layer; however, the pavement designers are not at ease with the application of geocell as there are limited guidance and guidelines regarding the construction and design of geocell-reinforced flexible pavement system. There is a major research need for a study that could identify the potential benefits of using geocell on expansive subgrade conditions and then develop a design methodology for the implementation of GRRBs.

## 1.3 Research Objectives

The primary objective of this thesis research is, therefore, to assess the performance of geocell reinforcement to address the issues associated with the utilization of inferior quality reclaimed material and mitigate the underlying expansive subgrade induced heaving and shrinking problems, thereby providing uniform support for flexible pavements. Several specific objectives are formulated to address the primary objective, and these are summarized below:

- Assess field performance of the GRRB layers based on vertical stress and deformation analysis within a pavement layer system.
- Evaluate the effectiveness of geocell reinforcement to mitigate the swell–shrink related issues associated with expansive subgrade conditions.
- Estimate the composite modulus of the geocell-reinforced section based on non-destructive tests (NDTs).
- Analyze the field test sections using a numerical model to understand the behavior of flexible pavement systems with a different configuration of loading, geometry, material properties, and reinforcement aspect ratio.
- Develop mechanistic design methodologies with charts for the geocell reinforced flexible pavements.
- Conduct life-cycle cost assessment (LCCA) and sustainability assessments of geocell reinforced flexible pavements.

## 1.4 Structure of the Dissertation

This dissertation discusses the previous findings, field performance, and future scope for the flexible pavement with GRRB layers. The contents of the dissertation are discussed below, which are categorized into eight major chapters.

Chapter 1, the current chapter, presents the problem statement, potential solution, project objectives, and tasks involved in this research. Chapter 2 discusses the major findings from the previous studies related to the utilization of Geocell for pavement infrastructures. This chapter will summarize the former discoveries from the analytical, laboratory, numerical, and field studies, thus determining the gap between the theory and field implementation of GRRB.

Chapter 3 explains the research methodologies adopted to fulfill the objectives under the major tasks involved in this project. The activity under individual tasks is presented in this chapter.

Chapter 4 presents the activities involved in construction, instrumentation, and monitoring of the fields test sections. This chapter also discusses the regular field survey, field data collection procedure, profiler testing, and corresponding outcomes to assess the performance of the GRRB sections. Chapter 5 summarizes the outcomes from the non-destructive field testing conducted during the monitoring periods. This chapter also shows the comparison between the elastic moduli obtained from the static and repeated load testing method.

Chapter 6 shows the development of numerical models for the flexible pavement with GRRB. The field responses collected from the field test sections are compared with the outcomes from the finite element model with ABAQUS.

Chapter 7 presents the framework for the development of a design chart for the flexible pavements with GRRB. This chapter will also discuss the LCCA for several types of pavement sections. Chapter 8 summarizes the overall performance of the GRRB, specially constructed over problematic soil conditions. Future scope and recommendations are also included in this chapter.

# CHAPTER II

# LITERATURE REVIEW

## 2.1 Introduction

Flexible pavements constructed over expansive subgrade soils suffer from different types of distresses, including rutting, cracking, and shoulder depressions (Punthutaecha et al., 2006; Puppala & Musenda, 2000). Transportation agencies are adopting different strategies to mitigate these issues; however, there is a need to development of an economical solution for such pavement, which can also enhance the sustainability of the project (Das et al., 2018). A sustainable solution can be achieved by replacing the virgin aggregate material with reclaimed one. Aggregate makes up the largest share of the mass and volume in a pavement structure and recycling this material for new construction or rehabilitation can provide an economical and sustainable solution. Aggregate resources are scarce, and hence practitioners are looking for reclaimed materials.

Transportation agencies utilize reclaimed material, e.g., reclaimed asphalt pavement (RAP), by blending them with virgin aggregates to enhance the sustainability of the pavement structures. The mechanical characteristics of this RAP material limit the maximum amount of RAP to 30% of the composite aggregate mixtures for the construction of the base layer (Copeland, 2011). The construction and rehabilitation work still need a huge volume of virgin aggregates, and hence, alternative solutions are always sought to maximize the utilization of the reclaimed aggregate material.

Researchers all over the world are trying to adopt different stabilization techniques to maximize the utilization of reclaimed materials (Hoyos et al., 2011; Khan et al., 2020; Saride et al., 2011).

The utilization of planar or two-dimensional (2D) geosynthetics can improve the performance of the reclaimed-base layer; however, cellular type three-dimensional (3D) geosynthetics can increase the load-bearing capacity and restrict the permanent deformation of the reclaimed-base layer by providing the lateral confinement. The performance of the geocell-reinforced reclaimed asphalt pavements has been studied in the laboratory; however, very little information is available regarding the construction feasibility and design approach for geocell-reinforced flexible pavements. The flowchart shown in Figure 1 describes the various topics covered under the literature review in a nutshell.

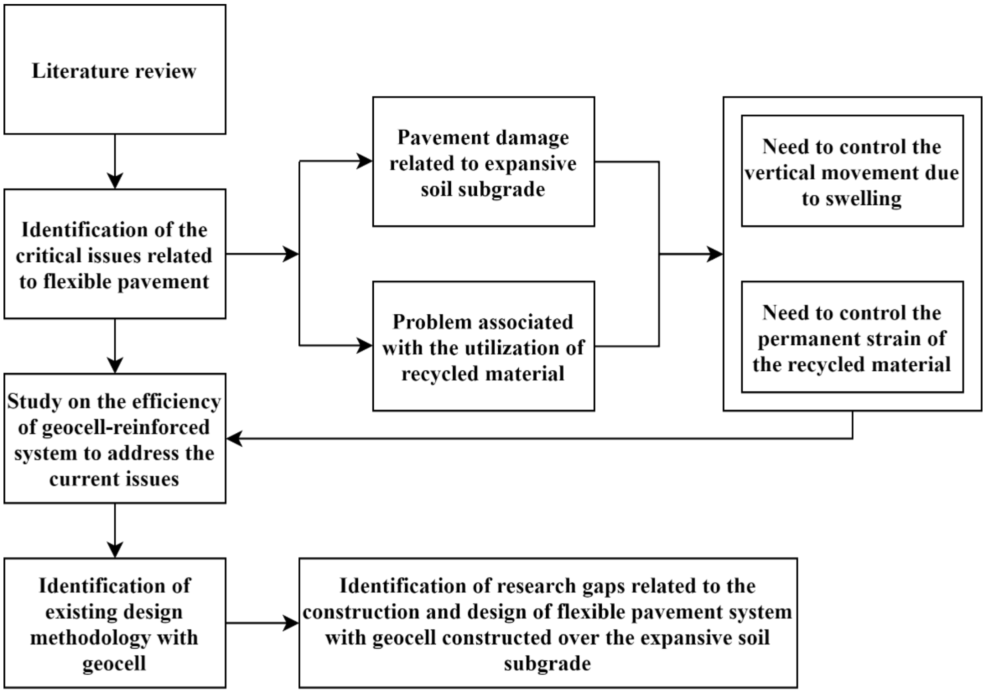

**Figure 1 Flow-diagram of the literature review**

## 2.2 Effect of Expansive Soil on the Performance of the Flexible Pavements

Expansive soils are commonly available in the southwestern United States and other parts of the world. The presence of expansive soil is considered one of the most common causes of pavement distresses (Dessouky et al., 2012). During the periods of heavy rainfall events, the moisture content of the subgrade soil increases and lead to an increase in soil volume, also known as “volumetric swell strains”. Conversely, the reduction of moisture content during the dry period is known as “volumetric shrinkage strains”. The cycles of swell and shrink related volume changes can result in significant deformation upper layers, including pavements, which is considered as the primary cause of pavement failures in the northern Texas region (Biswas et al., 2021; Khan et al., 2017; Pedarla et al., 2015; Puppala et al., 2008; Puppala et al., 2019).

### *2.2.1 Expansive Soil Induced Pavement Distresses*

One of the major types of distresses for low volume narrow roads is longitudinal cracking. This type of cracking is instigated during the drying process of highly plastic subgrades with a plasticity index greater than 35 (Sebesta 2002; Pedarla et al. 2015). The narrow pavements, having inadequate lateral support, suffers from shoulder dropping, cracking, and rutting along wheel-paths. The annual cost of repair associated with such distresses is billions of dollars, and researchers are investing this problem to find a sustainable solution (Das et al., 2019; Pokharel et al., 2016). The following sections will discuss the sustainable solution for the design of flexible pavement with the expansive subgrade.

### *2.2.2 Prediction of Pavement Roughness*

Pavement roughness is one of the primary criteria to understand the performance of the flexible pavement. Cyclic wetting and drying of the expansive subgrade led to the degradation of road infrastructure by increasing the roughness over time. The rate of change of international roughness index (*IRI*) can be predicted from the following Equation 1, proposed by Lytton et al. (2005).

$$\frac{dR}{dt} = \beta_1(\Delta H) + \beta_2 \qquad (1)$$

Where, $dR/dt$ is the rate of change of *IRI*;

$\Delta H$ is the vertical rise of the expansive soil;

$\beta_1 = 2.7014$ and $\beta_2 = 4.0146$.

The roughness is directly related to the vertical movement of the expansive subgrade. The reduction in vertical movement by any stabilization method will help to enhance the performance of the road. The following section will discuss various techniques adopted to minimize the vertical movement of the pavement subgrades.

### *2.2.3 Reduction of Vertical Movements of Expansive Soil*

The total replacement of the expansive soil with non-expansive material may provide strong structural support; nevertheless, the costs associated along with the long construction periods will not allow this method to be adopted by the state agencies. The preloading method can be adopted for low swelling potential soil (< 600 psf) by increasing the surcharge on top of expansive subgrade soil with suitable fill materials (Puppala & Musenda, 2000). However, this method is not suitable for soil with very high swelling potential.

Expansive soils with high swelling potential can be treated by mechanical, physical, or chemical alteration (Dessouky et al., 2012; Lytton et al., 2004; Puppala et al., 2008; Zornberg & Gupta, 2009). One of the widely used methods for the stabilization of expansive soil is the lime stabilization technique (Little et al., 2018; Puppala et al., 2006, 2019). The addition of chemicals helped to reduce the swelling potential of expansive soil, hence decreasing the overall vertical movement. The soil stabilization technique with lime may increase the swelling potential of the soil with high sulfate contents (Punthutaecha et al., 2006; Puppala et al., 2019, 2003).

Another method of controlling the volume change behavior of expansive soil is the fiber reinforcement technique. The addition of 0.3% of fibrillated polypropylene fibers can significantly reduce the volumetric strain of expansive soil, at the same time, increase the unconfined compressive strength by 50%. (Puppala & Musenda, 2000).

The heaving of the expansive soil during the life span of the pavement can be controlled by the prewetting method. This method has the potential to take care of the vertical movement before the construction of the pavement; however, the depth of penetration of moisture and time required for saturation will vary spatially (Nelson & Miller, 1997).

The differential movement of the subgrade soil leads to the uneven support condition for the pavement base layer. This problem can be mitigated by adding planar geosynthetic reinforcement at the bottom or within the base course layer to increase the load-bearing capacity of the structural system by developing tensile stresses within the geosynthetic reinforcements (Zornberg & Gupta, 2009). The application of cellular confinement within the base layer also helps to reduce the vertical movement of the expansive subgrade soil by distributing the upward swell pressure over a larger area. An experimental study conducted by Tamim (2017) showed that the addition of a geocell base layer on top of expansive soil could reduce the overall soil heaving by 29%. The reinforcement of the base layer with geocell may provide a structurally sound solution for the pavements constructed over an expansive subgrade; however, the economic and sustainability aspects of such pavement should be assessed based on life cycle cost and sustainability analyses.

## 2.3 Utilization and Characteristics of RAP as the Base Layer

The purpose of the preliminary literature review was to identify the existing methods for pavement rehabilitation and material usage. It is recognized that more focus is needed to study the behavior of the reclaimed material and the effect of geocell to enhance the properties of the reclaimed material, which often exhibits inferior characteristics while being used individually. The following subsections summarize the features of the RAP material and the notable findings of the previous studies to provide a glimpse into the behavior of geocell-reinforced sections under static and dynamic loadings.

### *2.3.1 Availability and Utilization of RAP*

According to National Asphalt Pavement Association (NAPA), the estimated amount of RAP stockpiled nationwide increased by 9.10%, from 93.59 million tons at the end of 2016 to 102.11 million tons at the end of 2017 (Williams et al., 2020). According to the reclaimed material policy of the Federal Highway Administration

(FHWA), reclaimed materials should get first consideration in material selection. However, state transportation agencies are concerned regarding the usage of a higher percentage of this material since there is a lack of guidance as well as a lack of data available on their performance (Copeland, 2011). Hence, the maximum utilization of RAP is limited in many states across the United States; for example, its usage in the state of Texas is restricted to 15 to 19% (George, 2018).

### *2.3.2 Mechanical Characteristics of RAP Materials*

The mechanical properties, including compacted unit weight, resilient modulus, California bearing ratio, and permanent strain under cyclic loading, are some of the major concerns for the design of flexible pavement. In comparison with the virgin aggregate material, the resilient modulus of the unbound RAP material is higher; however, the permanent deformation is 1.7 to 3.0 times that of aggregate layer (Bennert et al., 2000; Kim & Labuz, 2007). This underlines the poor mechanical properties of the RAP materials when used individually.

### *2.3.3 Stabilization of RAP Materials*

Transportation agencies are trying to overcome the mechanical issues of the unbound RAP materials by adopting different strategies, e.g., blending RAP with virgin aggregates, stabilizing with chemicals (Bozyurt et al., 2012; Hoyos, et al., 2011). The mixing of virgin aggregates with RAP helps to control the permanent strain; however, it decreases the resilient modulus (Attia & Abdelrahman, 2011a, 2011b; Bennert et al., 2000). The resilient modulus of the RAP material was higher due to the higher cohesion property, which is associated with the asphalt binder content present in the RAP material

(Thakur & Han, 2015). The application of cement or kiln dust can increase the dry density and compressive strength of the RAP material (Taha et al., 1999). The durability tests on cement/fly ash treated RAP showed a low volumetric strain and good retaining strength after multiple cycles of durability test (Puppala et al., 2017). One of the major concerns with the chemical stabilization method is environmental pollution, as the chemically treated bases can increase the pH of the surrounding area, which may affect the vegetation and water quality (Sambodh, 2017).

## 2.4 Application of Geocell for Pavement Infrastructures

The environmental problems associated with the current stabilization methods can be overcome by utilizing the cellular type three-dimensional geosynthetic reinforcement, which is also known as geocell. The following sections will discuss the usage of geosynthetic products and the potential of geocell for the stabilization of reclaimed or other inferior quality materials.

### *2.4.1 Geosynthetic Reinforcement for Pavement Structures*

The planar type geosynthetic, i.e., geotextile, geogrid, is widely used in pavement infrastructures to reduce the volume of virgin aggregate material and increase the service life of the pavement (Biswas & Ghosh, 2017; Li et al., 2018; Sun et al., 2021). The application of planar geosynthetic at the interface of the base and subgrade layers can reduce the required base layer thickness of an unpaved road section (Giroud & Han, 2004a, 2004b). The confinement provided by planar reinforcement can improve the bearing capacity of the reinforced section, although additional lateral confinement is required to restrain the excessive permanent deformation of the RAP material (Dash et al., 2001). The inclusion of geocell can provide additional confinement, which can eventually reduce the permanent deformation of the infill material. The effect of geocell has been studied by several researchers, focusing on base course reduction (*BCR*) percentage, bearing capacity improvement factor (*BIF*), and traffic benefit ratio (*TBR*) (Dash et al., 2003; Thakur et al., 2012; Thallak et al., 2007).

A few laboratory studies are currently available, which focus on the reinforcement of RAP material. Most of these laboratory studies are conducted with high modulus novel polymeric alloy (NPA) geocell, which is costlier than the widely available high-density polyethylene (HDPE) geocell. The large-scale laboratory study on HDPE geocell indicated that it could increase the stiffness of the RAP-base layer and significantly decrease the permanent deformation under the cyclic loading conditions (George et al., 2019). The improvement with geocell reinforcement has been quantified from laboratory studies; however, very few field studies are currently available to assess the performance of such pavements. The following sections describe the geocell reinforcement, converging towards its utilization to reinforce the RAP-base layer.

### *2.4.2 Geocell Reinforcement*

The Mohr-Coulomb failure envelope drawn from the triaxial compression test with and without cellular reinforcement shows that the infill material will gain some apparent cohesion due to the confining effect offered by geocell reinforcement (Bathurst & Karpurapu, 1993; Khan et al., 2020). The application of geocell can increase the lateral confinement (as shown in Figure 2a), which will lead to the development of apparent cohesion, assuming the angle of internal friction will not change. However, the repeated load tests on single-cell HDPE geocell, infilled with granular material, showed a minor effect on resilient modulus (Edil et al., 2006).

During a triaxial test, the vertical strain was more than 20% at failure, whereas the maximum axial deformation during the repeated load triaxial test (RLTT) was less than 4%. The higher axial strain, in the case of the triaxial compression test, will also generate higher radial strain, which helped to develop the hoop stress on the geocell wall. Due to higher hoop stress, the triaxial test showed significant improvement with the reinforcement. On the other hand, during RLTT, a lower radial strain led to lower hoop stress, resulting in a very low improvement in material strength (Bathurst & Karpurapu, 1993; Hegde & Sitharam, 2015).

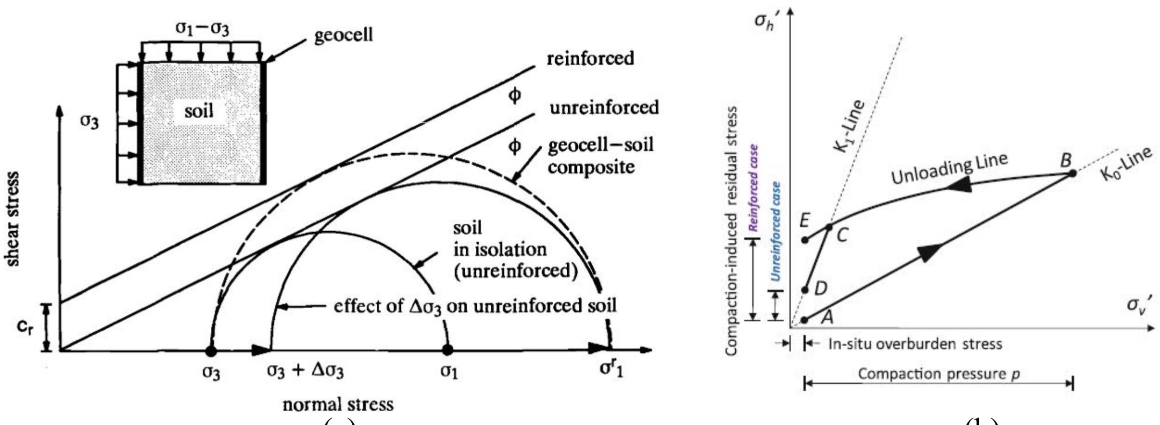

(a) (b)

**Figure 2 Geocell reinforcement mechanism: (a) triaxial compression test (Bathurst and Karpurapu 1993), (b) compaction induced horizontal stresses in the field (Yang et al. 2013)**

The current Mechanistic-Empirical Pavement Design Guide (MEPDG) does not consider the residual horizontal stress acting on the base layer. The stress applied on the base layer of a paved road due to traffic induce loading is much lower compared to the compaction-induced loading (Yang et al., 2013). The addition of geocell confinement can increase the compaction-induced horizontal stress (as shown in Figure 2b), and hence there will be an increase in actual bulk stress  (Yang et al., 2013).

### *2.4.3 Laboratory Studies on Cellular Confined Materials*

The researchers from different parts of the world studied the load-deformation characteristics of different infill materials reinforced with cellular type confinement (Han et al., 2013; Kumar & Saride, 2016; Pokharel et al., 2018). They performed either a static load test or a repeated load test to understand the benefits in terms of different improvement factors due to the addition of three-dimensional confinement. The improvement factors from the static load tests are the bearing capacity improvement factor (*BIF*), settlement reduction factor (*SRF*), and stress distribution angle (*SDA*). On the other hand, the improvement factors from the repeated load tests are the modulus improvement factor (*MIF*), traffic benefit ratio (*TBR*), and rut-depth reduction factor (*RDRF*). The rut depth of a flexible pavement can be determined from the mechanistic-empirical models, which are based on pavement layer properties and environmental conditions (Gu et al., 2016; Tseng & Lytton, 1989). The purpose of the cellular confinement system is to provide additional lateral support compared to the planar reinforcement systems such as geogrid (Rajagopal et al., 2014).

Though the shape, material, and construction techniques of the cellular confinement system varied in different studies; however, the reinforcement concept was the same, and hence, the term "geocell" was used to define any kind of cellular confinement. Most of the researchers have constructed geogrids to form the shape of geocells with different aspect ratios by varying the size of pockets and height of reinforcements (Dash, 2010; Mandal & Gupta, 1994; Mhaiskar & Mandal, 1996). Low-cost material, i.e., bamboo, has been used as a geocell to study the behavior of different infill materials under static loading (Saha & Mandal, 2018). The geocells made of HDPE and NPA are commercially available and have the potential for reinforcing inferior quality materials, i.e., RAP, quarry dust, and other reclaimed aggregates (Han et al., 2013).

#### 2.4.3.1 Static Load Tests

The load-deformation characteristics of the unreinforced and reinforced sections can be determined from a static load test. The material can exhibit three different types of responses: hardening, softening, and elastic-perfectly plastic response, depending on the stiffness of reinforcement and infill material. Figure 3 exhibits the load-characteristics behavior of different types of materials. The inclusion of geocell can provide additional lateral confinement, which can improve the bearing capacity by 1.3 to 10 times, depending on the types of infill material and subgrade conditions (Dash et al., 2003; Hegde & Sitharam, 2015; Rajagopal et al., 1999; Saride et al., 2009). The reinforced layer exhibits beam action up to a settlement ratio of 10%, whereas the membrane action was predominant when the settlement ratio was more than 20% (Mandal & Gupta, 1994). The material with geocell confinement showed composite behavior by transferring the vertical stress from the surface to a deeper layer, which helped to increase the load-bearing capacity of the soil (Saride et al., 2009).

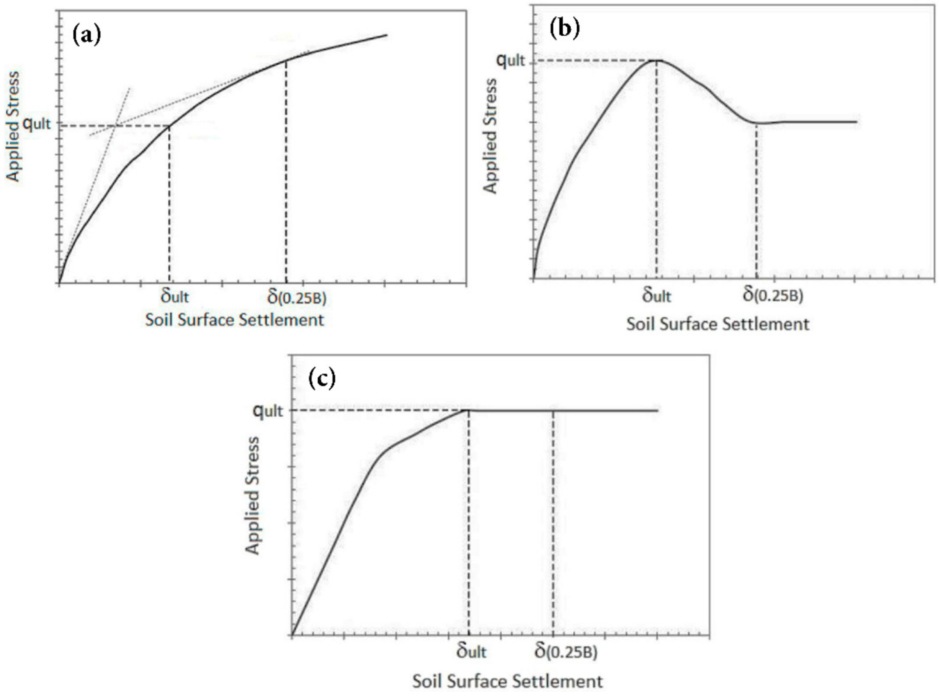

**Figure 3 Typical response from load-deformation curves for (a) hardening response, (b) softening response, (c) elastic-perfectly plastic response (Mehrjardi et al. 2019)**

The surface settlement curves obtained from the un-reinforced and reinforced sections prove that the punching type of failure occurred in the case of the unreinforced section, whereas the reinforced section showed general bearing capacity type failure (Dash et al., 2007; Dutta & Mandal, 2016). The relative density of the infill material can play a vital role, as the dilatancy-induced benefit was much higher with the cellular type confinement (Dash, 2010). The vertical stresses measured at the bottom of the reinforced sections exhibited that the vertical stress decreases under the loading area, although it increases adjacent to the loading area (Dash et al., 2007). This phenomenon indicates that the addition of reinforcement helps to distribute the vertical load over a larger area and hence increases the load-bearing capacity of the reinforced layer.

The subgrade reaction coefficient (k) is an important stiffness parameter for subgrade soil, which depends on the amount of vertical deformation under a particular vertical load. Since the addition of geocell helped to reduce the vertical settlement, which led to a higher k value (Zhou & Wen, 2008). Maximum benefits from the geocell can be achieved if the tensile strain acting on the geocell reaches up to a certain limit (10% in the case of NPA geocell), corresponding to the ultimate tensile strength of the reinforcing material; however, laboratory results indicated that the tensile strain measured on the wall of geocell was less than 1% (Yang, 2010). This may happen due to the improper compaction of the infill material and irregular output obtained from the strain gauges (Thakur et al., 2012).

The *BIF*s for the multi-cell geocell were slightly higher compared to that of the single-cell geocell, which may be attributed to the group action behavior (Pokharel et al., 2010). The inclusion of a second geocell layer can marginally increase the bearing capacity by 10% (Sherin et al., 2017). The static load test on geocell-reinforced-RAP-bases (GRRB) showed significant improvement over the unreinforced section. The *BIF* for the NPA-geocell was estimated as 1.52 for 10-inch (230 mm) thick base section, whereas *BIF*s for the HDPE-geocell were estimated as 1.50 and 1.95 for 4-inch (100 mm) and 6-inch (150 mm) thick base sections, respectively (Pokharel, 2010).

### 2.4.3.2 Repeated Load Tests

The outcome of the repeated load tests can be used to determine the permanent deformation model and composite resilient modulus of the reinforced material. The *TBR* for the reinforced section may range between 1.87 to 100, depending upon the type of infill material, foundation material, stiffness, and geometry of geocell (Hegde & Sitharam, 2016; Kumar & Saride, 2016; Pokharel et al., 2018).

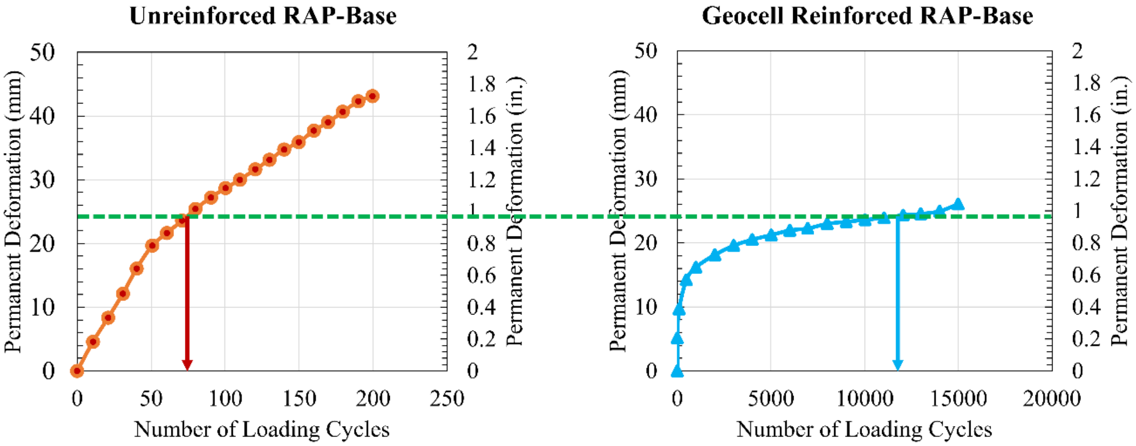

**Figure 4 Repeated load testing results for unreinforced and reinforced RAP-base sections (redrawn from Han et al. 2012)**

Geocell is a three-dimensional reinforcement with large opening sizes, which requires a larger test section area to properly understand the behavior under repeated loading (Rajagopal et al., 1999). The large-scale repeated load test results for the RAP-base section revealed that the geocell confinement could increase the *TBR* by more than 100 times, at a rut depth of 1 inch (Han et al., 2012), as shown in Figure 4. The slope of the elastic rebound curve, which is also known as the coefficient of elastic uniform compression, increases with the addition of geocell, which helps to reduce the magnitude of the permanent deformation (Hegde & Sitharam, 2016). A similar observation was made in another study, where the resilient proportion of the total deformation tends to have a constant value after several load cycles due to the densification of the material (Tafreshi et al., 2014). The initial moduli of the geocell-reinforced section were 1.26 to 2.04 times that of the unreinforced sections; consequently, the reduction in permanent deformations resulted in an increment of 12 times the *TBR* of the unreinforced sections (Pokharel et al., 2018).

The application of geocell will allow the utilization of 100% RAP material for the construction of GRRBs (George, 2018; Thakur et al., 2012). The behavior of the GRRB section depends on the thickness of the layer; a thicker layer will behave as a slab, whereas a thinner layer will behave as a slab under smaller loads, and as a membrane, under higher loads (Thakur et al., 2012). The result obtained from the RLT studies also showed that the increase in GRRB thickness from 4-inch (100 mm) to 6-inch (150 mm) improved the composite layer modulus by 1.1 to 2.7 times, respectively (George et al., 2019; Thakur et al., 2017). The aspect ratio of the reinforcement also plays a vital role as the improvement factors increase with the increase in the aspect ratio (height to depth) of the geocell (Mamatha & Dinesh, 2017).

### *2.4.4 Analytical and Numerical Studies*

The failure envelope of the reinforced and unreinforced sections obtained from the triaxial compression tests can be used to determine the apparent cohesion ($c_r$), with the following Equation 2 (Bathurst & Karpurapu, 1993).

$$C_r = \frac{\Delta\sigma_3}{2}\tan\left(\frac{\pi}{4} + \frac{\phi}{2}\right) \tag{2}$$

In Equation 2, $\phi$ is the friction angle of the soil; $\Delta\sigma_3$ is the increment in confining pressure due to geocell, which can be determined from the following Equation 3.

$$\Delta\sigma_3 = \frac{2M}{D}\left[\frac{1 - \sqrt{\left(1 - \varepsilon_a\right)}}{1 - \varepsilon_a}\right] \tag{3}$$

Where $M$ is the tensile modulus (a material property) of the geocell, d is the pocket diameter (geometric property) of the geocell, and $\varepsilon_a$ is the axial strain acting on the infill material. At the beginning of the test, when the axial strain is zero, the corresponding confining stress is also zero. It indicates that the improvement due to geocell can only be observed with the application of vertical load that can impart horizontal stresses on geocell and leads to the development of the additional confining stress within the layer.

The behavior of the geosynthetic reinforced section under repeated loading can be predicted without performing any large-scale test. The resilient modulus used in MEPDG is the secant modulus when the stress state of the soil is changed from hydrostatic stress ($\sigma_1 = \sigma_3$) to another stress state with an increased $\sigma_1$ ($\sigma_1 < \sigma_3$). In the case of cyclic loading with reinforcement, the axial stress in stage 1 increased from $\sigma_3$ to $\sigma_3 + \Delta\sigma_3$, to reach a hydrostatic condition, and during stage 2, the axial stress continues to increase from $\sigma_3 + \Delta\sigma_3$ to $\sigma_1$ (Yang et al., 2013). The effective, resilient modulus during stages 1 and 2 ($M_{r,1}$ & $M_{r,2}$) can be calculated separately from the MEPDG equation. Yang et al. (2013) modified the permanent deformation (*PD*) model (Tseng & Lytton, 1989) used in MEPDG to develop the following Equations 4 and 5 for geocell-reinforced material.

$$\varepsilon_{1,p} = \left[ -\frac{\Delta \sigma_3}{M_{r,1}} + \frac{\sigma_1 - (\sigma_3 + \Delta \sigma_3)}{M_{r,2}} \right] \left( \frac{\varepsilon_o}{\varepsilon_r} \right) e^{-\left( \frac{\rho}{N_{limit}} \right)^{\beta}} \tag{4}$$

$$\Delta \sigma_3 = \frac{M}{D} \left[ \frac{\Delta \sigma_3}{M_{r,1}} + \frac{\sigma_1 - (\sigma_3 + \Delta \sigma_3)}{M_{r,2}} \right] \left( \frac{\varepsilon o}{\varepsilon r} \right) e^{-\left( \frac{\rho}{N_{limit}} \right)^{\beta}} \left( \frac{1 + \sin\varphi}{1 - \sin\varphi} \right) \tag{5}$$

Where,

$\sigma_1$, $\sigma_3$ are principal stresses in vertical and radial directions.

$\Delta\sigma_3$ is the additional confining pressure for a particular level of axial strain.

*M* and *D* are the elastic modulus and diameter of the geocell material, respectively.

($\varepsilon_0/\varepsilon_r$), $\rho$, and $\beta$ are the PD parameters (determined by fitting measured PD curve), respectively; and $\Psi$ is the angle of dilatancy

The permanent strain for the geocell-reinforced material can be estimated from equation (3), using the $\Delta\sigma_3$ value obtained from equation (4) by trial and error.

Finite element or finite difference models have been used to study the effect of geometry and material stiffness of geocell with different types of infill material. Since geocell provides 3D confinement, a 2D model with plane strain condition cannot be used to accurately simulate this kind of reinforcement, and hence, 3d models were used by most of the previous studies listed in Table 1. Most of the numerical studies tried to simulate the static loading condition to study the load transfer mechanism with geocell (Dash et al., 2019; Mhaiskar & Mandal, 1996; Saride et al., 2009). A few studies have been conducted where RLT was simulated to predict the resilient modulus and permanent deformation characteristics of the geocell-reinforced material (George, 2018; Yang, 2010). Arvin et al. (2018) studied the effects of geocell in pavement structure with a large-scale pavement model to determine the shakedown coefficients. The stress-dependent mechanistic-empirical (M-E) model can be used to predict the permanent deformation model for the unbound base layer (Gu et al., 2016, 2017; Luo et al., 2017). A mechanistic-empirical approach has been proposed to quantify the influence of geogrid on the performance of flexible pavement structures (Gu et al., 2017). However, there are no such studies available for geocell-reinforced flexible pavement (GRFP).

**Table 1 Numerical Studies on Geocell Reinforced Soils**

| S.N. | Reference/ Source | Modeling approach | | Analysis type/Software | Loading type | The focus of the study |
|---|---|---|---|---|---|---|
| | | Geocell | Infill | | | |
| 1. | Mhaiskar and Mandal (1995) | Eight-noded isoperimetric solid element | Drucker-Prager | 3D FEM/ANSYS | Static | Determine the BCF |
| 2. | Saride et al. (2008) | Isotropic elastic | Mohr-Coulomb | 3D FDM/FLAC | Static | Determine the BCF |
| 3. | Dash et al. (2019) | Isotropic elastic | Mohr-Coulomb | 3D FEM/ABAQUS | Static | Contact pressure |
| 4. | Hegde and Sitharam (2015) | Isotropic elastic | Mohr-Coulomb | 3D FDM/FLAC | Static | Vertical stress distributions |
| 5. | Yang (2010) | Isotropic elastic | Duncan-Chang model | 3D FDM/FLAC | Static and RLT | Development of MEPDG |
| 6. | George (2018) | Isotropic elastic | Mohr–Coulomb | 3D FDM/FLAC | Static and RLT | BCF, resilient-modulus and permanent deformation |
| 7. | Arvin et al. (2017) | Isotropic elastic | Mohr-Coulomb | 3D FEM/ABAQUS | RLT | Determine the shakedown coefficients |

### *2.4.5 Field Monitoring Pavement Studies*

The effectiveness of geocell is well understood from the experimental data; however, there is a lack of knowledge about the field performance of GRFP sections, which restricts the practitioners in designing pavements with such reinforcement (TxDOT Pavement Manual, 2019). There are only a few case studies available on the geocell reinforced unpaved roads where the performance was monitored by observing the surface rutting after the end of short design periods (Kief et al., 2015; Pokharel et al., 2015; Rajagopal et al., 2014). The average settlements observed from the static field load tests were used to back-calculate the elastic modulus of the unreinforced and geocell-reinforced sections. The ratio of the elastic modulus was used to calculate the improvement factor, which was further used for the design of unpaved roads with geocell (Rajagopal et al., 2014). Pokharel et al. (2015) presented eight different case studies for unpaved geocell-reinforced roads, where the design rut depths were between 2.5 inches to 3.0 inches. The field performances were monitored based on the observed rutting during or at the end of the design period, as shown in Figure 5.


After completion

After 18 months of operation

**Figure 5: Condition of access road at CANFOR, Canada (Pokharel et al. 2015)**

Norouzi et al. (2019) presented a few case studies where geocell was used in a flexible pavement; however, the performance of such sections was only monitored with a visual inspection of rutting, cracking, and other distress. It was reported that the utilization of NPA geocell could cut down the thickness of asphalt and base layers by 25%. The performance of the geocell reinforced base layer was also compared with the cement-treated base layer. They showed that the utilization of geocell resulted in lesser pavement distresses compared to the cement-treated base layer with similar base thickness.

## 2.5 Pavement Design Guidelines with Geocell Layers

Most of the available design guidelines with geocell are focused on unpaved roads, where the modulus improvement factors or traffic benefit ratios are used to determine the reduction in layer thickness or improvement in design life (Pokharel, 2010; Sitharam et al., 2019). The traffic benefit ratios (*TBR*s) and layer coefficient ratios (*LCR*s) were proposed to design flexible pavement, where the parameters were estimated from the laboratory study conducted on the unpaved road section. It was proposed that the number of standard load repetitions for geocell-reinforced-paved road section can be determined by multiplying the standard load repetition for unreinforced-paved road section with the *TBR* obtained from large-scale laboratory tests on unpaved section. This is ambiguous since the available confining pressure in the base layer of the unpaved and paved road sections is significantly different.

For unpaved road design, the base layer thickness with geocell was determined by modifying the Giroud and Han method with the calibrated material parameters obtained from laboratory studies (Pokharel, 2010). Geocell-reinforced base layer thickness ($h_{gc}$) for the field condition can be determined from the following Equations 6 and 7.

$$h_{gc} = \frac{(0.868k'\log N)}{1 + 0.204(R_E - 1)}\left(\sqrt{\frac{P}{5.14c_u m\pi r^2}} - 1\right)r \tag{6}$$

$$k' = 0.52\left[\frac{r}{h_g}\right]^{1.5} \tag{7}$$

$N$ = number passes;

$r$ = radius of tire contact area (m);

$P$ = wheel load (kN);

$R_E$ = the modulus ratio of base to subgrade;

$c_u$ = undrained cohesion of the subgrade soil (kPa);

$k' = \alpha\left[\frac{r}{h_g}\right]^{\beta}$; $\alpha = 0.52$ and $\beta = 1.5$ for NPA geocell-reinforced granular base.

This approach is suitable for the unpaved road; however, the calibration parameters $\alpha$ and $\beta$ are required for different configurations of geocell with different infill materials. The deployment of this method is limited to the unpaved roads as the allowable maximum rutting is 3-inch. The permanent deformation ($PD$) for the geocell-reinforced layer can be calibrated from the Tseng and Lytton (1989) model as presented in Equation 8 (Thakur, 2011).

$$PD = \mathrm{K}h\varepsilon_v\left(\frac{\varepsilon_o}{\varepsilon_r}\right)e^{-\left(\frac{\rho}{N}\right)^{\beta}} \tag{8}$$

Here, $h$ = thickness of the pavement layer.

$\epsilon_V$ = average vertical strain acting on the layer

$\left(\frac{\epsilon_o}{\epsilon_r}\right)$, $\rho$, $\beta$ = material constant obtained from the large-scale repeated load test

K = 4.2 for unreinforced RAP and 2.7 for geocell-reinforced RAP layer

The calibration parameter "K" was introduced to convert the large-scale box testing condition to the standard triaxial test condition. Figure 6 demonstrates that the inclusion of geocell for paved road sections can reduce the permanent deformation of the asphalt and base layer. A 2-inch-thick asphalt layer was followed by different thicknesses of base layers.

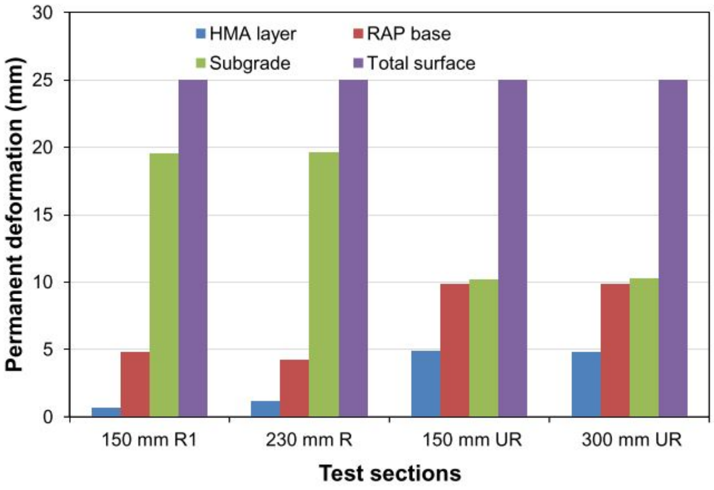

**Figure 6: Comparison of permanent deformation for different pavement layers with and without the geocell (Thakur 2011) [1 inch = 25 mm]**

It was observed that permanent deformations after 10,000 cycles for the geocell-reinforced section were more than 1-inch. The allowable standard load repetition to reach the maximum allowable rutting (0.50 inch) for the paved road section was less than 1000 cycles. The load-carrying capacity is way below the minimum required load-carrying capacity for thin asphalt pavement; hence there is a need for developing a design guideline for geocell-reinforced pavement based on actual field observations.

### *2.5.1 Design Guidelines of Geosynthetic Reinforced Flexible Pavements*

The design concept used for the planar geosynthetics products can be adopted for the design of geocell reinforced paved roads (Sitharam et al., 2019). The design approach for the paved road involves providing a protective layer over the subgrade layer to improve the serviceability under traffic and environmental loads (Zornberg & Gupta, 2010). The available design methods for the flexible pavements can be categorized into two major categories: the American Association of State Highway and Transportation Officials (AASHTO) Method and the Mechanistic-Empirical Pavement Design Guide (MEPDG) method. The design procedure of geosynthetic-reinforced paved road with these methods are discussed below.

#### **2.5.1.1 AASHTO Method**

This is the widely used flexible pavement design method, which uses empirical equations to determine the overall structural number ($SN_{UR}$) for a multi-layer pavement system without any geosynthetic reinforcement (AASHTO 1993). The required $SN_{UR}$ is determined from the following Equation 9, which is based on the design traffic loads, loss of serviceability, and subgrade resilient modulus.

$$\log(W_{18}) = Z_R S_o + 9.36\log_{10}(SN_{UR}+1) - 0.2 + \frac{\log_{10}\left[\frac{\Delta PSI}{4.2-1.5}\right]}{0.4+\frac{1094}{(SN_{UR}+1)^{5.19}}} + 2.32\log_{10}M_R - 8.02 \qquad (9)$$

Where $W_{18}$ is the anticipated cumulative 18-kip Equivalent Single-Axle Loads (ESALs) over the design life of the pavements without any geosynthetic reinforcement, $Z_R$ is the standard normal deviate for reliability level, $S_O$ is the overall standard deviation, ΔPSI is the allowable loss in serviceability, and $M_R$ is the resilient modulus of the subgrade layer. The thickness of the unreinforced pavement layer can be determined from the following equation (Equation 10) with a series of iteration.

$$SN_{UR'} = a_1 D_1 + a_2 D_2 m_2 + a_3 D_3 m_3 \qquad (10)$$

Where a, *D*, and m are the coefficient of relative strength, thickness, and drainage coefficients for the pavement layers. The subscript values in Equation 10 indicate the type of the pavement layer: 1, 2, and 3 denotes the asphalt concrete, base, and subgrade layer, respectively.

The load-carrying capacity of the geosynthetic reinforced pavement can be determined from the following Equation 11.

$$W_{18(reinforced)} = TBR * W_{18(unreinforced)} \qquad (11)$$

The *TBR* is the ratio of the load-carrying capacity of the geosynthetic reinforced sections with the unreinforced sections. This load-carrying capacity for the reinforced section ($W_{18(reinforced)}$) can be used to determine the reinforced pavement structural number ($SN_R$). The difference between the structural number of the reinforced and unreinforced sections can be used to determine the relative strength parameters of the geosynthetic reinforced layer. The *TBR* values for the geotextiles range from 1.5 and 10, and for geogrids between 1.5 to 70 (Shukla, 2002). There are very few studies available to determine the TBR for geocell reinforced RAP material. According to Thakur (2011), the *TBR* value for the 12-inch GRRB is 1.8, at a surface permanent deformation value of 1.2 inches. However, the total number of load cycles reported to reach the permanent deformation of 1.2 inches was less than 60. This indicates a very short life span; however, the actual field scenario is different, and further field investigation is required to quantify the benefit from geocell.

#### 2.5.1.2 MEPDG Method

The design of a paved road with a Mechanistic-Empirical (M-E) approach requires traffic load cycles corresponding to a limited level of surface distress. This approach allows the user to define the local material, which is advantageous to incorporate the added benefit from the geosynthetic products. The contribution of geosynthetic for a thin asphalt pavement can be incorporated in the properties of the base layer, whereas for the thick asphalt pavement, it can be simulated as an equivalent delay in the onset of fatigue cracking (Zornberg and Gupta 2010). The empirical data used to calibrate the responses of the unpaved roads are used for the design of geosynthetic-reinforced pavements (Yang et al., 2013; Giroud and Han, 2004). However, the allowable rutting depth for the paved road is much lower than the unpaved road section. As the M-E method is a performance-based method, the researchers are assessing the pavement performance based on field tests, laboratory tests, and numerical simulations.

One of the major performance criteria for the M-E design is the surface deflections, which can be evaluated using: (1) measurement of the surface deflections in terms of rutting depth and (2) measurement of surface deflections in response to the applied load to determine the structural capacity. The surface rutting is easy to measure and use for the comparison of the performance of the reinforced and unreinforced sections. On the other hand, the FWD can be used to characterize the properties of paving layers, which require inputs into the MEPDG for a new flexible pavement design (Smith et al., 2017).

### *2.5.2 Performance Evaluation of Flexible Pavements*

The performance of the pavement sections can be evaluated with the instrumented sensors, horizontal inclinometers, physical surveys, and non-destructive field testing (Cable et al., 1988; Khan et al., 2020; Khan et al., 2020; Kief et al., 2015; Puppala et al., 2012; Tabatabaee & Sebaaly, 1990; Taha et al., 2002). The following section will discuss the construction and field observation techniques for the flexible pavements built with geocell.

#### **2.5.2.1 Construction and Instrumentation of Flexible Pavements with Geocell**

There are limited studies available regarding the construction and instrumentation techniques for geocell reinforced flexible pavement structures. According to to-“Roadeo”, a field demonstration project in Florida, geocell can enhance the in-situ density of the infill material with the same number of standard roller pass (Schaefer & Berg, 2012). They have used planar geosynthetics products along with the cellular geocell to compare the performance during construction. The energy required by the roller equipment was recorded, which is also known as machine-driven power (MDP), can be used to compare the performance during construction of the base layer. With a similar number of passes, the MDP values were 7% higher for the geocell-reinforced section compared to the control section. This indicates that the utilization of geocell-reinforced sections absorbed more energy; consequently, a 60% increase in the layer modulus was recorded from the in-situ field testing with a lightweight deflectometer (LWD).

Earth pressure cells are commonly used to estimate the reduction of vertical stress beneath the geocell-reinforced base layer (Kief, 2015; Sitharam et al., 2019). Apart from the vertical stress, the vertical deformation under the pavement layer can be estimated from the horizontal inclinometers (Puppala et al., 2012, 2008). In-place inclinometers can be used to determine the continuous data with a system field accuracy of 0.3 inches per 100 ft (Machan & Bennett, 2008). This accuracy level may not be useful while detecting the seasonal variation of expansive soil subgrades. On the other hand, the accuracy of the Shape Array Accelerometers (SAAs) with the Micro Electro Mechanical Sensors (MEMSs) are precise to measure movements of 0.02 inch per 100 ft (*Shape Array*). This SAA with modern technology has the potential to track any small movements under the pavement base layer due to the change of volume of the expansive subgrade; however, there is very little information available regarding the utilization of this sensor to assess the performance for such cases.

#### 2.5.2.2 Field Distress Surveys

Measurement of pavement roughness

One of the major performance indicators of flexible pavements is the riding quality, which can be determined from the longitudinal profiler tests. It provides an overall image of the roughness of the pavement surface, commonly evaluated in terms of the international roughness index (*IRI*) value. Pavement serviceability rating (*PSR*) is another pavement performance indicator, which can be predicted from the *IRI* measurements. The Paterson method, as expressed by the following Equation 12**,** can be used to determine the *PSR* (Paterson, 1986).

$$PSR = 5exp^{-0.0018(IRI)} \tag{12}$$

The road can be classified into 5 major categories: very good (5 < *PSR* < 4), good (4 < *PSR* < 3), fair (3 < *PSR* < 2), poor (2 < *PSR* < 1), or very poor (*PSR* < 1). A roadway with very good condition is free of cracks, rutting, and other depressions (Al-Omari & Darter, 1994), whereas the roadway with poor condition is full of cracks, rutting, and potholes and is considered terminal in most cases.

Measurement of surface rutting

Rutting may be defined as the vertical permanent deformation that occurs on top of the pavement surface layer along the traffic wheel paths. The total depth of rut is the accumulation of the permanent deformation that occurred in one or more layers of the pavement structure. The densification and shear failure that occurred within different layers leads to the accumulation of rut with the increasing number of vehicular load repetitions (Simpson, 2001). It is one of the major criteria that is used to evaluate the performance of the in-service flexible pavement. It can be predicted based on the calibrated material parameters from the laboratory; however, the performance of the in-service pavements may deviate from the predicted values.

Field measurements of the rutting can provide very good insight into the performance of the pavement layers. In the case of asphalt pavement, the rutting develops quite precipitously during the first few years and then levels off to a considerably gentler rate (Huang, 2004). According to the Asphalt Institute's design method, the expected maximum rutting for flexible pavements should be less than 0.50. inch. The depth of rut can be measured with a straight edge placed transversely over the left/right wheel-paths of the road, where the visible depression has occurred. The maximum vertical distance from the bottom of the straight edge to the top surface of the pavement, measured with a gauge, is registered as the rut depth (Gogoi et al., 2020).

Nondestructive Field Testing

The structural performance of the pavement layers can be evaluated with non-destructive field testing. Falling weight deflectometer (FWD) has been used extensively to evaluate the in situ moduli of the pavement layers for the calibration of material models according to the Mechanistic-Empirical Design Guide (ASTM, 2015; Nazzal & Mohammad, 2011). The deflection parameters, i.e., maximum deflection, base layer index (*BLI*), and *AREA,* can be determined from the complete deflection bowls. The *BLI* is the difference in deflection at the center and 12-inch (300 mm) away from the center, reported in µm. The *BLI* and *AREA* can be determined from the following Equations 13 and 14.

$$BLI = D_o - D_1 \tag{13}$$

$$AREA = 6\left(1 + \frac{2D_1}{D_o} + \frac{2D_2}{D_0} + \frac{D_3}{D_o}\right) \tag{14}$$

Here,

$D_O$ = deflection under FWD load center

$D_1$ = deflection observed 12-inch away from load center

$D_2$ = deflection observed 24-inch away from load center

$D_3$ = deflection observed 36-inch away from load center

The *BLI* values generally ranged between 100 to 400; a lower value indicated a stiffer base layer, whereas a higher value indicated the deteriorating condition of the base layer (Horak, 2007). The field deflection data obtained from the FWD are used to determine the in situ equivalent elastic moduli of the pavement layers based on ASTM D5858. Linear regression methods were also used to correlate the maximum deflections with the pavement layer properties determined from the laboratory (Hoffman & Thompson, 1982). While estimating the base layer stiffness with a thin asphalt layer, a constant asphalt modulus is recommended for the back-calculation process. There are very few studies available where the performance of the geocell reinforced pavement was assessed with FWD (Al-Qadi & Hughes, 2000). The back-calculated modulus of the geocell-reinforced layer showed a two-fold increment in stiffness.

Nowadays, with the advancement of technology, large-scale cyclic load testing, which is also known as automated plate load testing (APLT), is available to capture the response of flexible pavements. The APLT system was designed to measure the impact of confining pressure and load cycles on in situ permanent deformation and resilient modulus (White & Vennapusa, 2017). There are a few case studies available where the composite modulus of the geogrid reinforced base layer was estimated with the APLT (Vennapusa et al., 2018; White & Vennapusa, 2017). However, according to the author's knowledge, there are no such field studies that are currently available for geocell reinforced flexible pavement sections with nondestructive cyclic load testing.

### *2.5.3 Life-Cycle Cost Assessment for Geocell Reinforced Pavements*

The sustainability of flexible pavement is a major concern for the state and federal agencies as they recommend the utilization of recycled materials. Most often, the recycled materials are required to stabilize to attain the minimum requirement in terms of structural performance. The initial cost of construction for the recycled material with reinforcement or other stabilization methods may be higher compared to the traditional material though the long-term benefit can be achieved in terms of performance and economy. Several tools and metrics are available to assess the sustainability of any geotechnical infrastructure (Das et al., 2018, 2019).

Life-cycle Cost Assessment (LCCA) study may be considered as one of the major decision-support tools for the transportation agencies by comparing the total agency cost and user cost of different project alternatives (Hu et al., 2013). As the LCCA is determined before the implementation of any project, it is important to predict the performance of different alternatives either from historical data or some other analytical or numerical approach. According to the TxDOT pavement manual, a pavement design option that produces a 20% lower life-cycle cost should be selected, and the LCCA is not required if the Average Daily Traffic (ADT) is less than 10000. According to USDOT, the following steps are involved in life-cycle cost analysis (Beatty, 2002).

1. Establishment of design alternatives
2. Determine activity timing

3. Estimate cost (agency and user)
4. Compute life-cycle costs
5. Analyze and results

#### *2.5.3.1 Establishment of Design Alternatives*

At least two mutually conclusive options must be considered for the LCCA approach, and the analysis period should be selected in such a way that it can demonstrate the economic difference between the alternatives. The analysis period should be long enough to include at least one rehabilitation activity for each alternative.

#### *2.5.3.2 Determining Activity Timing*

The performance of the pavement will deteriorate with time, which may be determined in terms of roughness, cracks, rutting, or other non-destructive pavement evaluation techniques. The rate of deterioration of the pavement can be used to determine the series of rehabilitation and maintenance activities throughout the analysis period. The expenses associated with the maintenance activities account for a substantial portion of the total life-cycle cost.

#### *2.5.3.3 Estimation of Cost*

The cost of agency and user of the roads are considered for the LCCA. According to USDOT, it is not required to consider all the costs associated with all the alternatives, whereas the cost that demonstrates that the difference between the alternatives should be explored. The cost of construction and maintenance of the road throughout the design period of the pavement can be considered under the agency cost. The cost associated with the vehicle operation, travel time, and crash costs are considered under the user cost. The *IRI* values can be used to determine the user cost, which will increase with the increase of *IRI,* as shown in Figure 7.

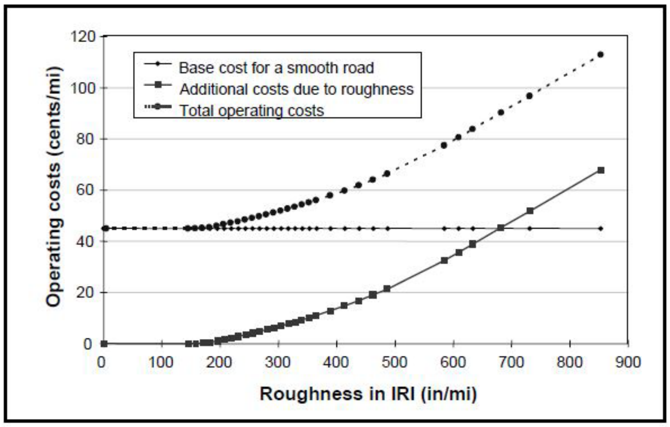

**Figure 7 Effect of road roughness on road user cost**

### *2.5.3.4 Compute Life-cycle Cost*

Life-cycle cost can be computed by knowing the activity timing, user, and agency cost. All the costs associated with different activities are converted to net present values to compare the alternatives directly. An expenditure stream diagram, as shown in Figure 8**,** may be developed for better visualization. The upward arrow in the diagram indicates expenditure, and the length of the arrow reflects the relative cost. The horizontal arrow segment presents the timing of the work zone activities and periods of normal operation between them. The salvage value of the pavement may be considered as a negative cost and can be represented with a downward arrow.

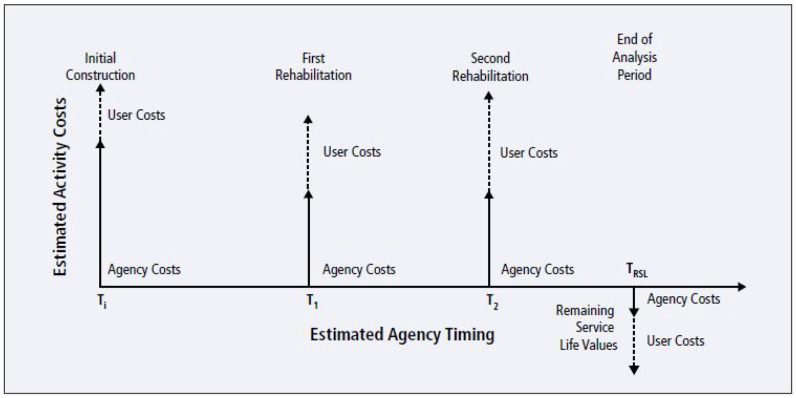

**Figure 8 Expenditure stream diagram (USDOT)**

*2.5.3.5 Analyze the Results*

Depending on variability and uncertainty associated with the LCCA, two approaches can be considered: deterministic and probabilistic (Abaza, 2004; Babashamsi et al., 2016; Das et al., 2019). In the deterministic approach, a fixed, discrete value is used as an input variable based on historical evidence or professional judgment. On the other hand, the probabilistic approach accounts for the uncertainty and variation in individual input parameters. In most cases, the alternatives are compared based on agency cost, whereas the user cost is estimated to check if any alternatives have an unreasonably high or minimal impact on the user. Traditionally, the deterministic LCCA approach is used, where the best alternative is chosen based on the lowest NPV.

## 2.6 Literature Gaps

Experimental studies on geocell-reinforced material showed promising results as the inclusion of geocell helped to improve the load-bearing capacity; however, limited studies are available for geocell reinforced RAP material and their application for the design of flexible pavements. The literature gaps identified in this study are listed in the following:

- There are no specific guidelines available for the construction of flexible pavement with single/double geocell layers
- There is a lack of knowledge about the field performance of the flexible pavement with GRRB and also on the pavements built on expansive soil subgrades. The application of geocell on top of expansive subgrade may have the potential to restrict the differential heaving on top of pavement surface, which should be verified from field studies
- There is a lack of field deflections data availability for the geocell-reinforced flexible pavement. The average deflection data obtained from the FWD are required to calibrate the material models for the M-E based design approach
- There is a need to develop a stress-dependent mechanistic-empirical model to predict the permanent deformation model for the geocell-reinforced unbound base layer
- The feasibility of using 100% RAP material in the field has not been explored adequately
- There is very little information available about the field performance of GRRBs constructed over the expansive soil

The dissertation research is an attempt to address some of the gaps identified in the GRRB studies, and the research works, including objectives, scope, and tasks performed, are presented in the following Chapters.

# CHAPTER III

# RESEARCH METHODOLOGY

The primary objective of the research is to assess the performance of geocell-reinforced reclaimed asphalt pavement-base (GRRB) layers based on prototype construction in real field conditions and then modeling the performance of the pavements in numerical studies. Accomplishments of this objective will lead to development design and construction guidance of the flexible pavements with GRRB layers. There are four major tasks involved in fulfilling the objectives of the current research study. The flowchart of the tasks and the associated activities are shown in Figure 9. The following section will discuss the purpose and methodology of each of the tasks.

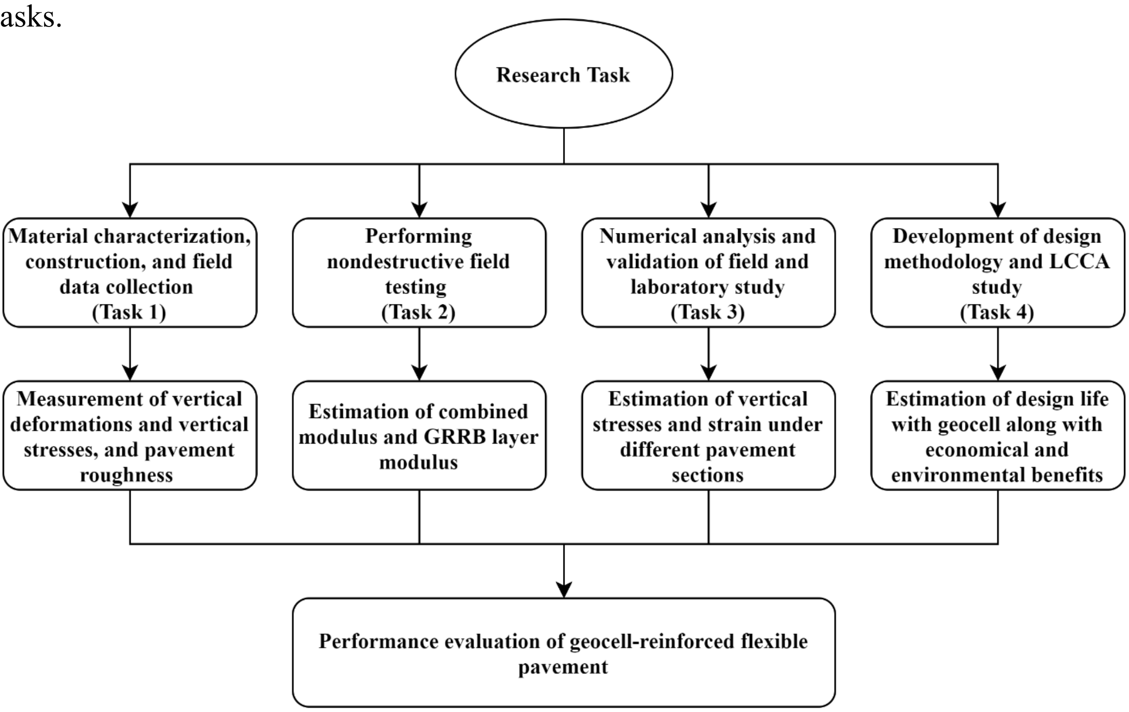

**Figure 9 Research Approach**

## 3.1 Material Characterization, Construction, Instrumentation and Field Data Collection & Analysis (Task 1)

The main purpose of this task is to monitor the performance of the reinforced pavement sections using field sensors. The data obtained from the field is primarily used to understand the behavior of the geocell-reinforced base layer under actual traffic loading. The deformation data obtained from the field is also used to develop pavement rutting models. Selection of appropriate site with expansive subsoil, investigation of the existing road sections, collection of expansive geomaterial, laboratory testing, design, analysis, and construction of test section, data collection, and analysis are the major activities involved in this task. The step-by-step activities involved in this task are shown in Figure 10.

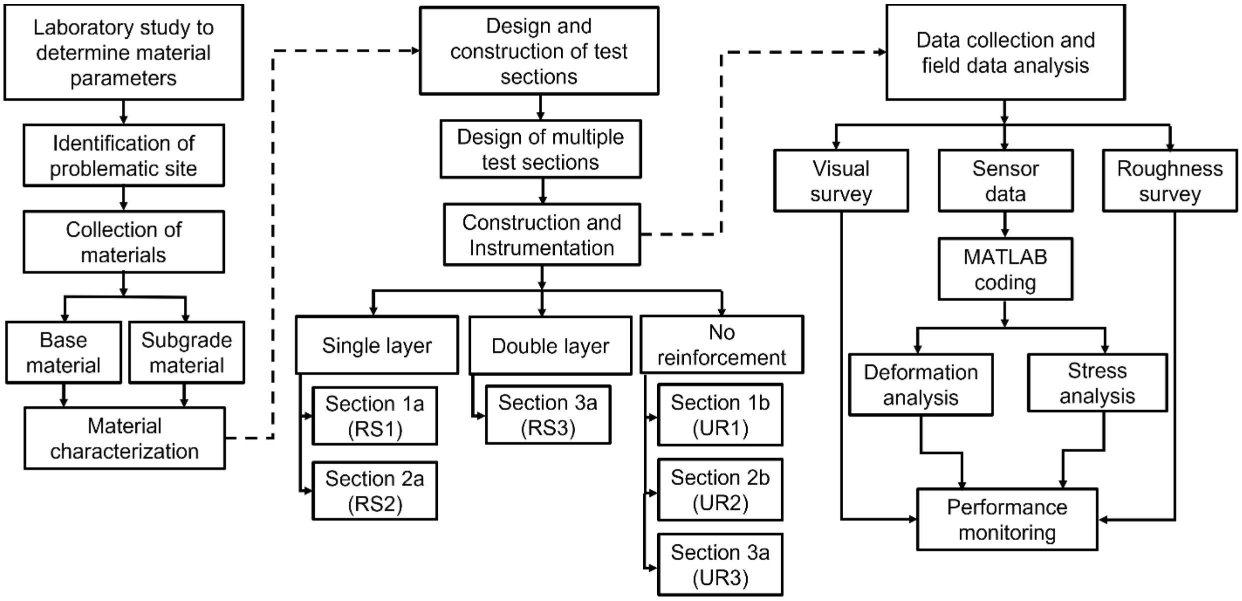

**Figure 10 Task 1-activity flowchart**

The appropriate site location was selected after investigating several locations where pavement distresses, including rutting, longitudinal cracking, and shoulder dropping, along with the presence of high expansive subgrade conditions, were observed. The subgrade material was collected from the site, and the RAP material was collected from the construction material stockpile in Alvarado, Texas. Basic material characteristics and resilient modulus tests were conducted on both subgrade and RAP materials. Material properties obtained from the current study and the composite modulus obtained from the large-scale repeated load tests conducted by George (2018) were then used to design the test sections with different configurations of geocells.

A total of three reinforced sections were constructed on the eastbound side of the FM 1807, Venus, Texas: reinforced section 1 (RS1) was constructed with 4-inch high geocell; reinforced section 2 (RS2) was constructed with 6-inch high geocell; reinforced section 3 (RS3) was constructed with two layers of 4-inch high geocell. The unreinforced sections: unreinforced section 1 (UR1), unreinforced section 2 (UR2), and unreinforced section 3 (UR3) were constructed on the westbound side by making trenches adjacent to the reinforced sections. The existing roadway on the westbound lane was used for the comparative study and defined as control section (CS). The total thickness and materials of the reinforced and control sections were similar; however, no geocell was used for the unreinforced sections.

All the reinforced sections were instrumented with shape array accelerometer (SAA) sensors and earth pressure cells (EPC). A similar type of instrumentation scheme was used for the unreinforced section; however, no earth pressure cells were used for

UR1 and UR3. The data obtained from the field sensors were collected regularly from the dataloggers installed in the field. The data-logger has five channels, and it can store data at any predefined frequency level. A data conversion protocol has been developed in MATLAB to process the collected raw data from the SAA to get the vertical deformations along the road sections. Apart from the instrumented data, regular field surveys are being conducted to observe and monitor field rutting and surface cracking of pavement sections. The results obtained from Task 1 are then used and analyzed to achieve the following outcomes:

- Field performance of the geocell reinforced Reclaimed Asphalt Pavement base layer termed here as GRRB layer based on vertical stress and deformation analysis
- Effectiveness of geocell reinforcement to mitigate the heaving due to expansive subgrade

## 3.2 Nondestructive Full-scale Pavement Testing (Task 2)

The purpose of this task is to evaluate the performance of different test sections by getting the responses from the static (FWD) and repeated load testing (APLT). The structural performance of the test sections (RS1, RS2, and RS3) and the existing road section (CS) can be evaluated with FWD and APLT. The FWD tests were conducted every 20 ft to observe the variation of stiffness along the length of the test sections. The FWD device drops a calibrated mass of approximately 9000 lb. (40 kN) on a 12-inch (300 mm) diameter loading plate, which is in firm contact with the surface of the pavement. The device can record the magnitude of the applied load and vertical deflection response of the pavement surface at seven locations, spaced at 12 inches apart. The raw data obtained from the field was used to back-calculate the stiffness of the pavement layer.

### 3.3 Numerical Analysis and Validation Studies (Task 3)

The purpose of the numerical study is to investigate the behavior of the GRRB layer under static load testing. The findings of this task are used to develop design methods for GRFP sections. The available test data from the lab and the field will be used to validate the numerical models with ABAQUS. The stress-strain relationship is required to be formulated for the cross-anisotropic material. In this study, one UMAT subroutine was developed to simulate the effect of geocell reinforcement in terms of modular ratio. The isotropic elastic material model was used for the asphalt layer, the geocell layer was modeled as shell elements with a linear isotopically elastic model, and the subgrade layer was modeled as elastic material. The pavement responses obtained from the field tests are compared with the numerical response model developed with ABAQUS/CAE. The response collected from the plate load tests on unreinforced and geocell reinforced base layer conducted by Thakur (2011) were used for the verification of the numerical model. The three-dimensional model has been prepared to validate the currently available static load test results. The results obtained from Task 3 are used to address the following outcomes.

- Numerical study to understand the behavior of flexible pavement with different configurations of loading, geometry, material properties, and reinforcement aspect ratios

- Simulation of FWD test conditions to compare the results obtained from the field

### 3.4 Development of Design Methodology and Life-Cycle Cost Analysis (Task 4)

The purpose of this task is to develop a design framework for the flexible pavement with GRRB based on the results obtained from the experimental, field, and numerical studies. The cost-benefit study is performed to compare the life-cycle cost of conventional pavement and pavements with GRRBs. The design of flexible pavement with geocell is not well understood due to a lack of knowledge about the performance of such pavement in the field. A design framework is hence developed based on the assessment of the field section and a parametric study conducted with the finite element model. Design methodology is developed to estimate the design life of reinforced pavements with a different configuration of geocell and types of infill materials. The material and equipment costs associated with such reinforced pavements are estimated along with the cost of maintenance for alternative rehabilitation techniques. The data obtained from this study is used to develop a framework to assess the life-cycle cost of the flexible pavements with GRRBs.

### 3.5 Summary

This chapter presents the methodology and activities involved under each individual task to achieve the primary objectives of the current study. The research methodology adopted in this study involves laboratory testing, field investigation, construction, and long-term monitoring of the geocell reinforced test sections. The field sections are instrumented with shape array sensors and earth pressure plates to collect the responses in terms of vertical deformations and stresses. Nondestructive field-testing studies are required to evaluate the structural performance of the reinforced test sections with different thicknesses of the GRRB layer. The layer properties evaluated from the field testing are used for the development and verification of numerical models. Flexible pavement responses obtained from parametric studies conducted with the numerical model are used to evaluate the design life for the reinforced and unreinforced pavements. The benefits of using geocell are also assessed in terms of economy and environment-related sustainability benefits based on the LCCA and sustainability studies.

# CHAPTER IV

# CONSTRUCTION, INSTRUMENTATION OF GRRB LAYERS, AND FIELD DATA COLLECTION

## 4.1 Background

Flexible pavement distresses such as roughness, cracking, and rutting are common for pavements that are categorized as medium to low volume roads. Frequent maintenance is required to uphold the performance of the road with a "Good" rating. The existence of non-uniform support is one of the major reasons for the recurrence of distresses on the reconstructed overlay. Providing cellular confinement for the base layer may provide additional support to enhance the performance of the pavement. The utilization of RAP material will also minimize the cost of construction and enhance the sustainability of the road infrastructures. Static and repeated load testing has been conducted in earlier studies to understand the behavior of the geocell-reinforced RAP base (GRRB) layer. To understand the performance of the GRRB layers under vehicular loading, a real-scale road section was required, where the existing base layer can be replaced with it. An ideal road section was selected for the field study investigations, where the existing road section suffered from several types of pavement distresses due to non-uniform support conditions and roughness conditions. The following section will discuss the study area.

## 4.2 Test Site Location

The study area was chosen after investigating several Farm to Market roads where pavement distresses were visible and regular maintenance works did not uphold the performance of the pavement. The study area selected for this study was FM 1807, which is a two-lane-two-way road. Longitudinal cracking, rutting, and shoulder depressions were the most common problems, and many of these are attributed to the underlying soil. This road section is located in Venus, the southern part of the Dallas-Fort-Worth (DFW) area, as shown in Figure 11.

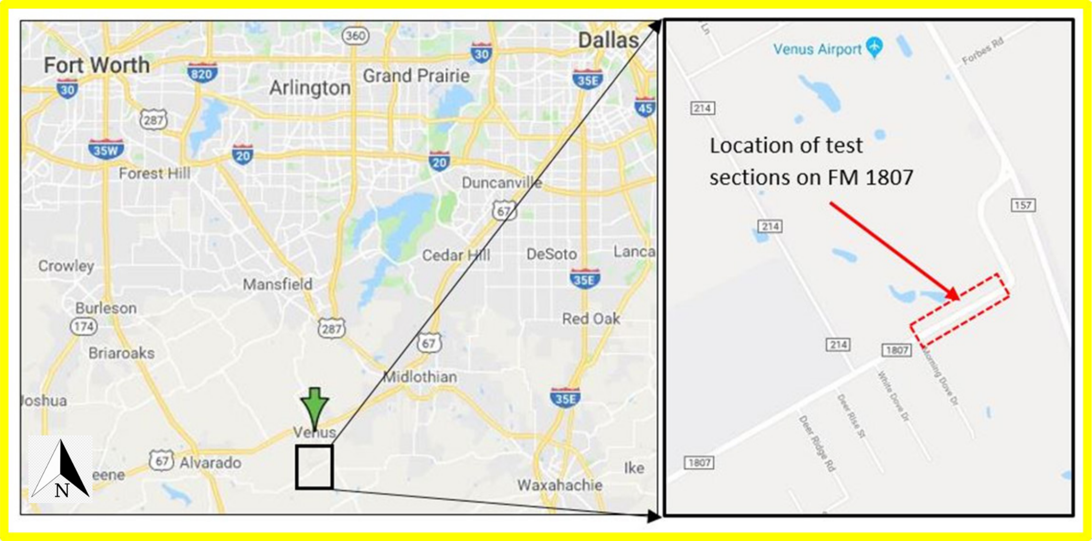

**Figure 11 Study location: FM 1807, Venus, Texas**

Most of the road networks within this region are constructed over expansive soil formation. This farm-to-market road, FM 1807 site, was highly compromised due to the presence of expansive subsoil conditions. Transportation agencies had to spend a lot of money on the maintenance and rehabilitation of this road. Severe channelized rutting and cracking were observed during May 2015, as shown in Figure 12a**.** The presence of expansive soil was identified as the primary reason for such distresses as this kind of soil changes its volume with the alternative wetting-drying cycles and leads to the differential movement of the subgrade layer and overlying layers. Most pavements with moderate thicknesses flexible pavements will experience distress on these soils.  Major rehabilitation work was necessitated during 2017 when a 2-inch-thick asphalt overlay was placed on top of the existing road surface. However, the longitudinal crack reappeared during January 2018 along the longitudinal direction of the eastbound lane, as shown in Figure 12b**.**  These unremitting failures of these pavement sections motivated to select this location as an ideal candidate for the construction of the test sections with GRRB layer.

(a) (b)

**Figure 12 Pavement distresses on FM 1807: a) channelized rutting observed during May 2016, b) longitudinal cracks observed after six months of the major rehabilitation work, during January 2018**

## 4.3 Material Properties

After finalizing the location, subgrade soil was collected from the study area, and the RAP material proposed for infill material for geocells was also collected from the nearby stockpile for the comprehensive material characterization. The geocell used for this study was made of the HDPE sheet and these with the cell height of 4-inch and 6-inch. The following sections discuss the material properties in detail.

### *4.3.1 Subgrade Soil*

The subgrade soil was collected from the project site by making trenches adjacent to the pavement shoulder, where visual depressions and cracking were observed. The Atterberg limit test showed that the soil had a liquid limit of 58 and a plasticity index of 31. This soil was classified as high plasticity clay (CH), according to the Unified Soil Classification System (USCS). The maximum dry density and optimum moisture content were 89.5 pcf and 26.8 %, respectively, which is shown in Figure 13. A Free-swell test was conducted according to ASTM D4546-14e1, which revealed that the soil had a high swelling potential of 8.5%, as shown in Figure 14**.**

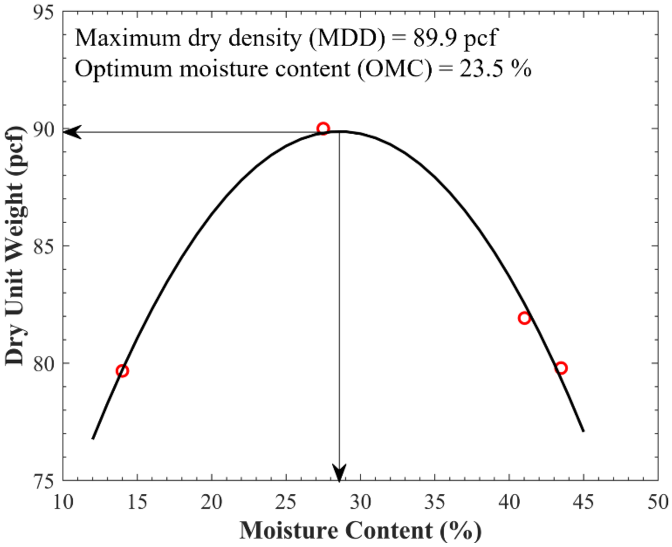

**Figure 13 Standard proctor test results for soil from the test site.**

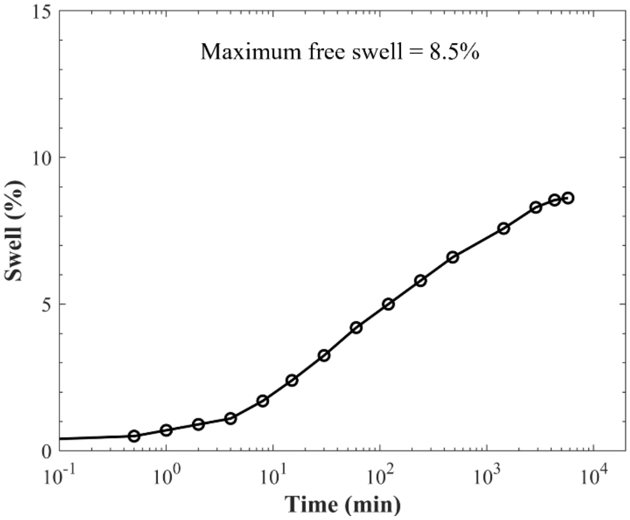

**Figure 14 Swell test results on the soil sample from field**

The resilient modulus of the subgrade soil ($M_{r(subg)}$) was determined based on the AASHTO T307 standard method, and the three-parameters model based on non-linear regression was developed analyzing the laboratory test results, and these results are shown in Equation 15.

$$M_{r(subg)} = 0.43P_a\left(\frac{\theta}{\mathrm{P_a}}\right)^{-0.228}\left(\frac{\tau_{oct}}{\mathrm{P_a}}+1\right)^{1.62} \tag{15}$$

Where,

$M_{r(subg)}$ = resilient modulus of the subgrade soil in

$\theta$ = bulk stress

$\tau_{oct}$ = octahedral shear stress

$\mathrm{P_a}$ = atmospheric pressure

The effect of deviator stress and confinement on resilient modulus are shown in Figure 15a and 15b, respectively. It was observed that the resilient modulus decreased with the increase of deviatoric stress at low confining stress of 2 psi; whereas the resilient modulus increased with the increase of deviatoric stress when higher confinement was applied. On the other hand, the increase in confinement at constant deviatoric stress reduces the resilient modulus. The behavior of the subgrade material is highly dependent on the applied deviatoric stress and confining pressure, and hence, the stress-dependent non-linear model should be used for the evaluation of the stiffness of the subgrade material. However, a constant elastic modulus can be determined from this resilient modulus model for any given magnitudes of deviator stress and confining pressure. This can be defined as the elastic modulus of the subgrade for the linear elastic analysis.

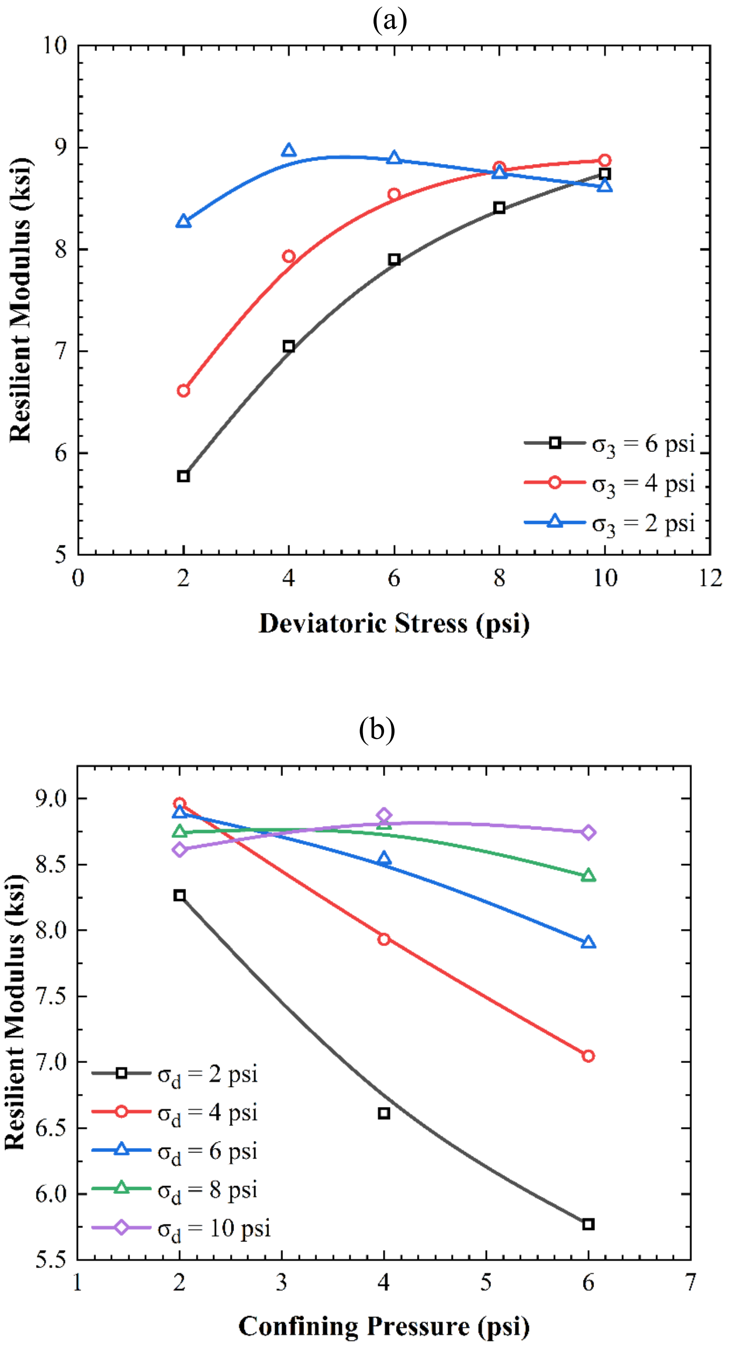

**Figure 15 Dependency of subgrade resilient modulus on a) deviatoric stress and b) confining pressure**

### *4.3.2 Reclaimed Asphalt Pavement (RAP) Material*

The RAP material was collected from a stockpile near highway I35, Alvarado, Texas. This stockpile is located 10 miles from the project site. The maximum dry density and moisture content for this material was 122 pcf and 4.5%, respectively. The grain size tests on RAP samples were performed according to the AASHTO T27 standard, as shown in Figure 16. Three tests were conducted to check the variability of RAP materials collected from various locations of the stockpile. It was observed that the grain-size curve obtained from separate locations followed a similar trend.

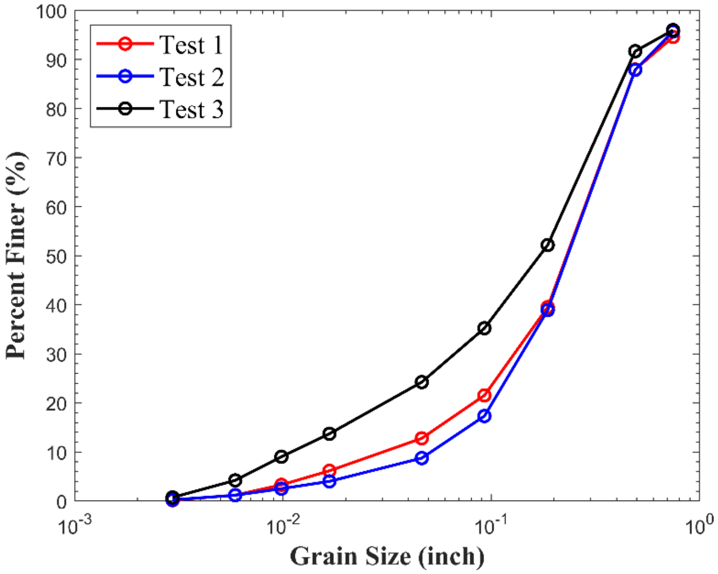

**Figure 16 Grain size distribution of RAP material**

The resilient modulus of the RAP material ($M_{r(base)}$) was also determined based on the NCHRP standard, and the three-parameters model based on non-linear regression was developed, as shown in Equation 16.

$$M_{r(base)} = 1.88 P_a \left( \frac{\theta}{P_a} \right)^{0.88} \left( \frac{\tau_{oct}}{P_a} + 1 \right)^{-1.25} \tag{16}$$

The effect of deviatoric stress and confining pressure on resilient modulus is shown in Figure 17. It was observed that at lower confinement (2 psi), the untreated RAP material showed some strength hardening behavior as the resilient modulus increase with the increase of deviatoric stress; however, at higher confining pressure, strength softening behavior was observed.

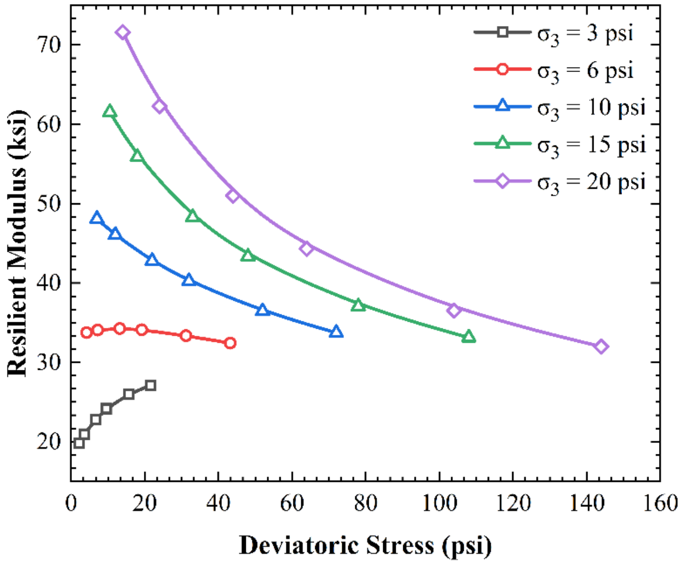

**Figure 17 Effect of deviatoric stress on resilient modulus for untreated reclaimed asphalt pavement material**

The standard applied stress on top of a flexible pavement from a single-wheel vehicular loading is around 80 psi (Huang, 2004). The average anticipated vertical stress within a base layer located under a thin layer of asphalt pavement will range between 30 and 60 psi, depending on the thickness of the base layer. The corresponding resilient modulus will range between 30 to 37 ksi based on the developed resilient modulus model for the untreated RAP material. It is expected that the resilient modulus of the geocell-reinforced RAP material will increase due to the inclusion of geocell; however, there is no standard guideline available to prepare samples with geocell for the repeated load triaxial test. The large-scale repeated load test conducted by George (2019) showed that the inclusion of geocell can increase the resilient modulus of the RAP material by 3 to 4 times. The modulus improvement factor with large-scale study showed significant improvement; however, a field study was required to determine the field calibration correlation factor for the geocell-reinforced base layers.

### *4.3.3 Geocell and Geotextile Reinforcements*

The geocell used for this study was primarily made from HDPE sheets. Geocell with two different heights (4-inch and 6-inch) were selected for the construction of test sections. The geometry and mechanical properties of geocell, as provided by the manufacturer, are also listed in Table 2. To prevent the loss of base material during construction, a non-woven geotextile with 140 N seam peel strength, also conforming to the design requirements as per TxDOT DMS 6200, was used to separate the base and subgrade layers.

### *4.3.4 Material Properties from Laboratory Analyses*

The following Table 2 summarizes all the material and their properties used for the current research work.

**Table 2 Material Properties**

| Material | Parameter | Value | | Standard |
|---|---|---|---|---|
| Subgrade | Liquid limit (%) | 58 | | ASTM D4318 |
| | Plasticity Index (%) | 31 | | ASTM D4318 |
| | Optimum moisture content (%) | 23.5 | | ASTM D698-14e1 |
| | Maximum dry density (pcf) | 89.9 | | |
| | Swell Potential (%) | 8.5 | | ASTM D4546 |
| | Resilient Modulus (ksi) | Equation 15 | | AASHTO T 307 |
| RAP (George et al., 2019) | Maximum dry density (pcf) | 122 | | Tex-113 E |
| | Optimum moisture content (%) | 4.5 | | Tex-113 E |
| | Resilient Modulus (ksi) | Equation 16 | | NCHRP |
| Geocell | Nominal expanded cell size (in.) | 12.6 x 11.3 | | Manufacturer |
| | Nominal expanded cell area (in2) | 71.3 | | - |
| | Cell depth (in.) | 4 | 6 | - |
| | Seam peel strength (lbf) | 320 | 480 | - |

Note: 1 in. = 2.54 cm and 1 ksi = 6.89 MPa; $\theta$ = bulk stress in ksi.

The material properties used in Table 2 were used to design the initial test sections with a different configuration of geocell. The following section will discuss the analysis of test sections for the preliminary design of the test sections.

## 4.4 Preliminary Design Analyses of Test Sections and Their Configurations

The test section was proposed to construct on an existing road that had a 4-inch asphalt layer at the top, followed by a 15-inch flex base layer on top of the existing subgrade. The thickness of the existing asphalt layer was the combination of a 2-inch old asphalt layer with an overlay of 2-inch. The analyses for the test sections were conducted considering a 2-inch-thick asphalt layer; the thickness of the GRRB layers varied from 6-inch to 12-inch, as reported in Table 3. The purpose of the field monitoring and investigations was to evaluate the performance of geocell in provided stable and uniform support; hence two distinct types of geocell (4-inch and 6-inch height) were used for this study. Single-layer reinforcement systems were considered for RS1 and RS2, respectively, which contained 4-inch and 6-inch geocells, respectively.

A double-layer system was considered for the third section (RS3), where two (2) layers of 4-inch geocells were studied. A minimum cover thickness of 1 inch was required to maintain a workable platform on top of the geocell layer; hence a 2-inch-thick RAP cover was considered on top of each geocell layer.

**Table 3 Test Section Details**

| **Section ID** | **Section Description** | $t_{asp}$ **(inch)** | $t_{base}$ **(inch)** | $h_{gc}$ **(inch)** | **Thickness of RAP Cover (in.)** | |
|---|---|---|---|---|---|---|
| | | | | | **top** | **intermediate** |
| RS1 | 6-inch GRRB | 2 | 6 | 4 | 2 | - |
| RS2 | 8-inch GRRB | 2 | 8 | 6 | 2 | - |
| RS3 | 2#6-inch GRRB | 2 | 12 | 4+4 | 2 | 2 |

Note: $t_{asp}$ = thickness of the asphalt layer; $t_{base}$ = thickness of the base layer; $h_{gc}$ = thickness of the geocell layer

All the test sections were analyzed for 20 years of service life using the FPS 21 software, as recommended by TxDOT pavement design guidance. The parameters used for this analysis are presented in Table 4. The actual depth of the subgrade of the existing section was unknown before the construction; hence a 12-inch-thick subgrade layer was considered for the initial analyses of the test sections.

**Table 4 Analysis of Test Section with FPS 21**

| **Description** | | **RS1** | **RS2** | **RS3** |
|---|---|---|---|---|
| Asphalt layer | Thickness (in.) | 2 | 2 | 2 |
| | Modulus (ksi) | 500 | 500 | 500 |
| | Poisson's ratio | 0.4 | 0.4 | 0.4 |
| GRRB layer | Thickness (in.) | 6 | 8 | 12 |
| | Modulus (ksi) | 50.8 | 50.8 | 50.8 |
| | Poisson ratio | 0.3 | 0.3 | 0.3 |
| Subgrade layer | Thickness (in.) | 12 | 12 | 12 |
| | Modulus (ksi) | 8.7 | 8.7 | 8.7 |
| | Poisson's ratio | 0.3 | 0.3 | 0.3 |
| Maximum tensile micro-strain bottom of HMA layer | | 221 | 216 | 213 |
| Maximum vertical micro-strain at the top of subgrade | | 570 | 430 | 345 |
| Rutting life (ESAL in million) | | 0.46 | 1.62 | 1.31 |
| Fatigue Cracking life (ESAL in million) | | 1.16 | 1.25 | 4.33 |

Note: 1 in. = 2.54 cm and 1 ksi = 6.89 Mpa

## 4.5 Construction of Test Sections

### *4.5.1 Construction Schedule*

There are several activities involved in each phase of the construction of test sections, as presented in Figure 18. The actual construction began on 5th November 2018, when three trenches were made on the westbound lane for the placement of PVC casing to accommodate the deflection sensors. The trenches constructed within the westbound lane were used as unreinforced sections. It required a single working day to construct one test section of 130 ft long, including the milling of existing road surface, preparation of roadbed, placement of geotextile, placement of GRRB layer, and temporary surface layer. The surfaces of all the test sections were initially covered with 2-inch-thick flex base material to keep the road sections open to traffic after each working day. The final surface layer with asphalt was constructed on December 12th,

2018. Deflection and pressure sensors, along with the data acquisition system, were installed on 3rd December 2018.

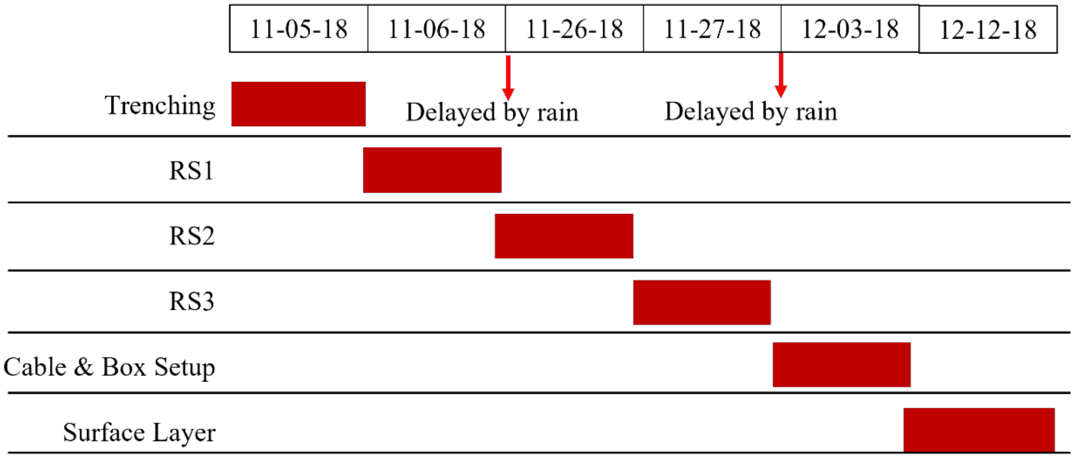

**Figure 18 Construction schedule**

### *4.5.2 Safety and Traffic Control*

Before the beginning of the field construction work, a safety meeting was held in Johnson County Office, Keene, Texas, on 5th November 2018, and all the members involved in the construction project work were advised to follow safety protocols. Temporary traffic signals were set up at both ends to divert the traffic from the lane of construction. In addition to the traffic signals, rumble strips and necessary traffic signs and markings were used to make aware the road traffic before entering the project site. In between the traffic signals, a dedicated person was kept near the entrance of access roads to control the traffic from the access road to FM 1807.

### *4.5.3 Construction Activities*

#### 4.4.3.1 Construction of Unreinforced Sections on the Westbound Lane

Three trenches were excavated on the westbound side of the road for the preparation of unreinforced test sections: UR1, UR2, and UR3, as shown in Table 5. During the construction of the unreinforced section, PVC casing was also placed at the bottom of the section for the shape array sensors. All the trenches were located at the middle of each test section, and the depth of trenches was made in such a way that the top of the PVC casings was aligned with the bottom of the adjacent reinforced sections. These trenches: UR1, UR2, and UR3 were filled up in such a way that they can serve as unreinforced test sections corresponding to the reinforced sections: RS1, RS2, and RS3. One earth pressure cell was also placed under the UR2 section to compare the vertical stresses with the reinforced section.

**Table 5 Trenches on the Westbound Lane**

| Section ID | Trench Size | | | PVC Installation | Earth Pressure Cell Installation |
|---|---|---|---|---|---|
| | Width (inch) | Depth (inch) | Length (feet) | | |
| UR1 | 12 | 10 | 15 | Yes | No |
| UR2 | 12 | 12 | 15 | Yes | Yes |
| UR3 | 12 | 15 | 15 | Yes | No |

Note: Westbound Lane including the UR1, UR2, and UR3 are defined as control section (CS)

**Preparation of Trenches:** A trencher (Figure 19a) with 12-inch cutting width was used to make all the trenches on the westbound lane. During this period, the westbound lane was closed, and the eastbound lane was open to traffic operations. Trenching was begun from the pavement shoulder and continued to the centerline of the pavement.

**Leveling Trench Bed:** A wacky packer was used to level all the trench beds, as shown in Figure 19b. The bottom of the trenches was further leveled with sand where some undulation was noticed.

**Installation of PVC Pipe Casing:** After the preparation of the trench bed, a 2-inch diameter, 40 grade PVC pipe was installed at the middle of each trench section (Figure 19c). The total length of the PVC pipe was 20 ft, which was formed by adding two 10 ft long pipes with a coupler. Both ends of the pipe were closed with pipe caps.

**Installation of Earth Pressure Cell:** Earth pressure cell was installed in the second trench (UR2), which is located adjacent to RS2. Before the installation of the pressure cell, a smooth bed was prepared with sand at the top of the PVC pipe, also shown in Figure 19d.

**Backfilling with Flex Base:** RAP material was used to backfill the trench up to a depth of 4-inch from the existing pavement surface. Bobcat was used to pour the material into the trench, which was compacted with a wacky packer (Figure 19e).

**Surfacing with Cold Mix Asphalt:** After the compaction of the base layer, cold-mix asphalt was used to prepare the surface layer, which was also compacted with a wacky packer, as shown in Figure 19f.

(a) (b)

(c) (d)

(e) (f)

**Figure 19 Construction of unreinforced sections and installation of PVC pipe on the westbound lane**

#### 4.4.3.2 Construction of Reinforced Sections

All the reinforced test sections were constructed in the eastbound lane by milling out the existing road section. The following sections describe the construction steps involved for RS1, RS2, and RS3 using GRRB layers, respectively.

*Construction of Reinforced Section, RS1*

**Step 1 (Milling of existing road section)**: The RX-600e cold planer machine (Figure 20a) with 4-track assemblies was used to excavate the road up to a depth of 10-inch. This is powered by a 675-horsepower engine, and the contractor can cut up to a depth of 13-inch with a width of 7 ft 2 inches. Two passes were required to excavate the whole width of 14 ft 4 inches.

**Step 2 (Preparation of roadbed):** After the milling process, a bobcat with a loader head was used to smooth the base of the reinforced section, and a pneumatic roller was used to achieve proper compaction. The compacted roadbed is shown in Figure 20b.

**Step 3 (Trenching and installation of PVC pipe casing):** A 4”x4” inch trench was prepared for the installation of PVC pile casing. A trencher with 4-inch cutting width was used to make the trench, as shown in Figure 20c. 20 ft long PVC pipe was installed (Figure 20d) within the trench, which was also connected with the PVC pipe previously installed on the westbound lane.

**Steps 4 (Placement of Earth Pressure Plates):** Two pressure cells were installed adjacent to the PVC pipe. A smooth sand bed was prepared at the top and bottom of these pressure cells (Figure 20e) for the uniform distribution of stresses. These pressure plates were located underneath the wheel path of the eastbound lane.

**Step 5 (Placement of Geotextile)** Mirafi 140N geotextile was used, which meets the criteria of TxDOT DMS 6200 type. Geotextile was placed between the prepared grade and geocell reinforced section, and the main purpose was the only separation. A 15 ft width roll of geotextile was used in this project, as shown in Figure 20f.

**Step 6 (Placement of Geocell and filling with RAP):** In this project 4 inch and 6-inch-high HDPE geocell panels were used for reinforcement. Section 1 was reinforced with 4-inch height geocell panels, and after the complete stretching, the width and length of the geocell panels were 7.5 ft and 30 ft., respectively. The longer direction of the panels was placed towards the direction of traffic, and two panels were required to fill up the road width. All the adjacent panels were tied with zip ties. 100% RAP material, transported from a stockpile located 4 miles away from the project site, was used to filling up the geocells (Figure 20g). A minimum cover thickness of 2-inch was maintained throughout the construction process.

**Step 7 (Compaction):** Pneumatic-type roller was used to compact the RAP layer, as shown in Figure 20h. After the placement of the RAP layer, a motor grader was used to scrap and maintain a leveled surface before the application of a pneumatic type of roller. A vibratory type of compactor was not used at the top of the RAP layer.

**Step 8 (Placement of temporary surface layer):** Motor grader (Figure 20i) was used to scrap up 2-inch from the compacted RAP layer, and this top layer was filled with flex base material (Figure 20j) which will serve as a temporary surface layer before the placement of final asphalt layer. This temporary flex base layer was compacted with a vibratory roller, as shown in Figure 20k. After the construction of each adjacent section, the lane was cleaned up with a cleaning vehicle (Figure 20l) to remove the dust and debris from the road surface.

**Figure 20 Construction of reinforced section 1 (RS1) with a single layer of 4-inch geocell**

*Construction of Reinforced Section 2 (RS2)*

The construction steps described for RS1 were followed for RS2. The depth of milling was 12 inches, and the height of geocells was 6-inch for RS2. Construction activities involved in the RS2 section are shown in Figure 21.

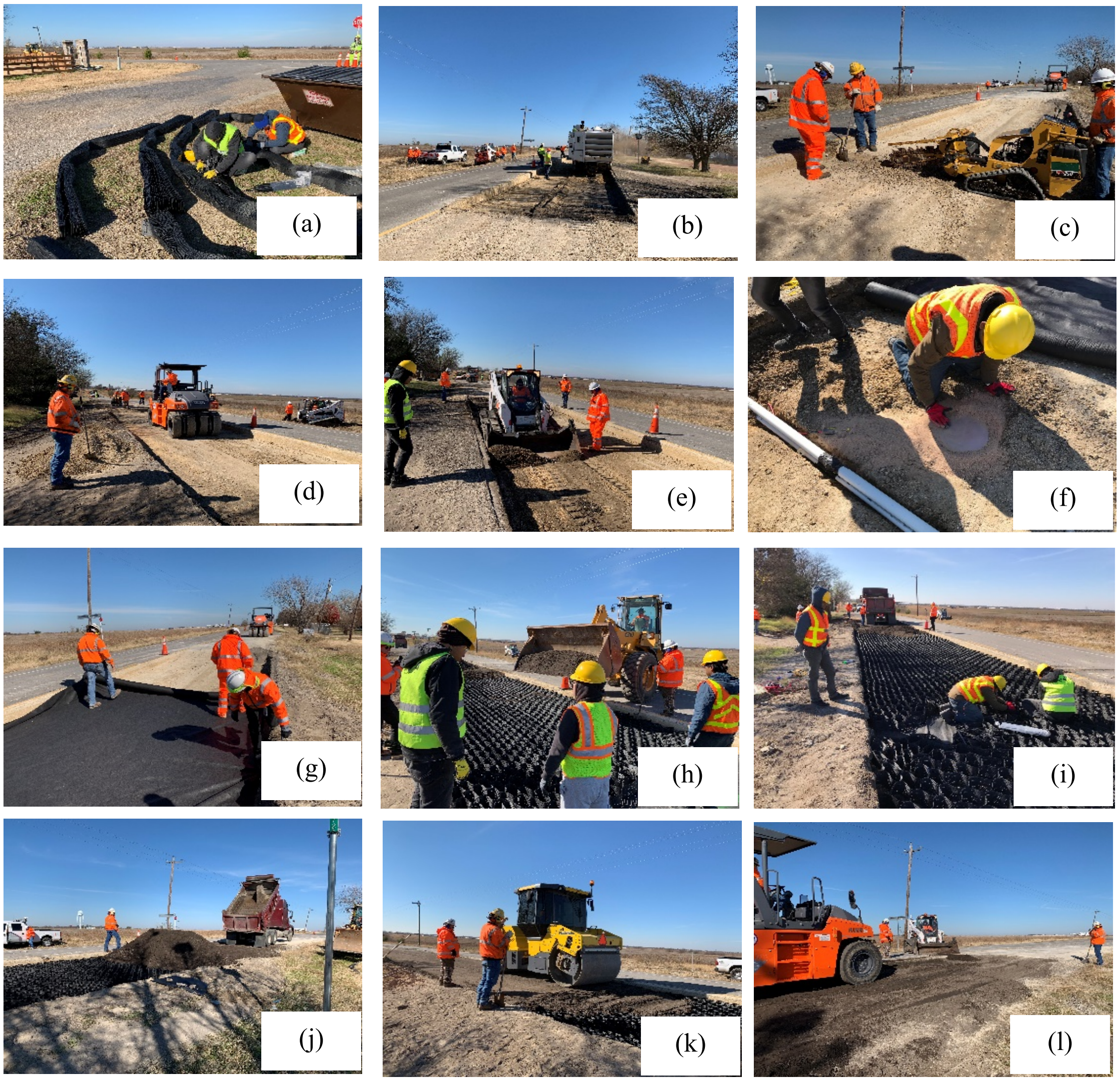

**Figure 21 Construction of reinforced Section 2 (RS2) with a single layer of 6-inch geocell**

### *Construction of Reinforced Section 3 (RS3)*

In the case of RS3, the depth of milling was 15 inches, and the total height of double-layer geocell was 12-inch for RS3. For the construction of the first layer, step 1 to step 7 were followed. After the construction of the first layer, the second layer of geocell was placed, and steps 6 to 8 were followed to construct this double layer reinforcement system. Construction activities involved for RS3 are shown in Figure 22.

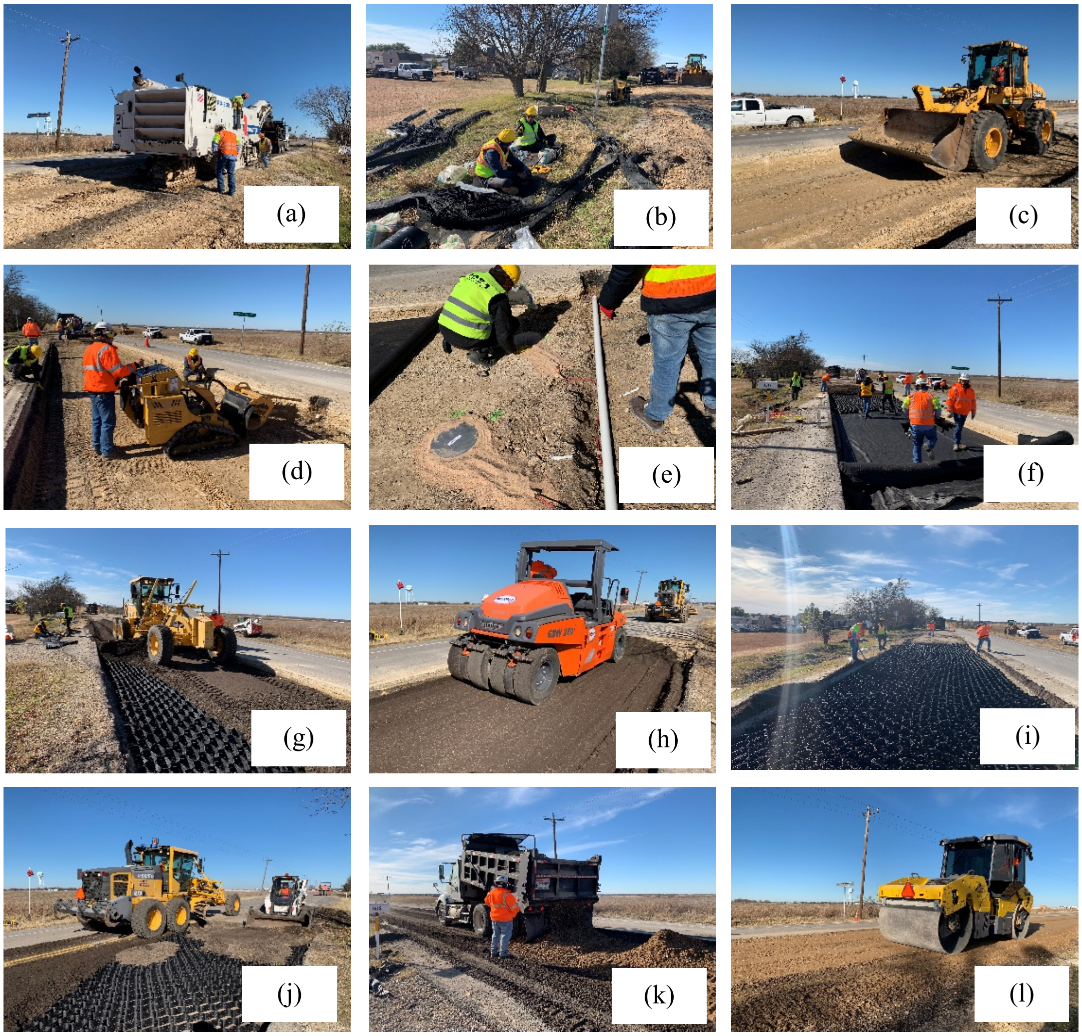

**Figure 22 Construction of reinforced section 3 (RS3) with 2 layers of 4-inch geocells**

## 4.6 As-Built Test Sections

The actual thickness of the constructed layers varied within the test section due to the adjustment of road slope for drainage conditions. The cover thicknesses of the RAP layer varied from 1 inch to 2 inches to accommodate the difference in thickness, as shown in Figure 23. Only a single lane (Eastbound) with 15 feet width was excavated for the construction of test sections, which did not allow the extension of the geocell panel beyond the centerline of the road. The location of wheel paths, as shown in Figure 23**,** portrays that the extended portion of the geocell panel under the right wheel path was more than 3 feet on either side; however, the extended portion of the geocell under the left wheel path was less than 2 feet., near to the centerline of the road. The as-built cross-section of the test section is shown in Figure 24.

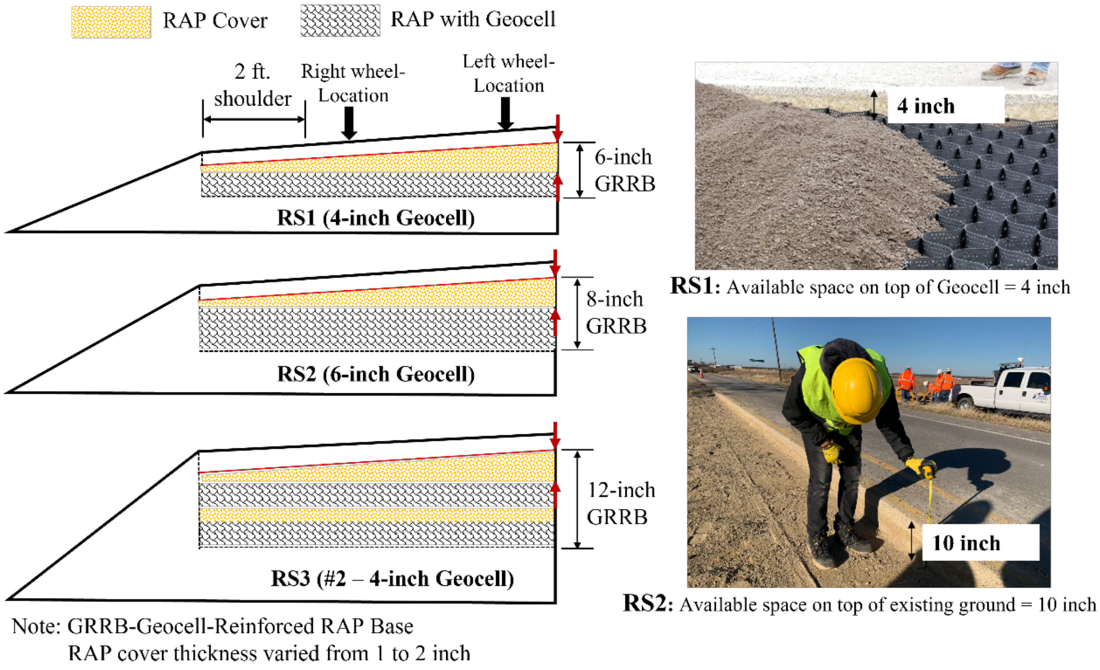

**RS1:** Available space on top of Geocell = 4 inch

**RS2:** Available space on top of existing ground = 10 inch

**Figure 23 Variability in RAP cover thickness across the test sections**

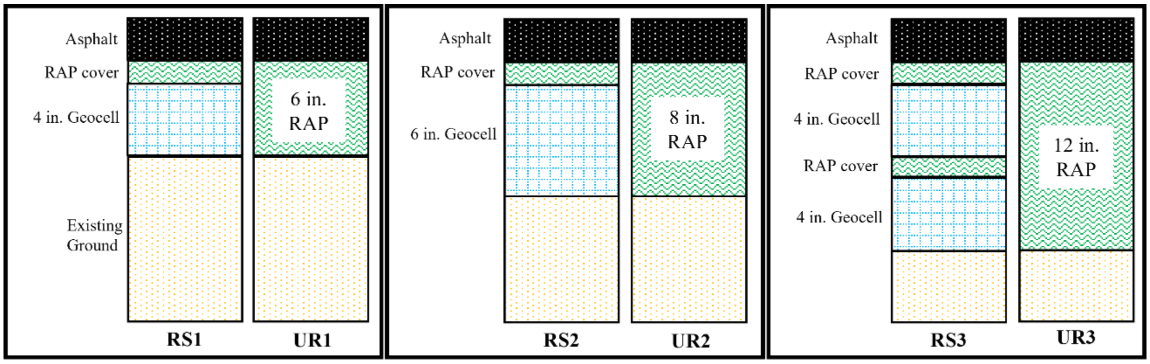

**Figure 24 Cross-section of different test sections (after construction)**

## Control Section (CS)

The westbound lane of the road, including the UR1, UR2, and UR3, is defined as the control section (CS). The longitudinal profile of the control section is shown in Figure 25. The total length of the control section is 390 ft.; however, for comparison purposes, the 130 ft. segment parallel to the RS2 section was considered for monitoring and comparing roughness and rutting distress in the control section.

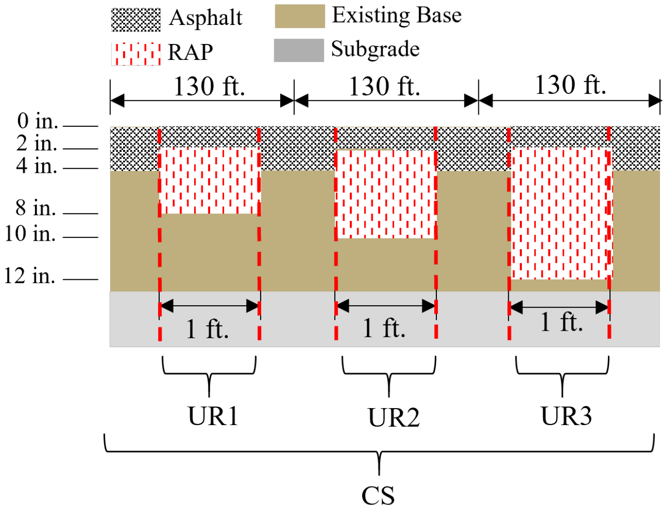

**Figure 25 Control sections construction within the westbound lane**

## 4.7 Installation Technique of Geocell Panels

The performance of the GRRB layers may vary depending on the height to depth (*h*/*d*) ratio of the geocell. To achieve two different geosynthetic layer aspect ratios, RS1 and RS2 sections were constructed with 4-inch and 6-inch geocells, having the same opening diameter of 10-inch. The geocells used for RS3 sections had the same *h/d* ratio as RS1; however, the total thickness of the GRRB layer was twice the value of RS1. Regardless of the *h/d* ratios, the size of panels is the same, and after full stretch, the geocell layer is 30 feet long × 7.5 feet wide. The sequential installation procedure of geocell panels is discussed below.

The plan area of each test section was 130 feet × 15 feet, which required at least eight panels of geocell to cover a single layer. Since the RS1 and RS2 were constructed as a double layer system, the total required panel number was 8; however, RS3 had a double layer with 16 panels. Sequential construction plan: step 1 to step 6 is shown in Figure 26. In the beginning, two geocell panels were placed adjacent to each other, as shown in step 1. Plastic zip ties were used to tie up the adjacent panels, as shown in step 2. After tying, the panel group was stretched up to 30 ft. towards the traffic direction, which is shown in step 3. For the intermediate panels, step 1 was followed, which is shown in step 4. The tying process between the stretched geocell panels with the unstretched panels is presented in step 5, and the stretching of the intermediate panels is shown in step 6. The installation steps 1 to 6 repeated was repeated one more time to cover the whole test section of 1950 square feet (sq. ft.).

No additional equipment was required for the construction of the geocell section. However, the additional time required for the placement of geocell was 2 hrs., which is about 16.25 sq. ft. per minute. Base stabilization with Geocell has the potential to be the faster stabilization technique as the time required for the construction of other base stabilization methods is significantly high.

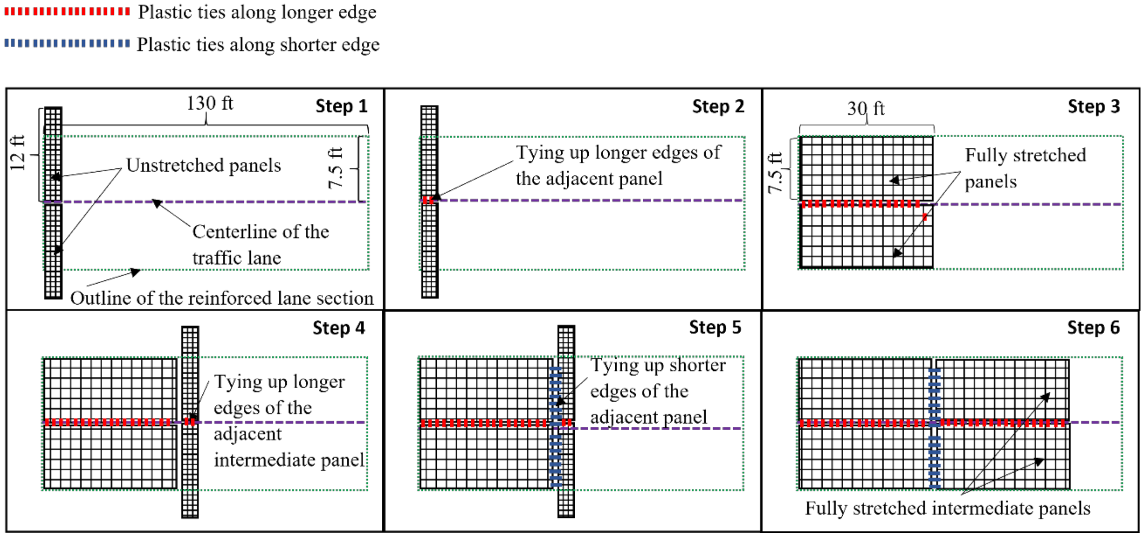

**Figure 26 Sequential installation of geocell panel**

## 4.8 Field Instrumentation Details

The test sections were instrumented with Shape Array Accelerometers (SAAs) and Earth Pressure Cells (EPCs) to collect the responses from the test sections in a specific time interval. The SAAs used in this study consisted of 18 segments, and the length of each segment was 19.7 inches. Each SAA segment consists of MEMS (Micro-electromechanical sensors) gravity sensors, which can measure the acceleration in x, y, and z directions. The acceleration data acquired from the system are converted into a three-dimensional coordinate system, which can generate the shape of the total length.

The deflection/deformations of any point can be estimated by monitoring the change of shape with time. These SAAs were installed within 2-inch diameter PVC casings, which were placed just under the GRRB layer. The first 9 segments (1 to 9) of the SAAs were located under the eastbound lane (RS1, RS2, and RS3), and the last 9 segments (10 to 18) were located under the westbound lane (UR1, UR2, and UR3). A 12-inch trench was dug to bury the connected wires from the sensor locations to the data logger box. The data logger box was set up close to the RS2, and the existing slope was excavated and filled with flex base material to flash the logger box with the ground surface.

A total of 6 EPCs were used for this project; 2 EPCs were installed under RS1 (right and left wheel paths), 1 EPC under RS2 (right wheel path), 2 EPCs under RS3 (right wheel path), and 1 EPC under UR2 (right wheel path). 4-20 mA type EPCs were used in this study to convert the pressure reading to a current signal within a range of 0 to 36 psi (0 to 250 kPa). This type of EPCs can provide dynamic reading when linked to an appropriate data logger; however, static readings were considered here for long-term monitoring. The detail of the instrumented pavement sections is shown in Figure 27. Though 7 EPCs were installed, two of the EPCs placed underneath the left wheel paths of RS2 and RS3 stopped responding after the initial monitoring period of 6 months; hence most of the analyses in this study were conducted with the rest of the EPCs excluding these two EPCs. The location of placement of SAAs and EPCs are shown in Figure 27.

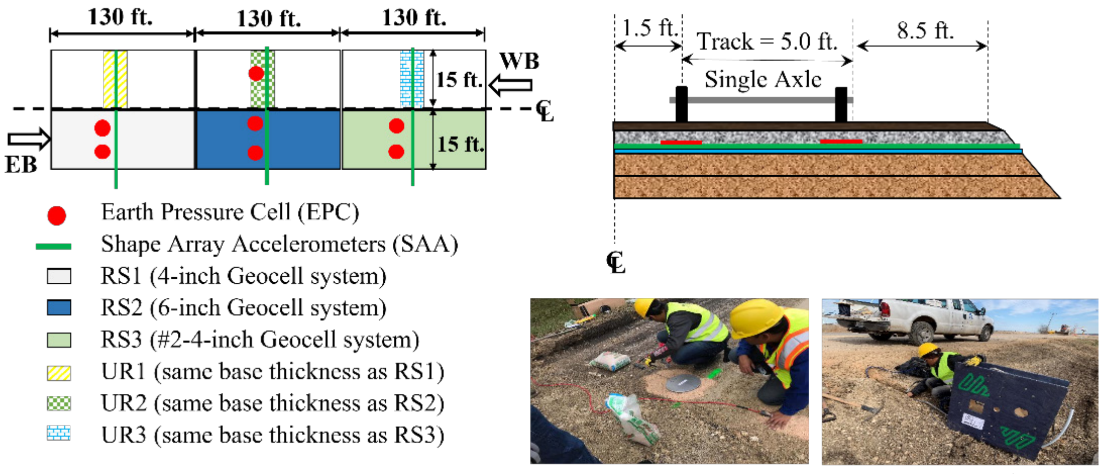

**Note:** EB – Eastbound; WB – Westbound

Installation of EPC

Installation of SAA

**Figure 27 Instrumentation details of the test sections**

## 4.9 Field Data Collection and Analysis

The long-term performance of the constructed test sections was monitored with the data collected from the instrumented sensors, regular field surveys, and profiler studies. The following sections will discuss about the performance of different test sections in terms of vertical deformation, vertical stress, permanent deformation, and roughness.

### *4.9.1 Vertical Stress*

The maximum vertical compressive stress acting under the base layer was computed based on the linear elastic approach (LEA), using the layer properties presented in Table 4. A single wheel load of 100 psi was applied on top of the asphalt layer in the case of the LEA approach. The measured vertical stresses from the field sections were compared with the estimated vertical stresses, as shown in Figure 28. It was observed that the vertical compressive stress decreased with the increase of the

GRRB thickness. The maximum vertical stresses recorded for the RS1, RS2, and RS3 were 4.6, 4.5, and 3.4 psi, respectively. The maximum vertical stress recorded under the UR2 was 5.9 psi., which indicates that the addition of geocell helped to reduce the vertical stress by 27% for RS2.

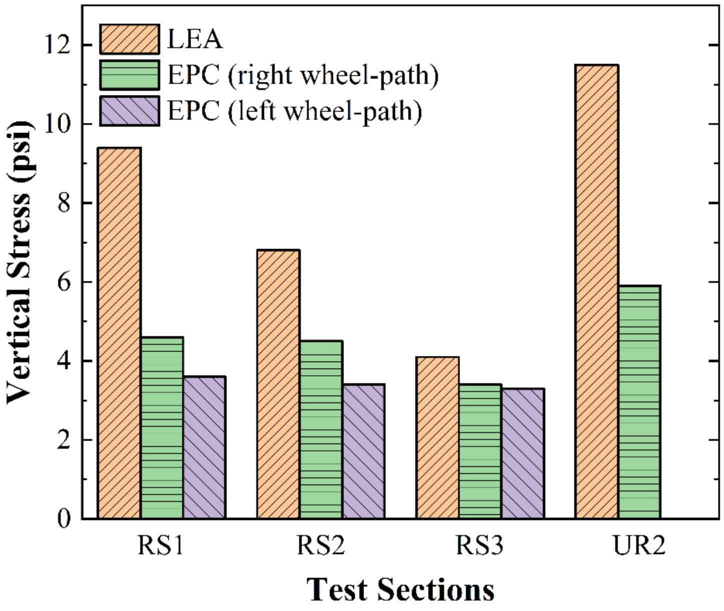

**Figure 28 Vertical stresses acting under the geocell-reinforced base layer determined from the field and estimated from the Linear Elastic Approach (LEA)**

The average vertical stress for RS3 was 3.4 psi, which was the lowest among all the test sections. A similar observation was made by Kief and Rajagopal (2008); it was reported that the geocell-reinforced gravel-base-layer reduced the vertical stresses up to 28%. The reduction in vertical stress indicates a wider distribution of stress due to the mattress effect of the geocell. The vertical stresses measured for RS1 and RS3 indicate that the vertical stresses under the pavement edges (near right-wheel path) were higher than those at the center (near road center). The measured stresses for the edge and center locations in RS1 were 4.7 psi and 3.7 psi, respectively. The vertical stress recorded under the right wheel-paths was slightly higher than the left wheel-path. The variation of the thickness of the RAP cover layer may lead to the difference in vertical stresses between two-wheel paths.

### *4.9.2 Vertical Deformations Recorded from SAAs*

The acceleration data collected from the Shape Array Accelerometers; SAAs were converted to measure the tilt angle at each time step. The changes in tilt angle were used to measure the deflection/deformation over time. A MATLAB program was written to process the raw data to get the actual deformations with time. The field data collection and analysis procedure are shown in Figure 29**.**

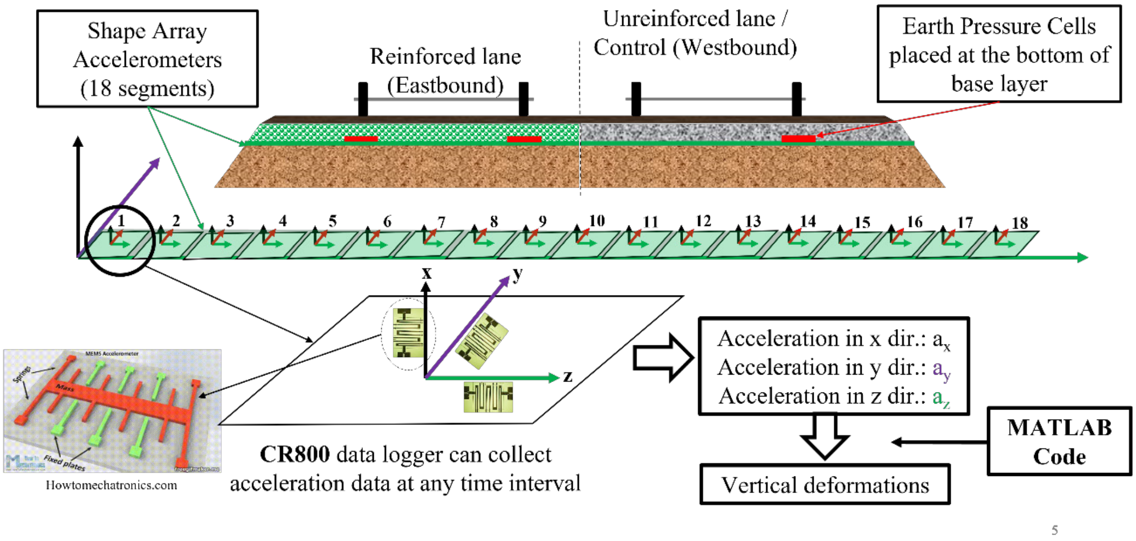

**Figure 29 Field data collection and analysis procedure**

A total of 3 SAA sensors were used for this study which ran across both reinforced and unreinforced sections/lanes. Each of the SAA had 18 segments: segment 1 to 9 are located under the eastbound lane, and segment 10 to 18 are located under the westbound lane, as shown in Figure 29. The results obtained from the first 9 segments are used for the analysis of the reinforced section, whereas the last 9 segments were used for the evaluation of the unreinforced section. The tentative locations of the right and left wheel-paths for the reinforced sections are segment-6 and segment-9, respectively. Similarly, the tentative locations of the right and left wheel-paths for the unreinforced sections are segment-11 and segment-15, respectively. The movement under the base layer may reflect the variation due to the movement of the underneath expansive subgrade. A positive deflection value represents the downward movement, and a negative value represents the upward movement. In general, the upward movement is known as heaving, and the downward movement is known as rutting. The following sections discuss the vertical deformation results observed with these SAAs.

#### 4.8.2.1 Vertical Deformations Under SAA1

SAA1 runs across the RS1 and UR1, located at a depth of 8-inch depth from the pavement surface. The results obtained from the SAA1 are shown in Figure 30. It was observed that there were upward and downward fluctuations of different segments (labeled as 1 to 18) of the SAA throughout the monitoring period. The range and magnitude of fluctuation are much lower in RS1 compared to the UR1 section. The maximum vertical deformation observed within the UR1 was around 0.45 inches, whereas the maximum vertical deformation under the RS1 was less than 0.25 inches. It was also observed that the vertical deformation was enhanced by some events of heavy rainfall during the Summer of 2020, as shown in Figure 30. The maximum heaving that occurred under the UR1 was 0.25 inches, which happened due to the fluctuation of expansive subgrade after the rainfall events.

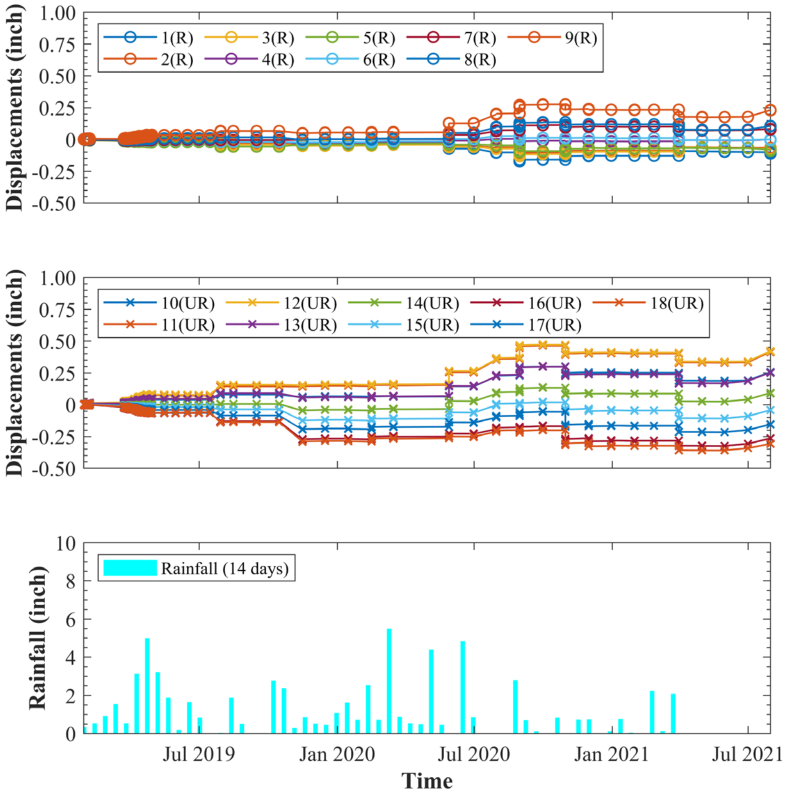

**Figure 30 Vertical deformations under the base layer of RS1 and UR1 from SAA1**

#### 4.8.2.2 Vertical Deformations Under SAA2

The SAA2 runs across the RS2 and UR2, located at a depth of 10-inch depth from the pavement surface. The results obtained from the SAA2 are shown in Figure 31. The vertical movement under this section was minimum compared to the other reinforced section. Though there were some upward soil-induced movements observed after the heavy rainfall events during Summer 2020, the maximum vertical deformations under the wheel-paths were minimum. The maximum vertical deformations observed within the RS2 and UR2 are 0.20 inches and 0.38 inches, respectively.

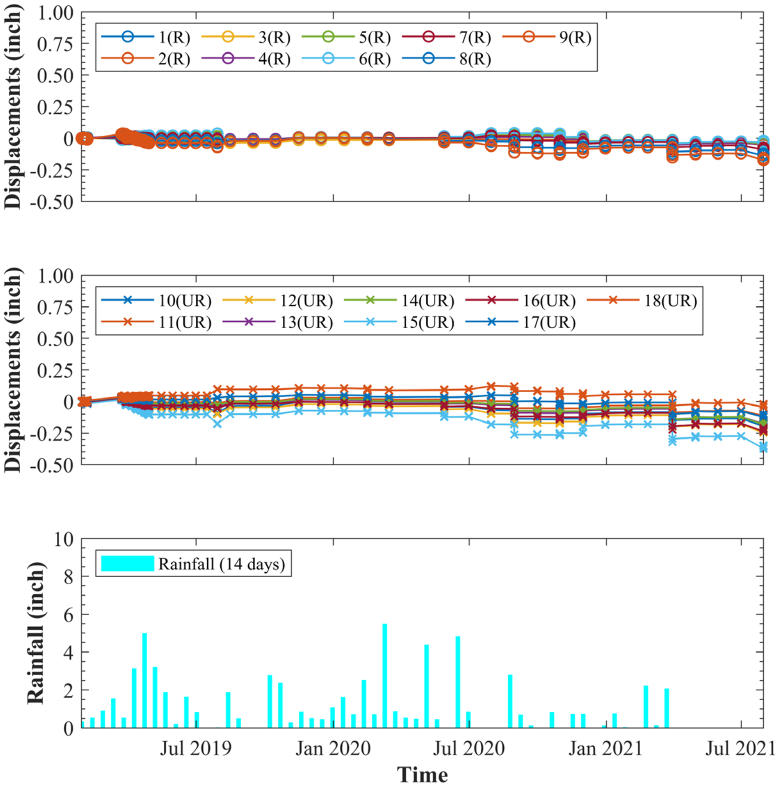

**Figure 31 Vertical deformations under the base layer of RS2 and UR2 from SAA2**

### 4.8.2.3 Vertical Deformations Under SAA3

SAA3 runs across the RS3 and UR3, located at a depth of 14-inch depth from the pavement surface. It was observed that there were significant movements for both RS3 and UR3 after the heavy rainfall events, as shown in Figure 32. The fluctuations of different segments under the RS3 were higher when compared to the RS2 section, though the total height of GRRB was higher for the RS3. The maximum vertical deformation recorded under the RS3 and UR3 was between +0.25 to -0.25 inches.

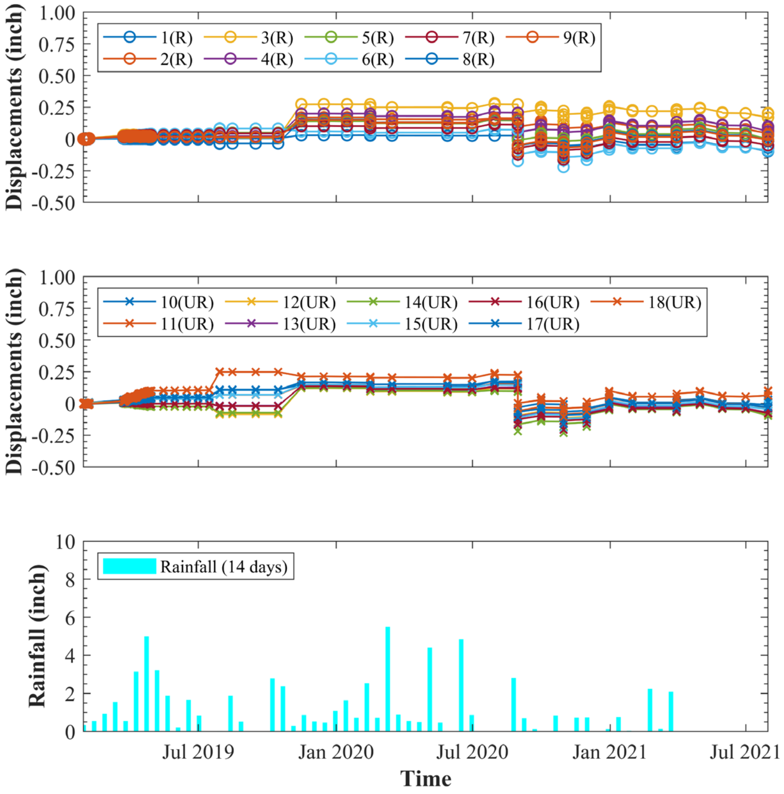

**Figure 32 Vertical deformations under the base layer of RS3 and UR3 from SAA3**

### *4.9.3 Comparison of Performance between the Test Sections*

The test sections were monitored for more than 30 months as they were constructed in December 2018. The vertical deformations recorded every 6-months period are summarized in Figure 33. To compare the performance of the reinforced sections, UR1 was selected, as all the unreinforced sections showed similar behavior. It was observed that the permanent vertical deformations increased with time, and higher deformation was observed in the UR1 section. The maximum permanent vertical deformations after 30 months from construction for RS1, RS2, RS3, and UR1 were 0.11, 0.07, 0.14, and 0.42 inches, respectively. The rate of change of vertical deformations for the reinforced test sections was much slower when compared to the UR1 site.

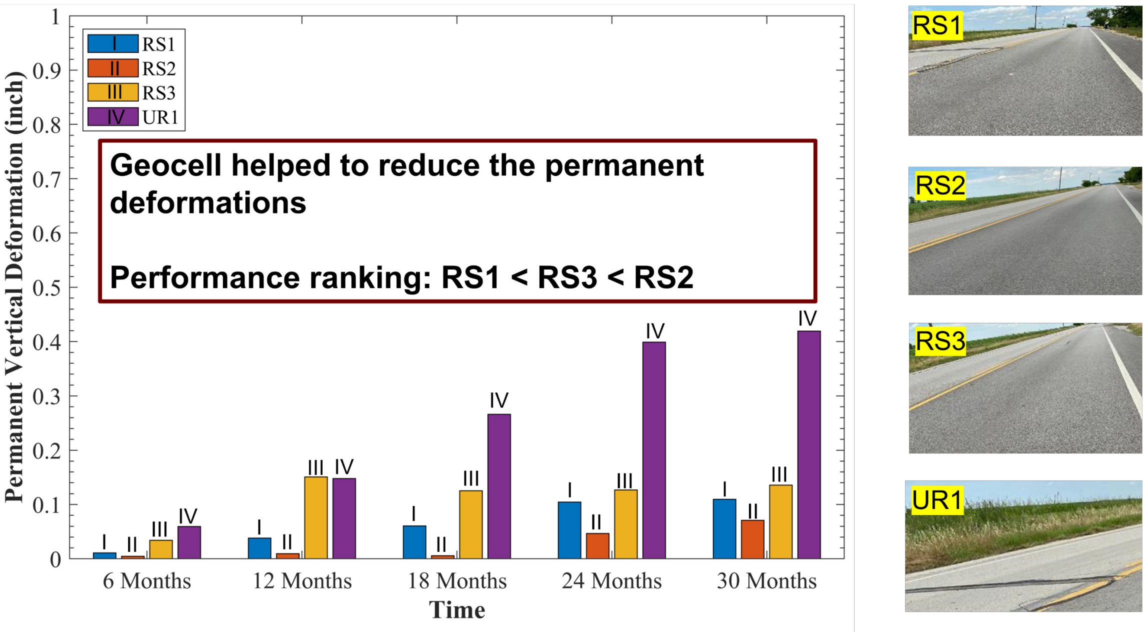

Geocell helped to reduce the permanent deformations

Performance ranking: RS1 < RS3 < RS2

**Figure 33 Comparison of permanent vertical deformations**

Rutting and heaving occurred within the test sections (RS1, RS2, RS3, UR1, UR2, and UR3) are also presented in Figure 34. All the reinforced sections performed better in terms of controlling the movement of the bottom of the base layer. It was observed that the RS2 had the minimum vertical deformations compared to the RS1 and RS3. The ratio of the total RAP cover ($c_t$) to the height of geocell ($h_{gc}$) plays a significant role in the overall performance of the reinforced sections. The $c_t/h_{gc}$ ratio for the RS1, RS2, and RS3 test sections are 0.50, 0.33, and 0.67, respectively. The lower $c_t/h_{gc}$ is observed for the RS2 section, which had minimum vertical deformation. The cover layers were necessary to maintain a working platform for the construction equipment.

The $c_t/h_{gc}$ ratio for the RS2 section is 0.50, which indicates that the thickness of the unreinforced RAP cover was 50% of the reinforced RAP layer, whereas the $c_t/h_{gc}$ ratio 0f 0.33 for the RS2 indicates the thickness of the unreinforced RAP cover is only 33% of the total RAP layer thickness. The reduction of RAP cover thickness may improve the overall performance of the GRRB layers.

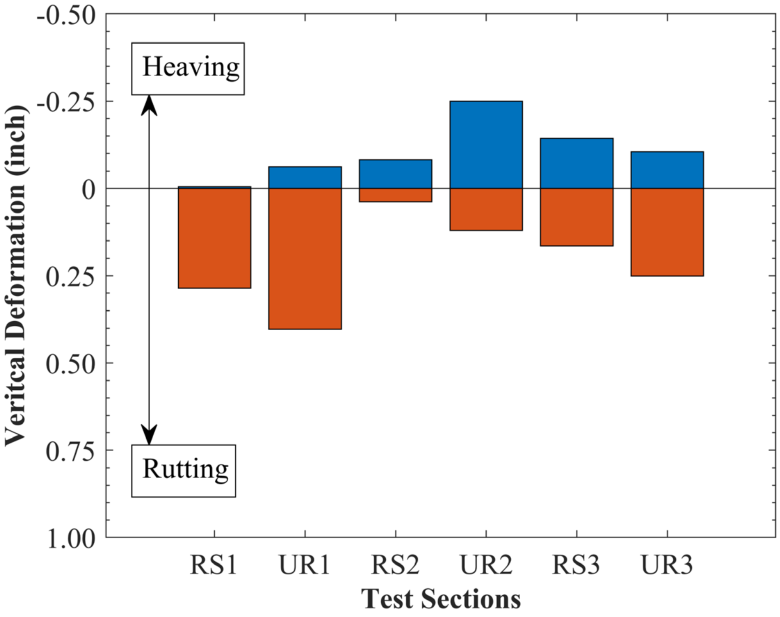

**Figure 34 Comparison of rutting and heaving among the test sections**

The maximum permanent deformation for the RS1, RS1, and RS3 were 0.11, 0.07, 0.14, and 0.42 inch, corresponding to the $c_t/h_{gc}$ values of 0.50, 0.33 and 0.67. It is a clear indication that the optimum performance was observed for the RS2, where the $c_t/h_{gc}$ value was the lowest.

### *4.9.4 Rutting*

The vertical deformation along the wheel-paths was measured for all the test sections following the ASTM E1703M standard using a straight edge. The test sections were monitored for visual rutting, cracking, and depressions since December 2018. During the first 6-months of monitoring, no visible distress was observed. The rut depths were measured every 6 months to check the trend and compare the performance of different test sections. The location of the left and right wheel paths, as shown in Figure 35**,** was used for the measurement of rutting.

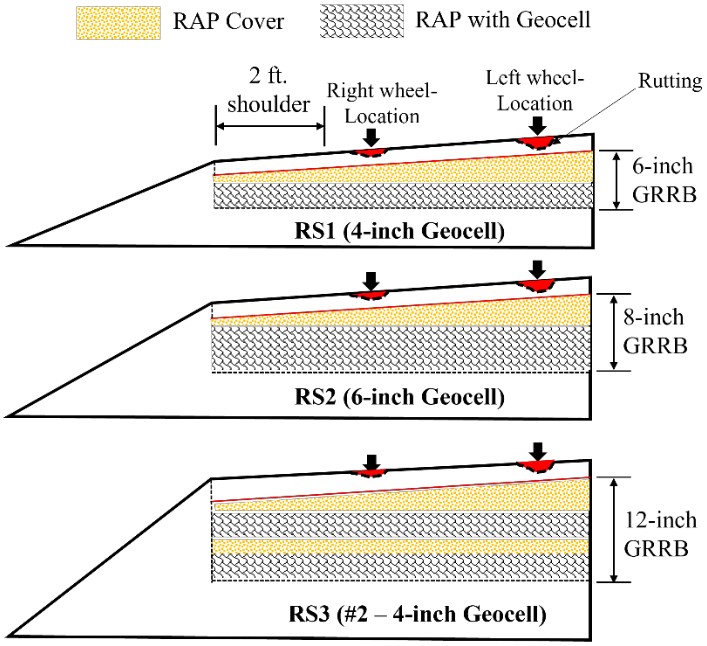

Note: GRRB-Geocell-Reinforced RAP Base
RAP cover thickness varied from 1 to 2 inch

**Figure 35 Rut-depth measuring locations (drawn not to scale)**

In general, the rut depth measured within the right wheel-paths (near to shoulder) was significant when compared to the rut measured within the left wheel-paths (near to the centerline of the road). This might have happened due to the following two reasons:

1. The depth of the RAP cover near the shoulder and centerline of the road were 1-inch and 2-inch, respectively. The higher thickness of unreinforced RAP cover may lead to additional deformation.
2. The extended portion of the geocell mattress beneath the right wheel paths was more than 3 feet, whereas the extended portion near the road centerline was less than 2 feet. The geocell was placed only under the eastbound lane, and it was not possible to extend the geocell mattress beyond the road centerline. Stress distribution angles under the right-wheel paths were much wider compared to the left-wheel paths. This may lead to the higher rutting observed within the right-wheel path.

As the rut values were observed within the left-wheel paths were higher, those were considered for evaluating the performance of the test sections, considering the extreme situation. The maximum rutting recorded under the test sections is shown in Figure 36. The maximum depth of rut or permanent deformation for the RS1, RS2, RS3, and CS sections were 0.23, 0.32, 0.29, and 0.50 inches, respectively, recorded after 30 months from the construction.

The maximum rutting under the CS was recorded under the UR2 section, where an 8-inch-thick unreinforced base layer was used. It indicates that the utilization of reinforcement helped to decrease the permanent deformation by restricting the lateral spreading of the RAP material. It was observed that the rate of change of rutting for the unreinforced section was 0.10 inches/year, whereas the rate of rutting for the reinforced section was less than 0.02 inches/year.

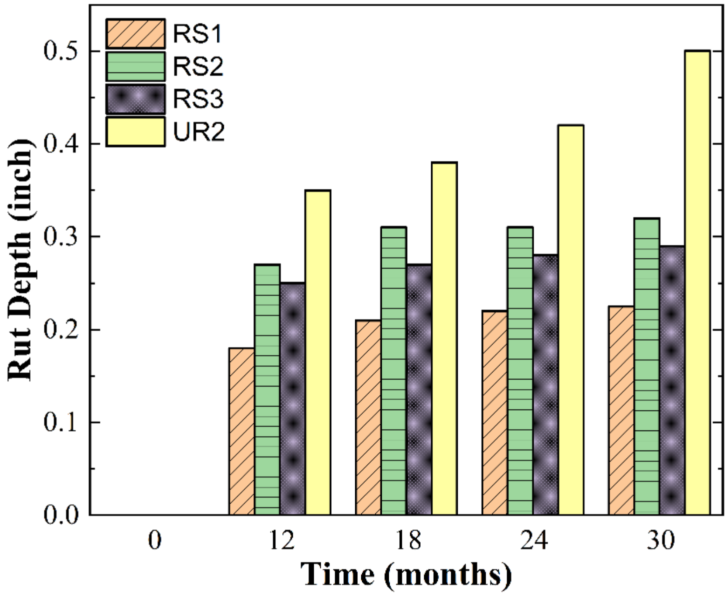

**Figure 36 Maximum rut depth for different test sections**

The maximum allowable depth of rutting for the flexible pavement is 0.50 inches when major rehabilitation work is required to bring back the pavement into service condition. The maximum rutting within the reinforced pavement test section was well below this limit, and the rate of change of rutting depth is slow, indicating a stable condition due to the utilization of the geocell base layer. In this research study, the maximum rutting was reported; however, the average rutting value is 50% less than the maximum rutting limit. It should be noted that the rutting value under the right-wheel path (near to the shoulder) was significantly low, which indicates that the full-width extension of the geocell layer under this wheel path might have helped to distribute the load over a wider area, hence reducing the magnitude of the permanent deformation.

### *4.9.5 Pavement Roughness*

Profiler studies were conducted during 2020 and 2021 to measure the smoothness of both westbound and eastbound lanes. Since the reinforced sections were located adjacent to each other, one single profiler test was conducted for a stretch of 390 feet. on the eastbound lane. The total length of the CS is 390 feet., which includes three unreinforced sections. The profiler data for the eastbound lane was separated into three segments to assess the individual test sections of 130 feet. length. For comparing the roughness with the reinforced sections, 130 feet. segment of the CS parallel to RS2 were considered, which also contains the unreinforced section UR2. The following sections will discuss the longitudinal profile, *IRI*, and *PSR* for different test sections.

#### **4.8.5.1 Longitudinal profile**

Figure 37 presents the longitudinal profiles of various sections for the years 2020 and 2021. It was observed that RS1 had more undulation when compared to RS2 and RS3. Maximum bump and dip of 0.48 inch and 0.51 inch, respectively, were recorded under the RS1 during 2021. On the other hand, the maximum bump under the RS2 and RS3 sections were less than 0.20 inches. Due to the increase in the thickness of the GRRB layer, the load-bearing capacity also increased for the RS2 and RS3. Geocell layer with a higher thickness value helped to distribute the load uniformly and reduced the overall undulations for the pavement structures.

The undulation observed within the CS was not significant, except the location of UR2, where a maximum dip of 0.54 inches was recorded during 2021. Apart from the UR2 location, the surface of CS was quite smooth compared to the reinforced sections located within the eastbound lane. The higher thickness of the asphalt layer in this zone contributed to the smoother profile. The maximum permanent deformation under the unreinforced section (UR2) was 0.54 inches, whereas the similar section with geocell (RS2) had a maximum permanent deformation of fewer than 0.20 inches. It indicates that the lateral confinement offered by the geocell helped to restrict the lateral movement of the RAP materials; correspondingly, lower permanent deformation was observed under the reinforced section.

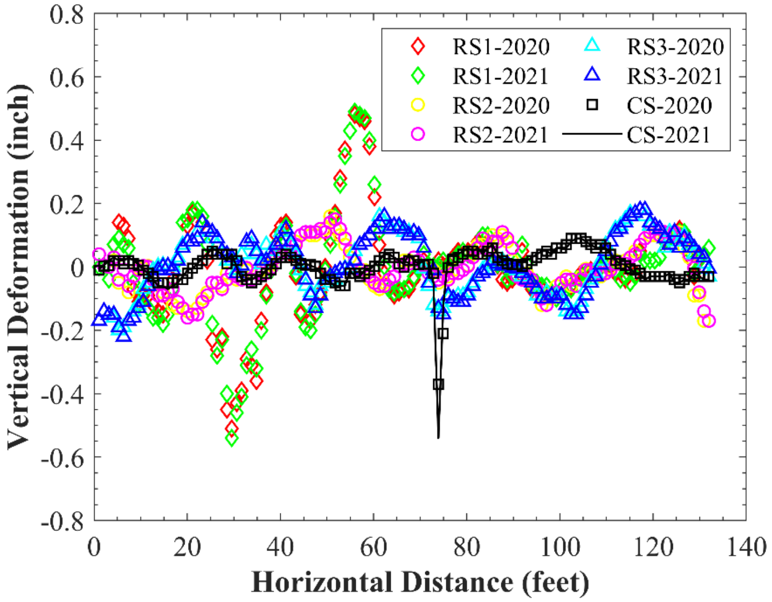

**Figure 37 Longitudinal profiles of different test sections during 2020 and 2021**

The rate of change of surface deformations for all the sections recorded during 2020 and 2021 was almost negligible, which indicated the stable condition of the test sections.

#### 4.8.5.2 International Roughness Index

The *IRI* values measured for the RS1, RS2, RS3, and CS for the year 2020 were 219.2, 108.7, 113.8, and 78.1, respectively. The maximum *IRI* was recorded under the RS1 sections, where a 6-inch GRRB layer was used. The *IRI* values for the RS2 and RS3 were significantly lower compared to the RS1 as the corresponding thickness of the GRRB layers were 8-inch and 12-inch, respectively. The increase in GRRB layer thickness leads to a smoother profile with a lower *IRI* value.

To track the change in *IRI*, another profiler test was conducted in 2021. The *IRI* values for the RS1, RS2, RS3, and CS for the year 2021 were 215.8, 101.9, 123.2, and 98.4, respectively. Though the *IRI* value of the RS1 was higher during the years 2020 and 2021; however, the rate of change of *IRI* was negligible. The rate of change of *IRI* for different test sections is presented in Figure 38.

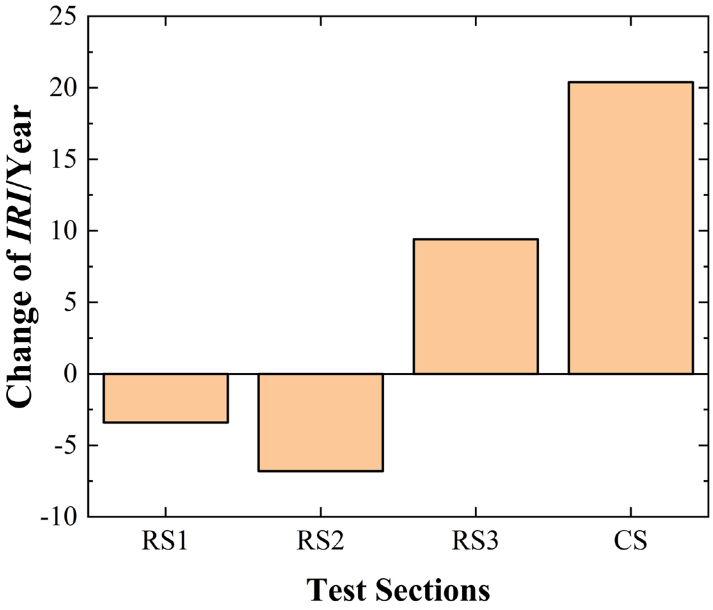

**Figure 38 Rate of change of *IRI* for the control and reinforced sections**

The rate of change of the *IRI* for the RS1 and RS2 were negative, indicating almost no change in the surface undulation. The rate of change of RS3 and CS sections were 9.8 and 20.3 inches/mile/year. A higher rate of degradation for the CS was due to the faster deformation of the UR2 section, having an unreinforced RAP layer of 8-inch. The permanent deformation of RAP was controlled with the cellular type of confinement, which leads to a stable condition for the reinforced section with a lower rate of degradation. The total RAP cover thickness of the RS3 was 4-inch (2-inch intermediate cover + 2-inch top cover), whereas the RAP cover thickness for the RS1 and RS2 was 2-inch. The lower thickness of the RAP cover may lead to a stable and better performance.

#### 4.8.5.3 Pavement Serviceability Rating (*PSR*) Values

Pavement Serviceability Rating (*PSR*) values are related to the roughness of the pavement surface and provide an overall idea about the current road conditions. The condition of a road can be classified as: very good ($5 < PSR < 4$), good ($4 < PSR < 3$), fair ($3 < PSR < 2$), poor ($2 < PSR < 1$), or very poor ($PSR < 1$). A newly constructed pavement that is free of cracks is classified as very good condition. Sign of random minor cracks and evidence of initial rutting indicates good condition with PSR ranging between 3 to 4. The flexible pavement will show different types of distresses with time until it reaches the poor condition with a PSR value less than 2, which is also considered as terminal in most cases (Hong et al., 2006). The *IRI* values are used to determine the pavement serviceability rating (*PSR*) based on the Paterson method as expressed by the following Equation 17 (Paterson, 1986).

$$PSR = 5\exp{-0.0018(IRI)} \qquad (17)$$

The increase in *IRI* value from 120 to 280 inches/mile will change the *PSR* value from 4.0 to 3.0. This information is useful to understand the present serviceability condition of the existing pavement section. The deterioration rate of the *PSR* with time will also help the transportation agencies to schedule future maintenance works.

The *PSR*s for different test sections were determined from the *IRI* based on the Paterson method, as presented in Figure 39. The *PSR* values of the RS1, RS2, RS3, and CS sections were 2.7, 3.7, 3.5, and 3.8, respectively, during 2020. The *PSR* for the RS1 was lower as the *IRI* was maximum for this section. The *PSR* for the RS2 and RS3 was comparable with the CS section. The *PSR* values provided important insight about the current status of the road and helped the transportation agencies to decide when to go for maintenance of major rehabilitation work. Generally, a *PSR* value less than 2 is considered a terminal condition when major rehabilitation work is required. A pavement with *PSR* = 2.0 will exhibit deep cracks, potholes, and rutting covering more than 50% of the road surface area. The visual observation from the field indicates that the maximum rutting was confined within a very small portion of the reinforced section, and no severe cracks or depressions were observed.

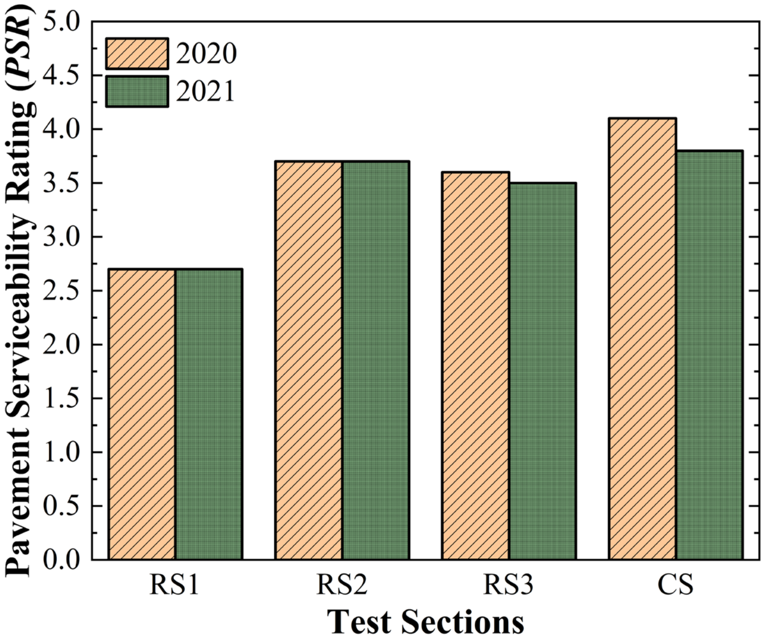

**Figure 39 Pavement serviceability rating (*PSR*) of test sections during 2020 and 2021**

Figure 39 also presents the PSR values for the year 2021, where the change of *PSR* was not significant for the reinforced sections. However, a small decrease in *PSR* was observed within the CS section due to the presence of UR2 within it. The UR2 section went for deeper rutting leading to a lower rating. The *PSR* for RS2 and RS3 were

3.7 and 3.5, which is almost similar to the CS section. The *PSR* values ranging between 3 and 4 indicate a decent condition with minimum rutting and cracking.

## 4.10 Summary

This chapter discusses the activity involved in material characterization, construction, instrumentation, field data collection. The sequential procedure of the construction of the flexible pavement sections with the GRRB layer is also discussed here. The performance of the test sections is presented in terms of controlling the vertical stresses and vertical deformations. The surface rutting measurements are also presented here to compare the rutting characteristics for different test sections. The field data collected from the profiler test during 2020 and 2021 are also presented in this chapter to understand the overall condition of the test sections. The outcome of the construction and monitoring activities are summarized below.

- The construction of the GRRB layer does not require any skilled labor or specific equipment or tools. The observations during the construction of the GRRB layers are listed below. The time required for the construction of GRRB is 20% more than the traditional flex base material, as the additional time required to install the geocell is 975 sq. feet per hour
- Due to the constraint of space, the portion of geocell near the road centerline was not extended beyond the 3 feet from the wheel path location for the development of the mattress effect. The geocell mattress should be extended beyond 3 feet from the centerline of the wheel path.

- The instrumented data collected from the field showed that the GRRB could reduce the average vertical stresses on the subgrade by 50%. The reduction of vertical stresses also helped to reduce the average permanent deformation by 36%
- The maximum permanent deformation recorded under the GRRB layers of the RS1, RS1, and RS3 were 0.11, 0.07, 0.14, and 0.42 inches, corresponding to the $c_t/h_{gc}$ values of 0.50, 0.33, and 0.67. The lowest $c_t/h_{gc}$ showed better performance in terms of permanent deformation or rutting under the GRRB layers
- The rate of change of *IRI* was lower for all the reinforced test sections when compared to the existing control section (CS), which indicates a stable condition of the base layer
- The estimated *PSR* values of the RS1, RS2, RS3, and CS sections were 2.7, 3.7, 3.5, and 3.8, respectively, which indicates the 6-inch GRRB showed better performance with the lowest $c_t/h_{gc}$ ratio.

# CHAPTER V

# NONDESTRUCTIVE FIELD TESTING

## 5.1 Background of Nondestructive (NDT) Testing

The structural performance of the test sections was evaluated with non-destructive pavement testing, including Falling weight deflectometer, FWD and Automated plate load tests, APLTs. Falling weight deflectometer (FWD) tests were conducted during September 2020 and June 2021 to track changes in the pavement performance under different weather conditions. Automated plate load tests (APLTs) were conducted during April 2020 to observe the response of the pavement under different frequencies of dynamic loading. Both types of NDTs were used to evaluate the pavement layer properties, especially for the GRRB layers. Photographs of the FWD and APLT tests are shown in Figure 40**.**

**(a)** **(b)**

**Figure 40 Nondestructive pavement testing: a) Falling weight deflectometer (FWD), and b) automated plate load test (APLT)**

## 5.2 Falling Weight Deflectometer (FWD) Testing

The FWD tests were conducted at 40 locations: 6 in RS1, 7 in RS2, 7 in RS3, and 20 in CS, as shown in Figure 41, and a global positioning system was used to mark the locations in preparation for the second set of tests during 2021. Figure 42 is a typical diagram of the FWD test that shows the locations of the deflection sensors. The field responses collected from the testing were used to determine the base layer index (BLI), base layer modulus, and GRRB layer modulus.

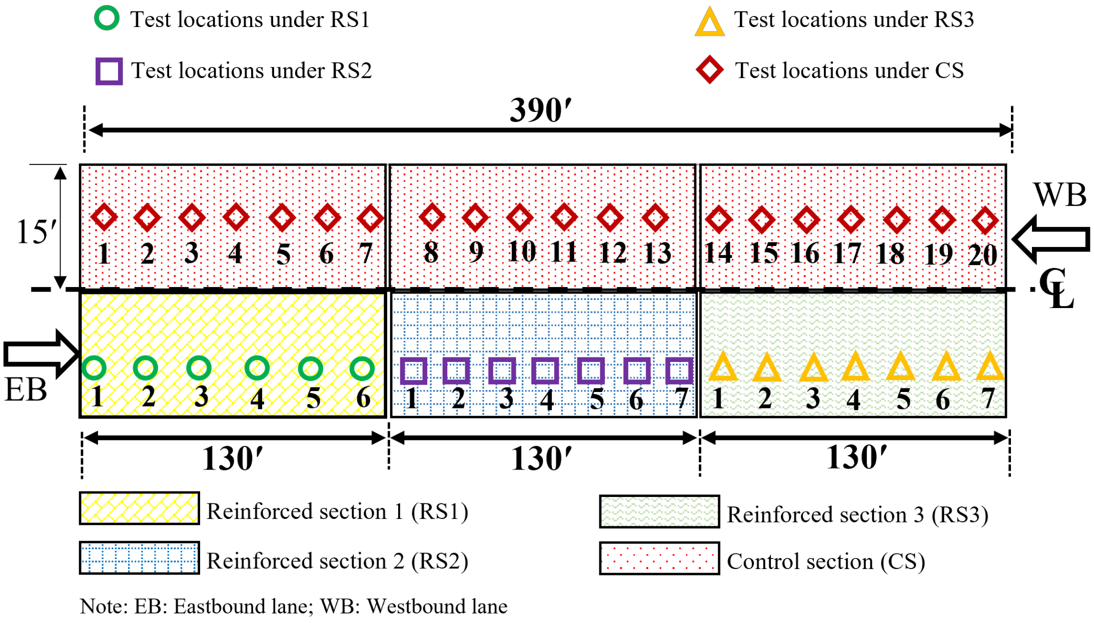

**Figure 41 FWD test locations**

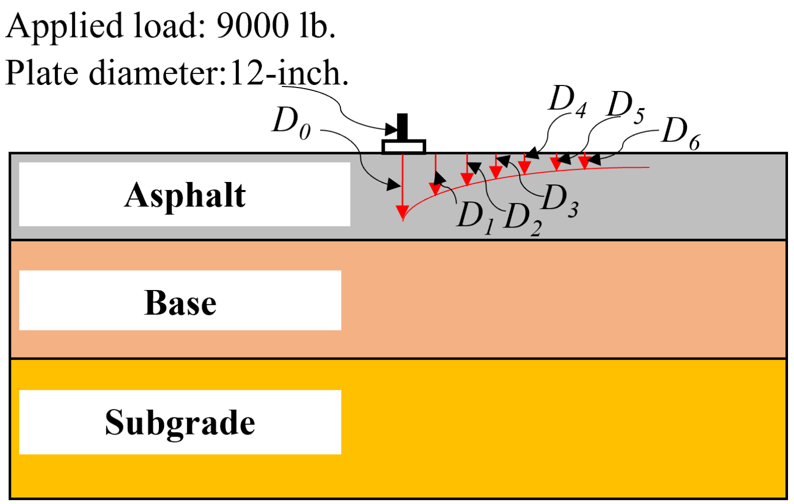

Note: $D_0$, $D_1$ , $D_2$ , $D_3$ , $D_4$ , $D_5$ and $D_6$ are the deflection measured at 0, 12, 24, 36, 48, 60, and 72 inch, respectively away from the load center

**Figure 42 FWD loading and deflection bowl**

### *5.2.1 Load-Deflection Characteristics*

The actual load applied varied from the standard loading condition by ±5%; hence the collected deflection data were normalized with respect to the reference load of 9000 lb. Since the FWD tests were conducted during two different time periods (2020 and 2021) and in four different sections (RS1, RS2, RS3, and CS), the data were classified into four major categories, EB-2020, EB-2021, WB-2020, and WB-2021, then divided into eight groups, RS1-2020, RS1-2021, RS2-2020, RS2-2021, RS3-2020, RS3-2021, CS-2020, and CS-2021. The first part of the classification indicates the lane/ID of the test section, and the last four digits reveal the year that the test was performed. The characteristics of the data collected from different sections are summarized in Table 6.

**Table 6 Deflection Parameters Obtained from FWD Studies**

| **Main Category** | **Section ID** | **$D_o$ ($10^{-3}$ inch)** | ***AREA* (inch)** | **$F_1$** | **$F_2$** |
|---|---|---|---|---|---|
| EB-2020 | RS1-2020 | 16.7- 22.3 | 16.6 – 18.3 | 0.89 – 1.22 | 1.22 – 1.41 |
| | RS2-2020 | 16.8 – 18.5 | 16.2 – 17.6 | 1.02 – 1.22 | 1.23 – 1.36 |
| | RS3-2020 | 16.2 – 18.6 | 17.6 – 18.8 | 1.05 – 1.21 | 1.23 – 1.37 |
| EB-2021 | RS1-2021 | 18.7 – 22.4 | 17.5 – 20.2 | 1.10 – 1.35 | 1.35 – 1.63 |
| | RS2-2021 | 19.8 – 24.6 | 17.5 – 19.1 | 1.21 – 1.43 | 1.36 – 1.53 |
| | RS3-2021 | 17.7 – 23.4 | 16.6 – 18.3 | 1.14 – 1.41 | 1.19 – 1.45 |
| WB-2020 | CS-2020 | 11.5 - 15.8 | 18.1 - 20.7 | 1.17 – 0.87 | 1.22 – 0.95 |
| WB-2021 | CS-2021 | 16.1 – 21.2 | 15.8 – 17.9 | 1.53 – 1.17 | 1.17 – 1.49 |

Note: $AREA = 6(1+\frac{2D_1}{D_o}+\frac{2D_2}{D_o}+\frac{2D_3}{D_o})$; $F_1 = \frac{D_o - D_2}{D_1}$; $F_2 = \frac{D_1 - D_3}{D_2}$

The roadway section (CS) had lower maximum deflections ($D_o$) compared to the other sections, as the thickness of the asphalt layer was 4 inches. The maximum $D_o$ values for CS-2020 and CS-2021 were 15.8 mils and 21.2 mils. The air temperatures recorded during the FWD tests were 75ºF and 90ºF for 2020 and 2021, respectively, which could lead to higher deflections and a decrease in the asphalt modulus. The characteristics of the deflection bowl can be evaluated with the other parameters, i.e., *AREA*, $F_1$, and $F_2$. These parameters are useful for performing linear regression analysis to correlate them with the pavement layer properties.

### *5.2.2 Back-Calculation Approach for FWD*

The primary focus of the FWD testing was to assess the structural performance of the GRRB layers. It is recommended that a three-layer analysis be performed to match the field deflection bowl with the predicted layer moduli. A four-layer analysis is sometimes required if the trend of the deflection bowl is significantly different than the predicted deflection bowl attained from the linear elastic analysis. The thickness of the flex base layer of CS was 15 inches; the total base layer thickness of the reinforced sections was 17 inches. As the GRRB layers were constructed by replacing the existing roadway section, the actual thickness of the base layer was divided into Base-1 (B1) and Base-2 (B2), with B1 being the newly constructed segment and B2 the existing flex base section. The actual thicknesses of the as-constructed sections and the existing roadway sections are listed in Table 7**.** A three-layer analysis was performed to interpret the moduli of the combined base (B1+B2). A four-layer analysis was required to obtain the individual moduli of B1 and B2, where B1 represents the modulus of the GRRB layer.

**Table 7 Details of the Test Sections**

| **Layer information** | | | **Existing Road (CS)** | **Reinforced Sections** | | |
|---|---|---|---|---|---|---|
| | | | | **RS1** | **RS2** | **RS3** |
| Asphalt | Thickness (inch) | | 4 | 2 | 2 | 2 |
| Base | Base-1 (B1) thickness (inch) | Top cover | - | 2 | 2 | 2 |
| | | Layer – 01 | - | 4 | 6 | 4 |
| | | Intermediate cover | - | - | - | 2 |
| | | Layer – 02 | - | - | - | 4 |
| | Base-2 (B2) thickness (inch) | Existing base | 15 | 11 | 9 | 5 |
| | Total base thickness (inch) | | 15 | 17 | 17 | 17 |
| Subgrade | Thickness (inch) | | - | - | - | - |

Note: The thickness of the GRRB for RS1, RS2, and RS3 is 6, 8, and 12 inches, respectively.
The thicknesses of the pavement sections were taken during the time of construction.
The cover thicknesses were considered as per FWD test locations and varied from 1 to 2 inches.

Since the focus of this study was to evaluate the base layer, the stiffness of the asphalt layer was kept constant for a particular temperature. The asphalt layer moduli were considered as 600 and 400 ksi, corresponding to the field temperature of 75ºF

(2020) and 90ºF (2021). The linear elastic approach was adopted to perform a three-layer analysis for EB-2020, EB-2021, WB-2020, and WB-2021, using the layer information presented in Table 8.

**Table 8 Pavement Layer Properties used for LEA with Three-layer Approach**

| | **WB-2020** | **WB-2021** | **EB-2020** | **EB-2021** |
|---|---|---|---|---|
| $t_{asp}$ (inch) | 4 | 4 | 2 | 2 |
| $E_{asp}$ (ksi) | 600 | 400 | 600 | 400 |
| $\mu_{asp}$ | 0.35 | 0.35 | 0.35 | 0.35 |
| $t_{base}$ (inch) | 15 | 15 | 17 | 17 |
| $E_{base}$ (ksi) | 30, 40, 50, 60, 70, 80, 90, 100 | 30, 40, 50, 60, 70, 80, 90, 100 | 30, 40, 50, 60, 70, 80, 90, 100 | 30, 40, 50, 60, 70, 80, 90, 100 |
| $\mu_{base}$ | 0.30 | 0.30 | 0.30 | 0.30 |
| $E_{subg}$ (ksi) | 5.0, 7.5, 10.0, 12.5, 15.0, 17.5, 20.0 | 5.0, 7.5, 10.0, 12.5, 15.0, 17.5, 20.0 | 5.0, 7.5, 10.0, 12.5, 15.0, 17.5, 20.0 | 5.0, 7.5, 10.0, 12.5, 15.0, 17.5, 20.0 |
| $\mu_{subg}$ | 0.35 | 0.35 | 0.35 | 0.35 |
| Total Scenarios | 56 | 56 | 56 | 56 |

Notes: $t_{asp}$, $E_{asp}$, and $\mu_{asp}$ are the thickness, modulus, and Poisson's ratio of the asphalt layer.
$t_{base}$, $E_{base}$, and $\mu_{base}$ are the thickness, modulus, and Poisson's ratio of the base layer.
$E_{subg}$, and $\mu_{subg}$ are the modulus and Poisson's ratio of subgrade layer.
LEA: Linear Elastic Approach

The trial moduli for the base layer varied from 30 to 100 ksi, and the subgrade layer moduli varied from 5 to 20 ksi; 56 scenarios were generated for each category, and the asphalt layer moduli were kept constant for each scenario. The combined base layer (B1+B2) thickness from the three-layer analyses was estimated from the approach presented in Figure 43.

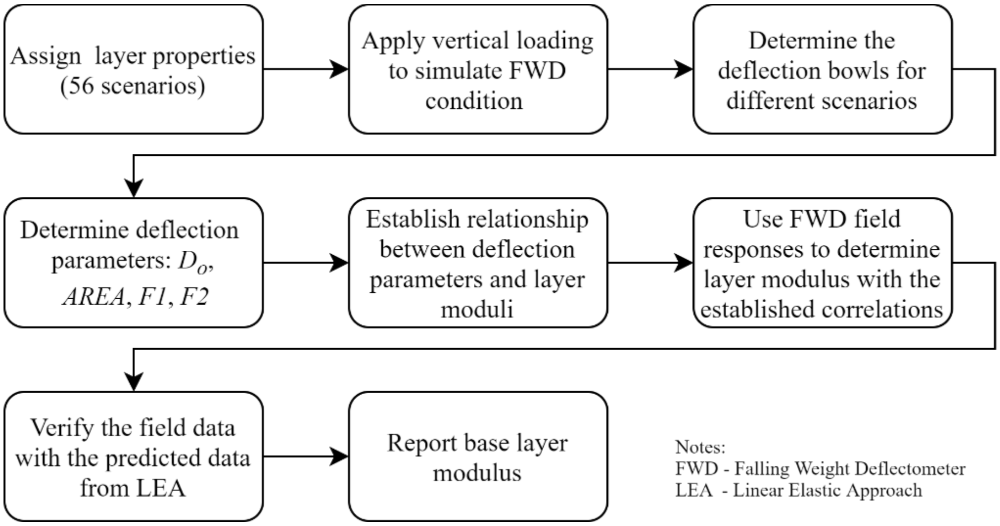

**Figure 43 Flowchart for the estimation of base layer modulus from the field FWD studies**

The deflection parameters $D_o$, *AREA*, $F_1$, and $F_2$ obtained from the linear elastic approach (LEA) were used to find a mathematical correlation with the bases and subgrade layer properties, following linear regression analysis. $D_o$ and *AREA* had better correlations with the layer's properties in terms of correlation coefficients and standard errors, with a 5% significance level. The logarithm of $D_o$ was correlated with the base and subgrade layer moduli of individual categories, as shown in Table 9**,** to predict the base layer modulus.

**Table 9 Linear Regression Analysis for Three-layer Approach**

| ID | Asphalt Thickness (inch) | $\sigma$ | $c$ | $p$ | $q$ | $R^{2a}$ (%) |
|---|---|---|---|---|---|---|
| EB-2020 | 2 | 0.028 | 1.7237 | -0.0161 | -0.0036 | 94.8 |
| EB-2021 | 2 | 0.028 | 1.7443 | -0.0161 | -0.0037 | 94.7 |
| WB-2020 | 4 | 0.025 | 1.6022 | -0.0189 | -0.0026 | 95.4 |
| WB-2021 | 4 | 0.026 | 1.6314 | -0.0118 | -0.0027 | 95.1 |

Note: Equation of the following form, $\log D_o = c + (p \times E_{\text{subg}}) + (q \times E_{base})$

A: Significant at 5% level, σ = standard error

$E_{base}$ = elastic modulus of the base

$E_{subg}$ = elastic modulus of the subgrade

The correlation coefficients presented in Table 9 were used to develop the following mathematical expressions (Equation 18-21):

$$E_{base(WB75)} = 610.6 - 7.2(E_{subg}) - 381.1(\log D_o) \quad (18)$$

$$E_{base(WB90)} = 594.4 - 4.3(E_{subg}) - 364.9(\log D_o) \quad (19)$$

$$E_{base(EB75)} = 473.6 - 4.4(E_{subg}) - 274.7(\log D_o) \quad (20)$$

$$E_{base(EB75)} = 470.2 - 4.3(E_{subg}) - 269.5(\log D_o) \quad (21)$$

### *5.2.3 Prediction of Base Layer Modulus (BLM)*

The field data collected under each category was used to determine the base layer modulus, using Equations 18-21. The asphalt layer properties were kept constant under each category, and the elastic modulus of the subgrade material determined from the laboratory was used. The predicted moduli were further used to perform additional pavement analyses to compare the trend of the measured deflection data with the predicted data from LEA, as shown in Figure 44.

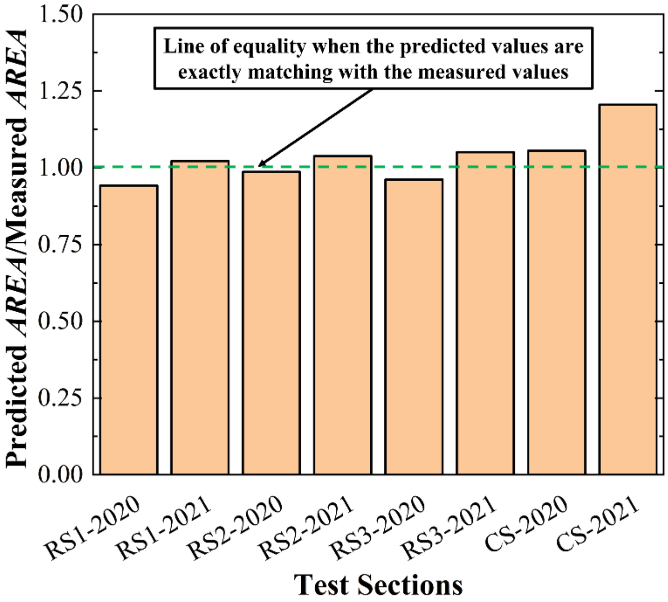

**Figure 44 Comparison of predicted and measured deflection bowl related *AREA***

The combined base moduli presented in Figure 45 indicates that the average elastic modulus of the base layer ranged between 56 to 67 ksi. The maximum base modulus was observed under the RS3 section, and the minimum base modulus was observed under the RS1 section. The GRRB layer in the RS3 sections was thicker than that in RSI, which resulted in a higher elastic modulus. Figure 45 also presents the minimum and maximum values within the error bar, which is a good indicator of the uniformity within the test sections. The variation within the CS section was higher than that of the other reinforced sections, which suggests that the base layers with geocells are uniformly providing a stiff response. The maximum and minimum moduli recorded under the CS sections were 32 and 90 ksi, respectively, during 2021 and the traditional flex base material without reinforcement demonstrated non-uniform stiffness.

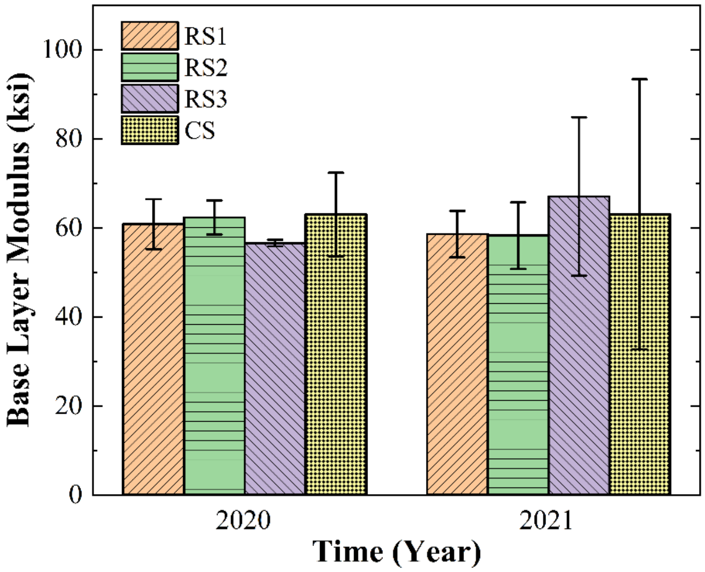

**Figure 45 Comparisons of base layer modulus obtained from three-layer analyses**

The average base layer moduli did not change considerably during the nine months from September 2020 to June 2021. The three-layer analyses showed an overall improvement of the base layer; however, four-layer analyses were required to determine the modulus of the GRRB layers.

Four-layer analyses were performed for the reinforced sections, using the FWD data collected during 2021. The thickness of the base layer was divided into B1 and B2, representing the GRRB and existing base layer, as described in Table 7. The moduli of the asphalt and subgrade layer were kept constant; the moduli of B1 and B2 varied, based on a trial-and-error approach to match the deflection parameters obtained from the field. The thickness of the base layer of RS1 for the three-layer analysis was 17 inches; however, this thickness was divided into 6 inches (GRRB/B-1) and 11 inches (existing base/B-2) for the four-layer analysis. The thickness of the B-1 and B-2 sections, along with the predicted modulus obtained from the trial-and-error approach, is shown in Table 10. The accuracy of the predicted moduli was verified with the predicted and measured ratios of the deflection parameters: $D_o/D_{of}$ *and* $AREA/AREA_f$.

**Table 10 Comparison of 3-layer and 4-layer Analyses**

| | **RS1** | | **RS2** | | **RS3** | |
|---|---|---|---|---|---|---|
| | **3 Layer** | **4 Layer** | **3 Layer** | **4 Layer** | **3 Layer** | **4 Layer** |
| B-1 thickness (inch) | 17 | 6 | 17 | 8 | 17 | 12 |
| B-1 modulus (ksi) | 60.9 | 65.0 | 62.3 | 72.0 | 56.9 | 58.0 |
| B-2 thickness (inch) | | 11 | | 9 | | 5 |
| B-2 modulus (ksi) | | 30.0 | | 30.0 | | 30.0 |
| $D_o/D_{of}$ | 0.87 | 0.99 | 0.94 | 1.00 | 0.97 | 1.00 |
| $AREA/AREA_f$ | 0.94 | 0.93 | 0.99 | 0.99 | 0.96 | 0.97 |

Notes:
$D_o$, $D_{of}$ - predicted and measured maximum deflections
$AREA$, $AREA_f$ - predicted and measured deflection parameters
A 2-inch-thick asphalt layer with an elastic modulus of 600 ksi was used for the analysis.
A constant subgrade modulus of 16.0 ksi was used.

The predicted moduli of the 6-inch, 8-inch, and 12-inch GRRB layers were 65.0, 72.0, and 58.0, respectively. The modulus of the GRRB layers ($M_{r(gc)}$) can be used to back-calculate the additional confining stress offered by the geocell layer, using Equation 22:

$$M_{r(gc)} = 1.88Pa\left(\frac{\theta + 2\Delta\sigma}{P_a}\right)^{0.88}\left(\frac{\tau_{oct}}{P_a} + 1\right)^{-1.25} \tag{22}$$

### *5.2.4 Contribution of Geocell Layer*

By applying Equation 22**,** the vertical stresses acting at the mid-depth of the GRRB layer were used to measure the average active bulk stress ($\theta$):

$$\theta = \left(\gamma h_m + \Delta\sigma_v\right)\left(1 + 2\frac{1 - \sin\phi}{1 + \sin\phi}\right) \tag{23}$$

Where,

$\gamma$ = average unit weight of pavement material

$h_m$ = depth of the mid-point of GRRB

$\Delta\sigma_v$ = observed stress increase from four-layer analyses

$\phi$ = internal friction angle for the RAP material

The average unit weight of the pavement materials was assumed to be 125 pcf, and the angle of internal friction of the RAP material was assumed to be $35^o$. The mid-point of the GRRB was 5, 6, and 8 inches, respectively, from the pavement surface. The additional confining pressure was estimated from Equation 22 based on the back-calculated modulus of the GRRB layers. The additional confining pressure offered by the geocell layer was 9.0, 7.5, and 10.5 psi for the GRRB layers located in RS1, RS2, and RS3, respectively. The additional confinement for the unreinforced section will be zero, which will lead to a reduced base modulus. The estimated modulus for the unreinforced RAP-base layer located within the UR1, UR2, and UR3 sections will be 43.1, 41.6, and 30.8 ksi, respectively. This shows that the addition of geocell confinement for the 6-inch, 8-inch, and 12-inch GRRBs increased the moduli by 50.8%, 73.1%, and 88.3%, respectively. The moduli enhancements are expected to improve the pavement performance in the field.

### *5.2.5 Determination of the Base Condition with Base Layer Index (BLI)*

*BLI* is the difference in the deflections measured under and 12 inches from the load center. It is usually reported in µm and is a good indicator of the structural condition of the base layer. The granular base layer may be classified into three distinct categories: sound (*BLI* < 200), warning (200 < *BLI* < 400), and severe (*BLI* > 400). This condition index represents the structural performance of the base layer and helps transportation agencies make decisions about major repair works when the BLI value is greater than 400. The *BLI* values for the reinforced and control sections are presented in Figure 46**.** It was observed that the average *BLI* values for the test sections were below 200, indicating that the base layer is in sound condition. No significant difference in the *BLI* was observed from 2020 to 2021, indicating that there was no deterioration in the base layer.

It was also observed that the difference between the minimum and maximum values of the *BLI* was greater for RS1 and smaller for RS3. The increase in the geocell thickness helped enhance the performance of the base layer by reducing the non-uniformity. The *BLI* index obtained from the regular FWD testing may be used to determine the *BLI* with time to determine the rate of deterioration of the base layer, which will help transportation agencies make decisions about future maintenance and/or rehabilitation works on those pavements. As the *BLI* values for RS1, RS2, RS3 are well below the warning levels, no major rehabilitation or maintenance work is necessary for the near future.

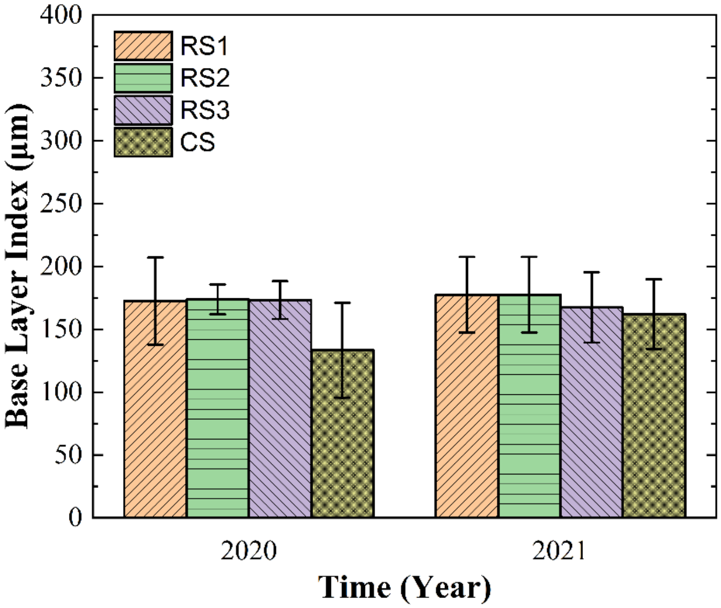

**Figure 46 Base layer index (*BLI*) based on FWD deflections data**

### 5.3 Automated Plate Load Testing

Eight APLTs were performed in the four test sections, as shown in Figure 47. A setup of 12-inch loading plates with four deflection sensors, located 2r, 3r, and 4r (r = radius of the loading plate) from the center of loading was used to perform the cyclic APLT test. The loading plate and deflection sensors assembly is shown in Figure 48. The sand was put at the bottom of the loading plate to provide a smooth surface that would ensure proper contact, and an infrared sensor was used to measure the road surface temperature at each test location.

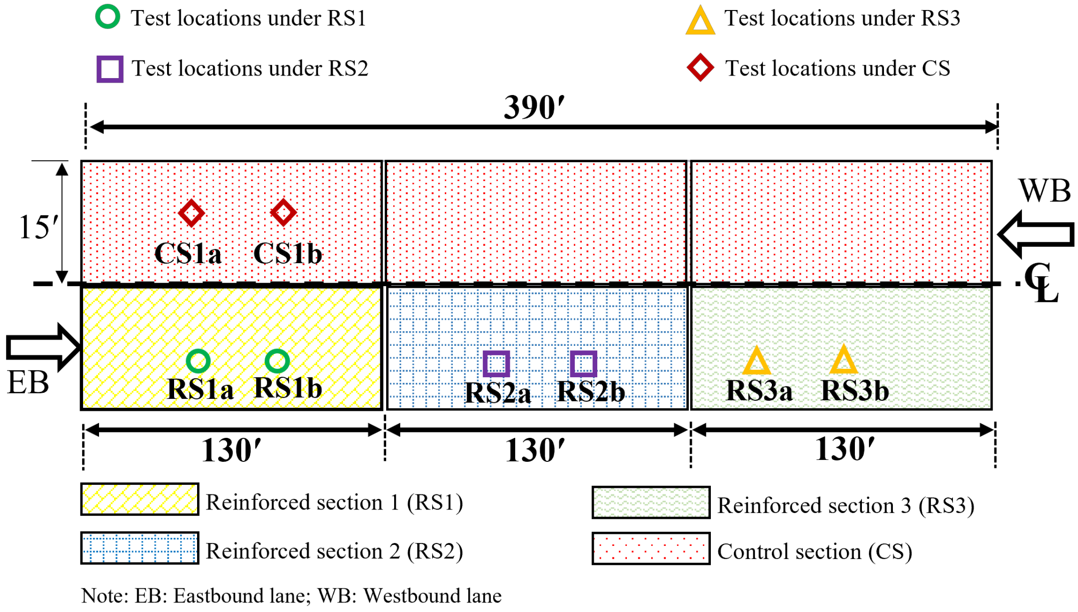

**Figure 47 APLT test locations**

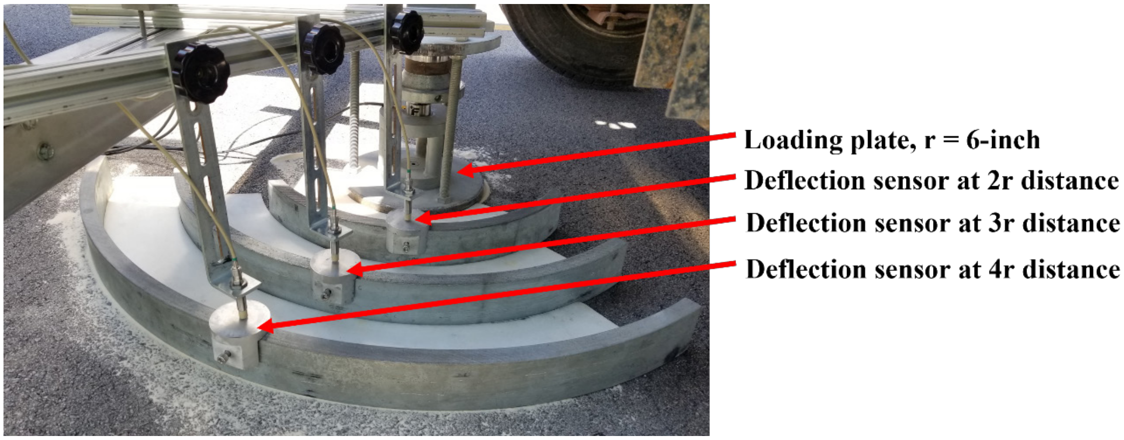

**Figure 48 Load and deflection sensors for APLT**

The loading schedule of the cyclic APLT, which included 12 load step sequences with four different loading rate frequencies at three different target stresses, is shown in Table 11. Applied stresses, rebound deformations, and permanent deformations were recorded for each load pulse. The first 168 cycles were conducted with a target cyclic stress of 150 psi, the second 168 cycles with 100 psi, and the third 168 cycles with 50 psi loading.

**Table 11 Loading Sequence for APLT Studies**

| Load Step | Number of Cycles, $N$ | Loading Frequency, $f$ (Hz) | Target Maximum Stress, $s_{max}$ (psi) | Target Cyclic Stress, $s_{cyclic}$, psi |
|---|---|---|---|---|
| 1 | 100 | 2.0 | 150 | 145 |
| 2 | 50 | 1.0 | 150 | 145 |
| 3 | 15 | 0.1 | 150 | 145 |
| 4 | 3 | 0.01 | 150 | 145 |
| 5 | 100 | 2.0 | 100 | 95 |
| 6 | 50 | 1.0 | 100 | 95 |
| 7 | 15 | 0.1 | 100 | 95 |
| 8 | 3 | 0.01 | 100 | 95 |
| 9 | 100 | 2.0 | 50 | 45 |
| 10 | 50 | 1.0 | 50 | 45 |
| 11 | 15 | 0.1 | 50 | 45 |
| 12 | 3 | 0.01 | 50 | 45 |

The deflections observed in each cycle had elastic and plastic components. The following sections will discuss the field responses from the different test sections and the potential benefits of replacing the existing flex base sections with geocell-reinforced sections.

### *5.3.1 Elastic/Resilient Deformations*

The elastic deformations measured for 504 load cycles with three different cyclic stress levels are shown in Table 11, which illustrates that the magnitudes of the resilient deformation varied with the loading amplitude and frequency. In general, the resilient deformations decreased with a decrease in the vertical cyclic stress and increased with a decrease in the loading frequency. The average resilient deformation under the loading plate for different frequency levels is shown in Figure 49.

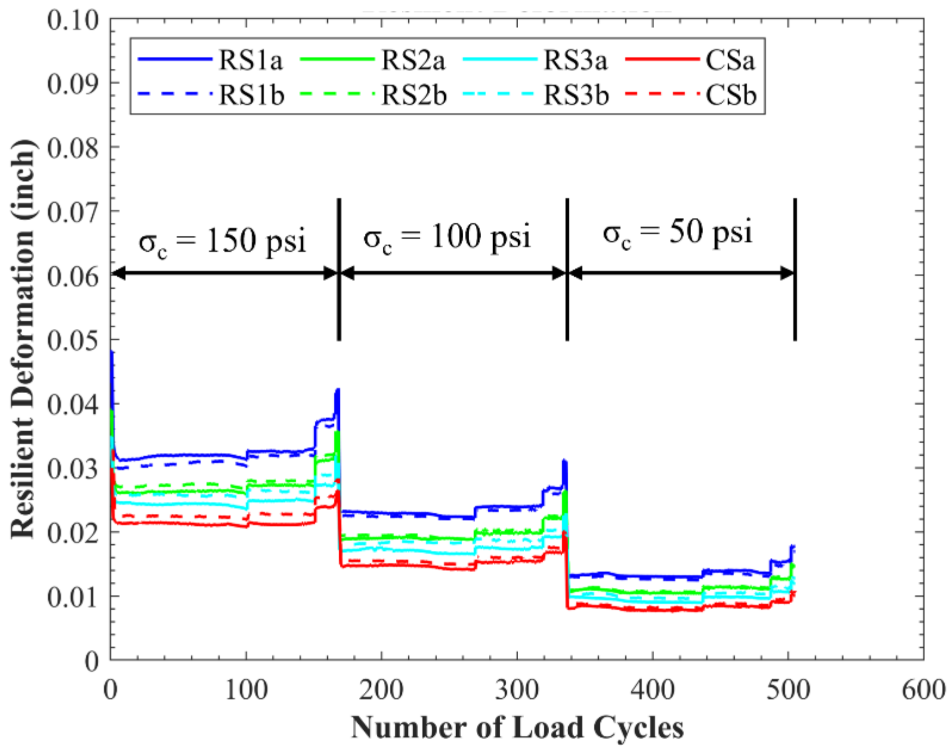

**Figure 49 Effect of cyclic stress on resilient deformations**

A maximum vertical resilient deformation of 0.042 was recorded for the RS1 section under the cyclic stress of 150 psi with a loading frequency of 0.1 Hz. An increase in frequency from 0.1 Hz to 2.0 Hz decreased the resilient deformation by 23.8%. Similar observations were made for the RS2 and RS3, as the resilient deformation decreased by 25.8% and 27.8% (Figure 50). The resilient deformation was found to be proportional to the applied cyclic stress.

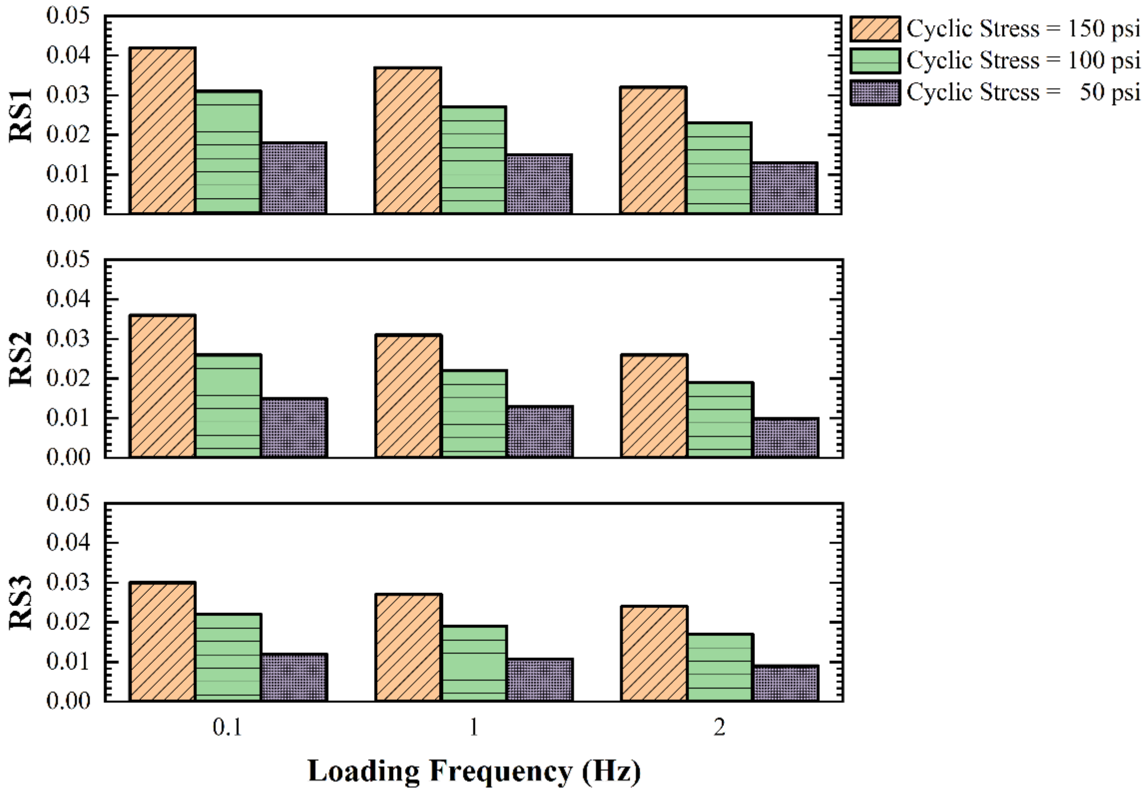

**Figure 50 Effect of loading frequency on resilient deformation (inch)**

The resilient deformation decreased by an average value of 58% when the applied cyclic stress reduced to 50 psi from 150 psi. It was also observed that vertical resilient deformation was almost proportional to the applied cyclic stress, which can be used to predict future deformations.

### *5.3.2 Surface Deflections*

The resilient deformations were recorded at 12, 18, and 24 inches away from the loading plate, as shown in Figure 51. The vertical deformations of reinforced sections decreased by 3 times at 4r (24 inches) from the load center. All recorded deformations showed a trend similar to the deformation recorded under the load center: they decreased with a reduction in the applied cyclic stress and loading frequency. The identical test performed under the same sections showed similar behavior, which ensures the repeatability of the automated plate load test. The vertical deformations obtained from these sections can be further used to correlate them with the pavement layer properties.

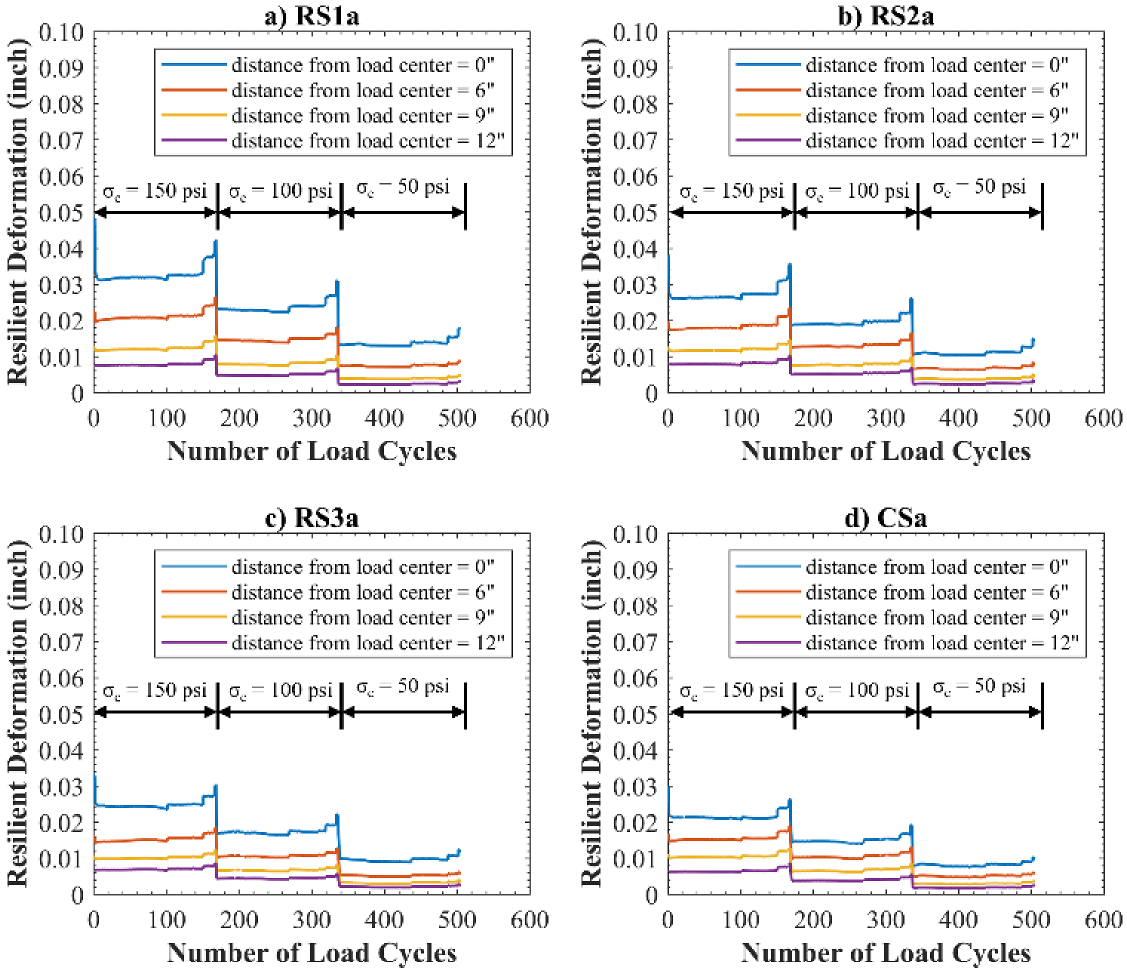

**Figure 51 Deflections at different distances from load center for a) RS1a, b) RS2a, c) RS3a, and d) CSa sections**

### *5.3.3 Determination of Combined Base Layer Modulus from APLT*

The total thickness of the base layer for the westbound (CS) road section was 15 inches, and for the eastbound (RS1, RS2, and RS3) test sections was 17 inches. It was previously reported that the asphalt layer modulus should be kept constant for thin asphalt pavements - approximately 500 ksi for the air temperature of 86°F. The subgrade layer modulus was assumed to be 16 ksi, based on the experimental results obtained from the repeated load triaxial testing. Several pavement analyses were performed to determine the maximum deflections under the vertical stresses of 50, 100, and 150 ksi. The layer properties used for the pavement analyses are reported in Table 12.

**Table 12 Layer Properties for the Determination of Combined Base Layer Modulus**

| Test Sections | $t_{asp}$ (inch) | $t_{base}$ (inch) | $E_{subg}$ (ksi) | $E_{base}$ (ksi) | Number of pavement analyses based on LEA |
|---|---|---|---|---|---|
| EB 50 | 4 | 15 | 10, 12.5, 15, 17.5, and 20 | 30, 40, 50, 60, 70, 80, 90, and 100 | 40 |
| EB 100 | 4 | 15 | | | 40 |
| EB 150 | 4 | 15 | | | 40 |
| WB 50 | 2 | 17 | | | 40 |
| WB 100 | 2 | 17 | | | 40 |
| WB 150 | 2 | 17 | | | 40 |
| Total = | | | | | 240 |

Notes: The first part of the classification of the test sections indicates the lane, and the second part indicates the applied cyclic stress. The modulus of the asphalt layer was assumed as 500 ksi, corresponding to the field temperature of 86°F.

The maximum vertical deformations obtained from the LEA with different cyclic stress levels were used to develop correlations with the pavement layer properties. The correlations developed for the vertical deflections, subgrade modulus, and base modulus are presented in Table 13. The accuracy of the predicted models with the correlation coefficients was very good in terms of $R^2$ value, which was greater than 0.95 for all the cases at a 95% level of significance. The standard errors were also very small, indicating a very good relationship obtained between the base layer modulus (BLM) and the deflection properties. The combined base layer modulus was determined by Equation 23**.**

$$E_{base} = c + p\left(E_{subg}\right) + q\left(\log D_o\right) \tag{23}$$

Here, $c$, $p$, and $q$ are the model constants for each category. Equations 24-29, presented below, were used to determine the combined base layer modulus for reinforced and unreinforced sections located within the westbound and eastbound lanes, respectively.

**Table 13 Correlation Coefficients for Combined Base Layer Modulus from APLT**

| **ID** | $\sigma$ | $c$ | $p$ | $q$ | **$R^2$ [a] (%)** |
|---|---|---|---|---|---|
| EB 50 | 4.88 | 368.89 | -2.92 | -249.39 | 0.96 |
| EB 100 | 4.83 | 442.91 | -2.90 | -248.80 | 0.96 |
| EB 150 | 4.86 | 486.57 | -2.90 | -248.87 | 0.96 |
| WB 50 | 4.89 | 464.07 | -4.59 | -346.7 | 0.96 |
| WB 100 | 4.63 | 572.67 | -4.59 | -347.82 | 0.96 |
| WB 150 | 4.68 | 633.25 | -4.78 | -347.62 | 0.96 |

**a** Significant at 5% level, $\sigma$ = standard error; $E_{base}$ = elastic modulus of the base; $E_{subg}$ = elastic modulus of the subgrade

$$E_{base(EB\ 50)} = 368.89 - 2.92\left(E_{subg}\right) - 249.39\left(\log D_o\right) \tag{24}$$

$$E_{base(EB\ 100)} = 442.91 - 2.90\left(E_{subg}\right) - 248.80\left(\log D_o\right) \tag{25}$$

$$E_{base(EB\ 150)} = 486.57 - 2.90\left(E_{subg}\right) - 248.87\left(\log D_o\right) \tag{26}$$

$$E_{base(WB\ 50)} = 464.07 - 4.59\left(E_{subg}\right) - 346.70\left(\log D_o\right) \tag{27}$$

$$E_{base(WB\ 100)} = 572.67 - 4.59\left(E_{subg}\right) - 347.82\left(\log D_o\right) \tag{28}$$

$$E_{base(WB\ 150)} = 633.25 - 4.78\left(E_{subg}\right) - 347.62\left(\log D_o\right) \tag{29}$$

For each set of tests, 504 repetitions were made under three different stress levels. The back-calculated elastic moduli values varied throughout the test. The average combined base moduli for RS1, RS2, RS3, and CS are referred to as $E_{RS1}$, $E_{RS2}$, $E_{RS3}$, and $E_{CS,}$ and these are presented in Figure 52**.** The in-situ elastic modulus of the base layer varied with the loading magnitude and frequency of the applied cyclic stress. The trend and nature of the responses collected from the field indicated that the base material behaved as a strength-hardening material as the elastic modulus increased with an increase of bulk stress. The thickness of the GRRB layers under RS1, RS2, and RS3 were 6, 8, and 12 inches, respectively. The increase in the thickness of the GRRB layers added to the overall stiffness of the base layer.

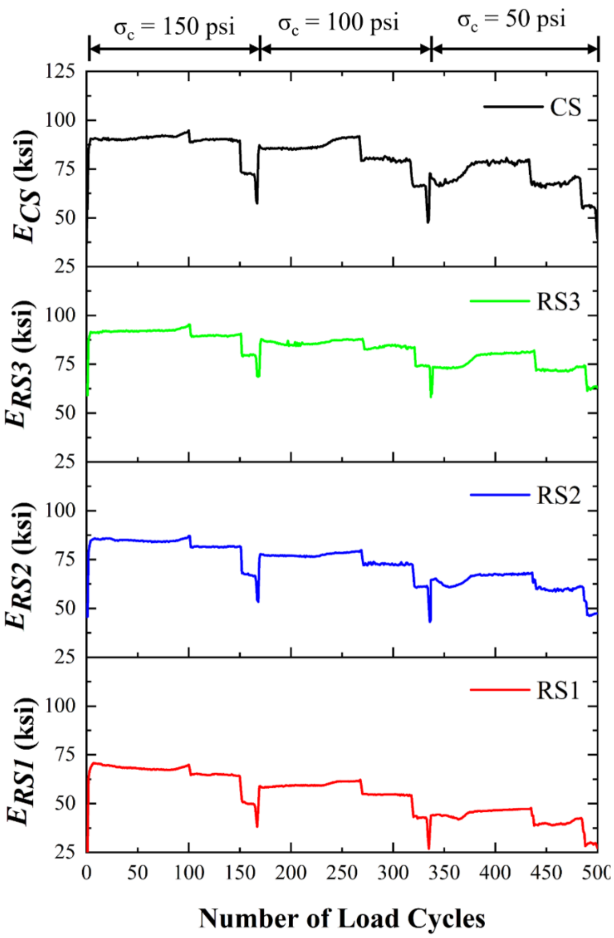

**Figure 52 Combined base moduli from APLT for different test sections**

Additional pavement analyses were performed to understand the contribution of the GRRB layer, and four-layer analyses were performed by dividing the base layer into two distinct layers: GRRB (B1) and the base layer section (B2). The elastic modulus of the base was 60 ksi, which was previously determined from the FWD tests. Table 14 presents the correlation coefficients of the models developed with maximum deflections and GRRB layer modulus for different test sections under three different cyclic stresses.

**Table 14 Correlation Coefficients for GRRB Modulus from APLT**

| ID | $\sigma$ | $c$ | $q$ | $R^{2a}$ (%) |
|---|---|---|---|---|
| RS1 50 | 5.07 | 267.34 | -19.08 | 0.94 |
| RS1 100 | 5.15 | 268.34 | -9.59 | 0.94 |
| RS1 150 | 4.93 | 269.00 | -6.42 | 0.95 |
| RS2 50 | 5.18 | 236.06 | -16.14 | 0.94 |
| RS2 100 | 5.20 | 236.22 | -8.07 | 0.94 |
| RS2 150 | 5.07 | 237.06 | -5.42 | 0.95 |
| RS3 50 | 5.11 | 206.25 | -13.31 | 0.94 |
| RS3 100 | 5.09 | 206.13 | -6.66 | 0.94 |
| RS3 150 | 5.13 | 206.89 | -4.47 | 0.94 |

**Note:** Equation of the following form, $E_{GRRB} = c + q \times \log D_O$

a = Significant at 5% level, $\sigma$ = standard error, $c$ = model constant,
$E_{GRRB}$ = elastic modulus of the GRRB layer
$E_{subg}$ = elastic modulus of the subgrade = 16.0 ksi. (Predicted from previous analysis)

The model parameters shown in Table 14 were used to determine the modulus of the GRRB layers $E_{6\text{-inch GRRB}}$, $E_{8\text{-inch GRRB}}$, and $E_{12\text{-inch GRRB}}$ that were located within the reinforced sections RS1, RS2, and RS3, respectively. Figure 53 shows the GRRB layer modulus throughout the 500 cycles of loading. The behavior of the GRRB layer was analogous to the behavior of the GRRB layers, as the modulus decreased with a decrease in the vertical stress and increased with an increase in the loading frequency. The GRRB layers also showed strength hardening behavior.

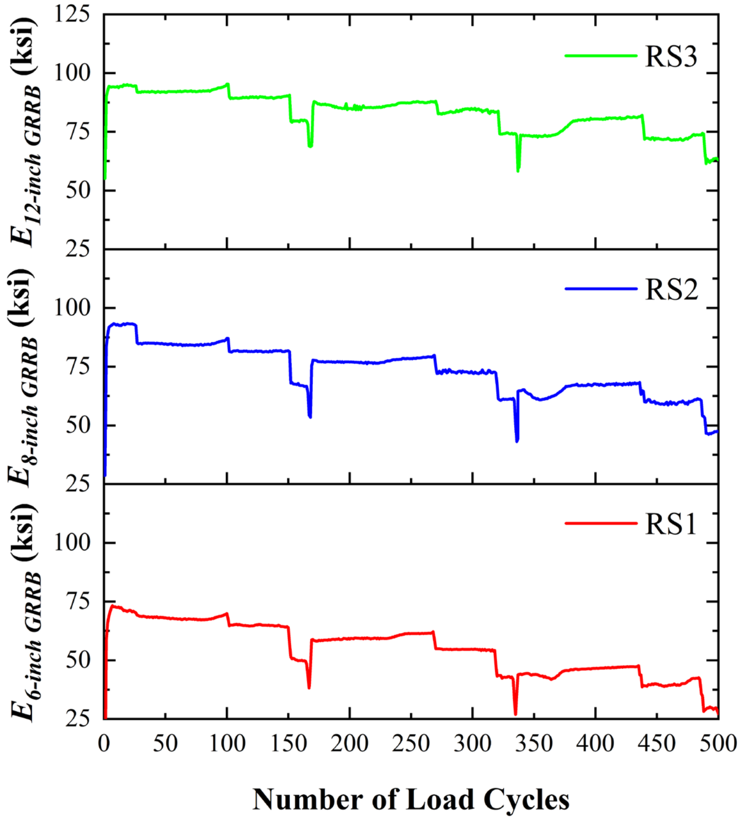

**Figure 53 GRRB layer modulus under repeated loading**

### *5.3.4 Effect of Loading Magnitude and Frequency*

A vehicular load is dynamic in nature, and the frequency of loading is directly related to the speed of the vehicles. The GRRB layer moduli increased with an increase in the loading frequency and magnitude of loading, as shown in Figure 54. The highest values of the layer modulus were obtained when the applied cyclic stress was 150 psi, and the loading frequency was 2.0 Hz. The estimated modulus values for the GRRB layers are 67.3, 88.5, and 95.0 ksi for reinforced sections RS1, RS2, and RS3, respectively. When the applied cyclic stress is 50 psi, and the loading frequency is 0.1 Hz, the estimated modulus values for the GRRB of the RS1, RS2, and RS3 sections are

6.8, 30.2, and 57.5 ksi, respectively. The elastic moduli of the pavement layers are not constant, as they vary with the loading magnitudes and frequencies. A modulus model of GRRB layers that is developed from field observations is needed in the pavement designs.

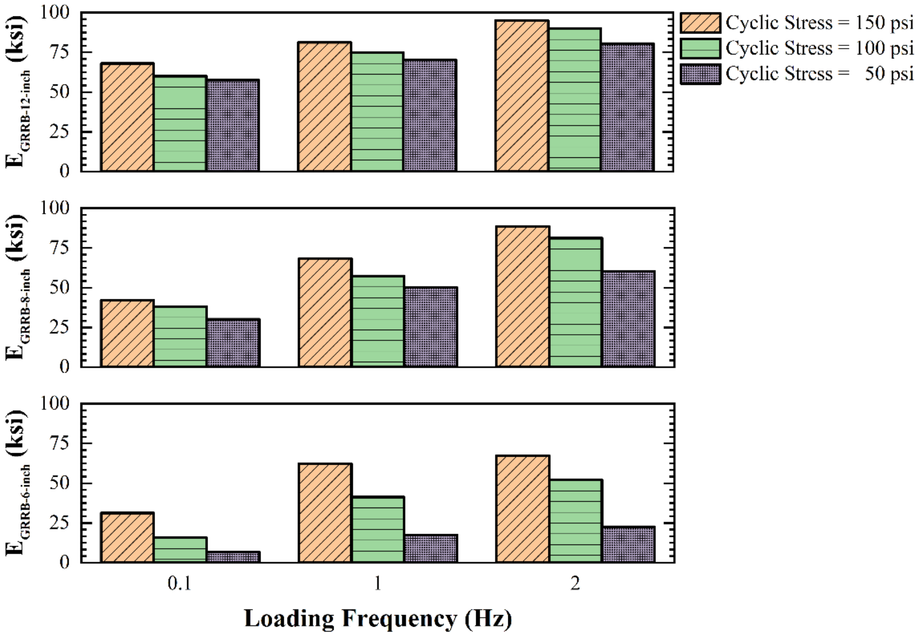

**Figure 54 Effect of loading frequency**

### *5.3.5 Development of Stress-dependent Material Model*

The elastic response of the pavement varies with an increase in the bulk stress, and the bulk stress depends on the magnitude of the applied vertical stress and the depth of the location from the pavement surface. The average elastic moduli of the GRRB layers for different vertical cyclic stress levels are shown in Figure 55. The modulus increased with an increase in the applied stress, regardless of the thickness of the GRRB layers. This information can be used to determine the moduli of the GRRB layer under the desired loading conditions.

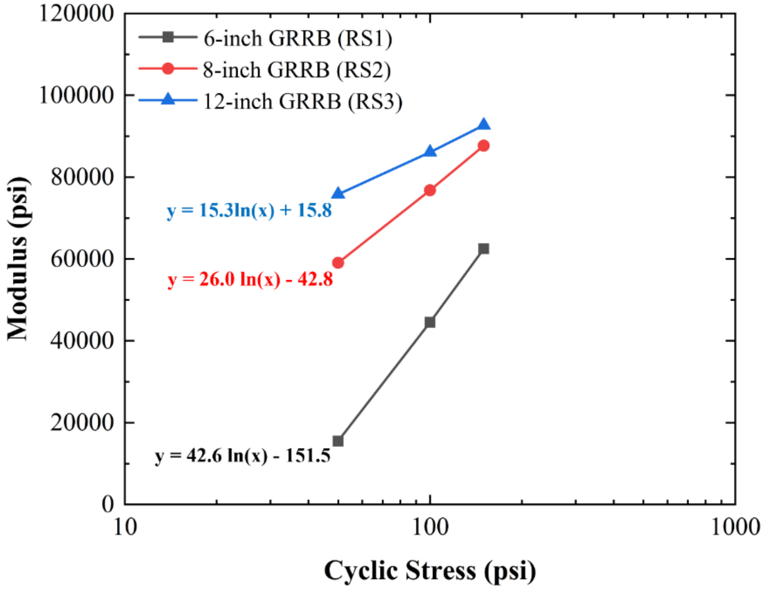

**Figure 55 Stiffness of GRRB layers at various stress levels**

When the applied vertical stress for a single wheel loading is approximately 80 psi, the corresponding elastic moduli of the 6-inch, 8-inch, and 12-inch GRRB layers will be 37, 70, and 82 ksi, respectively. According to MEPDG, the resilient modulus model for the base or subgrade material can be determined by Equation 30.

$$M_{r(subg)} = k_1 \mathrm{P_a} \left( \frac{\theta}{\mathrm{P_a}} \right)^{k_2} \left( \frac{\tau_{oct}}{\mathrm{P_a}} \right)^{k_3} \tag{30}$$

Where,

$M_{r(subg)}$ = resilient modulus of the GRRB

$\theta$ = bulk stress

$\tau_{oct}$ = octahedral shear stress

$\mathrm{P_a}$ = atmospheric pressure

$k_1$, $k_2$, and $k_3$ are the model parameters.

The average vertical stress acting at the mid-depth of the GRRB layers can be estimated from the self-weight of the pavement layers and the increase of the vertical stress that is due to the applied vertical stress. The available confinement at the desired location can be determined from the active earth pressure theory. In this case, the average unit weight of the pavement materials was assumed as 125 pcf, and an average angle of internal friction of 35° for the RAP material was used to estimate the bulk stress, and these results are presented in Table 15.

**Table 15 Parameters Used for the Development of Material Models**

| **Test section** | **Vertical stress** | **Average vertical stress at mid-depth of GRRB (psi)** | **Average horizontal stress at mid-depth of GRRB (psi)** | **Major principal stress (psi)** | **Minor principal stress (psi)** | **Bulk Stress (psi)** | **Octahedral shear stress (psi)** | **Resilient modulus (psi)** |
|---|---|---|---|---|---|---|---|---|
| | | $\sigma_v = \gamma(h_m) + \Delta\sigma_v$ | $\sigma_h = k\sigma_v$ | $\sigma_1$ | $\sigma_3$ | $\theta$ | $\tau_{oct}$ | $M_{r(subg)}$ |
| RS1 | 150 | 43.30 | 11.69 | 31.61 | 11.69 | 54.99 | 9.39 | 171000 |
| | 100 | 30.80 | 8.32 | 22.48 | 8.32 | 39.12 | 6.68 | 96000 |
| | 50 | 17.30 | 4.67 | 12.63 | 4.67 | 21.97 | 3.75 | 23000 |
| RS2 | 150 | 32.50 | 8.78 | 23.73 | 8.78 | 41.28 | 7.05 | 136000 |
| | 100 | 22.60 | 6.10 | 16.50 | 6.10 | 28.70 | 4.90 | 103000 |
| | 50 | 12.70 | 3.43 | 9.27 | 3.43 | 16.13 | 2.75 | 53000 |
| RS3 | 150 | 20.40 | 5.51 | 14.89 | 5.51 | 25.91 | 4.42 | 116000 |
| | 100 | 13.80 | 3.73 | 10.07 | 3.73 | 17.53 | 2.99 | 97000 |
| | 50 | 7.60 | 2.05 | 5.55 | 2.05 | 9.65 | 1.65 | 66000 |

**Note:**

$$\theta = \left(\gamma h_m + \Delta\sigma_v\right)\left(1 + 2\frac{1-\sin\phi}{1+\sin\phi}\right)$$

$$\tau_{oct} = \frac{1}{3}\sqrt{2\left(\sigma_v - \sigma_h\right)^2}$$

The estimated values shown in Table 15 were used to determine the resilient modulus model parameters, $k_1$, $k_2$, and $k_3$ derived from Equation 30**.** The coefficients of the three-parameter model for the GRRB layers are shown in Table 16.

**Table 16 Three-Parameter Model for Different GRRB Layers**

| Test sections | $k_1$ | $k_2$ | $k_3$ |
|---|---|---|---|
| 6-inch GRRB | 1595 | 4.58 | -8.22 |
| 8-inch GRRB | 6497 | 2.07 | -4.57 |
| 12-inch GRRB | 9390 | 1.02 | -2.82 |

The material models for the 6-inch, 8-inch, and 12-inch GRRB layers can be used to predict the resilient modulus of the geocell-reinforced flexible pavements based on the MEPDG method. It was observed that the material stiffness increased with an increase in the total height of the geocell system; however, the permanent deformation models need to be utilized to predict the remaining life of the existing pavement sections. The following section will discuss the performance of the test sections in terms of permanent deformation observed from the APLT.

### *5.3.6 Characteristics of Permanent Deformation with Cyclic Loading*

The permanent deformation of individual layers that contributes to the total permanent deformation is also known as rutting. The maximum surface rutting for the test sections was presented in the previous chapter. The magnitude of the maximum deformation was more than 200%, as there were significant differences in the maximum rutting observed within the right and left wheel paths. APLT tests were conducted between the wheel paths, and two consecutive tests were performed to check the consistency of the response of each test section. The permanent deformation throughout the APLT is shown in Figure 56. The tests were conducted for 504 cycles under vertical stresses of 150, 100, and 50 psi. A similar trend was observed for the additional tests conducted under the same test sections. It was also noted that the magnitude of the permanent deformation decreased with an increase in the number of loading cycles. The magnitude of the average permanent deformation recorded after 150 cycles for RS1, RS2, RS3, and CS was 0.068, 0.052, 0.041, and 0.037 inches, respectively.

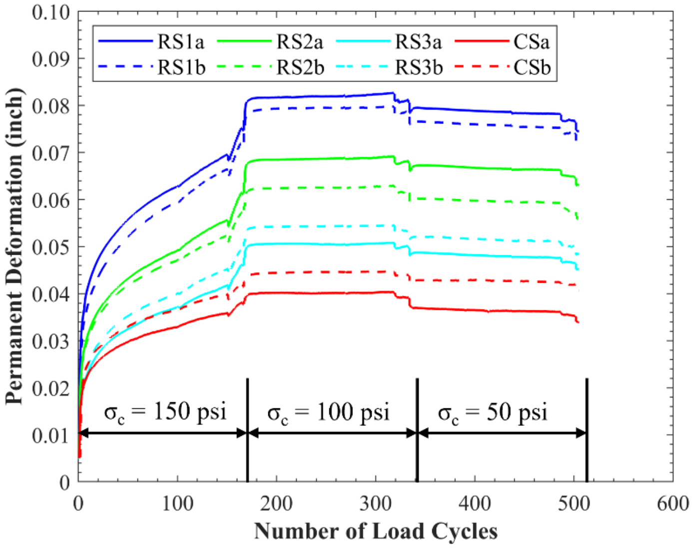

**Figure 56 Permanent deformations measured with APLT**

An increase in the GRRB layer thickness helped decrease the overall permanent deformation. Irrespective of the thickness of the GRRB layers, the trend of the permanent deformation was similar, as it increased with a decrease in the loading frequency. The following section will discuss the effects of loading frequency on permanent deformation.

Faster loading generated lower stresses within the pavement layer and resulted in lower permanent deformation, whereas the permanent deformation’s rate of change increased with a reduction in the frequency. The loading time and permanent deformation plot with loading cycles for RS1a, RS2a, RS3a, and CS are shown in Figure 57. The first 150 cycles were under *f* = 2 Hz, indicating faster loading of 1 cycle per 0.5 seconds. Similarly, the loading times for cycles 151 to 165 and 166 to 168 were 1 second and 10 seconds, respectively.

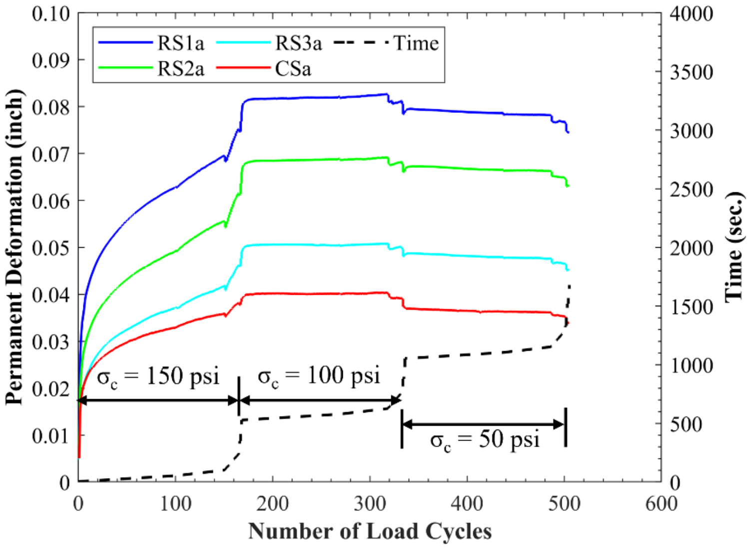

**Figure 57 Effect of loading frequency on the measured permanent deformation**

An increase in the amount of time required to complete each cycle also increased the magnitude of the vertical stress transferred to the pavement layers. Accordingly, a sharp increase was observed in the permanent deformations with a decrease in the loading frequency.

### *5.3.7 Development of Rutting Prediction Model Based on Field APLT Responses*

The total permanent deformation of typical pavement sections is the accumulation of the permanent deformation of the surface, base, and subgrade layers. The asphalt layer was only 2 inches thick; hence the permanent deformation observed within the pavement surface may be assumed as the permanent deformation accumulated within the base and subgrade materials. The permanent deformation captured under the first 150 cycles for different test sections was used to develop a permanent deformation model, using Equation 31.

$$\delta_{total} = \mathrm{A}N^{\mathrm{B}} \tag{31}$$

Where $\delta_{total}$ is the total permanent deformation

A and B are the model parameters

$N$ is the number of the loading cycle

The following sections will discuss the permanent deformation model (PDM) developed for the different test sections.

#### **5.3.7.1 Permanent Deformation Model for Reinforced Section 1 (RS1)**

The magnitude of loading used to analyze the rutting for the first 150 cycles was 150 psi. The permanent deformation plots for RS1a and RS1b are shown in Figure 58. It was observed that the trend and magnitude of the permanent deformation values were almost identical for the two tests conducted in the same test section. The average values of the permanent deformations were used to fit the PDM model based on a trial-and-error approach. The fitted model is shown in Equation 32.

$$\delta_{RS1} = 0.025N^{0.20} \tag{32}$$

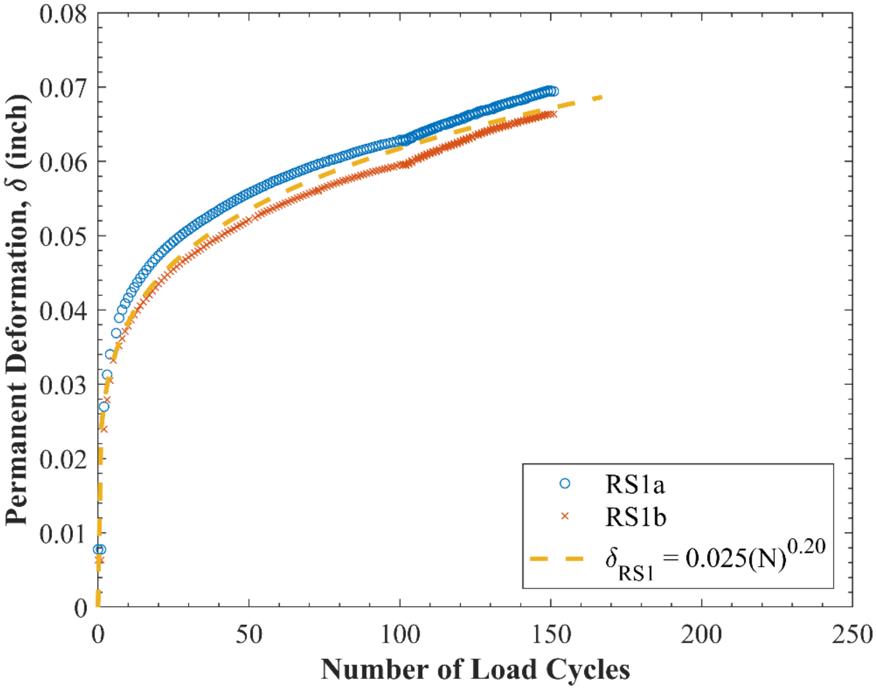

**Figure 58 Permanent deformation model for reinforced section 1 (RS1)**

#### 5.3.7.2 Permanent Deformation Model for Reinforced Section 2 (RS2)

Figure 59 depicts the permanent deformation plots for RS2a and RS2b and shows that the trend and magnitude of the permanent deformation values were almost identical. The fitted model is shown in Equation 33. It was observed that the ‘B’ parameter of the model was the same for both RS1 and RS2; however, the ‘A’ parameter varied. The similarity in the ‘B’ parameters indicates the comparable nature of the curve, and a decrease in the value of the ‘A’ parameter indicates the reduction in the magnitude of the permanent deformation.

$$\delta_{RS2} = 0.020N^{0.20} \tag{33}$$

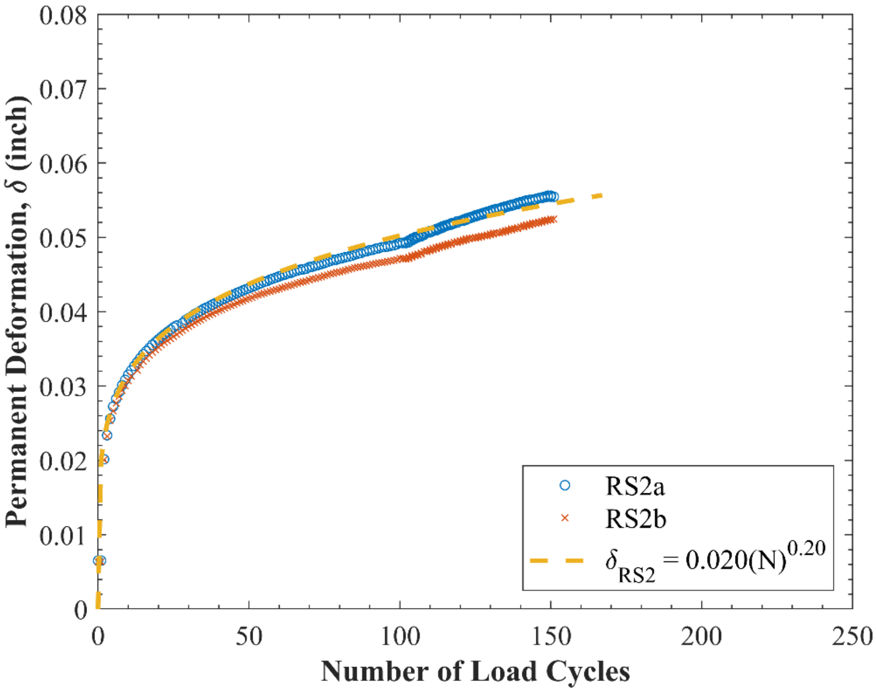

**Figure 59 Permanent deformation model for reinforced section 2 (RS2)**

### 5.3.7.3 Permanent Deformation Model for Reinforced Section 3 (RS3)

The permanent deformation plots for RS3a and RS3b depicted in Figure 60 show that the trend and magnitudes of the permanent deformation values were almost identical. The fitted model equation is shown in Equation 34. It was observed that the parameter ‘B’ remained the same (0.20) for all the geocell reinforced test sections; only ‘A’ decreased with a decrease in the thickness of the GRRB layer. The values of the ‘A’ parameter for RS1, RS2, and RS3 were 0.25, 0.20, and 0.16, respectively. It can be hypothesized that an increase in the GRRB layer thickness has the potential to reduce the permanent deformation of pavement structures.

$$\delta_{RS3} = 0.016N^{0.20} \tag{34}$$

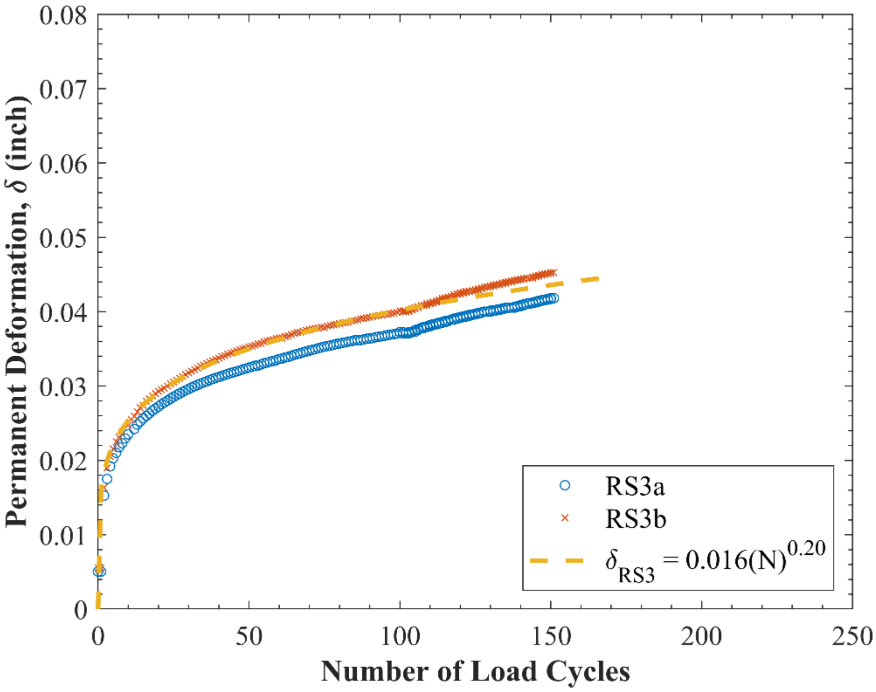

**Figure 60 Permanent deformation model for reinforced section 3 (RS3)**

#### 5.3.7.4 Permanent Deformation Model for Control Sections

The permanent deformation plots for CSa and CSb are shown in Figure 61 and reveal that the trend and magnitude of the permanent deformation values were almost identical. The fitted model equation is shown in Equation 35. Because of the reduction in vertical stress acting at the mid-depth of the base layer under consideration, the permanent deformations under the CS sections were slightly lower than the permanent deformations under RS3. The 4-inch thickness of the asphalt layer in CS helped to reduce the magnitude of the vertical stresses to the layer beneath it, and the reduction in vertical stresses helped to reduce the overall permanent deformations.

$$\delta_{CS}=0.014N^{0.20} \tag{35}$$

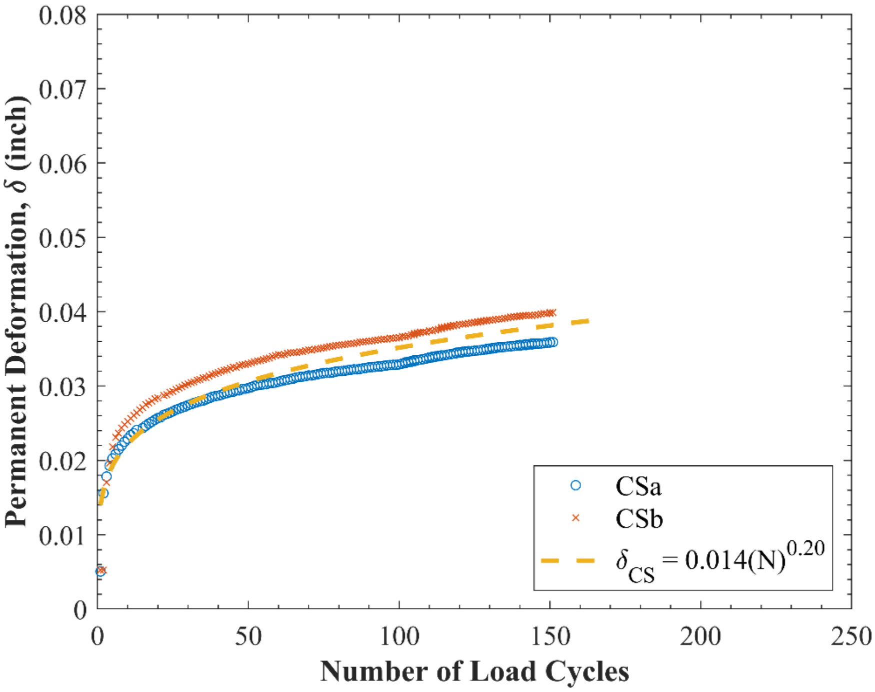

**Figure 61 Permanent deformation model for control section (CS)**

### *5.3.8 Comparison of Pavement Performance in Terms of Rut Life*

The PDM developed for the different test sections can be further used to predict the design life/rut life of the pavement. According to Asphalt Institute, the maximum rutting depth of the flexible pavement should be 0.50 inches. The number of allowable repeated loading cycles can be determined by using Equation 36.

$$N = 10^{\left(\frac{\log(\delta) - \log(A)}{B}\right)} \tag{36}$$

The predicted design life periods for the reinforced sections are shown in Table 17. The normalized rut life of RS1, RS2, RS3, and CS is 1.6, 4.9, 14.9, and 14.5, respectively. The increase in the thickness of the GRRB layers helped to enhance the performance.

**Table 17 Rutting Life Prediction Based on APLT**

| **Test Sections** | **GRRB thickness (inch)** | **A** | **B** | **N (Millions)** | **Normalized, N (Millions)** |
|---|---|---|---|---|---|
| RS1 | 6 | 0.025 | 0.20 | 3.2 | 1.6 |
| RS2 | 8 | 0.020 | 0.20 | 9.8 | 4.9 |
| RS3 | 12 | 0.016 | 0.20 | 29.8 | 14.9 |
| CS | N/A | 0.014 | 0.20 | 58.1 | 14.5 |

Note: Normalized N- Normalized with respect to Asphalt layer thickness

The rut life predicted from the APLT was based on a limited number of loading cycles; therefore, a more comprehensive study of a greater number of loading cycles is needed for a better understanding of the performance of the pavement sections. The following sections will discuss the contribution that geocells make to increasing the rut life of flexible pavements with GRRB layers.

### *5.3.9 Contribution of Geocell to Reduce Permanent Deformations*

The shear strength of pavement materials directly affects the amount of total rutting. The amount of confinement offered by a geocell was used to determine the shear strength parameters of the geocell-reinforced sections. The cohesion and friction angles of the infill material are $c'$ and $\phi'$. The failure envelopes for the unreinforced and reinforced material are shown in Figure 62. The additional confinement offered by the geocell helped increase the cohesion from OC to OD. The following section presents an estimation of the apparent cohesion in terms of additional confining pressure offered by the geocell.

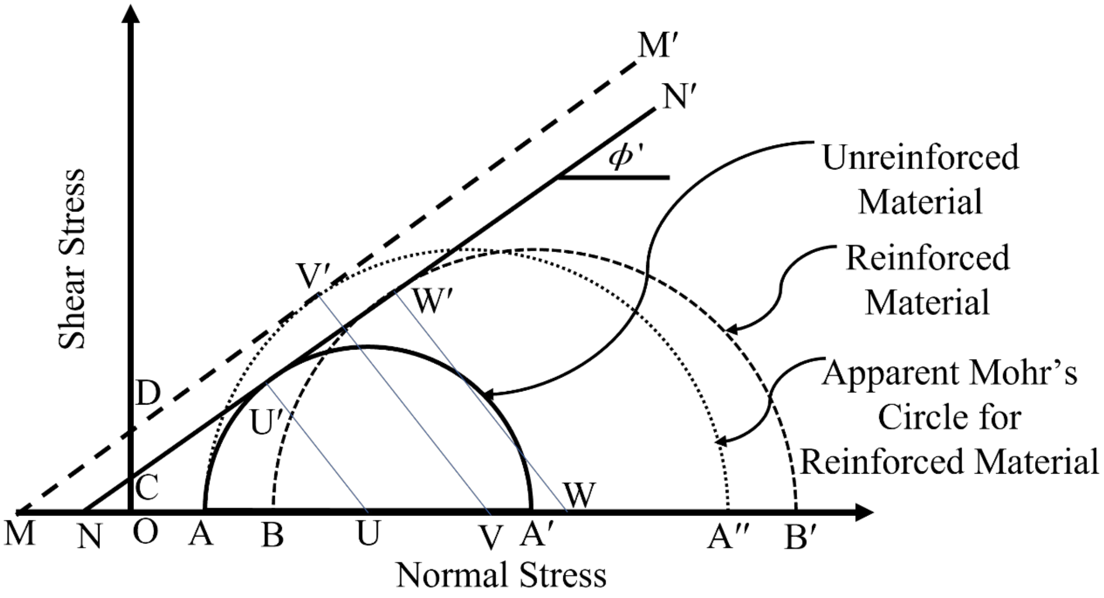

**Figure 62 Failure envelopes for reinforced and unreinforced sections**

**MC 1: Unreinforced Material from Figure 62**

Initial confining stress for unreinforced material = OA

Deviatoric stress for unreinforced material = AA′

Material cohesion = OC

Material friction angle = $\phi'$

**MC 2: Reinforced Material (increase in load capacity under same failure envelope) from Figure 62**

Additional confinement offered by geocell = AB

Initial confining stress for reinforced material = OB = OA+AB

Deviatoric stress for reinforced material = BB′

Material cohesion = OC

Material friction angle = $\phi'$

**MC 3: Apparent Mohr's Circle for Reinforced Material (change of cohesion) from Figure 62**

Initial confining stress for reinforced material = OA

Deviatoric stress for reinforced material = AA″ = BB′

Material cohesion = OD = OC + CD

Material friction angle = $\phi'$

The inclusion of a geocell helped to induce an apparent cohesion. The increase in cohesion (CD) can be determined from the following equations.

CD/CO = MN/NO = CO.MN/NO

$$= c'.\frac{\Delta\sigma}{2\tan\phi'} / \frac{c'}{\tan\phi'} = \frac{\Delta\sigma}{2}$$

Total cohesion for the reinforced material will be, $c_{gc} = c' + \frac{\Delta\sigma}{2}$

The additional confinement offered by the geocell-reinforced layer was back-calculated from the FWD study. The values of Δσ obtained from the FWD tests were used to determine the apparent cohesion of the GRRB layers presented in Table 18.

**Table 18 Apparent Cohesion of GRRB Layer**

| Test sections | GRRB thickness (inch) | $\Delta\sigma$ (psi) | $c'$ (psi) | $c_t/h_{gc}$ | $c_{gc}$ (psi) |
|---|---|---|---|---|---|
| RS1 | 6 | 9.0 | 14 | 0.55 | 18.5 |
| RS2 | 8 | 7.5 | 14 | 0.30 | 17.8 |
| RS3 | 12 | 10.5 | 14 | 0.67 | 19.3 |

Note: $c_t/h_{gc}$ is the ratio of the cover thickness to the height of the geocell.

The information tabulated under Table 18 was further used to correlate the geocell properties and the additional confining pressure. The linear relationship between the $c_t/h_{gc}$ ratio and the additional confining pressure, $\Delta\sigma$ is shown in Equation 37.

$$\Delta\sigma = 7.8\left(\frac{c_t}{h_{gc}}\right) + 5 \tag{37}$$

The apparent cohesion induced by the geocell-reinforced section can be determined from Equation 38.

$$c_{gc} = c' + 3.9\left(\frac{c_t}{h_{gc}}\right) + 2.5 \tag{38}$$

Where $c'$ = drained cohesion, the subgrade material

$c_t$ = total thickness of the RAP cover layer

$h_{gc}$ = height of the geocell

### *5.3.10 Rutting Model for GRRB Layer*

The rutting model presented in M-E design was less sensitive to the thickness and stiffness of the material and required modifications that were based on the Tseng and Lytton (1989) model, using Equations 39-41.

$$\varepsilon_p(N) = \varepsilon_o e^{-\left(\frac{\rho}{N}\right)^{\beta}} \left(\frac{\sqrt{J_2}}{P_a}\right)^{m} \left(\frac{\alpha I_1 + K}{P_a}\right)^{n} \left(P_a\right)^{-(m+n)} \tag{39}$$

$$\alpha = \frac{2\sin\phi'}{\sqrt{3}(3 - \sin\phi')} \tag{40}$$

$$K = \frac{c'.6\cos\phi'}{\sqrt{3}(3 - \sin\phi')} \tag{41}$$

Where $J_2$ is the second invariant of the deviatoric stress tensor

$I_1$ is the first invariant of the stress tensor

$\varepsilon_0$, $\rho$, $\beta$, $m$, and $n$ are model coefficients

$c'$ and $\phi'$ are effective cohesion and friction angle, respectively

The $K$ parameter as shown in the equation can be further modified for the geocell-reinforced section as shown in the following equation (Equation 42).

$$K_{geo} = \frac{\left(c' + \frac{3.9c}{h_{geo}} + 2.5\right).6\cos\phi'}{\sqrt{3}(3 - \sin\phi')} \tag{42}$$

According to the Lytton et al. (2019), the following set of correlations may be used to estimate model parameters as shown in Equations 43-47.

$$\log\varepsilon_o = 0.0170\left(P_4\right) - 0.0097(MDD) + 0.9900 \tag{43}$$

$$\log(\rho) = 0.0574\left(P_4\right) - 0.0937(MC) + 5.0756 \tag{44}$$

$$\beta = -0.0148\left(P_4\right) + 0.0081(MDD) - 0.0014(S) \tag{45}$$

$$\log(m) = -0.2153\left(\varepsilon_o\right) + 0.3960 \tag{46}$$

$$n = -0.2299(m) - 0.7460 \tag{47}$$

Where $P_4$ is the percent of material passing No. 4 sieve (unit: %)

*MDD* is the maximum dry density (lb/ft$^3$)

*MC* is the test moisture content (%)

*S* is the degree of saturation (%)

The $P_4$, *MDD*, *MC*, and *S* parameters of the base RAP material are 5%, 120 pcf, 4.5%, and 70%, respectively. The estimated values of the $\alpha$, $\varepsilon_o$, $\rho$, $\beta$, $m$ and $n$ are 0.25, 0.81, 87287, 0.80, 1.67, and -1.13, respectively. The $K$ values for the 6-inch, 8-inch, and 12-inch GRRB layers are 22.17, 21.01, and 22.73, respectively. The estimated values of the permanent deformation are presented in Table 19.

**Table 19 Permanent Strain Estimated from NCHRP Model (Lytton et al. 2019)**

| **Test section** | **Vertical stress** | $\sigma_v$ | $\sigma_h$ | $\sigma_1$ | $\sigma_3$ | $I_1$ | $J_2$ | $K$ | $\varepsilon_P$ ($\times 10^{-6}$) |
|---|---|---|---|---|---|---|---|---|---|
| RS1 | 150 | 43.3 | 11.7 | 31.6 | 11.7 | 54.9 | 132.2 | 22.2 | 278 |
| | 100 | 30.8 | 8.3 | 22.5 | 8.3 | 39.1 | 66.9 | 22.2 | 94 |
| | 50 | 17.3 | 4.7 | 12.6 | 4.7 | 21.9 | 21.1 | 22.2 | 14 |
| RS2 | 150 | 32.5 | 8.8 | 23.7 | 8.8 | 41.3 | 74.5 | 21.0 | 119 |
| | 100 | 22.6 | 6.1 | 16.5 | 6.1 | 28.7 | 36.0 | 21.0 | 37 |
| | 50 | 12.7 | 3.4 | 9.3 | 3.4 | 16.1 | 11.4 | 21.0 | 5 |
| RS3 | 150 | 20.4 | 5.5 | 14.9 | 5.5 | 25.9 | 29.3 | 22.7 | 24 |
| | 100 | 13.8 | 3.7 | 10.1 | 3.7 | 17.5 | 13.4 | 22.7 | 6 |
| | 50 | 7.6 | 2.1 | 5.6 | 2.1 | 9.7 | 4.1 | 22.7 | 0.8 |

Notes:

$\sigma_v = [\, \gamma(h_m) + \Delta\sigma v \,]$ =Average vertical stress at mid-depth of GRRB

$\sigma_h = k\sigma v$ = Average horizontal Stress at mid-depth of GRRB

$\sigma_1$ = major principal stress; $\sigma_2 = \sigma_3$ = minor principal stress

$$I_1 = \sigma_1 + \sigma_2 + \sigma_3$$

$$J_2 = \frac{1}{6}\left[\left(\sigma_1 - \sigma_2\right)^2 + \left(\sigma_2 - \sigma_3\right)^2 + \left(\sigma_3 - \sigma_1\right)^2\right]$$

It was observed that the permanent strain increased with the magnitude of the applied vertical stress and decreased with an increase of the GRRB layer thickness. The magnitude of permanent strain depends on the magnitude of applied vertical stresses on top of the pavement surface and available horizontal confinement. The increase of vertical stress from 100 psi to 150 psi leads to an increase of the base layer permanent strain for the RS1, RS2, and RS3 layers by 2.9, 3.2, and 4.0 times, respectively. On the other hand, a decrease of vertical stress from 100 to 50 psi reduces the base layer permanent strains for the RS1, RS2, and RS3 layers by 6.7, 7.4, and 7.5 times, respectively. The permanent strain corresponding to standard wheel loading can therefore be determined from the following Figure 63**.**

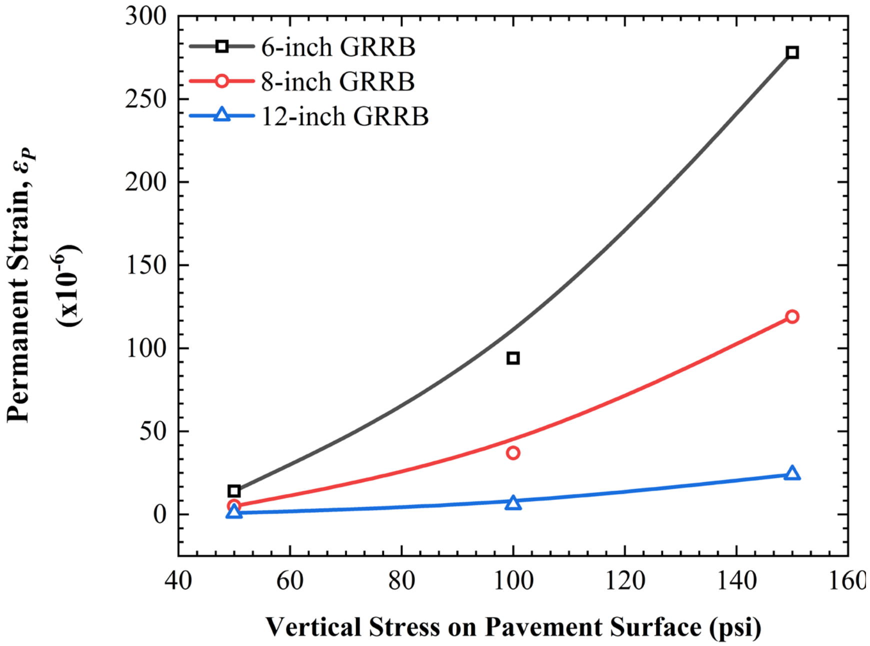

**Figure 63 Effect of applied vertical stress on the permanent strain of the GRRB layer**

The permanent strains corresponding to 80 psi vertical stress for the 6-inch GRRB, 8-inch GRRB, and 12-inch GRRB layers are $60\times10^{-6}$, $25\times10^{-6}$, and $15\times10^{-6}$, respectively. The increase in GRRB layer thickness helped to reduce the permanent strain on the base layer, which eventually helped to reduce the overall rutting of the pavement. The total rutting of the flexible pavement depends on the modulus, shear strength, thicknesses, and permanent deformation of the base layer (Lytton et al., 2019). The following section discusses the influence of the reinforced base layer to control the vertical rise of the expansive subgrade soil, based on the current study.

### 5.4 Reduction of Potential Vertical Rise (PVR) with Geocell-Reinforced RAP Base

Swelling and shrinking of subgrade soil lead to the vertical movement of the flexible pavement, which is also known as Potential Vertical Rise (PVR). The PVR is an important parameter for the flexible pavement constructed over expansive subgrade conditions. The PVR for the road section under the current project was determined with WINPRES software developed by Lytton et al. (2004). The input parameter for the analysis, as listed in Table 20**,** was used to determine the PVR.

**Table 20 Input parameters used for WINPRES software**

| Item | Parameters Used |
|---|---|
| Soil properties | Effective layer thickness = 12 inch<br>Liquid limit = 58%<br>Plasticity index = 31%<br>Dry unit weight = 89.5 pcf |
| Environmental and geometric conditions | Mean thornthwaite moisture index = 0<br>Width of pavement = 30 ft<br>Lateral drainage type = FILL |
| Traffi loading and reliability | Design life = 20 years<br>AADT = 1500<br>ESAL = 1 million<br>Reliability = 95% |
| Structural Properties from FWD Test | Subgrade modulus = 16.0 ksi |

The estimated PVR values for the 19-inch thick pavement section are 2.24 and 3.11 inches, measured at a distance of 2 ft. and 12 ft. away from the centerline of the pavement. It is expected that the pavement with fill-type lateral drainage will allow moisture migration from the side, which results in higher vertical movement near the edge of the pavement. The field measurements showed that the estimated value of the vertical movement was less than 0.40 inches for the reinforced sections. The inclusion of geocell helped to distribute the swelling induced upward pressure over a larger area; hence the differential movements were restricted.

### 5.5 Summary

Two types of non-destructive field studies using FWD and APLT tests were conducted on the reinforced test sections to evaluate the structural performance of the geocell reinforced flexible pavement. The pavement responses collected from the field were used to determine the stiffness. The applied vertical stresses for the FWD loading were around 80 psi, which represents the single wheel loading; however, the magnitude of the applied stresses for the APLT testing varied from 50 psi to 150 psi. The pavement responses under different magnitudes of stresses were used to determine the material parameters for the stress-dependent model. The major outcomes from the current chapter are summarized below.

### *5.5.1 Findings from FWD Test*

- Mathematical models were developed to predict the base layer modulus under different GRRB layer conditions. The deflection bowl characteristics parameter obtained from the proposed mathematical models were in good agreement with the monitored field data.
- The average elastic modulus of the combined base layer of the reinforced sections was consistent (varied from 56 to 67 ksi), whereas the elastic modulus of the base layer of the control section varied from 30 to 90 ksi. The inclusion of geocell helped to provide uniform support for the pavement.
- The estimated additional confinement offered by the geocell located in RS1, RS2, and RS3 were 9.0, 7.5, and 10.5 psi, which helped to increase the elastic modulus of the 6-inch, 8-inch, and 12-inch GRRB layers by 50.8%, 73.1%, and 88.3%, respectively.
- The estimated base layer indices (*BLI*s) for the reinforced sections were less than 200, which indicates a sound base condition. There is no momentous change in *BLI* from 2020 to 2021, which indicates a stable condition of the base layer was achieved during service.

### *5.5.2 Findings from APLT Test*

- The magnitude of elastic deformation depends on the magnitude and frequency of the applied loading. The increase in frequency from 0.1 Hz to 2.0 Hz decreased the resilient deformations for RS1, RS2, and RS3 by 23.8, 25.8, and 27.8%, respectively.
- The predicted modulus for the 6-inch, 8-inch, and 12-inch GRRB layers under single wheel loading (80 psi) were 37, 70, and 82 ksi, respectively. The increase in GRRB layer thickness helped to increase the overall resilient performance of the base layer
- The three-parameter resilient modulus model developed for the untreated RAP material was further calibrated with respect to the field data to get the model parameters for the GRRB layers, which can be incorporated for the M-E design.
- The remaining rut lives for the RS1, RS2, and RS3 sections were estimated as 3.2, 9.8, and 29.8 million, respectively.
- The apparent cohesion offered by the geocell for the RS1, RS2, and RS3 sections were 18.5, 17.8, and 19.3 psi, respectively

Based on the observed vertical movements from the current field studies, it can be stated that the geocell layer or GRRB layer section built as a part of paved layers on expansive soil conditions has reduced the differential heaving of the expansive subgrade soil. These results agree with field test section observations where no major cracking was recorded.

# CHAPTER VI

# NUMERICAL MODELING AND PARAMETRIC STUDY

## 6.1 General

Numerical modeling and analyses were performed to study the behavior of the base layer of geocell-reinforced RAP (GGRB) constructed within a flexible pavement system. The finite element method (FEM) was used to model the different test sections, including the reinforced and unreinforced sections. The field data obtained from the nondestructive pavement testing was used to validate the numerical models. An additional verification study was conducted based on the results of the plate load tests, and a parametric study was conducted to study the effects of the thicknesses of the asphalt concrete and GRRB layers on the design life of the flexible pavement system.

## 6.2 Numerical Finite Element Modeling

Predicting material behavior by applying constitutive models and related equations that are based on experimental results and embodied in finite element modeling (FEM) can provide insights into load-deformation characteristics under complex boundary conditions. In most cases, ABAQUS, a FEM software is used to find approximate solutions for the displacements, deformations, stresses, and forces in a solid body that is subjected to loading; the force and moment equilibrium will have to be maintained over an arbitrary volume of the solid body to find the exact solution. The basic equations for standard displacement-based finite element analysis rely on the virtual work principles shown in Equations 48-49 (Abaqus theory manual).

$$\int_V \boldsymbol{\sigma} : \delta \boldsymbol{D}\, dV = \int_S \boldsymbol{t}^T . \delta v dS + \int_V \boldsymbol{f}^{\,T} . \delta v dV \tag{48}$$

Here, $V$ is the volume occupied by a part of the body in the current configuration, and $S$ is the surface bounding this volume. The Cauchy stress matrix $\sigma$ represents the stress at any point. The surface traction at any point on $S$ is defined by the force $t$ per unit of the current area, and the body force at any point within the volume of the material under consideration is represented by $f$ per unit of the present volume. The left-hand side of this equation can be replaced by the integral over the reference volume of the virtual work rate per reference volume defined by any conjugate pairing of material stress ($\tau^c$) and strain ($\varepsilon$).

$$\int_{V^O} \tau^{\mathrm{c}} : \delta\varepsilon\, dV^O = \int_S \boldsymbol{t}^T . \delta v dS + \int_V \boldsymbol{f}^{\,T} . \delta v dV \tag{49}$$

The equilibrium equation for an infinitesimal element can be presented in terms of the displacement matrix [u], as shown in the following Equations 50-52.

$$[B]^T[C][B][u] - [f] = [0] \tag{50}$$

$$[\sigma] = [C][\gamma] \tag{51}$$

$$[\gamma] = [B][u] \tag{52}$$

Here, $[B]$ = strain displacement matrix

$[C]$ = Jacobian matrix

$[u]$ = displacement matrix

$[f]$ = body force matrix

Flexible pavement is a multi-layer system, and in most cases, the two-dimensional linear elastic approach is used for the numerical modeling analysis (Christopher et al., 2006; Huang, 2004; Smith et al., 2017). In this study, a three-dimensional reinforcing structure (geocell) was used, which necessitated the 3D FEM analysis. The purpose of this chapter is to assess the numerical FEM models and the geocell for different test sections and validate their predictions based on the pavement responses collected during the nondestructive field testing. The applied vertical load from the FWD device is an impulse load that is dynamic in nature (Pierce et al., 2009); however, it is recommended that the peak deflections be analyzed as if they are equivalent in magnitude to the deflections that would occur if a load of equal magnitude had been applied statically (ASTM D5858). In this modeling study, the vertical load was applied statically to simulate the field FWD condition.

## 6.3 Material Models

The pavement sections considered in this modeling consisted of asphalt concrete, base material, and subgrade layers. Since the main objective of this study was to understand the performance of base layer materials with geocells, extensive analyses were performed for the GRRB layers. The effects of introducing geocells can be incorporated into the material behavior by enhancing the shear strength parameter or introducing cross-anisotropic material behavior of the base layer. The following section will discuss the material models used in the FEM analysis.

### *6.3.1 Asphalt Concrete*

Pavement materials such as asphalt concrete are viscoelastic in nature. They exhibit elastic behavior at higher rates of loading, while viscous behavior exhibits elastic behavior at slower rates of loading. As the pavement loading is dynamic, the elastic layer theory is appropriate for pavement analysis, according to ASTM D5858. For thin layer asphalt concrete pavements, a fixed asphalt concrete layer modulus should be used, as the thickness of the layer is less than one-third of the loading plate diameter (ASTM D5858). The elastic modulus of the asphalt concrete layer is widely used for the analysis of flexible pavements (Gungor et al., 2017; Huang, 2004; Setiawan et al., 2017). The elastic modulus of the asphalt concrete layer is temperature dependent, e.g., the average elastic modulus for 75°F, 86°F, and 90°F are 600, 500, and 400 ksi, respectively (Michalak & Scullion, 1995). The Poisson's ratio of this material was taken as 0.40 for all the analyses.

### *6.3.2 Unbound Granular Base*

The base layer of the existing pavement was constructed with flex base material that was modeled as an elastic material. The inclusion of a geocell within the RAP base layer helped to increase the apparent cohesion of the reinforced composite layer, which resulted in an increase in the horizontal stiffness. The linear isotropic elastic material model was used for the unreinforced material, and an anisotropic elastic material model was used for the geocell-reinforced layer. When the elastic material is loaded, it sustains elastic strain, but the strain is reversible, and the material will spring back to its undeformed condition when the applied load is removed. The stress-strain relationship for the linear elastic isotropic material is depicted in Equation 53.

$$\begin{bmatrix}\sigma_{xx}\\ \sigma_{yy}\\ \sigma_{zz}\\ \sigma_{xy}\\ \sigma_{yz}\\ \sigma_{zx}\end{bmatrix}=\frac{E}{(1+\mu)(1-2\mu)}\begin{bmatrix}1-\mu & \mu & \mu & 0 & 0 & 0\\ \mu & 1-\mu & \mu & 0 & 0 & 0\\ \mu & \mu & 1-\mu & 0 & 0 & 0\\ 0 & 0 & 0 & 1-2\mu & 0 & 0\\ 0 & 0 & 0 & 0 & 1-2\mu & 0\\ 0 & 0 & 0 & 0 & 0 & 1-2\mu\end{bmatrix}\begin{bmatrix}\varepsilon_{xx}\\ \varepsilon_{yy}\\ \varepsilon_{zz}\\ \varepsilon_{xy}\\ \varepsilon_{yz}\\ \varepsilon_{zx}\end{bmatrix} \tag{53}$$

A horizontal barrier such as a geocell can increase the material stiffness in a lateral direction, which may lead to anisotropic material behavior. The field responses collected from the nondestructive field testing were used to determine the resilient modulus for the unreinforced and reinforced sections. The combined resilient modulus (reinforced section) can be used to determine the horizontal resilient modulus with the following equation proposed by Lytton et al. (2019), as shown in Equation 54.

$$M_R=\sqrt{\left(M_R\right)_v\left(M_R\right)_h} \tag{54}$$

Where $M_R$ = combined resilient modulus of the reinforced layer

$(M_R)_v$ = vertical resilient modulus determined from the unreinforced case

$(M_R)_h$ = horizontal resilient modulus

**Table 21 Determination of Anisotropic Parameter from Field Test**

| Test Section | $\sigma_v$ (psi) | $\Theta$ (psi) | $\tau_{oct}$ (psi) | $M_R$ (psi) | $M_{Rv}$ (psi) | $n$ | $n_s$ |
|---|---|---|---|---|---|---|---|
| RS1 | 150 | 54.9 | 9.4 | 171559 | 47594 | 13.0 | 3.5 |
| | 100 | 39.1 | 6.6 | 95715 | 40942 | 5.5 | |
| | 50 | 21.9 | 3.7 | 23212 | 29625 | 0.6 | |
| RS2 | 150 | 41.2 | 7.0 | 136952 | 42017 | 10.6 | 6.5 |
| | 100 | 28.7 | 4.9 | 103707 | 34754 | 8.9 | |
| | 50 | 16.1 | 2.7 | 53020 | 24194 | 4.8 | |
| RS3 | 150 | 25.9 | 4.4 | 116070 | 32752 | 12.6 | 14.8 |
| | 100 | 17.5 | 2.9 | 97307 | 25591 | 14.5 | |
| | 50 | 9.6 | 1.6 | 65586 | 16711 | 15.4 | |

Note:
$\sigma_v$ = applied vertical stress; $\theta$ = bulk stress; $M_R$ = combined resilient modulus; $M_{R(v)}$ = vertical resilient modulus; $n$ – modular ratio ($n = M_{R(h)}/ M_{R(v)}$ ); $n_s$ – modulus ratio for standard loading of 80 psi

A three-parameter resilient modulus model was used to determine the in-situ elastic modulus property under different stress conditions for the untreated reclaimed asphalt concrete (RAP) pavement base (RB) material located within UR1, UR2, and UR3, as shown in Figure 64.

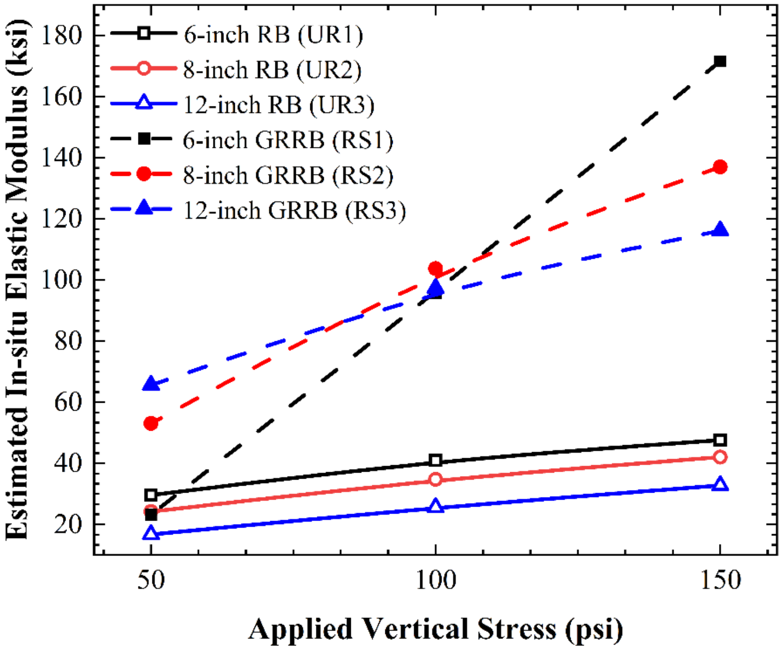

**Figure 64 In-situ elastic moduli of reclaimed asphalt concrete pavement base (RB) and geocell-reinforced reclaimed asphalt concrete pavement-base (GRRB)**

The estimated in-situ elastic moduli of the geocell-reinforced reclaimed asphalt concrete pavement bases (GRRB) of RS1, RS2, and RS3 are shown in Figure 64. The FWD tests were conducted under a standard wheel load of 80 psi that was used to determine the in-situ elastic modulus of the untreated and reinforced RAP layers. The in-situ elastic moduli of the unreinforced RAP layers of UR1, UR2, and UR3 were 22.5, 32.0, and 37.0 ksi, respectively. The in-situ elastic moduli of the reinforced RAP layers of RS1, RS2, and RS3 were 60.0, 78.0, and 80.0 ksi, respectively. The modular ratio for the unreinforced sections was assumed as 1, and the inclusion of geocells within RS1, RS2, and RS3 resulted in modular ratios of 3.5, 6.5, and 14.8, respectively, as shown in Table 21. An increase in the modular ratio indicates higher stiffness towards lateral directions. The three-dimensional confinement provided by the geocell acted as a horizontal barrier to restrict the lateral movement of the infill RAP material. The stiffness matrix for the geocell-reinforced cross-anisotropic material with a modular ratio of *n* is shown in Equation 55.

$$\begin{bmatrix}\sigma_{xx}\\ \sigma_{yy}\\ \sigma_{zz}\\ \sigma_{xy}\\ \sigma_{yz}\\ \sigma_{zx}\end{bmatrix}=\frac{E}{(1+\mu)(1-2\mu)}\begin{bmatrix}n(1-\mu) & n\mu & n\mu & 0 & 0 & 0\\ n\mu & n(1-\mu) & n\mu & 0 & 0 & 0\\ \mu & \mu & 1-\mu & 0 & 0 & 0\\ 0 & 0 & 0 & n(1-2\mu) & 0 & 0\\ 0 & 0 & 0 & 0 & n(1-2\mu) & 0\\ 0 & 0 & 0 & 0 & 0 & 1-2\mu\end{bmatrix}\begin{bmatrix}\varepsilon_{xx}\\ \varepsilon_{yy}\\ \varepsilon_{zz}\\ \varepsilon_{xy}\\ \varepsilon_{yz}\\ \varepsilon_{zx}\end{bmatrix} \quad (55)$$

### *6.3.3 Subgrade Soil*

A three-parameter resilient modulus model for the subgrade soil ($M_{r(subg)}$), was determined by analyzing the repeated load triaxial test results. The model attributes, $k_1$, $k_2$, and $k_3$ parameters were 429.3, -0.23, and 1.62, respectively. The location of the subgrade layer was 19 inches below the top asphalt concrete surface of the reinforced section. The vertical stress increase at the top of the subgrade layer under FWD loading varied between 4 and 5 psi. An average value of 4.5 psi was used to measure the stiffness of the subgrade based on the resilient modulus model. The resilient modulus under a particular state of stress can be considered as the elastic modulus for that specific condition (Gungor et al., 2017). The subgrade elastic modulus for the subgrade soil was determined from the resilient modulus model shown in Table 22.

**Table 22 Estimation of In-situ Modulus of Subgrade**

| Vertical stress | Average vertical stress at mid-depth of GRRB (psi) | Average horizontal stress (psi) | $\sigma_1$ (psi) | $\sigma_3$ (psi) | Bulk stress (psi) | Octahedral shear stress (psi) | Resilient modulus (psi) | Elastic modulus (psi) |
|---|---|---|---|---|---|---|---|---|
| | $\sigma_v = \gamma(h_m) + \Delta\sigma_v$ | $\sigma_h = k\sigma_v$ | $\sigma_1$ | $\sigma_3$ | $\theta$ | $\tau_{oct}$ | $M_{r(subg)}$ (psi) | $E_{subg}$ (psi) |
| 80 | 5.87 | 1.94 | 3.94 | 1.94 | 7.81 | 0.94 | 9000 | 9000 |

Notes:
$\sigma_1$ = major principal stress
$\sigma_3$ = minor principal stress

The in-situ elastic modulus of the subgrade estimated from the nondestructive test revealed that the actual modulus of the subgrade soil was quite high, as the field deflection recorded for the seventh deflection sensor (72 inches away from the loading center) showed very low deflections. The back-calculated in-situ elastic modulus of the subgrade soil was 16 ksi and was used in the modeling analysis. The subgrade layer was modeled as an elastic material.

### 6.4 Development of Pavement Simulation Models

The dimensions of the response model were selected to preclude minimum and boundary effects. The load-deflection curves obtained from the FWD test showed surface deflections 72 inches away from the loading location; the boundary of the model was set 110 inches away from the loading location to eliminate the effects of boundary conditions. The dimensions of the quarter-symmetric 3D model in the XY plane were110 inches × 110 inches; the depth of the model in the Z direction was 78 inches, which is six times greater than the diameter of the loading plate. The geocell pocket was modeled with an iso rectangular tropic shell element. The load was applied in a 12-inch diameter circular loading area. The geometry for the RS1 section is shown in Figure 65.

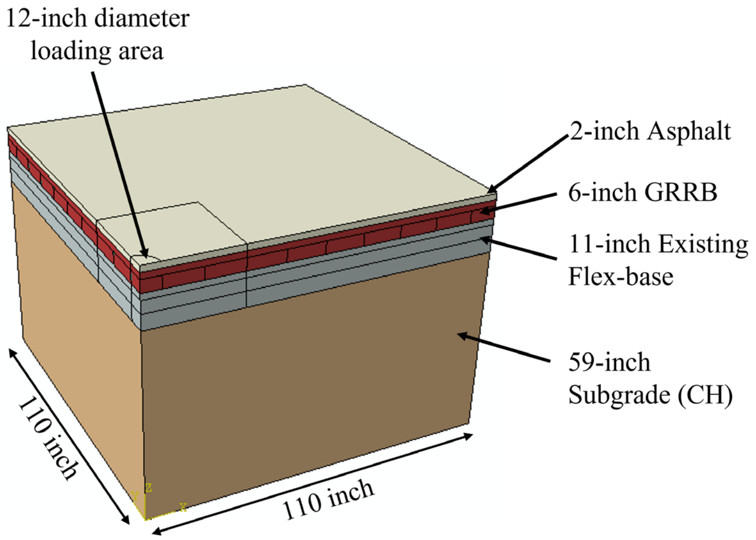

**Figure 65 Model geometry for reinforced section 1 (RS1)**

The material properties, along with the layer thickness used for the numerical modeling study, are listed in Table 23. The numerical model used for RS2 and RS3 are similar to that of RS1; however, the location and depth of the GRRB layers are different in each of the models.

**Table 23 Layer Properties Used for Response Models**

| | Layer | Thickness | Material Properties |
|---|---|---|---|
| RS1 | Asphalt concrete | 2 | $E_{asp}$ = 500 ksi; $\mu_{asp}$= 0.35 |
| | B1_RS1 | 6 | $E_{v(RAP)}$ = 22.5 ksi; $\mu_{RAP}$ = 0.30; $n$ = 3.5 |
| | B2 | 11 | $E_{fb}$ = 30 ksi; $\mu_{fb}$ = 0.30 |
| | Subgrade | 59 | $E_{subg}$ = 16.0 ksi |
| RS2 | Asphalt concrete | 2 | $E_{asp}$ = 500 ksi; $\mu_{asp}$= 0.35 |
| | B1_RS2 | 8 | $E_{v(RAP)}$ = 32 ksi; $\mu_{RAP}$ = 0.30; $n$ = 6.5 |
| | B2 | 9 | $E_{fb}$ = 30 ksi; $\mu_{fb}$ = 0.30 |
| | Subgrade | 59 | $E_{subg}$ = 16.0 ksi |
| RS3 | Asphalt concrete | 2 | $E_{asp}$ = 500 ksi; $\mu_{asp}$= 0.35 |
| | B1_RS3 | 12 | $E_{v(RAP)}$ = 37 ksi; $\mu_{RAP}$ = 0.30; $n$ = 5.0 |
| | B2 | 5 | $E_{fb}$ = 30 ksi; $\mu_{fb}$ = 0.30 |
| | Subgrade | 59 | $E_{subg}$ = 16.0 ksi |
| UR1 | Asphalt concrete | 2 | $E_{asp}$ = 500 ksi; $\mu_{asp}$= 0.35 |
| | B1_RAP | 6 | $E_{v(RAP)}$ = 22.5 ksi; $\mu_{RAP}$ = 0.30; $n$ = 1 |
| | B2 | 11 | $E_{fb}$ = 30 ksi; $\mu_{fb}$ = 0.30 |
| | Subgrade | 59 | $E_{subg}$ = 16.0 ksi |
| UR2 | Asphalt concrete | 2 | $E_{asp}$ = 500 ksi; $\mu_{asp}$= 0.35 |
| | B1_RAP | 8 | $E_{v(RAP)}$ = 32 ksi; $\mu_{RAP}$ = 0.30; $n$ = 1 |
| | B2 | 9 | $E_{fb}$ = 30 ksi; $\mu_{fb}$ = 0.30 |
| | Subgrade | 59 | $E_{subg}$ = 16.0 ksi |
| UR3 | Asphalt concrete | 2 | $E_{asp}$ = 500 ksi; $\mu_{asp}$= 0.35 |
| | B1_RAP | 12 | $E_{v(RAP)}$ = 37 ksi; $\mu_{RAP}$ = 0.30; $n$ = 1 |
| | B2 | 5 | $E_{fb}$ = 30 ksi; $\mu_{fb}$ = 0.30 |
| | Subgrade | 59 | $E_{subg}$ = 16.0 ksi |

The UR1, UR2, and UR3 sections were numerically modeled with similar boundary conditions but different sets of unreinforced material properties, as presented in Table 23. The base layer properties for the reinforced sections were determined from the nondestructive field testing, and the elastic modulus for the unreinforced RAP layer was estimated from the laboratory study.

### ABAQUS Input Parameters for Reinforced Section 1 (RS1)

The details of the various input parameters used for the FEM RS1 model are described below.

**Nodes and Elements:** The model geometry was defined rather than the nodes and elements, as they are generated automatically with the preprocessor with ABAQUS/CAE. A total of 18,291 nodes were created for the RS1, some of which were grouped together to assign the boundary conditions. The 6-noded continuum linear element (C3D6), including the asphalt concrete, base, and subgrade materials, was used for the soil elements with a full integration method. A total of 32,920 C3D6 elements were used for the RS1 model. The S4R, which is a 4-noded doubly curved shell with a reduced integration method, was used to define the HDPE geocells. A total of 200 S4R elements were used for the RS1 model.

**User Material:** A simplified UMAT was introduced to mitigate the anisotropic behavior of the reinforced base layer. The input parameters used for the UMAT were Poisson’s ratio ($d_{nu}$), modular ratio ($d_n$), and vertical elastic modulus of the unreinforced RAP layer (EMOD). The outline of the UMAT subroutine is shown below in Figure 66.

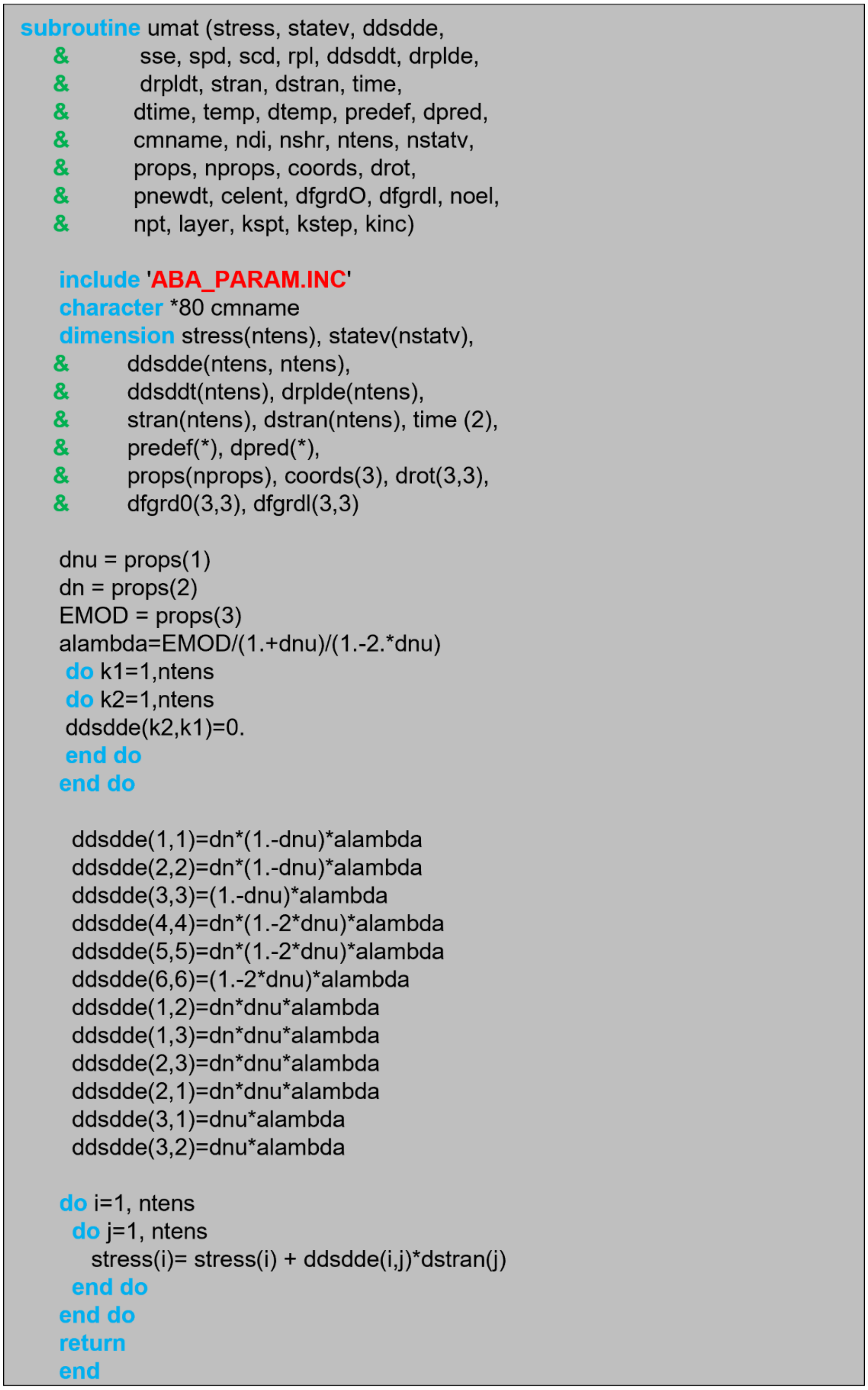

```
subroutine umat (stress, statev, ddsdde,
   &          sse, spd, scd, rpl, ddsddt, drplde,
   &          drpldt, stran, dstran, time,
   &         dtime, temp, dtemp, predef, dpred,
   &         cmname, ndi, nshr, ntens, nstatv,
   &         props, nprops, coords, drot,
   &         pnewdt, celent, dfgrdO, dfgrdl, noel,
   &         npt, layer, kspt, kstep, kinc)

    include 'ABA_PARAM.INC'
    character *80 cmname
    dimension stress(ntens), statev(nstatv),
   &        ddsdde(ntens, ntens),
   &        ddsddt(ntens), drplde(ntens),
   &        stran(ntens), dstran(ntens), time (2),
   &        predef(*), dpred(*),
   &        props(nprops), coords(3), drot(3,3),
   &        dfgrd0(3,3), dfgrdl(3,3)

    dnu = props(1)
    dn = props(2)
    EMOD = props(3)
    alambda=EMOD/(1.+dnu)/(1.-2.*dnu)
     do k1=1,ntens
     do k2=1,ntens
     ddsdde(k2,k1)=0.
     end do
    end do

      ddsdde(1,1)=dn*(1.-dnu)*alambda
      ddsdde(2,2)=dn*(1.-dnu)*alambda
      ddsdde(3,3)=(1.-dnu)*alambda
      ddsdde(4,4)=dn*(1.-2*dnu)*alambda
      ddsdde(5,5)=dn*(1.-2*dnu)*alambda
      ddsdde(6,6)=(1.-2*dnu)*alambda
      ddsdde(1,2)=dn*dnu*alambda
      ddsdde(1,3)=dn*dnu*alambda
      ddsdde(2,3)=dn*dnu*alambda
      ddsdde(2,1)=dn*dnu*alambda
      ddsdde(3,1)=dnu*alambda
      ddsdde(3,2)=dnu*alambda

    do i=1, ntens
      do j=1, ntens
        stress(i)= stress(i) + ddsdde(i,j)*dstran(j)
      end do
    end do
    return
    end
```

Figure 66 ABAQUS UMAT input subroutine

**Boundary Conditions:** A displacement/rotation type boundary condition was used for the outside boundary, and a symmetry/antisymmetry/encastre condition was used for the inside boundary, as shown in Figure 67. The boundary condition was designed so that the section acted as a quarter symmetric model. A vertical load of 84 psi (580 kPa or 0.58 MPa) was applied to one-fourth of the area of a six-inch radius circle.

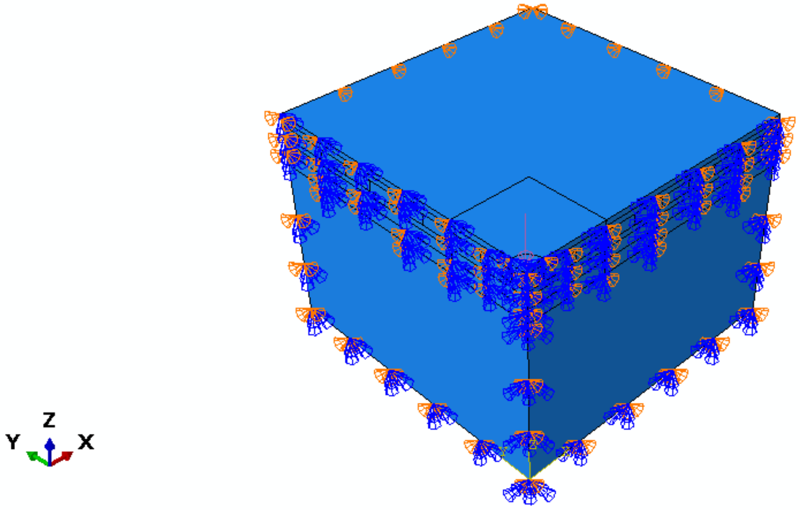

**Figure 67 Boundary conditions for reinforced section 1 (RS1)**

## 6.5 Static Load Testing

The purpose of static load testing was to understand how the GRRB layers enhance the performance of the pavement sections by decreasing the resilient deformations. Three reinforced sections (RS1, RS2, and RS3) and three unreinforced sections (UR1, UR2, and UR3) were modeled to study the effect of geocell-induced anisotropy. The estimated modulus for the unreinforced section was calculated with modular ratio, *n* =1; the modular ratio for the geocell reinforced layer varied from 3.5 to 6.5. The vertical deformation plots for the test sections are presented in Figure 68-73.

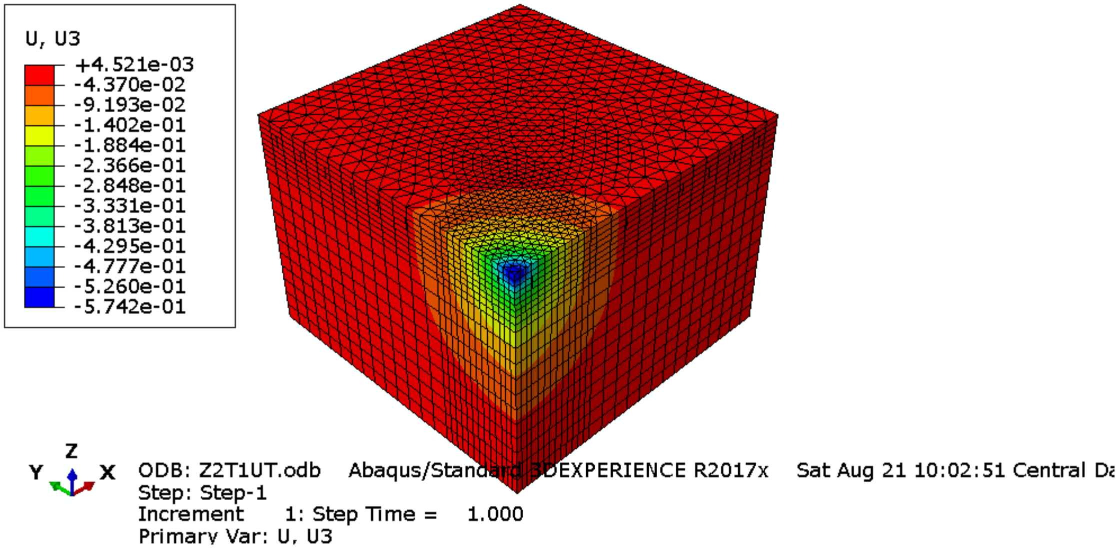

**Figure 68 Vertical deformation of unreinforced section 1 (UR1)**

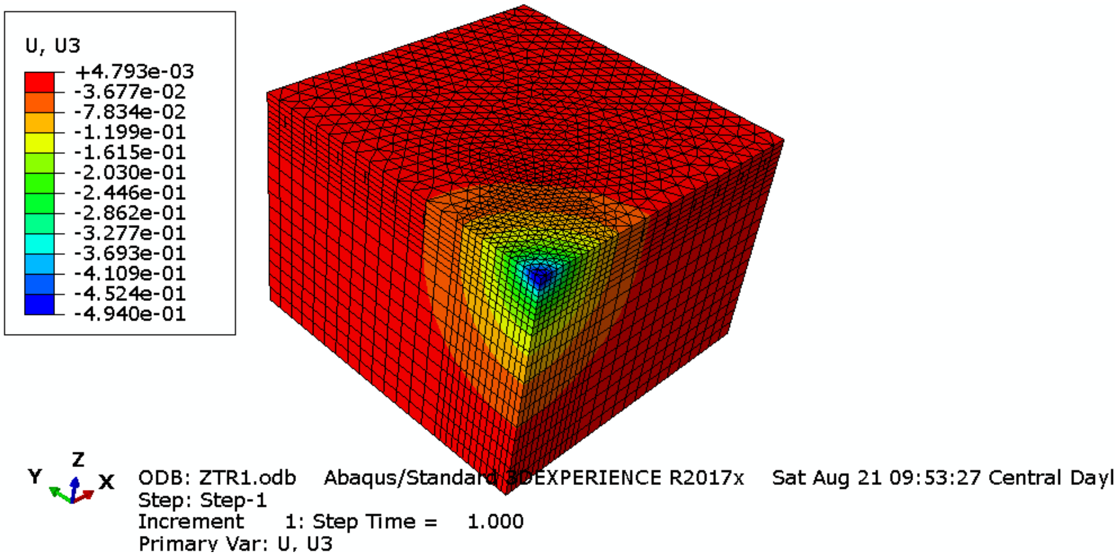

**Figure 69 Vertical deformation of reinforced section 1 (RS1) with 4-inch geocell**

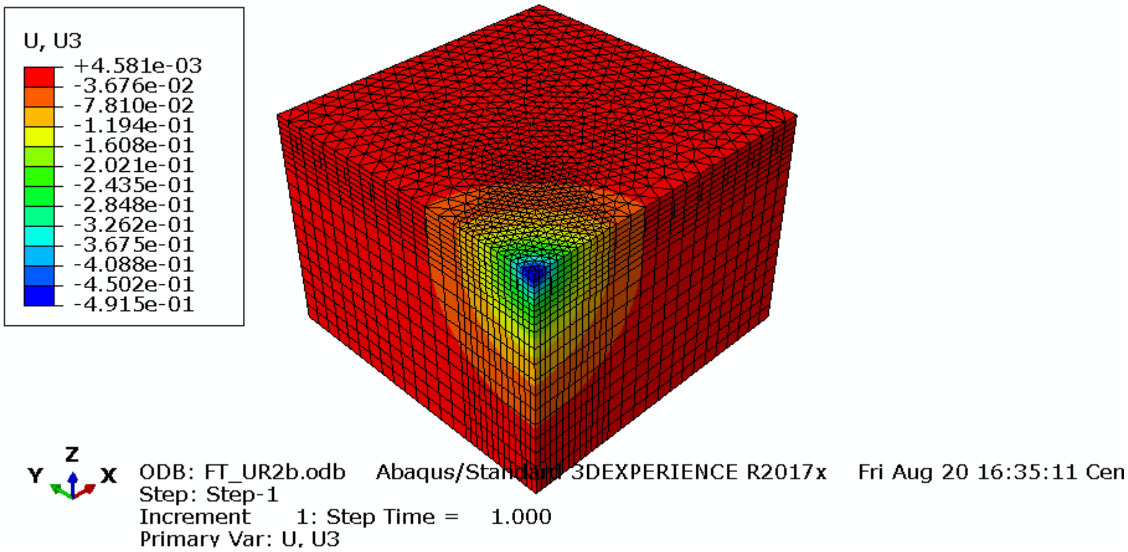

Figure 70 Vertical deformation of unreinforced section 2 (UR2)

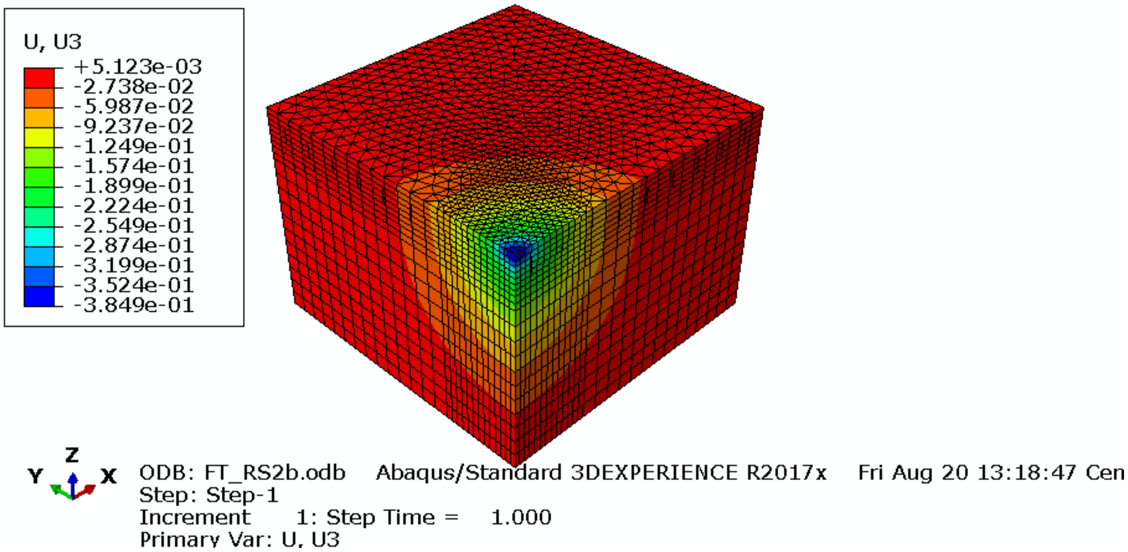

Figure 71 Vertical deformation of reinforced section 2 (RS2) with 6-inch geocell

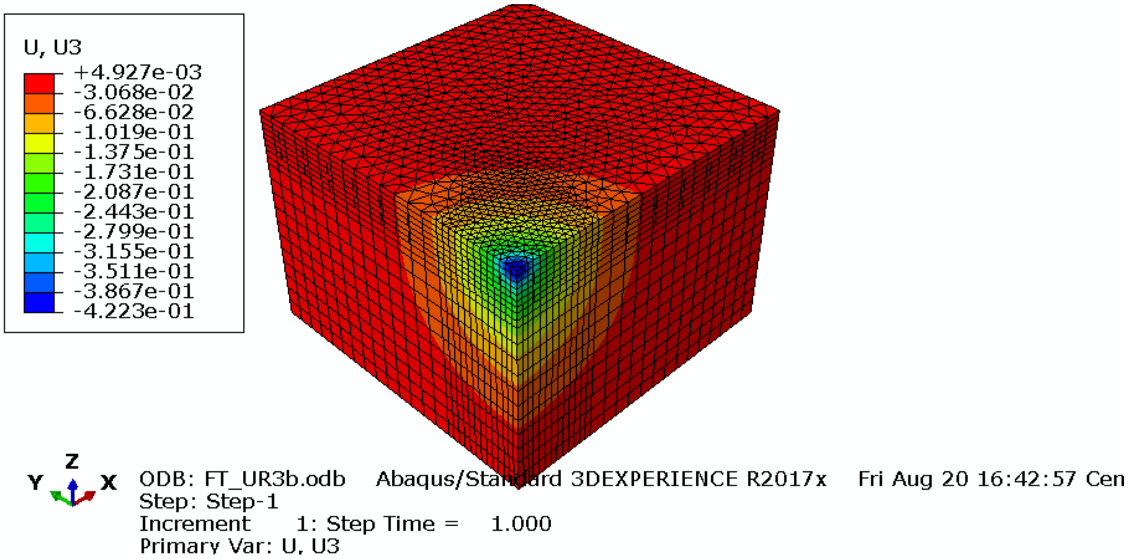

Figure 72 Vertical deformation of unreinforced section 3 (UR3)

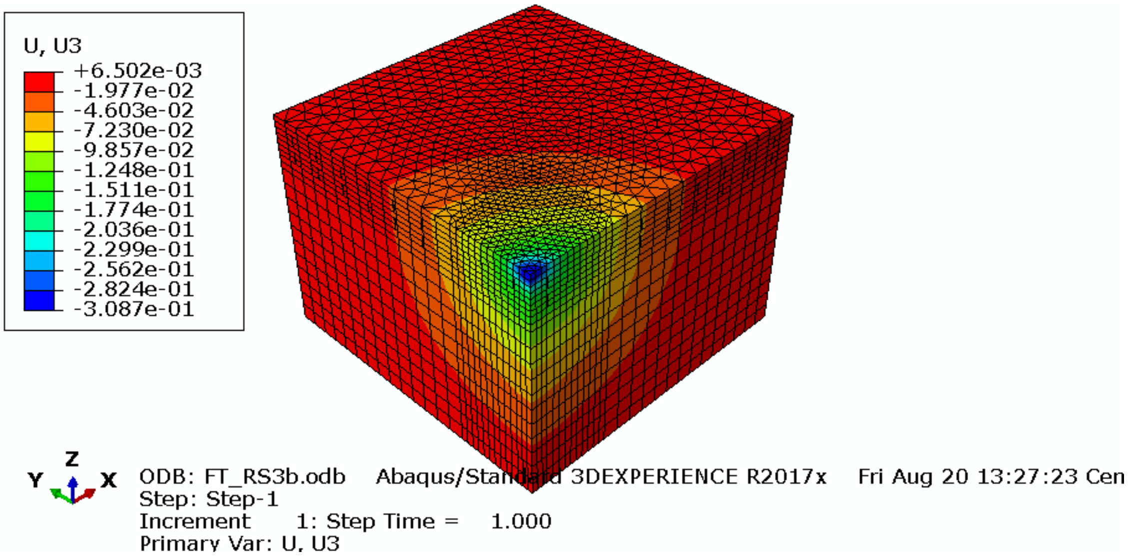

Figure 73 Vertical deformation of reinforced section 3 (RS3) with 2 layers of 4-inch geocells

### *6.5.1 Vertical Deformations*

The FWD tests were conducted at 20 different locations: 6 in RS1, 7 in RS2, and 7 in RS3. The vertical deflections were collected for seven locations at distances of 0, 12, 24, 36, 48, 60, and 72 inches from the center of the loading area. The vertical deformations collected from the response models were compared with the field deformation responses; the field and numerical data comparisons are discussed in the following sections. FWD tests conducted during 2020 were used for comparison purposes.

#### **6.5.1.1 Response from Reinforced Section 1 (RS1) with 4-inch Geocell**

The GRRB layer in this section was 6 inches thick, containing a 4-inch geocell layer with a 2-inch RAP cover. Figure 74 presents the pavement responses collected from the field and estimated from the numerical model. It was observed that the maximum deflection in the field under the loading plate varied from 0.016 to 0.019 inches. The variation in deflection decreased with the distance from the loading axis. The estimated maximum deflection from the response model was 0.018 inches, and the minimum deflection, recorded 72 inches from the load center, was less than 0.001 inches. The magnitude of the deflections estimated from the response model was lower than the observed value from the field; however, the nature of the deflection bowls was almost identical. The ratio of the estimated deflections and average field deflection for this section was 0.96; the *AREA* ratio was 0.74. The base layer indexes (*BLI*) estimated from the numerical and field studies were 267 and 172, respectively, indicating that a sound base layer was provided with a 4-inch geocell layer. It should be noted that the *BLI* needs to be less than 300 to meet the criteria for an acceptable base layer.

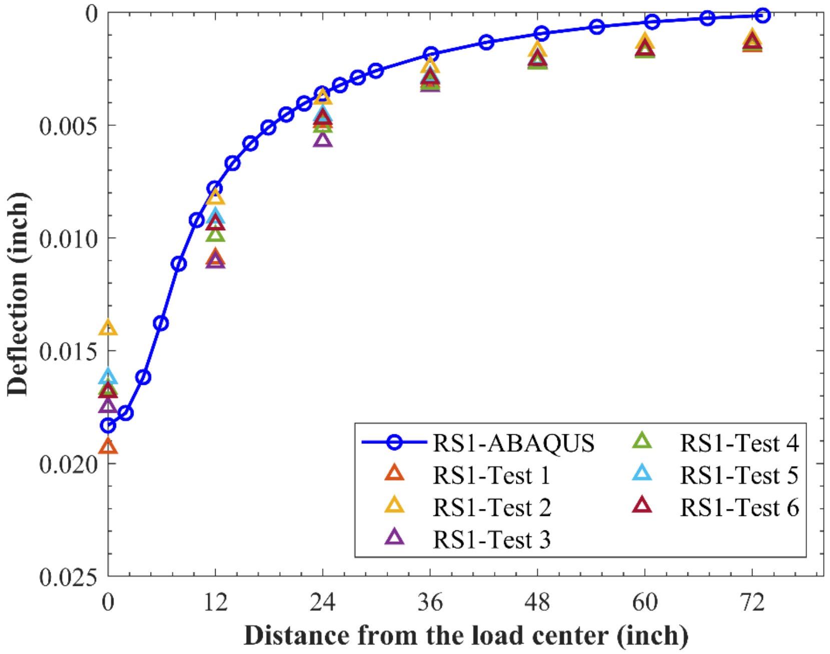

**Figure 74 Comparison of field and numerical model responses for reinforced section 1 with 4-inch geocell**

### 6.5.1.2 Response from Reinforced Section 2 (RS2) with 6-inch Geocell

The GRRB layer in this section was 8 inches thick with a 6-inch thick geocell layer and a 2-inch-thick RAP cover. Figure 75 presents the pavement responses collected from the field and estimated from the numerical model. The maximum deflection in the field under the loading plate varied from 0.017 to 0.018 inches, and the maximum deflection under the RS2 sections was lower than the RS1 due to the increase in thickness of the GRRB layer. The estimated maximum deflection from the response model was 0.015 inches, and the minimum deflection was less than 0.001 inches, recorded 72 inches from the loading axis. The magnitude of the deflections estimated from the response model was similar to the average values obtained from the field. The ratio of the estimated deflections and average field deflection for this section was 0.87; the *AREA* ratio was 0.91. The *BLI* indices estimated from the numerical and field studies were 185 and 175, respectively. The less-than-300 *BLI* values indicate that a sound base layer condition was provided by the 6-inch geocell layer.

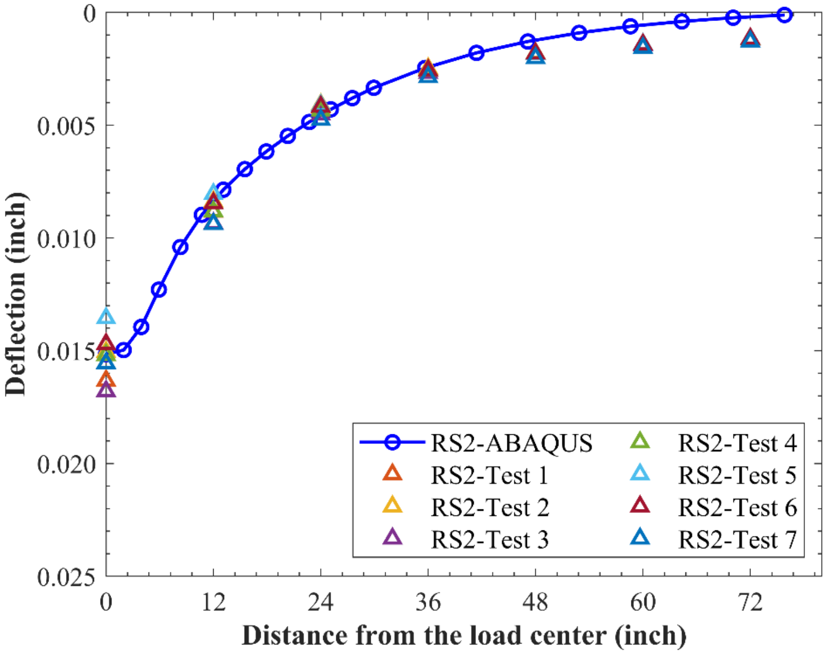

**Figure 75 Comparison of field and numerical model responses for reinforced section 2 (RS2) with 6-inch geocell**

### 6.5.1.3 Response from Reinforced Section 3 (RS3) with Two Layers of 4-inch Geocells

The GRRB layer in this section was 12 inches thick. Two layers of the 4-inch thick geocell layer were used, with a 2-inch-thick RAP cover at the top and a 2-inch intermediate cover between the geocell layers. Figure 76 presents the pavement responses collected from the field and estimated by the numerical model. The maximum deflection in the field under the loading plate varied from 0.016 to 0.018 inches. The average value of the deflections under the load center for the RS3 section was lower than that of RS2 due to the increase in GRRB layer thickness. The estimated maximum deflection from the response model was 0.012 inches, and the minimum deflection was less than 0.001 inches, recorded 72 inches from the center of loading. The magnitudes of the deflections estimated from the response model were slightly lower than the average values obtained from the field. The ratio of the estimated deflections and average field deflection for this section was 0.70; the *AREA* ratio was 0.93. The *BLI* index estimated from the numerical and field studies was 150 and 170, respectively. The *BLI* values less than 300 indicated that a sound base layer condition was provided with two 4-inch geocell layers.

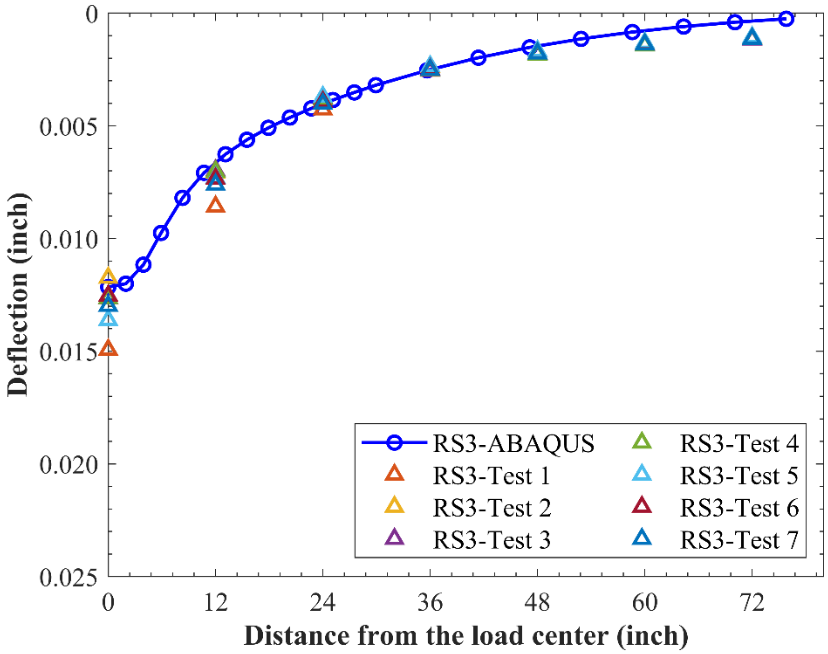

**Figure 76 Comparison of field and numerical model responses for reinforced section 3 with layers of 4-inch geocell**

### *6.5.2 Verification Studies*

To verify the geocell-reinforced RAP behavior, a large-scale static load test conducted by Pokharel (2009) was modeled with ABAQUS. Plate load tests were conducted for both unreinforced and geocell-reinforced (GR) RAP sections. For the GR section, a geocell with dimensions of 7.87 inches × 8.8 inches and 4-inch height was embedded in a 31.5-inch × 31.5-inch × 4.7-inch large-scale soil box specimen that was enclosed by a rigid container (Figure 77). Stress from 0 to 86 psi was applied gradually, using a 6-inch diameter rigid circular plate. The material properties used for the analyses are listed in Table 24**.**

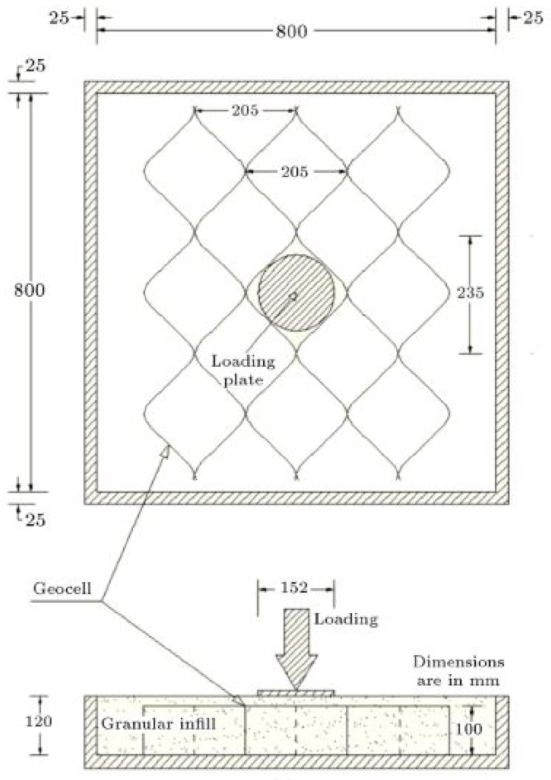

**Figure 77 Large-scale laboratory test on geocell-reinforced RAP material by Thakur (2010)**

**Table 24 Properties of RAP and Geocell Used by Thakur (2009)**

| Material | Cohesion (psi) | Friction angle ($^{O}$) | Modulus of elasticity (psi) | Poisson's Ratio |
|---|---|---|---|---|
| RAP | 4.4 | 12.9 | 28,400 | 0.35 |
| Geocell | - | - | 50,700 | 0.35 |

The geometry, materials, and boundary conditions of the static load test were simulated in ABAQUS. The model geometry for the unreinforced and reinforced sections are shown in Figure 78a and 78b, respectively.

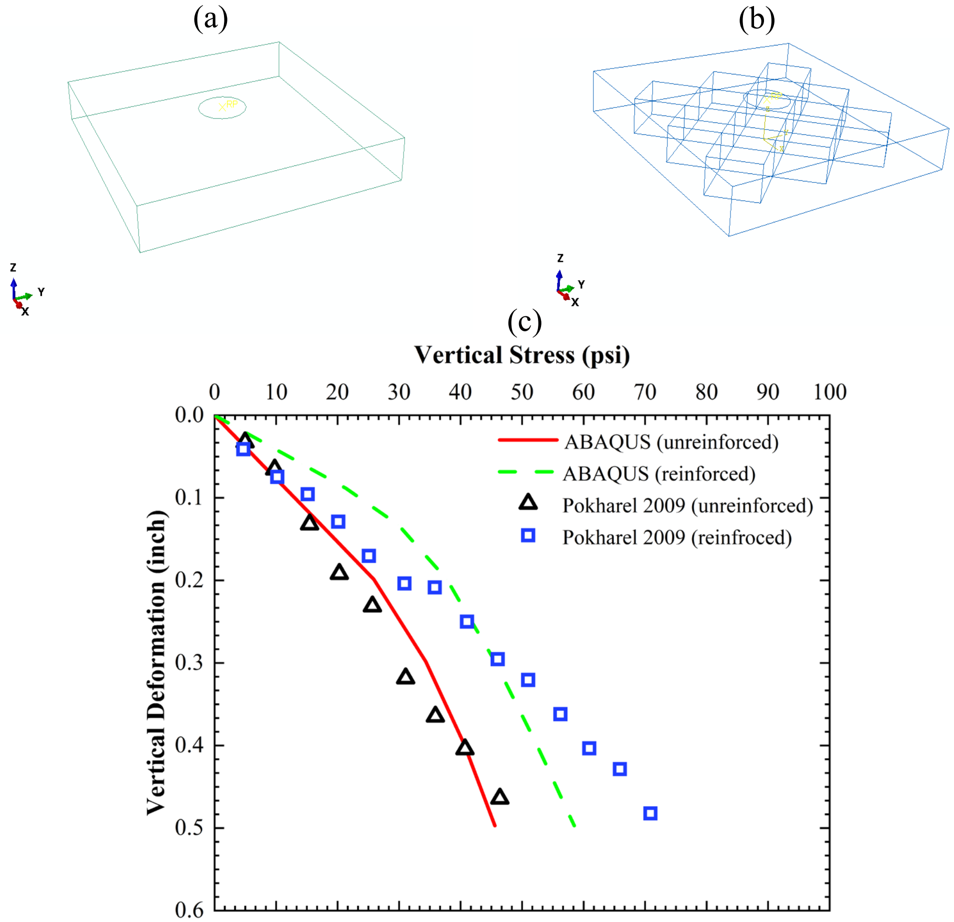

**Figure 78 Verification study models: (a) unreinforced section, (b) reinforced sections; (c) comparison of stress-displacement curves obtained from laboratory tests conducted by Thakur (2009) and current numerical models**

The vertical stress vs. deformation plot obtained from the laboratory tests, along with the predicted data from the ABAQUS model, are shown in Figure 78c. The laboratory tests and the computer numerical modeling for both the reinforced and unreinforced test sections were in relatively good agreement.

### *6.5.3 Stresses and Strains Acting on Geocell Wall*

When a thin asphalt concrete layer is applied to the surface of the pavement, the underlying base material may be subjected to tension under vehicular loading. This material is generally designed for carrying compressive loads; however, the lateral movement of the base material that is due to tensile stress can be restricted by adding lateral support. The application of geocells within the base layer helps control the lateral movement of the base material and enhance the overall bearing capacity of the pavement system. The geocells used for the RS1 and RS2 sections were 4 inches and 6 inches high and had similarly sized openings. Rather than one 8-inch geocell, two layers of 4-inch geocells were used for the third reinforced section.

As the geocells were modeled as shell elements, they were able to resist tension/compression within the plane of the shale (11 and 22 direction). The vertical stress-induced compressions acted in parallel to the direction of the applied load, whereas the horizontal stress-induced tension acted perpendicular to the direction of load, creating tension within the shale structure. Positive values of stresses indicate tension, and negative values indicate compression in ABAQUS. The following section discusses the stress-strain conditions in geocells of various reinforced sections.

#### 6.5.3.1 Stress and Strain Acting on Single-layer 4-inch Geocell Located in Reinforced Section 1 (RS1)

The stresses acting on the 4-inch geocell located in the RS1 section are shown in Figure 79**.** The maximum horizontal stress acting within the geocell under the load center was around 7.0 psi (0.048 MPa), whereas the maximum vertical compressive stress was around 73 psi (0.501 MPa). The horizontal tensile stress acting in the geocell developed hoop stress, which generated additional confinement for the base material that resulted in an increase in the load-bearing capacity of the base layer.

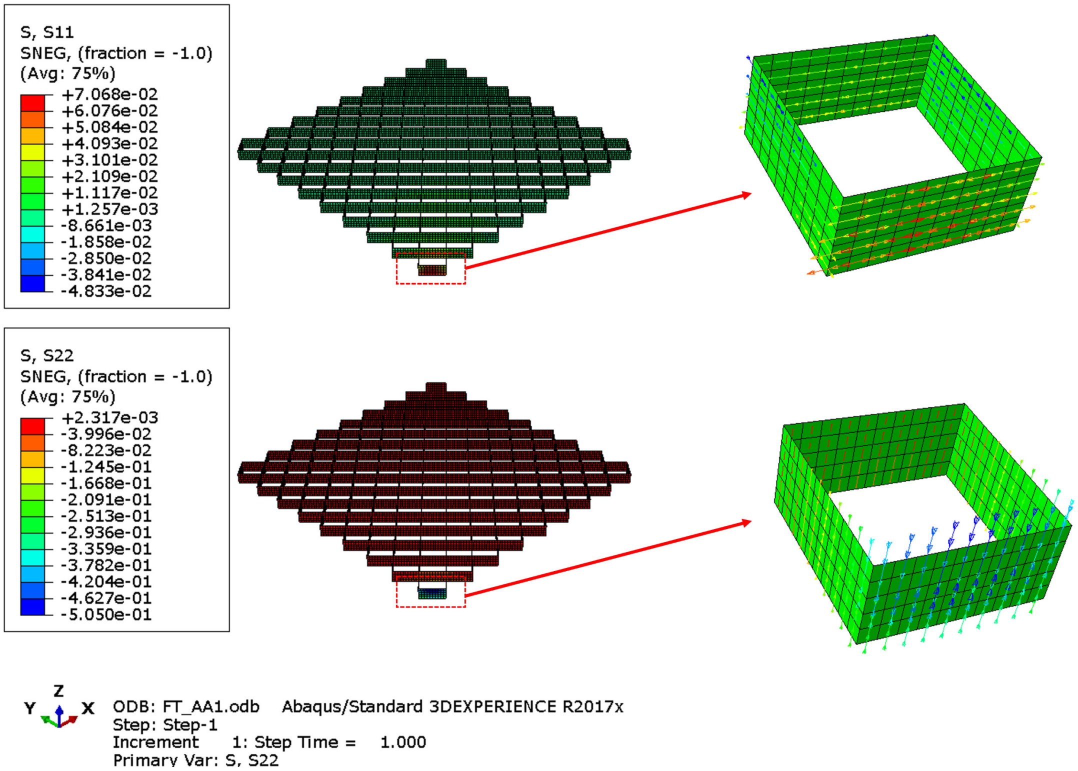

**Figure 79 Stress acting on geocell located in reinforced section 1 (RS1)**

#### 6.5.3.2 Stress and Strain Acting on Single-layer 6-inch Geocell Located in Reinforced Section 2 (RS2)

The stresses acting on the 6-inch geocell located in the RS2 section are shown in Figure 80**.** The maximum horizontal stress acting in the geocell under the load center was around 4.6 psi (0.032 MPa); the maximum vertical compressive stress was around 52 psi (0.355 MPa). The maximum horizontal tensile stress acting in a 6-inch geocell was 34% less than the stress acting on a 4-inch geocell. The increase in the height of the geocell helped distribute the load over a wider area, resulting in a reduction of stresses.

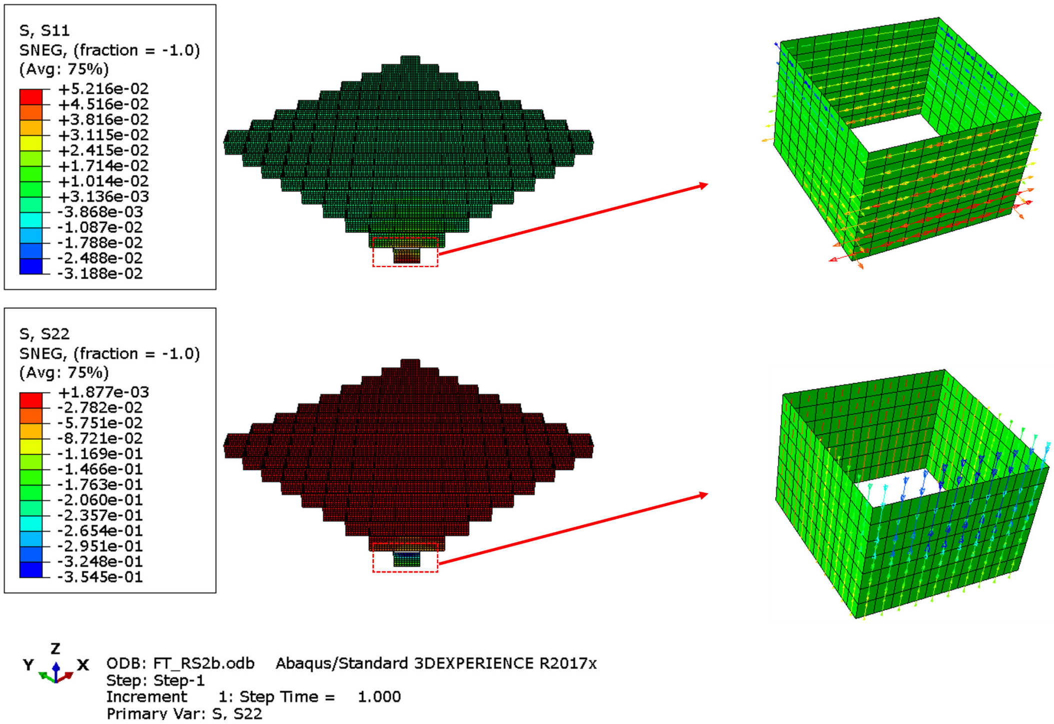

**Figure 80 Stress acting on geocell located in reinforced section 2 (RS2)**

### 6.5.3.3 Stress and Strain Acting on the Top and Bottom Layers of 4-inch Geocell Located in the Reinforced Section 3 (RS3)

The stresses acting on the 12-inch GRRB in the RS3 section are shown in Figure 81**.** The maximum horizontal stress acting within the geocell under the load center was around 4.6 psi (0.032 MPa), whereas the maximum vertical compressive stress was around 48 psi (0.329 MPa). The maximum horizontal tensile stress acting within the top geocell layer of RS3 was almost identical to that of the 6-inch geocell located in RS2; however, the vertical compressive stress within the double layer section was 50% less than that of the single-layer section.

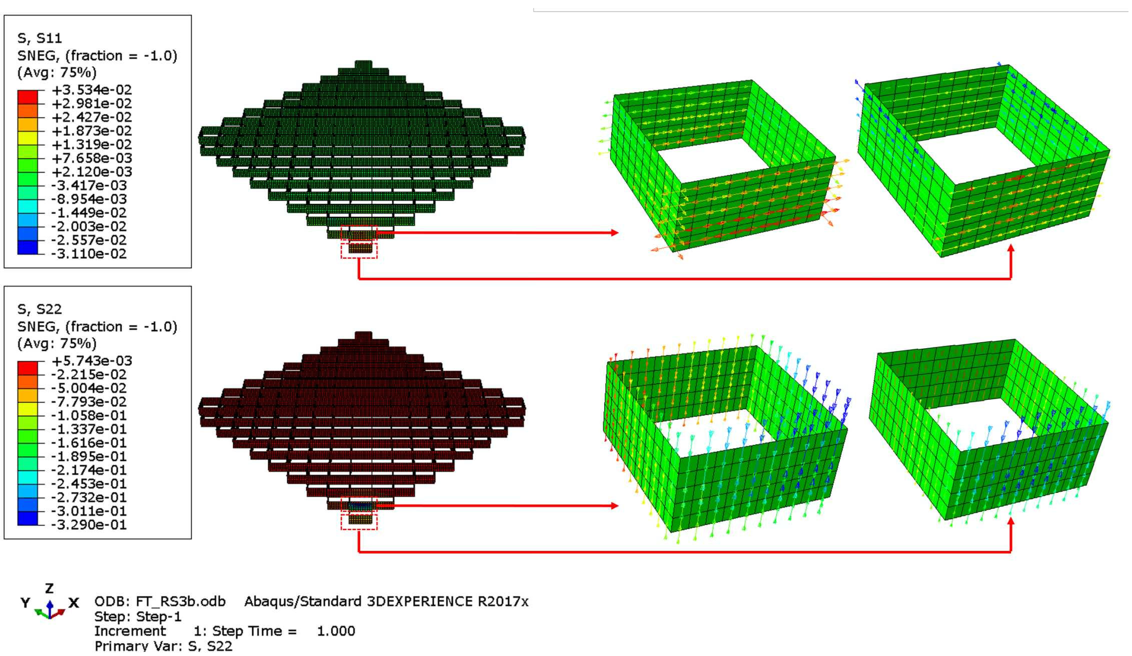

**Figure 81 Stress acting on geocell located in reinforced section 3 (RS3)**

### 6.5.3.4 Comparisons of Horizontal Stresses and Strains on Geocell Wall

The horizontal stress acting on the walls of geocells varied with the height of the reinforced layer, as shown in Figure 82. The horizontal stress was not constant throughout the wall, as it increased up to a certain depth in both the 4-inch and 6-inch geocell sections. The maximum tensile stress of 10.0 psi was observed at a depth of $0.75h_{gc}$ ($h_{gc}$ = height of geocell) in RS1; the maximum tensile stress of 7.6 psi was observed at the bottom of the geocell in RS2. The average tensile stress acting on the first and second layers of geocells was approximately 4.0 psi. The horizontal tensile strain varied with depth for all the sections, and the maximum strain was observed within the RS1 layer. The average horizontal strains acting within RS1, RS2, and the first layer of RS3 were 0.00025, 0.00016, and 0.00013, respectively. The distribution of horizontal strains in the different sections is shown in Figure 83. The horizontal strain acting on the second layer of the RS3 was almost negligible and varied little throughout the depth of geocell.

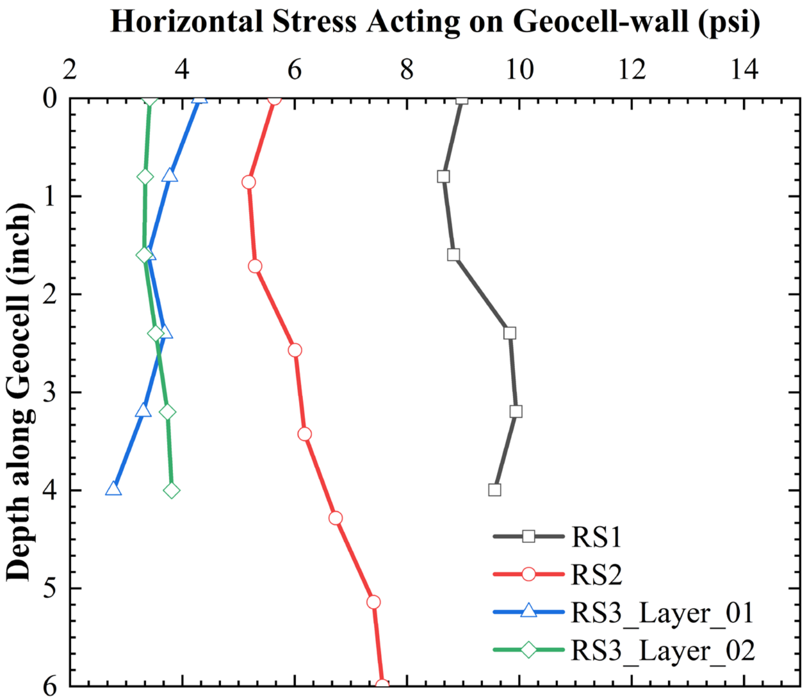

**Figure 82 Comparison of horizontal stresses on geocell-walls**

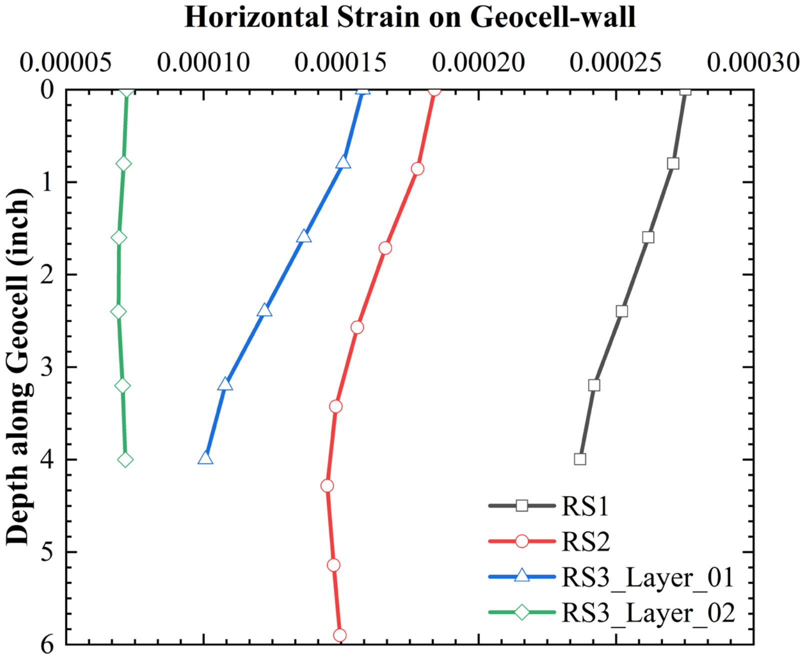

**Figure 83 Comparison of horizontal strains acting on geocell walls**

### *6.5.4 Percentage Reductions in Vertical Stresses (PRS)*

The vertical stresses and strains acting on top of the subgrade level are important parameters for the design of flexible pavement sections. The rutting life of the flexible pavement is estimated based on the vertical compressive strains acting on top of the subgrade level. The following sections discuss the effects of the GRRB layer on the percentage reductions in vertical stresses (*PRS*) for different test sections.

#### 6.5.4.1 Reduction of Vertical Stresses in Reinforced Section 1 (RS1)

The vertical stresses, acting on the subgrade layer for the unreinforced (UR1) and reinforced (RS1) sections, are shown in Figure 84. The maximum vertical stress acting on the subgrade soil was reduced by 20.2% due to the 6-inch GRRB layer. The reduction in vertical stress also indicates a wider distribution of stresses, which is due to the mattress effect of the geocell. The reduction in vertical stress also helped reduce the vertical compressive strain, as it decreased from 369×10$^{-6}$ to 297×10$^{-6}$. According to the Asphalt Concrete Institute method, a 19.5% decrease in the vertical compressive strain can increase the rutting life of the pavement by 2.6 times. The overall increase in the design life of the flexible pavement also indicates a lower maintenance cost per year.

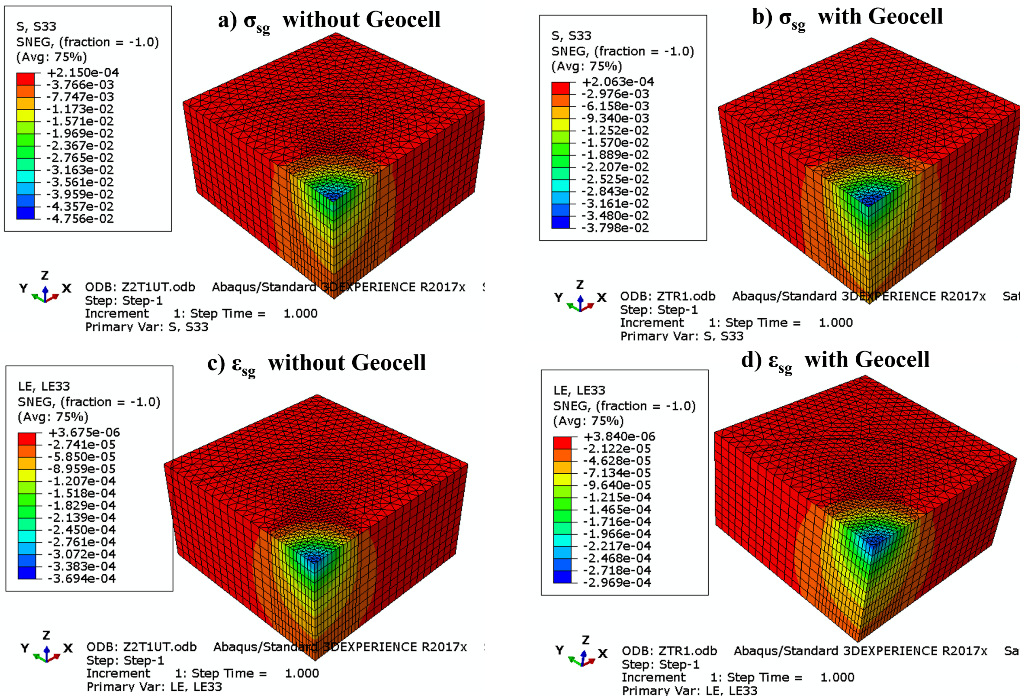

**Figure 84 Vertical stresses and strains on subgrade of RS1: a) vertical stress without geocell; b) vertical stress with geocell; c) vertical compressive strain without geocell; d) vertical compressive strain with geocell**

### 6.5.4.2 Reduction of Vertical Stresses in Reinforced Section 2 (RS2)

The vertical stresses acting on the subgrade layer of the unreinforced (UR2) and reinforced sections (RS2) are shown in Figure 85. The maximum vertical stress acting on the subgrade soil was reduced by 29.0% due to the 8-inch GRRB layer with a 6-inch thick geocell. The reduction in vertical stress was larger in RS2 than in RS1 due to the greater thickness of the reinforced layer. The reduction in vertical stress also helped reduce the vertical compressive strain, as it decreased from $350\times10^{-6}$ to $240\times10^{-6}$. A 29.0% decrease in the vertical compressive strain can increase the rutting life of the pavement by 5.4 times.

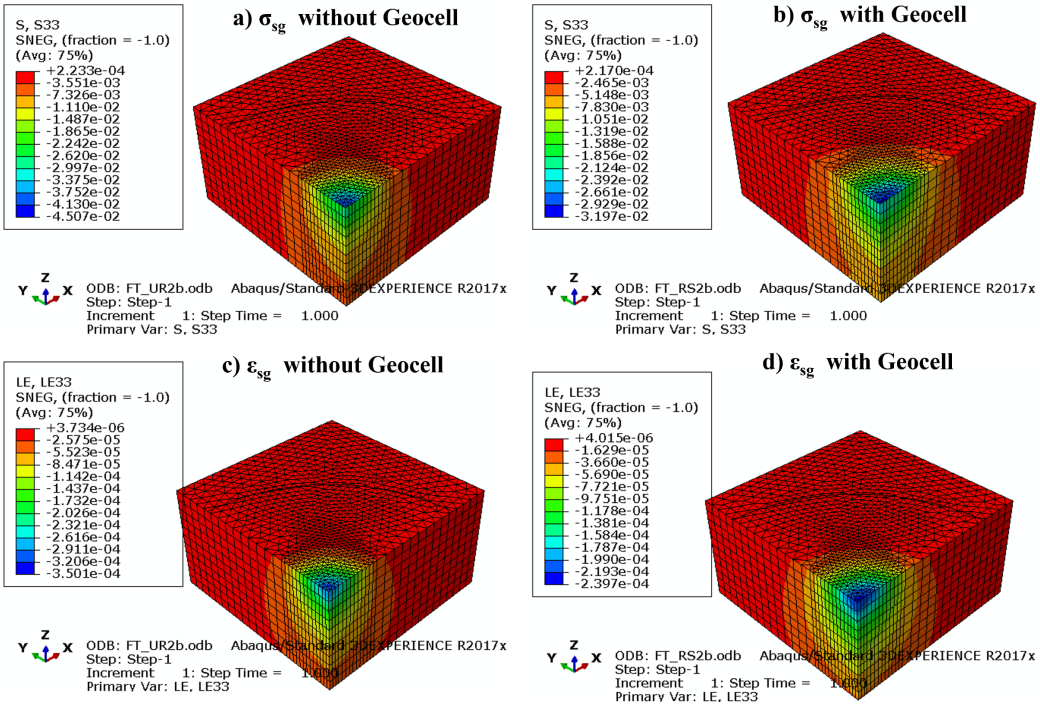

**Figure 85 Vertical stresses and strains on subgrade for RS2: a) vertical stress without geocell; b) vertical stress with geocell; c) vertical compressive strain without geocell; d) vertical compressive strain with geocell**

### 6.5.4.3 Reduction of Vertical Stresses in Reinforced Section 3 (RS3)

The vertical stresses acting on the subgrade layer of the unreinforced (UR3) and reinforced sections (RS3) are shown in Figure 86. The maximum vertical stress acting on the subgrade soil for the unreinforced section in RS3 was 15.0% lower than that of RS2. The reduction in vertical stress indicates that the increase in the GRRB layer thickness enhanced the load-carrying capacity. The application of a 12-inch GRRB layer also helped reduce the vertical compressive stress by 43.0%, which is significantly higher than that of the RS1 and RS2 sections. The reduction in vertical stress also helped to reduce the vertical compressive strain, as it decreased from 320×10$^{-6}$ to 159×10$^{-6}$. A 43.0% decrease in the vertical compressive strain can increase the rutting life of the pavement by 22.9 times.

a) $\sigma_{sg}$ without Geocell

b) $\sigma_{sg}$ with Geocell

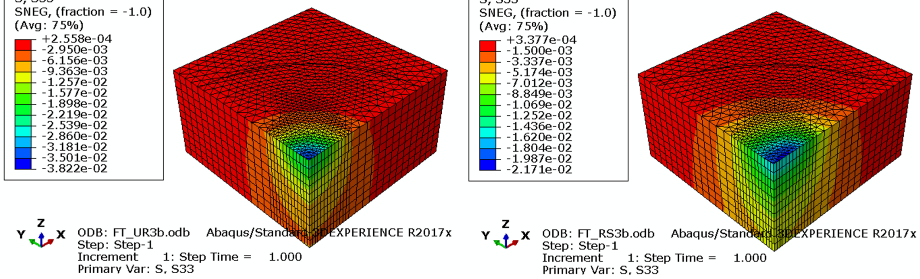

c) $\varepsilon_{sg}$ without Geocell

d) $\varepsilon_{sg}$ with Geocell

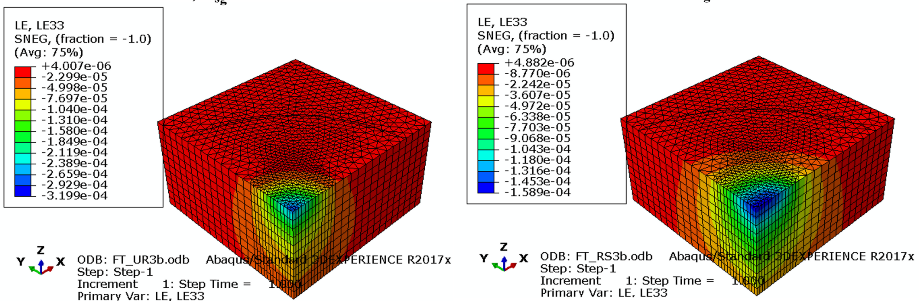

**Figure 86 Vertical stresses and strains on subgrade of RS3: a) vertical stress without geocell; b) vertical stress with geocell; c) vertical compressive strain without geocell; d) vertical compressive strain with geocell**

Overall, the increase in the thickness of the GRRB layer helped in decreasing the vertical compressive stresses, as the mattress effect offered by the geocell helped distribute the vertical load over a wider area. The reduction of vertical stress also enhanced the design life of the flexible pavement by decreasing the vertical subgrade strain. According to the Asphalt Institute (AI) method, the traffic benefit ratio (*TBR*) can be estimated with respect to the percentage reduction in vertical strain (*PRST*). The percentage reduction of stress (*PRS*) increases with an increase of the *PRST*.

The performance of the reinforced test sections in terms of PRS and PRST were determined and are presented in Table 25.

**Table 25 Performance of Test Sections Based on Reduction of Vertical Stress and Strain on Subgrade**

| **Section** | ***PRS*** **(%)** | ***PRST*** **(%)** | ***TBR*** **= $(1 - \text{PRST})^{-4.477}$** |
|---|---|---|---|
| RS1 | 20.2 | 19.5 | 2.6 |
| RS2 | 29.0 | 31.4 | 5.4 |
| RS3 | 43.0 | 50.3 | 22.9 |

Note: PRS: percentage reduction in vertical stress on top of the subgrade
PRST: percentage reduction in vertical strain on top of the subgrade
TBR: Traffic benefit ratio (estimated based on the rutting life determined from AI method)

It was observed that the *TBR* value significantly increases with an increase in the thickness of the geocell base layer, but further investigation is required to explore the benefits of using geocells under different geometries of pavement and subgrade conditions. The following section discusses the effects of asphalt concrete layer thickness and elastic modulus of the subgrade layer on flexible pavement sections, based on comprehensive parametric studies conducted for this study.

### 6.6 Parametric Studies

The primary purpose of the parametric studies was to understand how the thickness of the asphalt concrete layer and modulus of the subgrade affect the performance of 6-inch, 8-inch, and 12-inch GRRB layers. The thickness of the asphalt concrete layer varied from 2 to 6 inches, and the subgrade modulus varied from 5 to 20 ksi. The percentage reduction in vertical stress (*PRS*) and traffic benefit ratio (*TBR*) estimated for the 2-inch, 4-inch, and 6-inch asphalt concrete layers are presented in Table 26, Table 27**,** and Table 28, respectively. These tables summarize the vertical compressive stresses and strains for both unreinforced and reinforced test sections. The difference in the vertical stresses in the reinforced and unreinforced sections was used to determine the *PRS*. The vertical strain acting on top of the subgrade of the unreinforced and reinforced sections was used to determine the *TBR*. It was observed that the *PRS* values depend on the thickness of the base layer as well as the thickness of the asphalt concrete layer modulus.

## Table 26 Parametric Study Results for 2-inch Asphalt Concrete Layer

| SL.N. | $t_{asp}$ (inch) | $t_{GRRB}$ (inch) | $E_{subg}$ (ksi) | Vertical Stress (psi) | | Vertical Strain ($10^{-6}$) | | $N_{d(u)}$ ($10^6$) | $N_{d(R)}$ ($10^6$) | *PRS* (%) | *TBR* |
|---|---|---|---|---|---|---|---|---|---|---|---|
| | | | | UR | RS | UR | RS | | | | |
| 1 | 2 | 6 | 5 | 11.7 | 9.4 | 2317 | 1258 | 0.001 | 0.015 | 19.8 | 15.4 |
| 2 | 2 | 6 | 10 | 15.5 | 11.0 | 1556 | 1076 | 0.005 | 0.0265 | 29.0 | 5.2 |
| 3 | 2 | 6 | 15 | 17.9 | 13.7 | 1190 | 865 | 0.017 | 0.0701 | 23.4 | 4.2 |
| 4 | 2 | 6 | 20 | 19.5 | 14.6 | 971 | 733 | 0.042 | 0.148 | 25.2 | 3.5 |
| 5 | 2 | 8 | 5 | 7.3 | 3.7 | 1498 | 678 | 0.001 | 0.210 | 49.0 | 34.8 |
| 6 | 2 | 8 | 10 | 10.2 | 5.4 | 1050 | 514 | 0.029 | 0.725 | 47.3 | 24.5 |
| 7 | 2 | 8 | 15 | 12.0 | 6.6 | 824 | 427 | 0.088 | 1.661 | 44.6 | 19.0 |
| 8 | 2 | 8 | 20 | 13.3 | 7.8 | 685 | 388 | 0.201 | 2.552 | 41.3 | 12.7 |
| 9 | 2 | 12 | 5 | 5.9 | 2.0 | 817 | 384 | 0.091 | 2.670 | 65.9 | 29.4 |
| 10 | 2 | 12 | 10 | 7.1 | 3.0 | 586 | 291 | 0.403 | 9.252 | 57.1 | 23.0 |
| 11 | 2 | 12 | 15 | 7.8 | 3.7 | 467 | 242 | 1.113 | 21.121 | 51.9 | 19.0 |
| 12 | 2 | 12 | 20 | 7.3 | 4.2 | 392 | 211 | 2.438 | 39.101 | 42.6 | 16.0 |

Note: SL.N. = serial number; $t_{asp}$ = asphalt layer thickness; $t_{GRRB}$ = GRRB layer thickness; $E_{subg}$ = subgrade elastic modulus; UR = unreinforced section; RS = reinforced section; $N_{d(u)}$ = Number of allowable repetitions for unreinforced flexible pavement; $N_{d(R)}$ = Number of allowable repetitions for geocell-reinforced flexible pavement; *PRS* = Percentage reduction in vertical stress; *TBR* = Traffic benefit ratio ($TBR = \frac{N_{d(u)}}{N_{d(R)}}$)

**Table 27 Parametric Study Results for 4-inch Asphalt Concrete Layer**

| SL.N. | $t_{asp}$ (inch) | $t_{GRRB}$ (inch) | $E_{subg}$ (ksi) | Vertical Stress (psi) | | Vertical Strain ($10^{-6}$) | | $N_{d(u)}$ ($10^6$) | $N_{d(R)}$ ($10^6$) | *PRS* (%) | *TBR* |
|---|---|---|---|---|---|---|---|---|---|---|---|
| | | | | **UR** | **RS** | **UR** | **RS** | | | | |
| 1 | 4 | 6 | 5 | 6.8 | 4.9 | 1367 | 947 | 0.009 | 0.047 | 27.7 | 5.2 |
| 2 | 4 | 6 | 10 | 9.2 | 7.1 | 938 | 695 | 0.049 | 0.188 | 23.4 | 3.8 |
| 3 | 4 | 6 | 15 | 10.8 | 8.4 | 728 | 564 | 0.152 | 0.478 | 22.7 | 3.1 |
| 4 | 4 | 6 | 20 | 11.8 | 9.4 | 600 | 481 | 0.362 | 0.975 | 20.7 | 2.7 |
| 5 | 4 | 8 | 5 | 4.9 | 2.6 | 1001 | 487 | 0.037 | 0.923 | 47.1 | 25.2 |
| 6 | 4 | 8 | 10 | 6.9 | 3.9 | 707 | 373 | 0.174 | 3.001 | 43.8 | 17.5 |
| 7 | 4 | 8 | 15 | 8.2 | 4.7 | 559 | 313 | 0.498 | 6.680 | 42.1 | 13.4 |
| 8 | 4 | 8 | 20 | 8.9 | 5.5 | 467 | 274 | 1.113 | 12.100 | 38.7 | 10.9 |
| 9 | 4 | 12 | 5 | 3.0 | 1.5 | 614 | 302 | 0.327 | 7.841 | 47.6 | 24.0 |
| 10 | 4 | 12 | 10 | 4.2 | 2.3 | 442 | 231 | 1.424 | 26.001 | 44.8 | 18.3 |
| 11 | 4 | 12 | 15 | 4.9 | 3.0 | 353 | 194 | 3.897 | 56.821 | 38.2 | 14.6 |
| 12 | 4 | 12 | 20 | 5.5 | 3.3 | 297 | 169 | 8.445 | 105.102 | 39.5 | 12.5 |

Note: SL.N. = serial number; $t_{asp}$ = asphalt layer thickness; $t_{GRRB}$ = GRRB layer thickness; $E_{subg}$ = subgrade elastic modulus; UR = unreinforced section; RS = reinforced section; $N_{d(u)}$ = Number of allowable repetitions for unreinforced flexible pavement; $N_{d(R)}$ = Number of allowable repetitions for geocell-reinforced flexible pavement; *PRS* = Percentage reduction in vertical stress; *TBR* = Traffic benefit ratio ($TBR = \frac{N_{d(u)}}{N_{d(R)}}$)

**Table 28 Parametric Study Results for 6-inch Asphalt Concrete Layer**

| SL.N. | $t_{asp}$ (inch) | $t_{GRRB}$ (inch) | $E_{subg}$ (ksi) | Vertical Stress (psi) | | Vertical Strain ($10^{-6}$) | | $N_{d(u)}$ ($10^6$) | $N_{d(R)}$ ($10^6$) | *PRS* (%) | *TBR* |
|---|---|---|---|---|---|---|---|---|---|---|---|
| | | | | **UR** | **RS** | **UR** | **RS** | | | | |
| 1 | 6 | 6 | 5 | 4.2 | 3.3 | 867 | 643 | 0.069 | 2.661 | 20.7 | 3.8 |
| 2 | 6 | 6 | 10 | 5.9 | 4.7 | 609 | 476 | 0.339 | 1.021 | 19.5 | 3.0 |
| 3 | 6 | 6 | 15 | 7.1 | 5.9 | 480 | 391 | 0.984 | 2.472 | 16.3 | 2.5 |
| 4 | 6 | 6 | 20 | 7.8 | 6.5 | 399 | 335 | 2.252 | 4.933 | 16.7 | 2.2 |
| 5 | 6 | 8 | 5 | 3.3 | 2.0 | 691 | 363 | 0.193 | 3.440 | 39.1 | 17.9 |
| 6 | 6 | 8 | 10 | 4.7 | 3.0 | 494 | 280 | 0.866 | 11.102 | 36.4 | 12.7 |
| 7 | 6 | 8 | 15 | 5.6 | 3.7 | 394 | 236 | 2.383 | 23.610 | 33.3 | 9.9 |
| 8 | 6 | 8 | 20 | 6.3 | 4.2 | 331 | 208 | 5.198 | 41.602 | 34.1 | 8.0 |
| 9 | 6 | 12 | 5 | 2.1 | 1.3 | 481 | 246 | 0.975 | 19.601 | 40.0 | 20.1 |
| 10 | 6 | 12 | 10 | 3.0 | 1.8 | 349 | 190 | 4.101 | 62.420 | 38.1 | 15.2 |
| 11 | 6 | 12 | 15 | 3.4 | 2.3 | 280 | 160 | 10.995 | 135.121 | 33.3 | 12.2 |
| 12 | 6 | 12 | 20 | 3.9 | 2.6 | 237 | 141 | 23.194 | 237.021 | 33.3 | 10.2 |

Note: SL.N. = serial number; $t_{asp}$ = asphalt layer thickness; $t_{GRRB}$ = GRRB layer thickness; $E_{subg}$ = subgrade elastic modulus; UR = unreinforced section; RS = reinforced section; $N_{d(u)}$ = Number of allowable repetitions for unreinforced flexible pavement; $N_{d(R)}$ = Number of allowable repetitions for geocell-reinforced flexible pavement; *PRS* = Percentage reduction in vertical stress; *TBR* = Traffic benefit ratio ($TBR = \frac{N_{d(u)}}{N_{d(R)}}$)

### *6.6.1 Impact of Thickness of Asphalt Concrete Layer*

An increase in the thickness of the asphalt concrete layer enhances the structural capacity of the pavement; however, the overall improvement due to geocells decreases for pavements with thicker asphalt concrete layers. The *PRS* values for 6-, 8- and 12-inch base layers decreased with an increase in the thickness of the asphalt concrete layer, as shown in Figure 87. The percentage reduction in stress for the 6-inch base layer reduced from 30% to 20% when the asphalt concrete layer thickness was increased from 2 to 6 inches. Similar observations were made for the 8-inch and 12-inch base layers. The PRS value for the 6-inch asphalt concrete layer was the same for the 8-inch and 12-inch base sections. This indicates that increasing the height of the geocell layer is not beneficial if a thicker asphalt concrete layer is used. An increase in the thickness of the asphalt concrete layer reduces the overall vertical stresses on the geocell layer; hence the improvement is significantly less than that of a thinner asphalt concrete layer.

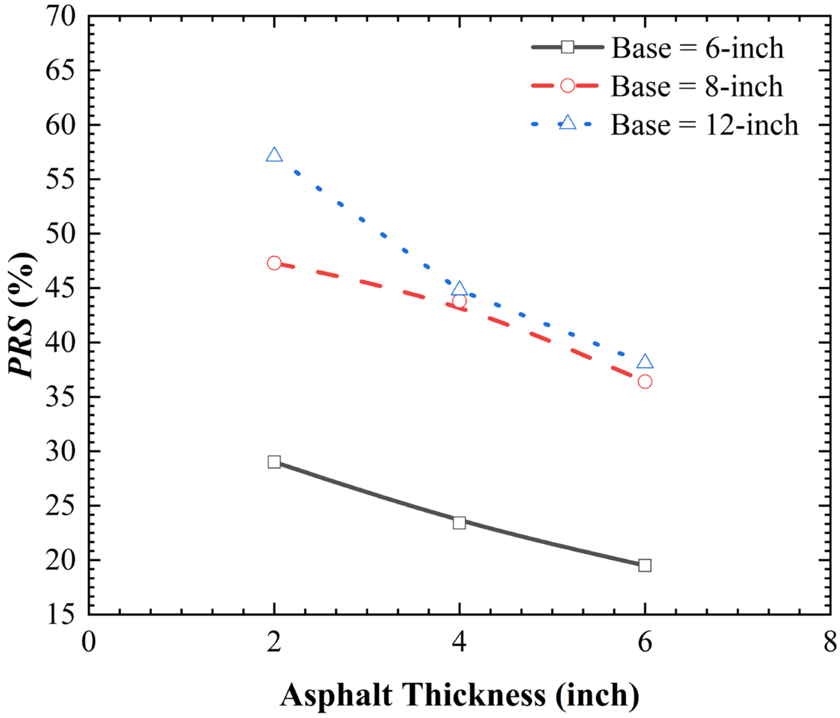

**Figure 87 Effect of Asphalt concrete layer thickness (subgrade modulus = 10 ksi)**

### *6.6.2 Effect of GRRB Layer Thickness*

The field data obtained from the nondestructive test indicated that an increase in the GRRB layer thickness improved the overall performance of the reinforced sections, and the results obtained from the numerical study support the field observations, as the PRS value increased with an increase in the GRRB layer thickness. The effects of the thickness of the GRRB layer for different subgrade moduli are presented in Figure 88. The *PRS* increased with an increase of the GRRB layer thickness, regardless of the modulus of the subgrade. It was also observed that the *PRS* value decreased with an increase of the subgrade layer modulus. The *PRS* values of the 12-inch GRRB layer for the subgrade moduli of 5, 10, 15, and 20 ksi were 66%, 58%, 52%, and 42%, respectively, indicating that the GRRB layer is more beneficial for low-quality subgrade conditions.

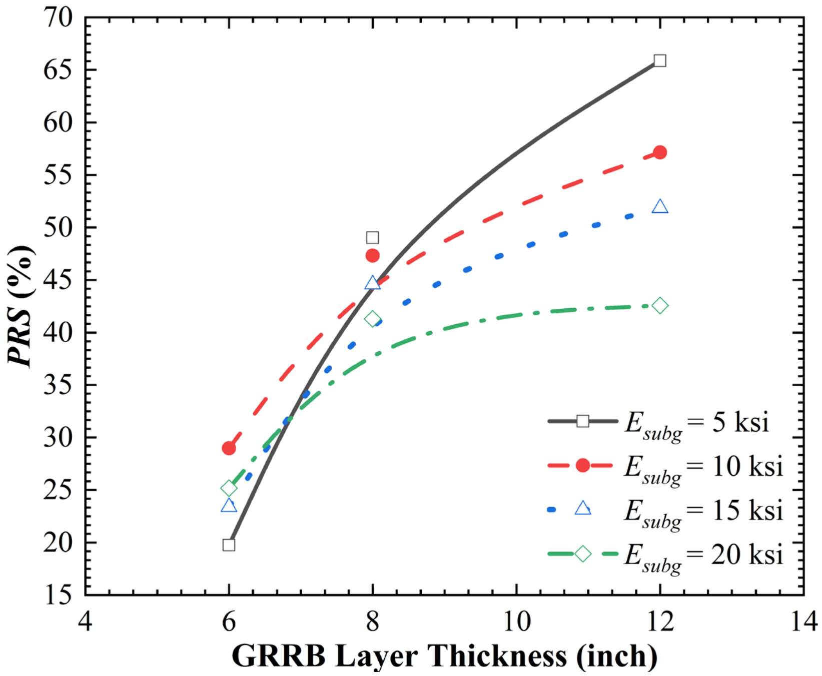

**Figure 88 Effect of thickness of GRRB layer (Asphalt concrete layer thickness = 2-inch)**

### *6.6.3 Effect of Subgrade Stiffness*

The effect of the subgrade modulus for the 6-inch GRRB layer is shown in Figure 89. The modulus of the subgrade layer plays an important role, as it is the weakest layer of the pavement system and contributes to most of the rutting throughout the design life of the flexible pavement. The *PRS* value decreases with an increase of the subgrade modulus. For the 2-inch asphalt concrete layer, the *PRS* value decreased from 49% to 41% when the subgrade modulus increased from 5 to 20 ksi. An increase in subgrade layer modulus will eventually increase the overall capacity of the unreinforced section and will reduce the benefits of the geocell.

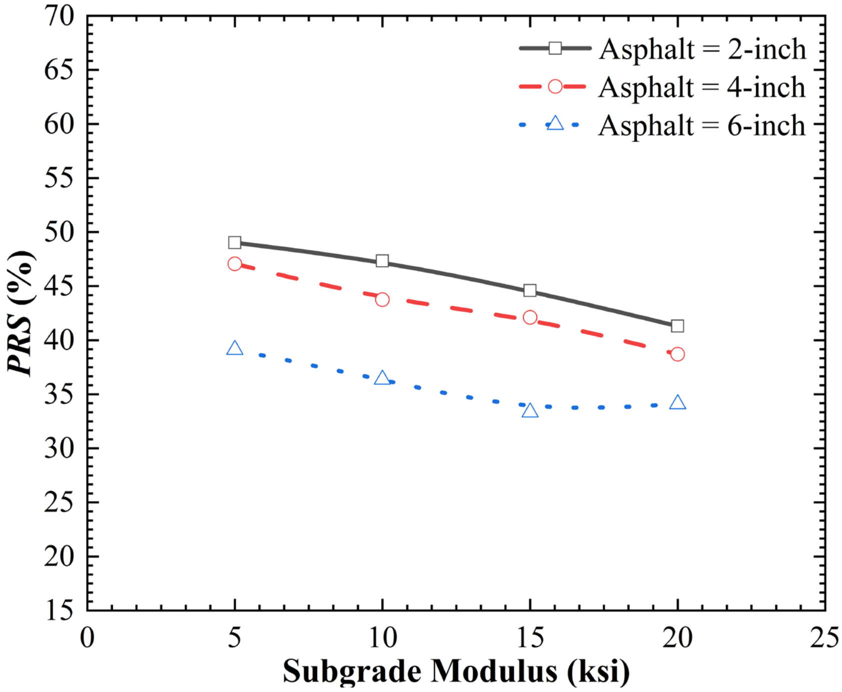

**Figure 89 Effect of subgrade modulus (GRRB Thickness = 6-inch)**

### 6.7 Summary

This chapter presented the numerical approach and material models used for the analyses of the geocell-reinforced base layer. The results obtained from the nondestructive field tests were used to simulate and validate the numerical models and their predictions. Three reinforced sections (RS1, RS2, and RS3) were modeled, and deflection bowls obtained from the field under FWD loading conditions were used to validate the numerical models. Parametric studies were also performed to understand the parameters that are effective for flexible pavement design with geocells. The outcomes of the numerical study are summarized below.

- The application of a geocell within the base layer increased the horizontal stiffness, which resulted in an increase in the overall stiffness of the base layer.

The estimated modular ratios for the 6-, 8- and 12-inch GRRB layers were 3.5, 6.5, and 5, respectively.

- The magnitude and trend of deflection bowls obtained from the numerical study were in good agreement with the NDT results. An increase in the GRRB layer thickness decreased the maximum deflection under the loading plate. The average horizontal stresses acting on the geocells in the first layer of RS1, RS2, and RS3 are 10.0, 7.6, and 4.0 psi, respectively. The average horizontal strains acting within the geocells of RS1, RS2, and the first layer of RS3 were 0.00025, 0.00016, and 0.00013, respectively. The increase in GRRB layer thickness helped reduce the overall lateral movements of the infill materials.
- The estimated reductions in vertical stresses due to 6-, 8-, and 12-inch GRRB layers are 19.5, 29.0, and 43.0%, respectively. According to the Asphalt Concrete Institute method, the estimated traffic benefit ratios for the RS1, RS2, and RS3 sections are 2.6, 5.4, and 22.9, respectively. The increase in asphalt concrete layer thickness reduces the overall vertical stresses on the geocell layer; hence the improvement is significantly lower than that of the thinner asphalt concrete layer. An increase in the subgrade layer modulus will increase the overall capacity of the unreinforced section and result in the reduction of added benefits from the geocell.

# CHAPTER VII

# DEVELOPMENT OF DESIGN METHOD, LIFE-CYCLE COST, AND SUSTAINABILITY ANALYSIS

## 7.1 General

One of the major goals in designing flexible pavements on expansive soils is to control and limit subgrade rutting and heave-induced cracking. The rutting is dependent on the vertical compressive strain on top of the subgrade, and the base layer in a flexible pavement system helps to reduce the vertical compressive strain on the subgrade by distributing the load over a wider area. In this case, the load-carrying capacity of the base layer was enhanced by a geocell that was studied and validated by both field and numerical studies reported in earlier chapters. The traffic loading on a pavement's surface is not uniform, as the magnitude of stress varies with the type of vehicle and tire configuration. In this study, the traffic loading was normalized as an 18-kip load to simulate the load of a single wheel. The loads are considered as equivalent single axle loads (ESALs), by which each type of vehicle that passes over the pavement structure is generalized.

Flexible pavements are also subjected to other types of loading, i.e., aging and environmental loading; however, only traffic loading was considered for estimating the pavement design life in this study. It is possible to design several pavement sections with different combinations of materials but similar structural capacity; however, the life-cycle cost analysis of each pavement will vary with the options used in each case. This chapter discusses flexible pavements design using geocell base layers as reinforced bases, addresses economic feasibility based on life cycle cost analysis (LCCA) of pavement configurations, and assesses the sustainability of using geocell layers as pavement base layers.

## 7.2 Effects of Geocell Reinforcement on Pavement Rutting Life

Geocell offers additional confinement, which helps to enhance the stiffness of the infill material, i.e., RAP. The back-calculated field moduli were used in parametric studies on both the reinforced and unreinforced sections. The results obtained from the parametric study presented in Chapter 6 and results showed that the pavement design life was improved by incorporating a geocell-reinforced base layer with RAP as infill material. An increase in the life span of reinforced layers depends on the thickness of the surface and base layers and stiffness of the subgrade material. The results obtained from the FEM analysis were used to determine the design life improvement factor for structures reinforced with geocells, and the results are presented in Figure 90. The design life periods for both the unreinforced and reinforced pavement sections were determined from the vertical compressive strain acting on top of the subgrade, using the Asphalt Institute (AI) method.

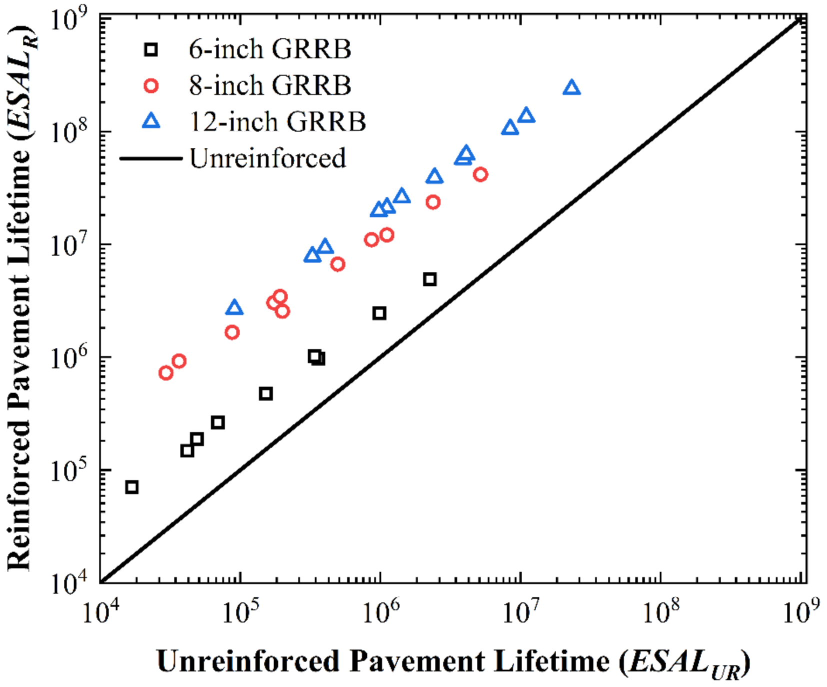

**Figure 90 Lifetime equivalent single axle loads (ESAL) of reinforced and unreinforced soils predicted by the numerical modeling studies**

The FEM data and their results were grouped into three series, and each of these groups corresponded to a single base layer thickness, and the trends of these results was then fitted with a power function. The design life improvement factor (*DIF*) for the pavement structure with reinforced geocell base layers was estimated with the following Equation 56.

$$DIF = \frac{ESAL_R}{ESAL_{UR}} \geq 1 \qquad (56)$$

Where $ESAL_R$ is the number of ESALs that can be supported by the geocell-reinforced pavement section, and $ESAL_{UR}$ is the number of ESALs that can be supported by the unreinforced pavement section. The *DIF* value is always greater than or equal to one, as the inclusion of geocells positively influences the performance of the pavement (Mengelt et al., 2000). The *DIF*s of various pavement sections with different GRRB layer thicknesses are shown in Figure 91**.** The reinforced layer thickness was kept constant, and the other layers were changed in this FEM study and subsequent *DIF* analyses. Parametric analyses presented in the previous chapter cover these results.

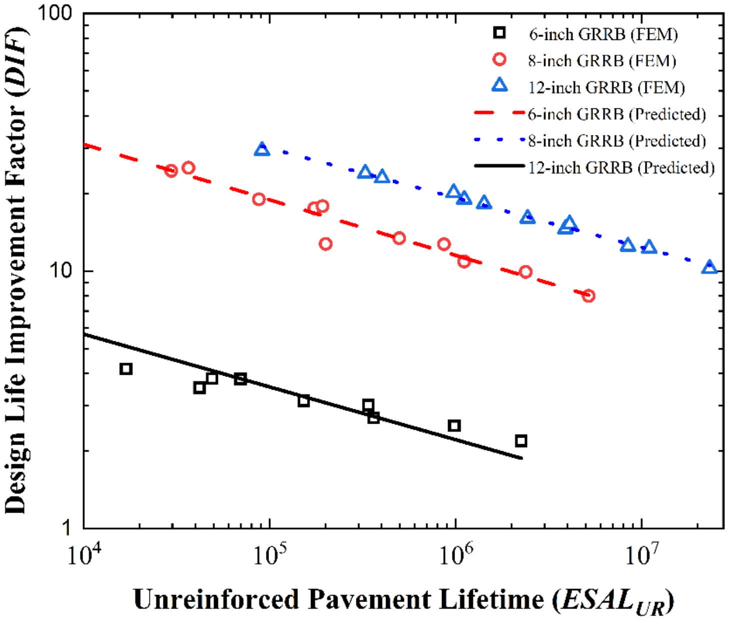

**Figure 91 Design life improvement factor for geocell-reinforced pavements with varying GRRB layer thicknesses**

The *DIF* is a function of the thickness of both the asphalt layer and the base layer. At any given thickness of the asphalt layer, the relative degree of improvement afforded by the geocell will decrease due to the reduction of subgrade contact pressure, and the reduced subgrade contact pressure will eventually increase the rutting life of the unreinforced pavement section. The slopes of the trendlines for 6-, 8-, and 12-inch GRRB layers are 0.205, 0.216, and 0.192, with an average slope of 0.204. This average value was used to develop the following *DIF* prediction model for the geocell-reinforced pavement structures and is defined as (Equation 57):

$$DIF = k[ESAL]^{-0.204} \tag{57}$$

Where *k* is a constant and is a function of the geocell-reinforced base layer thickness ($t_{gc}$). This constant for any base layer thickness can be determined using the following Equation 58, which was developed based on the data obtained from the parametric studies, and this correlation has an $R^2$ value of 0.96, indicating a strong correlation for this constant parameter, *k*.

$$k = 285.6(t_{gc}) - 13.7(t_{gc})^2 - 1184 \tag{58}$$

### 7.3 Development of Design Methodology with Geocell-Reinforced Pavement

The incorporation of geocells helps increase the design life of the pavement and allows designers to choose thinner pavement layers. According to the Federal Highway Administration (FHWA), the base/subbase, subgrade, and bedrock groups are the geotechnical materials that are considered for the design of pavement infrastructure. The stiffness of the pavement materials, quantified in terms of the resilient modulus, is one of the most important geotechnical properties according to the most widely used pavement design method (1993 AASHTO Pavement Design Guide). Swelling/expansive soil is considered a special case as the estimated damage to pavement caused by this type of soil is well over $1 Billion each year (Christopher et al., 2006). The following is the equation (Equation 59) recommended by the AASHTO 1993 method for the design of flexible pavements:

$$\log(W_{18}) = Z_R S_o + 9.36\log_{10}(SN_{UR}+1) - 0.2 + \frac{\log_{10}\left[\frac{\Delta PSI}{4.2-1.5}\right]}{0.4+\frac{1094}{(SN_{UR}+1)^{5.19}}} + 2.32\log_{10}M_R - 8.02 \quad (59)$$

Where,

$W_{18}$ = predicted number of 80 kN (18,000 lb.) ESALs

$Z_R$ = standard normal deviate

$S_o$ = combined standard error of the traffic prediction and performance prediction

$\Delta PSI$ = difference between the initial design serviceability index, $p_o$, and the design terminal serviceability index, $p_t$

$M_R$ = subgrade resilient modulus (in psi)

It is obvious that the modulus of the subgrade soil plays an important role in selecting the overall thickness of a pavement system. The following section discusses the geotechnical factors used in the design of flexible pavements.

### *7.3.1 Sensitivity of Pavement Design to Geotechnical Factors*

The surface is the most significant layer of flexible pavement, and both the strength and stiffness of the subgrade soil play a key role by controlling the required thickness of the base layer. The influence of the subgrade's California bearing ratio (*CBR*) on the required thickness of the base layer is shown in Figure 92, as per the AASHTO 1993 pavement design guideline. The contribution of the granular base layer to the overall structural capacity of the pavement varies from 68% for a low *CBR* value of 3 to 27% for a higher *CBR* value of 73. The influence of the quality of the base layer on the design of the base layer thickness is shown in Figure 93**.** An increase in the stiffness of the base layer helps decrease the thickness of the base layer, and a decrease in the subgrade *CBR* value from 8 to 4 can increase the overall material cost by 20%. Since the early 1990s, the resilient modulus of subgrade was used in the pavement design as this parameter better represents the subgrade condition under repeated loading. It is important to quantify the enhancement of base layer stiffness with a geocell layer for different types of subgrade soil conditions, as subgrade resilient modulus has a major impact on the overall structural design of the pavement.

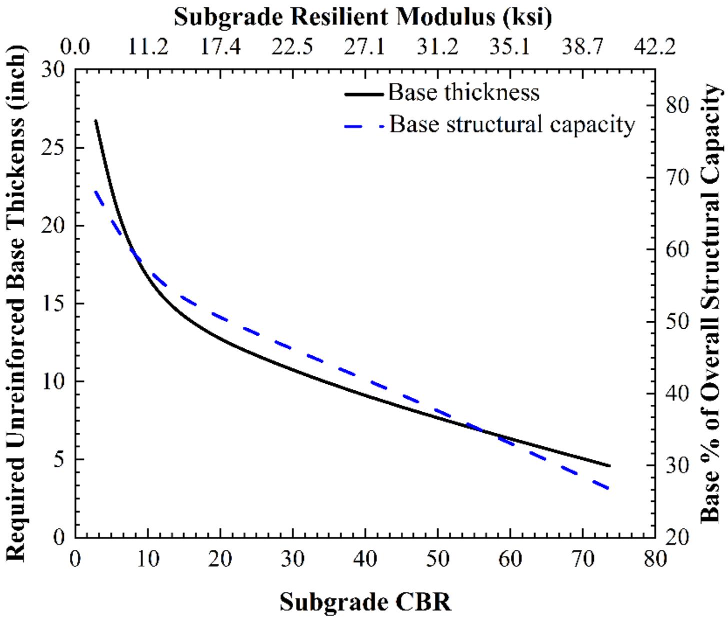

**Figure 92 Impact of subgrade strength on pavement structural design (AASHTO 93 Design Guide: $W_{18}$ = 10 million, 85% reliability, $So$ = 0.4; $\Delta PSI$ = 1.5, $D_1$ = 4 inch; $a_1$ = 0.44, $a_2$=0.14, $m_2$=1)**

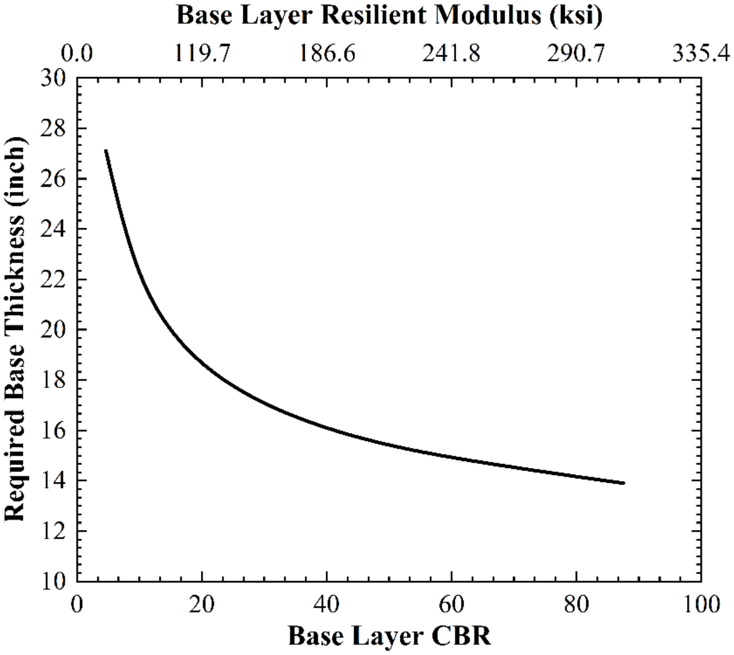

**Figure 93 Impact of base strength on pavement structural design (AASHTO 93 Design Guide: $W_{18}$ = 10 million, 85% reliability $S_o$= 0.4, $\Delta PSI$ = 1.5, $D_1$ = 4 inch; $a_1$ = 0.44, $m_2$ = 1, Subgrade CBR = 5)**

Increasing the base layer stiffness by stabilization or by any form of reinforcement will therefore help decrease the thickness of the base layer, which is economically beneficial due to the saving of virgin aggregate materials. The estimated benefit from the geocell needs to be adjusted based on the field observations. The following section presents the procedure adopted to determine the field calibration correlation factor.

This study focuses on the effectiveness of geocell-reinforced pavement constructed on expansive soil. The data collected from the field was used to calibrate the design life improvement factors. The rut depths measured over the past 30 months are presented in Table 29. The number of standard load repetitions (*N*) was estimated with a projected AADT of 1500 and a traffic growth rate of 2%.

**Table 29 Measured Rut Depths and Curve Fitting Parameters**

| | | | Base = 6-inch | | Base = 8-inch | | Base = 12-inch | |
|---|---|---|---|---|---|---|---|---|
| | | | **RS1 (F)** | **UR1 (F)** | **RS2 (F)** | **UR2 (F)** | **RS3 (F)** | **UR3 (F)** |
| Field Data (F) | Number of load cycles, *N* | 0 | 0 | 0 | 0 | 0 | 0 | 0 |
| | | 24000 | 0.18 | 0.35 | 0.2 | 0.33 | 0.19 | 0.34 |
| | | 36000 | 0.21 | 0.38 | 0.27 | 0.39 | 0.24 | 0.41 |
| | | 49000 | 0.23 | 0.42 | 0.31 | 0.45 | 0.27 | 0.49 |
| | | 61000 | 0.26 | 0.5 | 0.32 | 0.52 | 0.29 | 0.54 |
| Curve Fitting Parameters | | A | 0.0039 | 0.0018 | 0.0012 | 0.0026 | 0.0020 | 0.0021 |
| | | B | 0.3806 | 0.5109 | 0.5150 | 0.4787 | 0.4538 | 0.5037 |
| | | $R^2$ | 0.98 | 0.96 | 0.94 | 0.99 | 0.98 | 0.99 |

Note: Curve fitting equation, $\delta = AN^B$.

The field data were fitted with a two-parameter rutting model, as shown in Table 29. The number of standard load repetitions corresponding to the target rutting of 0.50 inches was estimated by using Equation 60. The recommended rutting for the flexible pavement is 0.50 inches as per TxDOT Pavement Design Manual; hence the number of load repetitions, corresponding to 0.50 inches of rutting was used to predict the total standard load repetition here. The field data, along with the predicted data for the reinforced and unreinforced sections, are presented in Figure 94.

$$N = \left( \frac{0.50}{A} \right)^{\frac{1}{B}} \tag{60}$$

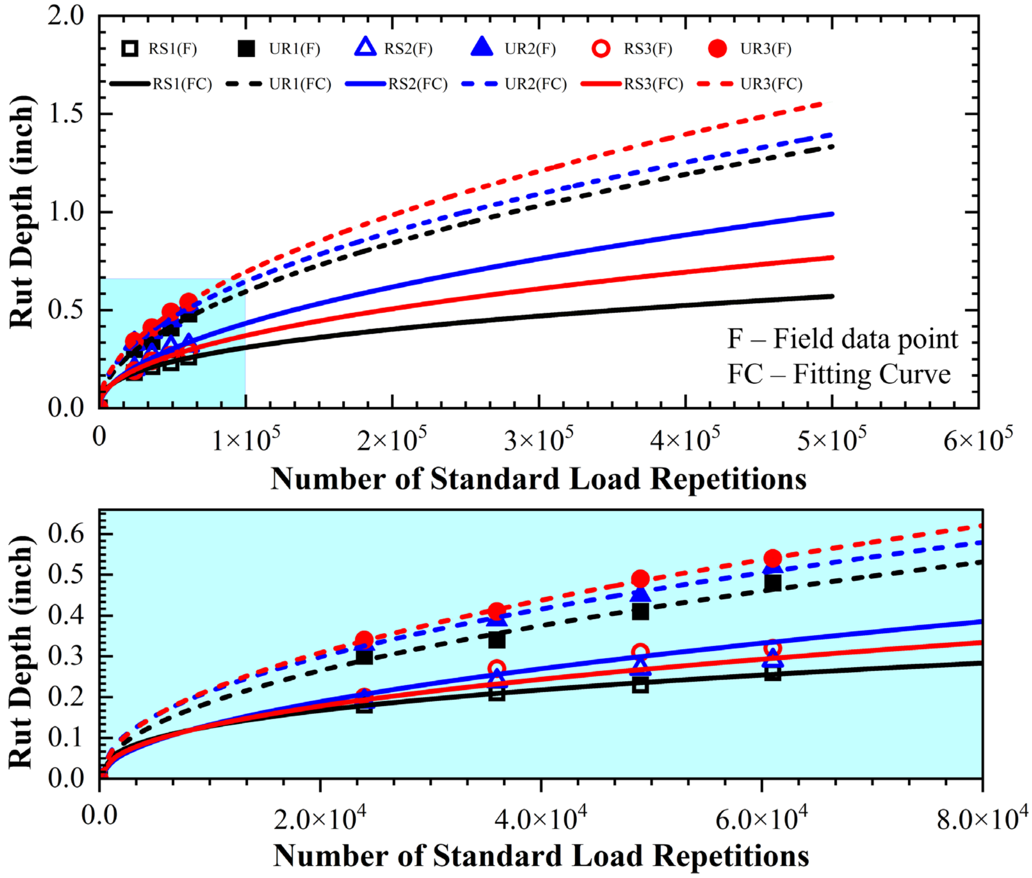

**Figure 94 Rut depths of reinforced (RS1, RS2, and RS3) and unreinforced (UR1, UR2, and UR3) sections, measured from the field (F) and based on fitting curve (FC)**

Rut-depths were measured 12, 18, 24, and 30 months after the construction of the test sections. The number of standard load repetitions corresponding to those times was used to plot the graph shown in Figure 94. The estimated allowable load repetitions for the reinforced and unreinforced pavement sections, corresponding to a rut depth of 0.5 inches, are presented in Table 30. The traffic benefit ratio (*TBR*) observed from the field data ($TBR_{field}$), and the estimated traffic benefit ratio ($TBR_{estimated}$) from FEM studies were used to determine the field calibration correlation factor, $\alpha$, based on the following equation (Equation 61).

$$\alpha = \left( \frac{TBR_{field}}{TBR_{estimated}} \right) \qquad (61)$$

**Table 30 Field Calibration Correlation Factor ($\alpha$)**

| Base Thickness | Reinforced Section (Field) | Unreinforced Section (Field) | $TBR_{field}$ | $TBR_{estimated}$ | Field Calibration factor, $\alpha$ |
|---|---|---|---|---|---|
| 6-inch | 354,450 | 70,837 | 5.0 | 2.6 | 1.92 |
| 8-inhc | 132,665 | 58,714 | 2.3 | 5.4 | 0.43 |
| 12-inch | 194,600 | 52,097 | 3.7 | 22.9 | 0.16 |

Note: Estimated *TBR* is based on the FEM study presented in chapter 6.

The field calibration factor varies with the thickness of the base layer. The relationship between the field calibration factor ($\alpha$) and the thickness of the base layer ($t_{base}$) is presented in Figure 95. The estimated design life improvement factor derived from Equation 57 was further modified (Equation 62) to incorporate the field calibration correlation factor.

$$DIF = \alpha k [ESAL]^{-0.204} \qquad (62)$$

Where *DIF* = Design life improvement factor

$\alpha$ = filed calibration correlation factor

*ESAL* = design traffic capacity corresponding to the unreinforced pavement section

*k* = influence factor due to the thickness of geocell layer (Equation 58)

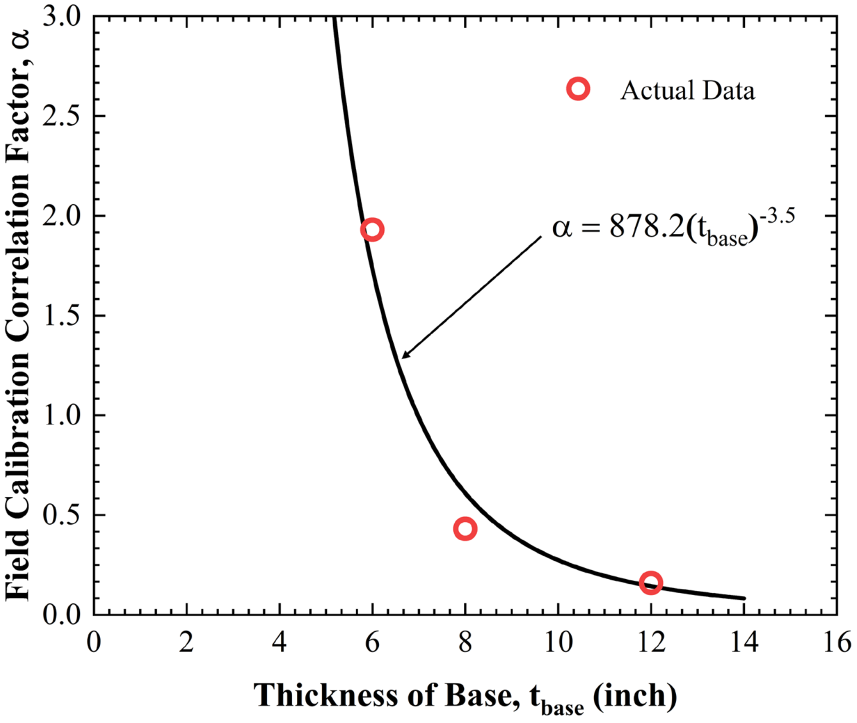

**Figure 95 Relationship between field calibration correlation factor and the base layer thickness**

Figure 95 shows that an increase in the thickness of the base layer reduces the traffic benefit ratio, and an increase in the thickness of the reclaimed asphalt layer thickness, increases the depth of the ruts in the base layer and leads to a shortened design life. The expected rut life of flexible pavement will be the same as the field condition when the thickness of the base layer is approximately 7 inches. A strong relationship exists between $\alpha$ and $t_{base}$, which can be expressed with the following Equation 63, and the $R^2$ value of this equation is 0.98, indicating a strong correlation. It is anticipated that more field data will be helpful to further refine this equation.

$$\alpha = 878.2(t_{base})^{-3.5} \tag{63}$$

The design life influence factor as presented in Equation 62 can be further modified with the following equation (Equation 64).

$$DIF = 878.2\left(t_{base}\right)^{-3.5k}\left[ESAL\right]^{-0.204} \tag{64}$$

Using the above parameters, the pavement design methods for a geocell-reinforced pavement system per the AASHTO method are formulated and discussed in the following section.

### *7.3.2 GRRB Design Based on AASHTO Method*

The design influence factor-based method can be adopted to reduce the thickness of the base course layer and extend the service life of the pavement. According to the American Association of State and Highway Officials (AASHTO), the overall structural number (*SN*) is calculated based on the products of layer thickness and layer coefficients ($SN = a_1.D_1 + a_2.D_2 + a_3.D_3$). As the load-carrying capacity of geocell-reinforced pavement is higher than that of unreinforced pavement with the same thickness of the base layer, the *DIF* values can be used to measure the structural number of the pavement section with the reinforced base.

**Step 1:** The traditional approach to designing unreinforced pavement requires subgrade soil properties, including resilient modulus and loss of serviceability, due to the swelling behavior of the expansive soil. The resilient modulus of the subgrade ($M_R$) soil can be determined from repeated load triaxial tests or by using the following correlation with the field *CBR* values, as shown in Equation 65.

$M_R = 1500\ (CBR)$ (65)

**Step 2:** Estimate the total allowable design traffic for the unreinforced condition based on the design life and available traffic data. The allowable design traffic for the reinforced case can be estimated from Equations 56, 58, and 64. The structural number corresponding to the unreinforced ($SN_{UR}$) and reinforced ($SN_R$) sections can be estimated based on the AASHTO 1993 flexible pavement design equation (Equation 59**)**. The $SN_{UR}$ is the structural number corresponding to $ESAL_{UR}$ and $SN_R$ is the structural number corresponding to the reinforced section $ESAL_R$ ($ESAL_R = DIF$ x $ESAL_{UR}$). The difference between the structural numbers can be used to predict the layer coefficient ($a_{2R}$) of the geocell-reinforced base layer with the following equation (Equation 66).

$$a_{2R} = \frac{S_R - SN_{UR}}{D_2} + a_2 \tag{66}$$

Where $a_2$ and $D_2$ are the structural coefficient and thickness of the unreinforced base layer.

**Step 3:** The layer coefficient obtained from Equation 66 can be used to determine the thickness of the base layer or to adjust the thickness of the asphalt layer based on the life cycle cost assessment. The layer coefficient for the GRRB layer may range between 0.15 to 0.40; however further field studies are required to confirm the structural contribution of the GRRB layers.

### *7.3.3 Design based on MEPDG Method*

According to the MEPDG design method, pavement distresses are evaluated by using a mechanistic response model and an empirical design model. The pavement responses (stresses and strains) can be estimated by employing the linear elastic approach (LEA) or the finite element method (FEM) using linear material parameters. The estimated pavement responses from geocell-reinforced pavement base layers can be used to determine rutting distress and pavement cracking, both of which are based on an empirical damage model, using the transfer functions. The permanent deformation or rutting of a geocell-reinforced base layer can be estimated from the resilient strains of the response model. According to an NCHRP report, the following transfer function (Equation 67) can be used to calculate the permanent deformation of an unbound layer for any number of load repetitions, *N*.

$$\Delta_p = h_{geo}\varepsilon_o e^{-\left(\frac{\rho}{N}\right)^{\beta}} \left(\frac{\sqrt{J_2}}{P_a}\right)^{m} \left(\frac{\alpha I_1 + \frac{\left(c' + \frac{3.9c}{h_{geo}} + 2.5\right).6\cos\phi'}{\sqrt{3}(3-\sin\phi')}}{P_a}\right)^{n} \left(P_a\right)^{-(m+n)} \tag{67}$$

The parameters used to develop the permanent deformation response are described in Chapter 5. The back-calculated parameters for the GRRB layer can be used to compute the resilient modulus according to the MEPDG method. The three-parameter model and its parameters ($k_1$, $k_2$, and $k_3$) are listed in Table 31 and can be used for design purposes with 6-, 8-, and 12-inch GRRB layers.

**Table 31 MEPDG Model Parameters for GRRB**

| Test Sections | $k_1$ | $k_2$ | $k_3$ |
|---|---|---|---|
| 6-inch GRRB | 1558 | 4.45 | -7.81 |
| 8-inch GRRB | 6647 | 2.11 | -4.70 |
| 12-inch GRRB | 9832 | 1.08 | -3.16 |

The M-E model developed in this study is in congruent with the current MEPDG method used in the United States. The modifications of the damage model and the proposed resilient modulus parameters based on the field study provided a suitable solution for the design of the geocell-reinforced base layers.

### *7.3.4 Pavement Design Example*

The inclusion of the GRRB layer increases the design life of the pavement, which can also be presented in terms of the reduction of the layer thickness. A design example of a 6-inch GRRB layer is shown in the following section, based on the 1993 AASHTO Design method. The design input parameters are listed in Table 32.

**Table 32 Design Inputs for AASHTO 1993**

| Parameters | Values/Range/Source |
|---|---|
| Design reliability | 95% |
| Design *ESAL*s, $10^6$ | 2.0 |
| ΔPSI (loss of serviceability) | 2.0 |
| Subgrade resilient modulus, $M_{sg}$ (psi) | 9000 |
| Structural coefficient of unreinforced RAP | 0.12 |
| Structural coefficient of reinforced RAP | Equation 66 |
| Drainage coefficients for any layer | 1.0 |

The first step in designing unreinforced pavement is to determine the structural number that will withstand a traffic volume of 2 million, which according to Equation 59**,** is 3.72 ($SN_{UR}$). After that, the design life influence factor can be determined from Equation 64. The estimated DIF for a 6-inch GRRB and unreinforced section capacity of

2 million is 3.13. According to Equation 56, the projected *ESAL* for the geocell-reinforced case is therefore 6.26 million, which is associated with an enhanced structural number of 4.41 ($SN_R$). The structural coefficient of the geocell-reinforced base layer estimated from Equation 66 is shown below.

$$\mathrm{a}_{2\mathrm{R}} = \frac{SN_R - SN_{UR}}{D_2} + \mathrm{a}_{2(\mathrm{UR})} = \frac{4.41 - 3.72}{6} + 0.12 = 0.24$$

The thickness of the subbase layers of both the unreinforced and reinforced sections can be estimated based on the structural coefficients of each layer by using Equations 68 and 69, respectively.

$$D_3 = \frac{SN_{UR} - a_1 D_1 - a_{2(\mathrm{UR})} D_2}{a_3} \tag{68}$$

$$D_3 = \frac{SN_{UR} - a_1 D_1 - a_{2R} D_{2R}}{a_3} \tag{69}$$

Here, $a_1$ and $a_3$ are the structural layer coefficients for the asphalt and subbase layers; $D_1$ and $D_3$ are the thicknesses of the asphalt subbase layers. A structural layer coefficient of 0.12 for the unreinforced RAP layer ($a_{2(UR)}$) was estimated from the resilient modulus determined from the laboratory experiments. The recommended layer coefficient of 0.11 was used for both the unreinforced and reinforced subbase layers. The thickness of the subbase layer for the unreinforced pavement was estimated as 11.3 inches, and the thickness of the subbase layer for the reinforced pavement was estimated as 4.7 inches. It was observed that the inclusion of geocells helped reduce the subbase layer thickness by 58%, which can be a considerable economic saving. Other alternative designs, including asphalt layer thickness reductions, are also possible.

The efficiency of the 6-inch GRRB layer was compared with a 6-inch flex base (FB) layer for five different levels of traffic volume. A comparison of the thickness required for the subbase layer of the GRRB layer and FB base layer is shown in Figure 96. The 1993 AASHTO design guide recommended that a layer coefficient of 0.14 be used for the flex base layer. It was observed that replacing a traditional flex base aggregate layer with GRRB can save the volume of pavement materials. The required thickness of the subbase layer for GRRB is nearly 4.8 times less than that required for traditional pavements with FB at a design *EASL*s of 1 million. Pavement sections with three different types of base materials are shown in Figure 97.

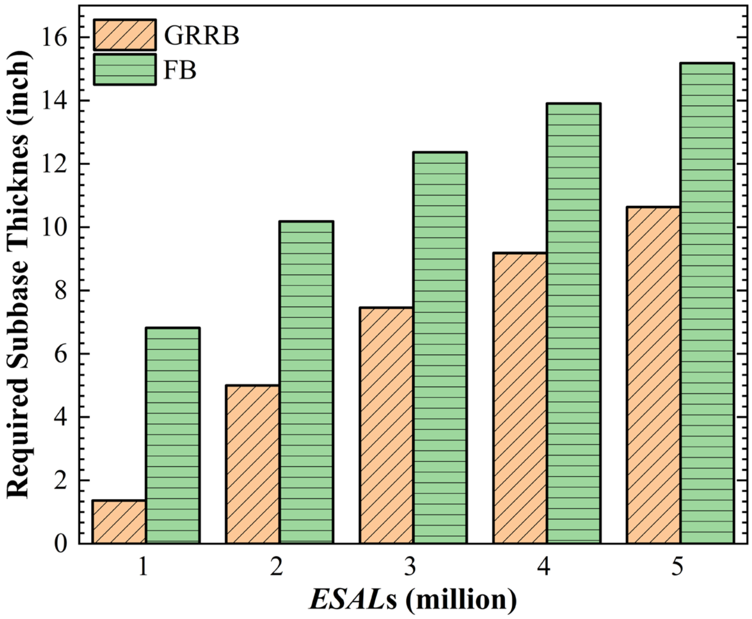

**Figure 96 Comparison of required thickness of subbase layer for different GRRB and traditional flex base (FB) materials for different *ESAL*s**

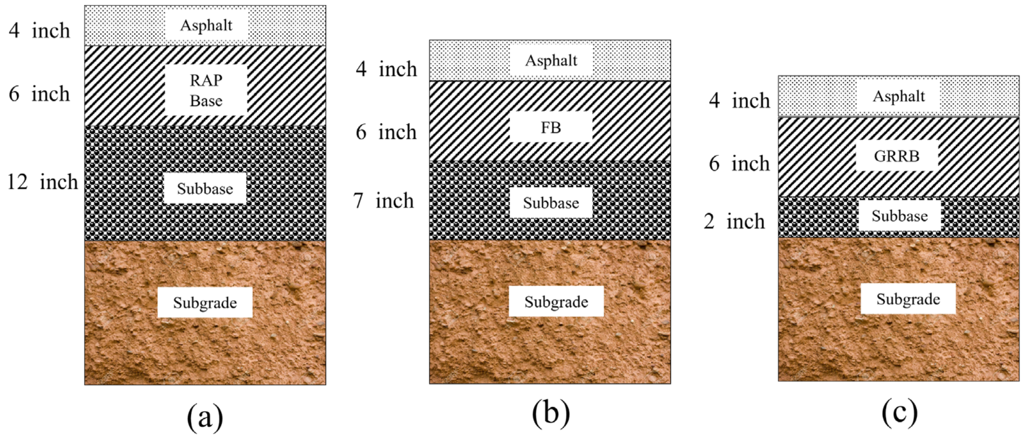

**Figure 97 Pavement sections corresponding to 1 million *ESAL*s for a) RAP base, b) flexible base (FB), and c) geocell-reinforced RAP base (GRRB)**

Overall, a GRRB layer has the potential to reduce the subbase layer thickness, which is beneficial economically, and the utilization of reclaimed pavement materials in the base layer adds even more benefits. However, the inclusion of geocells will increase the initial cost, which should be considered when estimating the overall advantages. The following section will discuss the life cycle cost and sustainability benefits, and these methods assess both the cost and sustainability-related benefits of flexible pavements with GRRBs.

### 7.4 Life-cycle Cost Analysis for Geocell-Reinforced Pavement Systems

Utilizing geocells can provide distress-free pavement performance with longer design life; however, a life-cycle cost analysis (LCCA) is needed to help the designer select the alternative that will be the most economical and sustainable. This research focuses on reinforcing the pavement base layer with geocells, which allows 100% utilization of recycled materials, such as RAP material, as a base layer. The replacement of RAP with traditional flex base material has also proven to be cost-effective since this results in a 50% reduction of the base material, which can be realized as a 30% saving of total material cost; however, the cost of the geocell itself has to be factored in. The purpose of the LCCA analysis is to help transportation agencies achieve maximum benefits without compromising performance.

### *7.4.1 Establishment of Design Alternatives*

Pavement life cycle cost is comprised of raw material production, construction, utilization, maintenance/rehabilitation, and end of life. The agency and user costs were estimated separately for each phase. Three alternatives with different types of base materials with the same thicknesses are considered, and this analysis is assumed to be performed for a service life of 30 years. The materials considered for the base layers for alternative 1 (A1), alternative 2 (A2), and alternative 3 (A3) were flex base (FB), cement-treated base (CTB), and geocell-reinforced base (GRRB), respectively. The thicknesses of the asphalt and base layers were 4 inches and 8 inches, respectively. The main reason for assuming the same layer thicknesses, this will be helpful in evaluating the cost benefits with more clarity. One important aspect is the repair of each section is dependent on the magnitude of distresses, and these are evaluated from numerical studies on the same sections.  The initial pavement sections for the alternatives are shown in Figure 98. It is expected that all the alternatives will perform similarly; however, the number of maintenance/rehabilitation activities may vary.

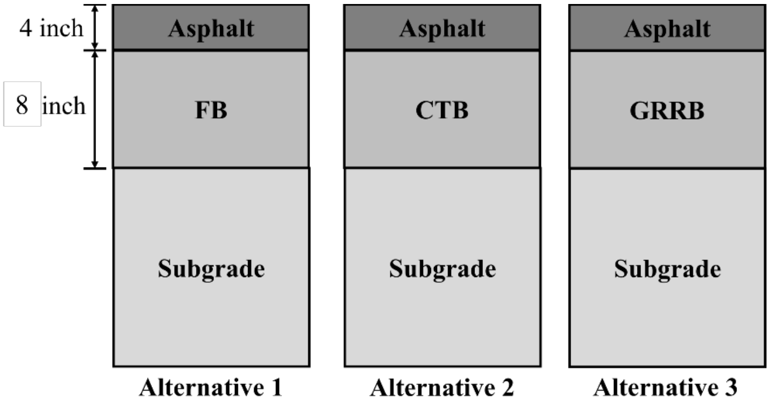

**Figure 98 Alternative Pavement Sections: Alternative 1 (FB), Alternative 2 (CTB), and Alternative 3 (GRRB)**

According to the strategic plan, LCCA is only required if the volume of the annual average daily traffic (AADT) is higher than 10,000, which is the volume that this LCCA study was designed for. The traffic consisted of 10.6% trucks and 89.4% passenger cars, and traffic growth was assumed to be 0.75% for the design life. The subgrade condition was considered similar for all the alternatives. It is expected that all the pavement sections will have at least two major rehabilitations during their service life of 30 years.

### *7.4.2 LCCA Approach*

An LCCA can be conducted by using either a deterministic or probabilistic approach (Babashamsi et al., 2016; Inti, 2016). The deterministic approach applies all the techniques and procedures without considering the variability of the inputs. In this study, both the deterministic and probabilistic approaches were used for determining the LCCA, based on RealCost 2.5 software, which is recommended by FHWA. The following sections describe both approaches used in this research.

#### 7.4.2.1 Deterministic Approach

The cost of the different alternatives was determined based on agency and user cost. Some of the cost elements were not considered in this LCCA, as they were either unavailable or may not have a significant impact on the analysis.

**Agency Costs:** The cost of construction, maintenance, and other costs associated with the demolition of pavement at the end of life is considered the agency's cost. In this study, salvage values were considered, as the pavements will not be destroyed at the end of the design life. The cost of construction was estimated for a one-mile-long section. The unit prices of individual items for A1, A2, and A3 are shown in Table 33, Table 34, and Table 35**,** respectively. The unit cost of the elements was obtained from the average low bid prices of the Fort Worth District that are published by TxDOT.

**Table 33 Unit Material Costs for Alternative 1 (FB)**

| **S.N.** | **Item** | **L** | **W** | **A** | **Unit cost** | **Amount** |
|---|---|---|---|---|---|---|
| | | **(ft)** | **(ft)** | **SY** | (USD) | (USD) |
| 1 | Asphalt concrete 4 inch thick | 5,280 | 15 | 8,800 | 15.40 | 135,520 |
| 2 | Tack coat | 5,280 | 15 | 8,800 | 1.60 | 14,080 |
| 3 | Prime coat | 5,280 | 15 | 8,800 | 0.60 | 5,280 |
| 4 | Flexible base 8 inch thick | 5,280 | 15 | 8,800 | 16.90 | 148,720 |
| 5 | Subgrade Preparation | 5,280 | 15 | 8,800 | 3.20 | 281,60 |
| Total Unit Cost Per Mile | | | | | | 331,760 |

Note: L =length; W = width; A = area.

**Table 34 Unit Material Costs for Alternative 2 (CTB)**

| S.N. | Item | L | W | A | Unit cost | Amount |
|---|---|---|---|---|---|---|
| | | (ft) | (ft) | SY | (USD) | (USD) |
| 1 | Asphalt concrete 4 inch thick | 5,280 | 15 | 8,800 | 15.40 | 135,520 |
| 2 | Tack coat | 5,280 | 15 | 8,800 | 1.60 | 140,80 |
| 3 | Prime coat | 5,280 | 15 | 8,800 | 0.60 | 5,280 |
| 4 | Cement Treated base 8 inch thick | 5,280 | 15 | 8,800 | 19.40 | 170,720 |
| 5 | Subgrade Preparation | 5,280 | 15 | 8,800 | 3.20 | 28,160 |
| Total Unit Cost Per Mile | | | | | | 353,760 |

Note: L =length; W = width; A = area.

**Table 35 Unit Material Costs for Alternative 3 (GRRB)**

| S.N. | Item | L | W | A | Unit cost | Amount |
|---|---|---|---|---|---|---|
| | | (ft) | (ft) | SY | (USD) | (USD) |
| 1 | Asphalt concrete 4 inch thick | 5,280 | 15 | 8,800 | 15.40 | 135,520 |
| 2 | Tack coat | 5,280 | 15 | 8,800 | 1.60 | 140,80 |
| 3 | Prime coat | 5,280 | 15 | 8,800 | 0.60 | 5,280 |
| 4 | GRRB 8 inch thick | 5,280 | 15 | 8,800 | 13.75 | 121,000 |
| 5 | Subgrade Preparation | 5,280 | 15 | 8,800 | 3.20 | 28,160 |
| Total Unit Cost Per Mile | | | | | | 304,040 |

Note: L =length; W = width; A = area.

**Costs of GRRB Layers:** The material cost of the GRRB layer was calculated based on RAP's cost and the geocell's cost per unit area. The cost of RAP material is 2.4 times lower than that of flex base material, and an additional saving was realized because the material didn't have to be hauled from a distance. It was expected that the existing roadway section could be milled and placed at the same time, saving time and money; however, the cost of the geocell, which varies with the height of the layer, would increase the cost of the GRRB layer. The unit costs for 4-inch and 6-inch geocells are

$0.50 and $0.75 per square feet (SF), which is equivalent to $4.50 and $6.75 per square yard (SY), respectively. The overall unit cost of RAP material is $7.00 per SY for an 8-inch-thick section, resulting in a total cost of $13.75 per SY. The cost of traditional flex base material for an 8-inch-thick section is $16.90 per SY, which is 22.9% more than the material cost for an 8-inch thick GRRB layer.

**Maintenance Activities:** Pavement analyses were conducted to determine the number of rehabilitations required for each alternative for an assumed service life period of 30 years. The elastic modulus and subgrade modulus were assumed as 500 ksi and 12 ksi for all the alternatives. The elastic moduli for the flex base, cement-treated base, and GRRB were considered as 50, 70, and 80 ksi, respectively. A 2-inch-thick overlay was considered as the major rehabilitation work that would be needed for all the alternatives at different times, as shown in the schematic diagram depicted in Figure 99. Due to the budget constraint, TxDOT flexible pavement design manual (2021) allows two or three major rehabilitation activities within the total analysis period of the flexible pavement. The initial performance periods are estimated based on the subgrade rutting criteria and from the TxDOT recommended software tool (FPS 21).

The cost of a 2-inch-thick overlay ($6.90 per square yard) and the milling of the existing road section before placement of the overlay ($1.40 per square yard) were considered as the costs for the rehabilitation works during the first phase (R1), and the maintenance works needed to service the pavements in the second phase (R2).

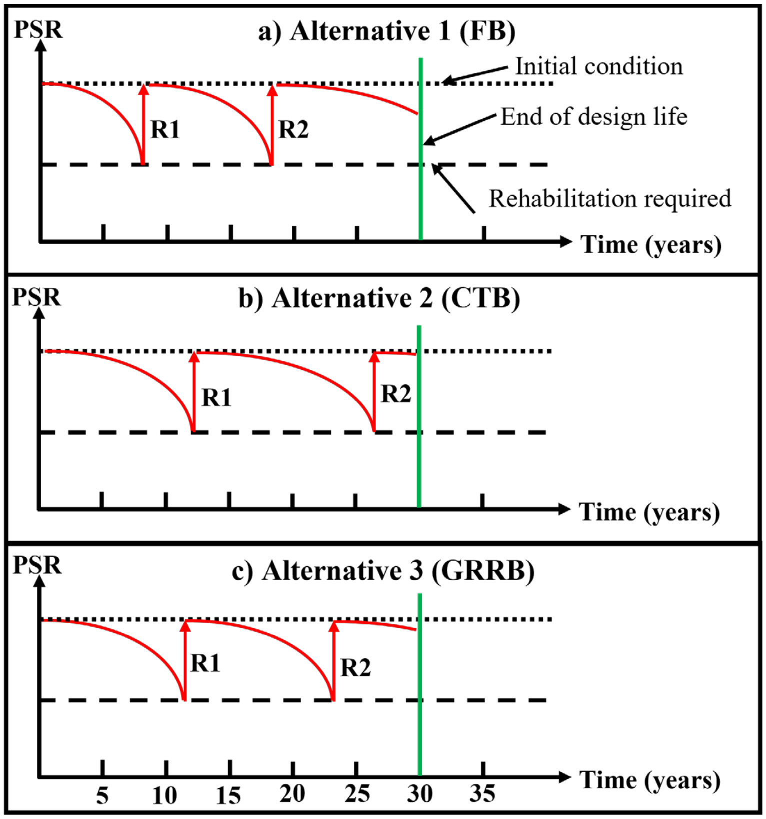

**Figure 99 Rehabilitation schedule for Alternative 1 (FB), Alternative 2 (CTB), and Alternative 3 (GRRB)**

**User Costs:** The user costs include the cost of the roadway, which is comprised of vehicle operation cost (VOC), crash costs, and delay costs. The vehicle operating costs were not considered for the LCCA studies as it was expected that all the alternatives would provide a similar level of service throughout the design life. On the other hand, the user delay cost that will occur during construction, maintenance, and rehabilitation was high in terms of sustainability. The user delay cost may vary for different alternatives, as the amount of time required to prepare the base layer will not be the same. The user delay cost is estimated each year by the transportation agencies, and it is significantly different for different types of vehicles. The user delay costs estimated by TxDOT for the last five years are summarized in Table 36.

**Table 36 TxDOT User Costs from 2017 to 2021(TxDOT)**

| Year / Cost Element | 2017 | 2018 | 2019 | 2020 | 2021 |
|---|---|---|---|---|---|
| Passenger Car (USD/Vehicle hour) | 22.4 | 28.7 | 29.4 | 30.1 | 30.5 |
| Truck per hour (USD/Vehicle hour) | 32.7 | 36.3 | 39.5 | 41.3 | 41.9 |

The user costs were estimated based on the distribution of traffic, the number of lanes open to traffic, work zone capacity, work zone speed, queue dissipation capacity, working hours during maintenance, duration of maintenance work, and discount rate. The input required for the RealCost 2.5 software is listed in Table 37. A discount rate of 4% was taken based on the recommendation from Inti (2016), and other parameters were collected during the construction of the test section.

**Table 37 Software Inputs Required for User Cost Analysis**

| Parameters | Value |
|---|---|
| Annual Average Daily Traffic (AADT) | 10,000 |
| Percentage of cars in AADT | 89.4 |
| Percentage of the single-unit truck in AADT | 10.6 |
| Annual traffic growth rate | 0.75 |
| Discount rate | 4 |
| Number of lanes in each direction | 1 |
| Free-flow capacity (vphpl) | 2000 |
| Traffic distribution type | Urban |
| Queue dissipation capacity (vphpl) | 1818 |
| Maximum total AADT | 12,000 |
| Work hours | 9AM-5PM |
| Speed limit under normal operating conditions | 60 |
| Work zone speed limit (mph) | 40 |
| Work zone length (miles) | 2 |
| Num of lanes open in each direction | 2 |
| Maximum queue length (miles) | 5 |
| Work zone capacity (vphpl) | 1415 |

Note: vphpl-vehicle per hour per lane

#### 7.4.2.2 Probabilistic Approach

Probabilistic analyses were conducted to account for the variability of the discount rates, queue dissipation capacity, value of time for different types of vehicles, work zone capacity, and agency construction costs, as listed in Table 38.

**Table 38 Inputs Considered for Probabilistic Approach**

| Parameters | Probability distribution | Values | | | | | Remarks |
|---|---|---|---|---|---|---|---|
| | | Min. | M.L. | Max. | Avg. | S.D. | |
| Discount rate (%) | Triangular | 3 | 4 | 7 | - | - | Inti (2016) |
| Queue dissipation capacity (vphpl) | Normal | | | | 1818 | 144 | Greenroads Manual v1.5 |
| Value of time for passenger cars ($) | Triangular | 22.4 | 30.5 | 30.0 | | | Table 5 |
| Value of time for trucks ($) | Triangular | 33.7 | 41.0 | 41.9 | | | Table 5 |
| Work zone capacity (vphpl) | Normal | | | | 1415 | 200 | Inti (2016) |
| Agency construction cost (%) | Normal | | | | - | 10 | Assumed |

Notes:
vphpl – vehicle per hour per lane
Min. - minimum; M.L. – most likely; Max. – maximum; Avg. – Average; S.D. – standard deviation

### *7.4.3 LCCA Results Summary*

The purpose of these analyses was to select the best alternatives based on the overall life cycle cost. It is obvious from the results that alternative 1 (A1), utilizing traditional flex base material according to the AASHTO 1993 pavement design guideline, results in the maximum utilization of natural resources; the other alternatives contribute by either partially or totally replacing the natural resources. The application of a cement-treated base enhances the capacity and contributes to a higher activity period. Figure 97 shows that A1 will require rehabilitation in approximately 8 years, while A2 section does not need rehabilitation for approximately 12 years. The addition of geocells enhances the performance of pavement sections, and therefore less distress will be noted, and as a result, this section needs rehabilitation works for approximately 11 years.

The user delay costs for different sections vary due to the differences in the amount of time required to construct them. A1 is expected to be constructed in the least amount of time with fewer user delays, whereas a longer construction time is required for cement-treated base layers due to the additional time required for the curing process. It takes slightly longer to construct a GRRB than it does to construct a flex base aggregate section, and it takes approximately 20% extra time to install a geocell-reinforced base layer than it does to install a base layer without a geocell. This information was incorporated into the LCCA study, and the results obtained for both the deterministic and probabilistic approaches are shown in Table 39.

The deterministic approach showed that alternative 3 (A3) had the lowest agency cost, whereas alternative 1 (A1) had the lowest user cost. The agency cost and the user cost for alternative 2 (A2) were higher, as the money and time required to purchase and cure the cement increased the overall cost. The results obtained from the probabilistic analysis showed that the average agency cost for A1, A2, and A3 is \$402,500, \$404,200, and \$354,200, respectively. The average user cost for A1, A2, and A3 is \$3,300, \$10,800, and \$3,600, respectively. The standard deviations for both agency cost and user cost were found to be the lowest for A3.

**Table 39 LCCA Summary**

| Approach | Costs | | Cost per lane per mile ($1000) | | |
|---|---|---|---|---|---|
| | | | **A1 (FB)** | **A2 (CTB)** | **A3 (GRRB)** |
| Deterministic Approach | Agency | | 400.8 | 402.7 | 352.7 |
| | User | | 3.1 | 10.3 | 3.4 |
| Probabilistic Approach | Agency | Min. | 389.9 | 393.5 | 343.5 |
| | | Max. | 408.7 | 409.6 | 359.6 |
| | | Mean | 402.5 | 404.2 | 354.2 |
| | | S.D. | 4.1 | 3.5 | 3.5 |
| | User | Min. | 2.6 | 8.9 | 2.9 |
| | | Max. | 3.7 | 11.5 | 3.9 |
| | | Mean | 3.33 | 10.8 | 3.6 |
| | | S.D. | 0.2 | 0.5 | 0.2 |

Note:
Min. - minimum; Max. – maximum; Avg. – Average; S.D. – standard deviation

The cumulative probability plot for the agency cost and user cost is shown in Figure 100. The relative positions of the alternatives (A1, A2, and A3) change, as the rankings for an alternative for user costs, are 3, 1, and 2, respectively. The lowest user cost was observed for A1, and the highest user cost was observed for A3. These results will be helpful to designers and owners as they select the most effective alternative design option for pavement construction.

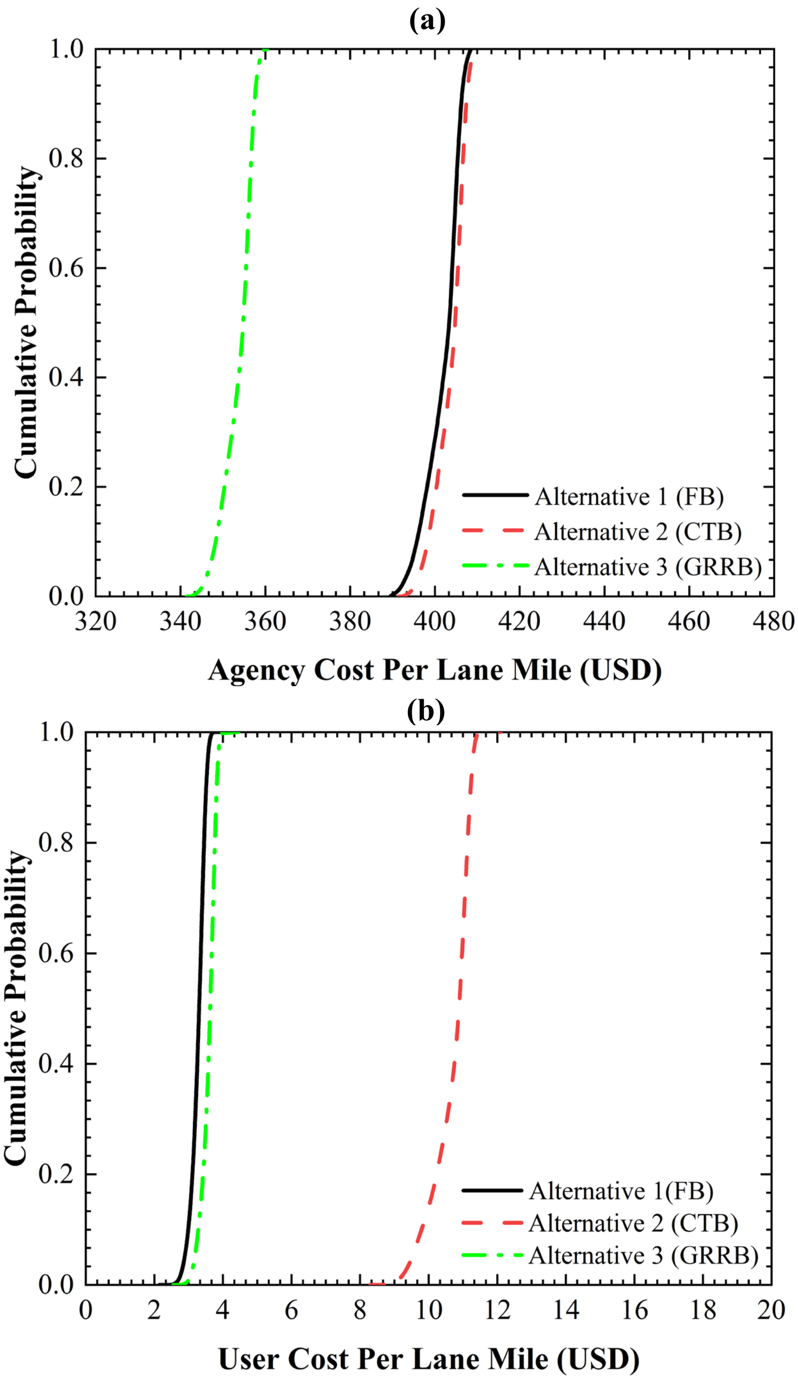

**Figure 100 Cumulative probability plots: a) agency cost, b) user cost**

The overall cost for alternative 3 (A3) is the lowest, and it should provide economic benefits. However, it is still necessary to evaluate the sustainable aspects of geocell-reinforced pavements. The next section provides a comprehensive sustainability analysis of GRRB sections, along with a flex base aggregate layer section and other base options that are typically used for supporting pavements built over expansive subgrades.

## 7.5 Life Cycle Sustainability Analyses (LCSA) of Geocell-Reinforced Pavement Sections

The application of geocells is economically advantageous; however, the environmental aspects should be explored before installing GRRB layers of pavement on expansive soils. Maximizing the utilization of RAP enhances the sustainability benefits, as it is predominantly reclaimed material, but the addition of an HDPE geocell layer, which is a polymeric-rich material, may have some negative environmental impacts. The overall performance and life cycle environment of the geocell-reinforced pavement should be assessed for the duration of the design period; otherwise, the only environmental issues that will be assessed may be ones that transpire from rehabilitation works that are needed due to the distress caused by expansive subsoils. The following section will discuss the methodology adopted for the environmental assessment.

### *7.5.1 Life Cycle Sustainability Assessment Approach*

Environmental impacts considered for a life cycle sustainability analysis are generally related to the production of raw materials, transport, construction of pavement, and end-of-life use. In this study, the scope of the environmental analysis was limited to the impacts associated with the raw material production, transport, construction, and design of the base materials for the three different alternatives discussed above. An excel-based software, PaLATE, was used to estimate the environmental impact of the flex base, cement-treated base, and RAP-based layers, but it did not have a database for the inclusion of the effects of geocells.

The environmental impacts associated with the production of geocells were assessed separately and then combined with the data obtained for the RAP base layer to determine the environmental impacts of the GRRB layer. The process, material, and energy required to produce a single panel of geocells are shown in Figure 101. One single geocell panel was produced from 13.5 lb. (6.14 kg) of HDPE sheets. The process, energy, and materials required to produce the geocells were collected from the manufacturer and HDPE production processes described by Treenate et al. (2017).

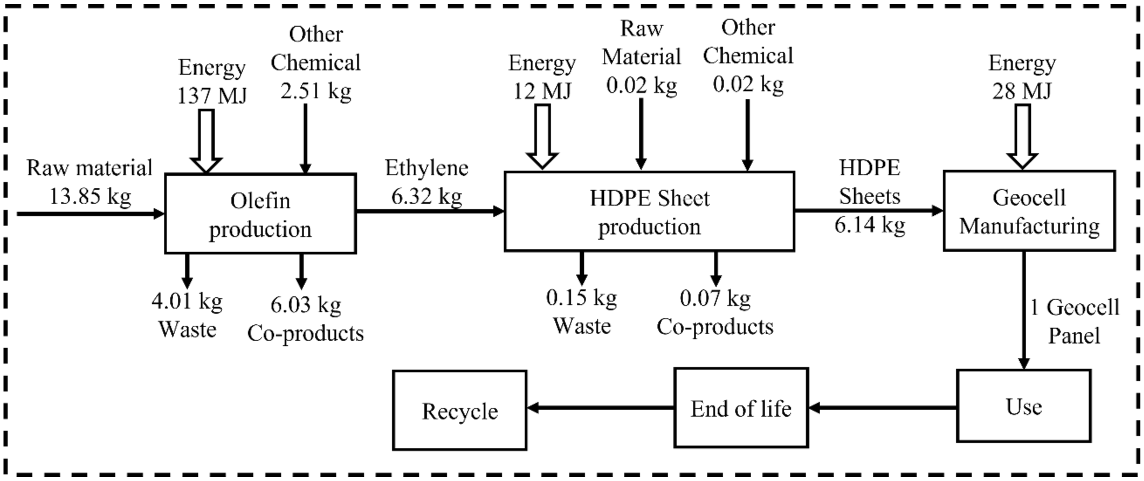

**Figure 101 System boundary for production of a geocell panel**

The environmental impacts caused by transporting the geocells from the manufacturing facility to the project site were estimated using PaLATE software and an average hauling distance of 100 miles. The following section will discuss the assessment of the environmental impacts and the results of the present analysis.

### *7.5.2 Life Cycle Sustainability Assessment Results*

The traditional approach to constructing flexible pavement is to utilize the flex base material as described for alternative 1 (A1). As it will not be readily available at the site, transporting it, especially if from a long distance, will have environmental impacts. Processing the raw material for the flex base will also have some negative impacts, as it uses natural resources. The addition of cement in alternative 2 (A2) will increase the capacity and enhance the longevity of the pavement; however, the environmental impact will be higher as the addition of 5% cement to the flex base material will have a severe negative impact on the carbon footprint.

Using RAP material alone is the most sustainable approach; however, it does not perform satisfactorily due to its excessive permanent deformation. The addition of geocells to RAP as described in alternative 3 (A3) enhances the capacity but will have negative impacts on the environment due to the emissions and energy costs associated with the polymeric manufacturing process. The HDPE used to produce geocells has a very low carbon black content (<1.5%). The environmental assessment results for different alternatives are summarized in Table 40.

**Table 40 Summary of Environmental Assessment Results for One-Lane Mile**

| **Alternatives** | A1 | A2 | - | A3 |
|---|---|---|---|---|
| **Base Type** | FB | CTB | RAP | Geocell+RAP |
| **Energy (GJ)** | 1712 | 2074 | 579 | 899 |
| **Water Consumption (kg)** | 177 | 234 | 3 | 47 |
| **$CO_2$ (Mg) = GWP** | 89 | 114 | 11 | 30 |
| **$NO_x$ (kg)** | 2,468 | 2,587 | 503 | 1,532 |
| **$PM_{10}$ (kg)** | 1,056 | 1,072 | 5 | 205 |
| **$SO_2$ (kg)** | 40,577 | 42,597 | 40,418 | 40,480 |
| **CO (kg)** | 227 | 227 | 14 | 100 |
| **Hg (g)** | 0.4 | 0.6 | 0.1 | 0 |
| **Pb (g)** | 30 | 41 | 1 | 10 |
| **RCRA HW (kg)** | 4,344 | 6,754 | 240 | 2,101 |
| **HTP (Cancer)** | 74,060 | 76,988 | 52,983 | 58,517 |
| **HTP (Non-cancer)** | 817,814,644 | 821,406,899 | 94,340,801 | 101,129,315 |

Notes:
FB- Flex base; CTB- Cement treated base; RAP- Reclaimed asphalt pavement.
$CO_2$ – Carbon dioxide; $NO_x$ – Nitric oxide; $PM_{10}$ – Particulate matter; $SO_2$ – Sulphur dioxide.
CO – Carbon monoxide; Hg – Mercury; Pb – lead;
RCRA HW - Resource Conservation and Recovery Act. Hazardous waste
HTP – Human Toxicity Potential

The amount of total energy required for the generation of $CO_2$ and water is significantly lower for geocell-reinforced pavement than for the other feasible alternatives. The overall performance of the three alternatives is presented in a radar chart format, as shown in Figure 102. There are 12 categories that are normalized with the values corresponding to alternative 1 (A1). An impact factor of one was assigned to each category under A1. The relative impact factors for A2 are greater than one; the impact relative factors for A3 are less than one.

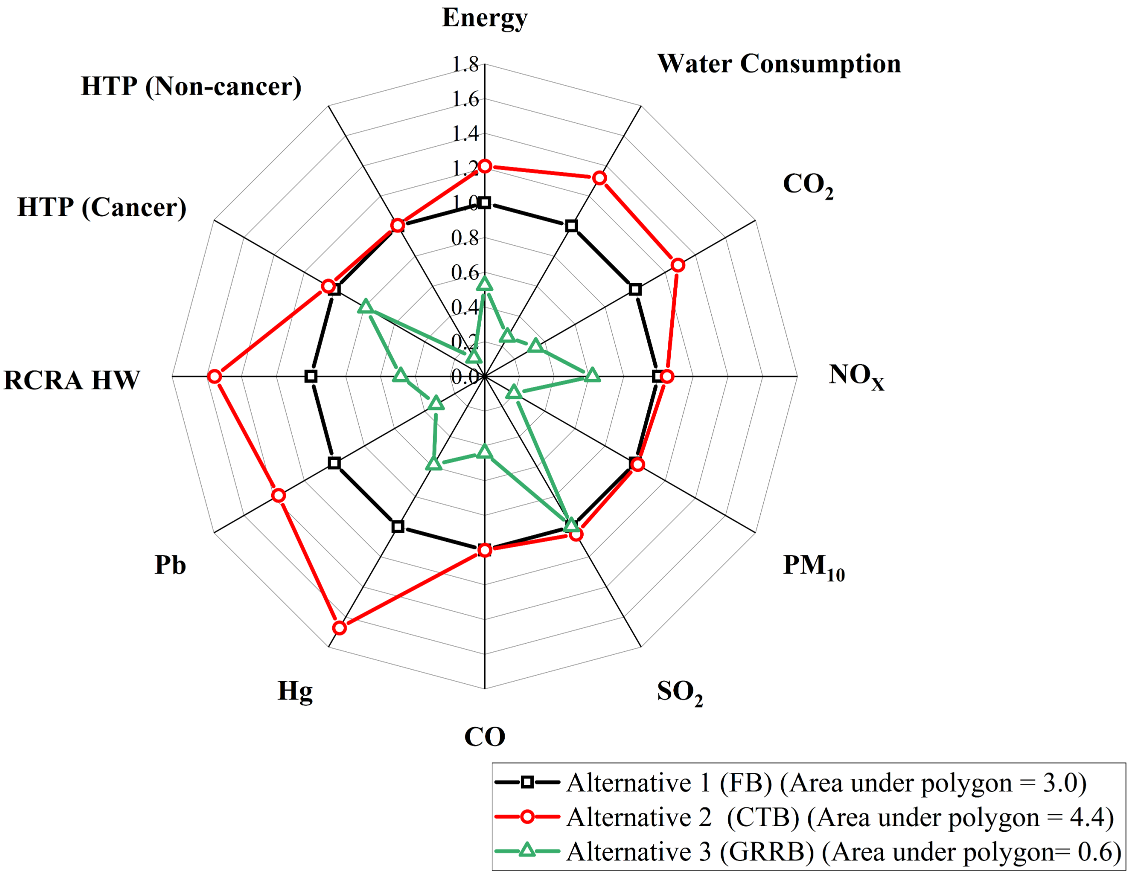

**Figure 102 Comparative Performance of Alternative 1 (FB), Alternative 2 (CTB), and Alternative 3 (GRRB)**

The best design alternative with the most sustainable practice solution is the one with the lowest area under the polygon. The length of each side of the polygon was used to measure the area for A1, A2, and A3 and resulted in measurements under the polygon of 3.0 for A1, 4.4 for A2, and 0.6 for A3. It can, therefore, be concluded that A3 has the lowest environmental impact and is the most sustainable option. The difference in the generation of $CO_2$ may be used to quantify the benefits. The selection of A3 over A1 will reduce the generation of $CO_2$ by 59 tons for each lane mile. According to the EPA, a reduction of 59 tons of $CO_2$ from the environment is equivalent to recycling 20.1 tons of waste, recycling the waste in 2.9 garbage trucks, and recycling 2510 trash bags of waste rather than sending all of it to the landfill (Figure 103).

**Figure 103 Environmental impact of replacing traditional flex base with GRRB for the single-lane mile (estimated based on EPA guidelines)**

The above analysis shows that a flexible pavement with a GRRB layer provides an excellent sustainable solution for building pavement sections with GRRB with RAP layers on expansive subgrade conditions. The pavements with GRRB layers provided the best performance in both LCCA and LCSA studies and hence are recommended for designing sustainable and resilient pavements on expansive subsoil conditions.

## 7.6 Summary

The design of flexible pavement with geocell layers allows the pavement designer to choose the reclaimed material for the base layer application, which is essential to the design of low-distress pavements on expansive soil. The confinement offered by the geocell enhances the performance of the geocell-reinforced base layer, which in turn provides stable and uniform support to pavements with less rutting and reflective and other types of cracking. The data obtained from the parametric study were used to develop the design charts for selecting the thickness of the GRRB layers of flexible pavements. This chapter also discussed the pavement design procedures of the

AASHTO and MEPDG approaches. The feasibility of the current stabilization method with geocells was further assessed by comparing it with other alternatives based on the LCCA and LCSA study analyses. The major outcomes from developing designs that incorporate geocells and LCCA and LCSA are summarized below.

- The design life of pavements built on expansive subsoil is significantly enhanced with the addition of geocells in the base layer. The design life improvement factor (*DIF*) was introduced, which can be used to predict the total number of *ESAL*s with the GRRB layer.

- The calibrated design life improvement factor was further used to determine the increase in structural capacity due to the addition of a geocell layer. A design methodology was proposed, based on AASHTO 1993, to determine the layer coefficient of the GRRB layer, which can be further used to determine the overall thickness of the pavement layers.

- The resilient modulus parameters and damage model parameters estimated from this study can be directly used for the mechanistic-empirical (M-E) design approach.

- The cost of constructing the GRRB was estimated and compared with other possible alternatives, and it was found that replacing the traditional flex-base layer with a GRRB layer is cost-efficient for the agency. The initial performance of the cement-treated base was the best in terms of structural performance; however, the overall life cycle cost for this alternative was the highest. Both the deterministic and probabilistic approaches to the LCCA study showed that alternative 3 (A3) with GRRB had the lowest agency cost.

- The application of geocells with RAP in the pavements also provided a sustainable solution to replacing the traditional flex base layer with GRRB and will reduce the $CO_2$ emission by 59 tons for each lane mile.

It should be noted that some of these analyses are performed for the first time on geocell bases, and hence one should expect some changes as these analyses and their attributes get developed and validated in the near future. Nevertheless, the analyses and studies provide salient benefits of using these geocells for cost-effective field applications with high sustainability.

# CHAPTER VIII

# CONCLUSIONS, RECOMMENDATIONS, AND FUTURE WORKS

## 8.1 Overview

The primary focus of the current dissertation research was to provide a sustainable and long-term, cost-effective solution for flexible pavement structures, which suffer from distresses due to the presence of expansive subgrade soils. The study is based on the results of comprehensive field and numerical investigations and aims to identify the potential benefit of utilizing a geocell-reinforced RAP base (GRRB) layer to mitigate the distresses associated with the problematic expansive soil conditions. The scope of the study was limited to one subgrade soil condition with high swelling potential. The base layer was prepared with geocells, which allowed the utilization of 100% RAP material as infill material within the Geocell. The field sections were constructed over an existing farm-to-market road (FM 1807) that was built over expansive subgrade soil. This existing road sections suffered from rutting, longitudinal cracking, and shoulder depressions due to the presence of the expansive subgrade.

The field monitoring of the reinforced test sections constructed over such a harsh environment revealed that the geocells helped restrict the differential movements of the pavement foundation by distributing the load over a wider area. In addition to the regular field monitoring, nondestructive tests were conducted to evaluate the structural performance of the pavement sections. The material parameters estimated from the field study were used to generate numerical models with ABAQUS/CAE. The parametric study conducted with the numerical method was used to develop design charts for the geocell-reinforced pavement. The choice of flexible pavement with GRRB was further assessed with the LCCA study by comparing its life cycle cost with other feasible alternatives.

## 8.2 Conclusions

The four major tasks of this study were interconnected, and the major conclusions reached by completing various tasks are discussed in the following section.

### *8.2.1 Construction and Field Monitoring*

The test sections were constructed and instrumented with shape array accelerometers (SAAs) and earth pressure cells (EPCs) to monitor the vertical deformations and vertical stresses over time. They were also used to monitor rutting and cracking for a period of 30 months, and profiler tests were conducted 21 and 30 months after test section construction. The outcomes of the construction and monitoring activities are summarized below.

- It takes 20% longer time to construct a GRRB than it takes to construct a traditional flex base layer, as it takes 975 square feet per hour to install the geocell. The same equipment used for the construction of the traditional base layer was used for the construction of the GRRB layer, and no additional equipment was required for the installation of the geocells.
- The maximum permanent deformations recorded under the GRRB layers of RS1, RS1, and RS3 were 0.11, 0.07, and 0.14 inches, respectively, and these are

corresponded to the $c_t/h_{gc}$ values of 0.50, 0.33, and 0.67. The lowest $c_t/h_{gc}$ showed better performance in terms of deformation under the GRRB layers.

- *IRI* values measured for RS1, RS2, RS3, and CS for the year 2020 were 219.2, 108.7, 113.8, and 78.1, respectively. *IRI* values for RS1, RS2, RS3, and CS for the year 2021were 215.8, 101.9, 123.2, and 98.4, respectively. The rate of change of the *IRI* was lower for all the reinforced sections, which indicates that the base layer was in a stable condition.
- Based on the field monitoring data, the GRRB can reduce the average vertical stresses on subgrades by 50%, which also helps reduce the average permanent deformation by 36%.

### *8.2.2 Nondestructive Field Testing*

Nondestructive studies, including the FWD and APLT methods, were conducted for different test sections and revealed their overall structural conditions. The resilient responses collected from the tests were used to determine the moduli of the GRRB layers. The major outcomes from the FWD and APLT testing are listed below:

- The average elastic modulus of the combined base layers of the reinforced sections (RS1 with 6 in. GRRB layer, RS2 with 8 in. GRRB layer, and RS3 with 12 in GRRB layer) varied from 56 to 67 ksi and varied from 30 to 90 ksi for the CS sections. The estimated additional confinement offered by the geocells located in RS1, RS2, and RS3 were 9.0, 7.5, and 10.5 psi, which helped to increase the moduli of the 6-inch, 8-inch, and 12-inch GRRB layers by 50.8%, 73.1%, and 88.3%, respectively.

- The increase in frequency from 0.1 Hz to 2.0 Hz decreased the resilient deformations for RS1, RS2, and RS3 by 23.8, 25.8, and 27.8%, respectively. The increase in the thickness of the GRRB layer helped to improve the performance.
- The predicted modulus for the 6-inch, 8-inch, and 12-inch GRRB layers under single wheel loading (80 psi) was 37, 70, and 82 ksi, respectively. The increase in the thickness of the GRRB layer helped increase the overall resilience performance of the base layer.
- Permanent deformation models that corresponded to 100 psi vertical stresses to predict the remaining life of the pavement sections were developed for RS1, RS2, and RS3 sections, respectively. The remaining rut-life of the RS1, RS2, and RS3 sections was estimated as 3.2, 9.8, and 29.8 million, respectively.

### *8.2.3 Numerical Study*

The purpose of the numerical study was to investigate the cross-anisotropic behavior of the reinforced base layer. The field data obtained from the nondestructive FWD testing were used to validate the pavement response model. The response model was further used for the parametric studies. The major outcomes from the numerical study are listed below:

- The estimated modular ratios for the 6-, 8- and 12-inch GRRB layers were 3.5, 6.5, and 5, respectively. The magnitude and trend of deflection bowls obtained from the numerical study were in good agreement with the NDT testing results.
- The increase in the thickness of the GRRB layer from 6 inches to 8 inches helped reduce the vertical stress by 24% and the vertical compressive strain on the

subgrade by 36%. The estimated reductions in the vertical stress due to 6-, 8-, and 12-inch GRRB layers were 19.5, 29.0, and 43.0%, respectively, when compared to the unreinforced section.

- According to the Asphalt Institute method, the estimated traffic benefit ratios for the RS1, RS2, and RS3 sections are 2.6, 5.4, and 22.9, respectively. A geocell is beneficial when the subgrade capacity is low.

### *8.2.4 Development of Design Methodology and LCCA*

The design methodology developed for geocell-reinforced flexible pavements will help pavement engineers select the appropriate thickness of the base layer. This study also provides LCCA evaluation for geocell-reinforced pavements, along with other alternatives that can be compared for their economic feasibility. The major outcomes are listed below.

- The design life improvement factor (*DIF*) was introduced and can be used to estimate the *EASL* carrying capacity of geocell-reinforced sections. Pavement designers can choose the appropriate thickness of the base layer based on the design volume of traffic.
- The design approach with the AASHTO method was proposed with the *DIF* value which is dependent on geocell layer thickness. The current M-E design method requires a stress-dependent resilient modulus model and parameters for damage models. The associated model parameters for the GRRB layers were determined from the current field study.

- The unit costs of 4-inch and 6-inch geocells are \$4.50 and \$6.75 per square yard (SY), respectively. The overall unit cost for the RAP materials is \$7.00 per SY for an 8-inch-thick section, resulting in a total cost of \$13.75 per SY. The cost of materials for an 8-inch-thick traditional flex base section is \$16.90 per SY, which is 22.9% more than the material cost for an 8-inch thick GRRB layer.
- The life cycle sustainability analysis showed that replacing a traditional base layer with a GRRB layer reduces the $CO_2$ production by 59 tons for each lane mile, which is equivalent to recycling, rather than landfilling, 2510 bags of trash.

## 8.3 Recommendations

The following recommendations are suggested for the efficient use of geocells in pavement base layers, and these are based on the knowledge gained from the current field study.

- Geocells are beneficial for thinner asphalt pavement (<3 inch), as the load transfer underneath the geocell layer is significant.
- When faced with selecting the appropriate alternative, designers should conduct LCCA studies, as proposed in this study.
- The geocell panel should extend 3 ft. beyond the projected location of the wheel paths. A traffic management plan is required, as closing an additional lane will provide better access and a better working environment for filling up the infill base material from the shorter or longer side of the pavement lane.
- The three-parameter model and damage model parameters estimated from the field study can be used for the M-E design of flexible pavement with GRRB.

- The design methodology developed in this study can be used for choosing the appropriate thickness of the GRRB layer by estimating the *DIF* values. However, more field pavement sections with GRRBs will enhance the proposed methodology in the future.

## 8.4 Limitations

This study was based on a field evaluation of geocell-reinforced test sections constructed over expansive subgrade soil. The study's limitations are listed below.

- Only one type of HDPE geocell was considered, and the effects of stiffness of the geocell material were not included in the scope of this study.
- The geocell reinforcements were placed within the eastbound lane, and it was not possible to extend them beyond the centerline of the road.
- Moisture content changes within the subgrade soil were not studied, although the rainfall data collected from the nearby weather station was used to understand the fluctuations in the level of moisture contents within the subsoil.
- FWD tests were conducted for only two seasons, and further tests are needed to understand the performance of the base material under different climatic conditions.
- The APLT tests were conducted for 504 cycles; a higher number of load cycles is needed to develop more reliable rutting models.

The LCCA conducted under this study was limited to the available information and future predictions. Long-term pavement performance data are required for a comprehensive LCCA study. Similarly, the sustainability analysis presented here is preliminary and has scope for improvements in the future with the development of more sustainability methods and tools.

## 8.5 Future Work

This study presented the performance of RAP material with cellular type confinement. Future research on this topic should be conducted in the following areas.

- Large-scale repeated load testing should be conducted under different subgrade conditions to study the effects of geocell reinforcement,
- APLT tests should be conducted for at least 10,000 cycles under field conditions to develop a comprehensive model that can predict the total rut depth.
- A stress-dependent cross-anisotropic three-dimensional material model could be developed to study the effects of confinement with numerical analysis.
- The effect of the cover thickness on top of the geocell layer could be studied under repeated loading conditions.

## 8.6 Summary

This study presents the effective utilization of 100% RAP material for the construction of a flexible pavement base layer with geocell reinforcement over expansive subgrade conditions. Major findings of the current study are summarized below.

- Lab and field monitoring studies showed that the GRRB helped to reduce the average vertical stress by 50% and reduce subgrade heaving by 36%, which indicates an effective stabilization on expansive subgrades. Rutting of the GRRB layer depends on the cover thickness to height ratio of the geocell layer, and the structural performance of the GRRB layer depends on the thickness of the geocell layer. The structural layer coefficient of the GRRB layer is significantly higher than that of the unreinforced base layer.

- Cracking distress was not observed in the test sections which is attributed to the tensile strengths of Geocell layers as they will provide resistance to any movements from underlying expansive soil conditions.
- The back-calculated in-situ elastic modulus of the base layer from the nondestructive field studies showed improved performance of GRRB sections over flex bases. APLT studies showed low permanent deformation in GRRB layers due to the confinement and reinforcement effect of the geocell.
- Numerical studies showed that the GRRB layer increased bearing capacity and reduced stresses and deformations in underlying layers. Parametric analysis showed geocell enhances structural support.
- LCCA and sustainability study showed that the GRRB had provided cost-effective and sustainable solutions when supporting pavements in expansive soils. Additional time required for the construction of GRRB is not significant, and no additional equipment is required.

Overall, based on comprehensive data collection and analysis on lab and field studies as well as numerical and LCCA & Sustainability studies presented in this research, it is concluded that – “Geocell Reinforced RAP Base (GRRB) offer better support to flexible pavements leading to resilient and sustainable flexible pavement designs on expansive soil subgrade conditions”.

# REFERENCES

Abaza, K. A. (2004). Deterministic Performance Prediction Model for Rehabilitation and Management of Flexible Pavement. *International Journal of Pavement Engineering*, *5*(2), 111–121. https://doi.org/10.1080/10298430412331286977

Al-Omari, B., & Darter, M. I. (1994). Relationships between international roughness index and present serviceability rating. *Transportation Research Record*, *1435*, 130–136.

Al-Qadi, I. L., & Hughes, J. J. (2000). Field evaluation of geocell use in flexible pavements. *Transportation Research Record*, *1709*(1), 26–35. https://doi.org/10.3141/1709-04

Arvin, M. R., Rezaei, E., & Bahmani S., M. (2018). Numerical evaluation of geocell-reinforced flexible pavements under traffic loads. *Scientia Iranica*, *25*(2), 493–504. https://doi.org/10.24200/sci.2017.4191

ASTM. (2015). Standard Test Method for Deflections with a Falling-Weight-Type Impulse Load Device. *ASTM International*, *D4694-09*(Reapproved 2020). https://doi.org/10.1520/D4694-09R20

Attia, M., & Abdelrahman, M. (2011a). Effect of state of stress on the resilient modulus of base layer containing reclaimed asphalt pavement. *Road Materials and Pavement Design*, *12*(1), 79–97. https://doi.org/10.1080/14680629.2011.9690353

Babashamsi, P., Yusoff, N. I. M., Ceylan, H., Nor, N. G. M., & Jenatabadi, H. S. (2016). Evaluation of pavement life cycle cost analysis: Review and analysis. *International Journal of Pavement Research and Technology*, *9*(4), 241–254. https://doi.org/10.1016/j.ijprt.2016.08.004

Bathurst, R. J., & Karpurapu, R. (1993). Large-Scale Triaxial Compression Testing of Geocell-Reinforced Granular Soils. *Geotechnical Testing Journal*, *16*(3), 296–303. https://doi.org/10.1520/GTJ10050J

Beatty, T. (2002). Life-Cycle Cost Analysis Primer Life-Cycle Cost Analysis Primer. U.S. Department of Transportation.

Bennert, T., Papp, J., Maher, A., & Gucunski, N. (2000). Utilization of construction and demolition debris under traffic-type loading in base and subbase applications. *Transportation Research Record*, *1714(1)*, 33–39. https://doi.org/10.3141/1714-05

Biswas, N., & Ghosh, P. (2017). Bearing Capacity Factors for Isolated Surface Strip

Footing Resting on Multi-layered Reinforced Soil Bed. *Indian Geotechnical Journal*, 49(1), 1–13. https://doi.org/10.1007/s40098-017-0293-z

Biswas, N., Puppala, A. J., Khan, M. A., Congress, S. S. C., Banerjee, A., & Chakraborty, S. (2021). Evaluating the Performance of Wicking Geotextile in Providing Drainage for Flexible Pavements Built over Expansive Soils. *Transportation Research Record: Journal of the Transportation Research Board*. https://doi.org/10.1177/03611981211001381

Bozyurt, O., Tinjum, J. M., Son, Y.-H., Edil, T. B., & Benson, C. H. (2012). Resilient Modulus of Reclaimed Asphalt Pavement and Reclaimed Concrete Aggregate. *GeoCongress 2012*, 3901–3910. https://doi.org/10.1061/9780784412121.400

Cable, J. K., Klaiber, F. W., & Lee, D. Y. (1988). *Pavement Instrumentation*.

Christopher, B. R., Schwartz, C., & Boudreau, R. (2006). *Geotechnical Aspects of Pavements*. (No. *FHWA NHI-05-037*). https://www.fhwa.dot.gov/engineering/geotech/pubs/05037/05037.pdf

Copeland, A. (2011). *Reclaimed Asphalt Pavement in Asphalt Mixtures: State of the Practice*. (No. FHWA-HRT-11-021). https://doi.org/10.1016/j.proeng.2016.06.119

Das, J. T., Banerjee, A., Chakraborty, S., & Puppala, A. J. (2018). *A Framework for Assessment of Sustainability and Resilience in Subgrade Stabilization for a High-Volume Road*. In Transportation Research Board, 97th Annual Meeting, Washington, D.C.

Das, J. T., Banerjee, A., Puppala, A. J., & Chakraborty, S. (2019). Sustainability and Resilience in Pavement Infrastructure. *Environmental Geotechnics*, 1–13. https://doi.org/10.1680/jenge.19.00035

Dash, S. K., Sireesh, S., & Sitharam, T. G. (2003). Behaviour of geocell-reinforced sand beds under circular footing. *Proceedings of the Institution of Civil Engineers - Ground Improvement*, *7*(3), 111–115. https://doi.org/10.1680/grim.2003.7.3.111

Dash, S. K. (2010). Influence of Relative Density of Soil on Performance of Geocell-Reinforced Sand Foundations. *Journal of Materials in Civil Engineering*, *22*(5), 533–538. https://doi.org/10.1061/(asce)mt.1943-5533.0000040

Dash, S. K., Rajagopal, K., & Krishnaswamy, N. R. (2001). Strip footing on geocell reinforced sand beds with additional planar reinforcement. *Geotextiles and Geomembranes*, *19*(8), 529–538. https://doi.org/10.1016/S0266-1144(01)00022-X

Dash, S. K., Rajagopal, K., & Krishnaswamy, N. R. (2007). Behaviour of geocell-reinforced sand beds under strip loading. *Canadian Geotechnical Journal*, *44*(7), 905–916. https://doi.org/10.1139/t07-035

Dash, S. K. Saikia, R., & Nimbalkar, S. (2019). *Contact Pressure Distribution on Subgrade Soil Underlying Geocell Reinforced Foundation Beds*. *5*, 1–8. https://doi.org/10.3389/fbuil.2019.00137

Dash, S. K. Sireesh, S., & Sitharam, T. G. (2003). Model studies on circular footing supported on geocell reinforced sand underlain by soft clay. *Geotextiles and Geomembranes*, *21*(4), 197–219. https://doi.org/10.1016/S0266-1144(03)00017-7

Dessouky, S. H., Ho, Oh, J., Yang, M., Ilias, M., Lee, I. S., Freeman, T., Bourland, M., & Jao, M. (2012). *Pavement Repair Strategies For Selected Distresses In Fm Roadways* (No. FHWA/TX-11/006589-1). Texas Transportation Institute

Dutta, S., & Mandal, J. N. (2016). *Model Studies on Geocell-Reinforced Fly Ash Bed Overlying Soft Clay*. *28*(2), 1–13. https://doi.org/10.1061/(ASCE)MT.1943-5533.0001356

Edil, T. B., Benson, C. H., & Mengelt, M. (2006). Resilient modulus and plastic deformation of soil confined in a geocell. *Geosynthetics International*, *13*(5), 195–205. https://doi.org/10.1680/gein.2006.13.5.195

Meininger, R. C. & Stokowski, S. J. (2011) *Wherefore Art Thou Aggregate Resources for Highways?* https://www.fhwa.dot.gov/publications/publicroads/11septoct/06.cfm

George, A. M. (2018). Utilization of geocell-reinforced rap material base layer in flexible pavements: experimental and numerical studies. The University of Texas at Arlington, Arlington, Texas

George, A. M., Banerjee, A., Puppala, A. J., & Saladhi, M. (2019). Performance evaluation of geocell-reinforced reclaimed asphalt pavement (RAP) bases in flexible pavements. *International Journal of Pavement Engineering*, 1–11. https://doi.org/10.1080/10298436.2019.1587437

Giroud, J. P., & Han, J. (2004a). Design Method for Geogrid-Reinforced Unpaved Roads. II. Calibration and Applications. *Journal of Geotechnical and Geoenvironmental Engineering*, *130*(8), 787–797. https://doi.org/10.1061/(ASCE)1090-0241(2004)130:8(787)

Giroud, J. P., & Han, J. (2004b). Design Method for Geogrid-Reinforced Unpaved Roads . I . Development of Design Method. *Journal of Geotechnical and Geoenvironmental Engineering*, *130*(8), 775–786. https://doi.org/10.1061/(ASCE)1090-0241(2004)130:8(775)

Gogoi, R., Das, A., & Chakroborty, P. (2020). Rut depth measurement of an asphalt pavement from its original profile. *Australian Journal of Civil Engineering*, 18(2):119–125. https://doi.org/10.1080/14488353.2020.1742024

Gu, F., Luo, X., Luo, R., Hajj, E. Y., & Lytton, R. L. (2017). A mechanistic-empirical approach to quantify the influence of geogrid on the performance of flexible pavement structures. *Transportation Geotechnics*, *13*, 69–80. https://doi.org/10.1016/j.trgeo.2017.08.005

Gu, F., Luo, X., Zhang, Y., Lytton, R., & Sahin, H. (2016). Modeling of unsaturated granular materials in flexible pavements. In *E3S Web of Conferences*. EDP Sciences.

Gungor, O. E., Al-Qadi, I. L., Gamez, A., & Hernandez, J. A. (2017). Development of adjustment factors for MEPDG pavement responses utilizing finite-element analysis. *Journal of Transportation Engineering*, *143*(7), 1–10. https://doi.org/10.1061/JTEPBS.0000040

Han, J., Thakur, J. K., Parsons, R. L., Pokharel, S. K., Leshchinsky, D., & Yang, X. (2013). A summary of research on geocell-reinforced base courses. In H. J. and T. F. Ling H, Gottardi G, Cazzuffi D (Ed.), *Design and Practice of Geosynthetic-Reinforced Soil Structures* (Issue October 2013, pp. 331–340). https://doi.org/10.13140/RG.2.1.4185.7129

Han, J., Acharya, B., Thakur, J. K., & Parsons, R. L. (2012). *Onsite Use of Reclaimed Asphalt Pavement Materials and Geocells to Reconstruct Pavements Damaged by Heavy Trucks* (No. 25-1121-0001-462). Mid-America Transportation Center.

Hegde, A. M., & Sitharam, T. G. (2015). Effect of infill materials on the performance of geocell reinforced soft clay beds. *Geomechanics and Geoengineering: An International Journal*, *10*(3), 163–173. https://doi.org/10.1080/17486025.2014.921334

Hegde, A., & Sitharam, T. G. (2015). Joint strength and wall deformation characteristics of a single-cell geocell subjected to uniaxial compression. *International Journal of Geomechanics*, *15*(5), 1–8. https://doi.org/10.1061/(ASCE)GM.1943-5622.0000433

Hegde, A., & Sitharam, T. G. (2016). Behaviour of geocell reinforced soft clay bed subjected to incremental cyclic loading. *Geomechanics and Engineering*, *10*(4), 405–422. https://doi.org/10.12989/gae.2016.10.4.405

Hoffman, M. S., & Thompson, M. R. (1982). Backcalculating nonlinear resilient moduli from deflection data. *Transportation Research Record*, *852*(852), 42–51. http://onlinepubs.trb.org/Onlinepubs/trr/1982/852/852-006.pdf

Hong, G. T., Bulut, R., Aubeny, C. P., Jayatilaka, R., & Lytton, R. L. (2006). Design model for roughness and serviceability of pavements on expansive soils. *Transportation Research Record*, *1967*, 103–111. https://doi.org/10.1177/0361198106196700111

Hoppe, E. J., Lane, D. S., Fitch, G. M., & Shetty, S. (2015). *Feasibility of Reclaimed Asphalt Pavement (RAP) Use As Road Base and Subbase Material* (No. VCTIR 15-R6). Virginia Center for Transportation Innovation and Research. https://insights.ovid.com/crossref?an=00042192-200916020-00009

Horak, E. (2007). Surface moduli determined with the falling weight deflectometer used as benchmarking tool. *26th Annual Southern African Transport Conference: The Challenges of Implementing Policy*. Pretoria, South Africa.

Hoyos, L. R., Puppala, A. J., & Ordonez, C. A. (2011). Characterization of Cement-Fiber-Treated Reclaimed Asphalt Pavement Aggregates: Preliminary Investigation. *Journal of Materials in Civil Engineering*, *23*(7), 977–989.

Huang, Y. H. (2004). *Pavement analysis and design* (2nd ed.). Pearson Prentice Hall.

Inti, S. (2016). *A decision making approach for selection of sustainable (LCCA), life cycle assessment (LCA) of environmental and social impacts*. The University of Texas at El Paso.

Khan, M. A., Hossain, M. S., Khan, M. S., Samir, S., & Aramoon, A. (2017). Impact of wet-dry cycles on the shear strength of high plastic clay based on direct shear testing. *Geotechnical Special Publication*, *GSP 280*, 615–622. https://doi.org/10.1061/9780784480472.065

Khan, M. A., Biswas, N., Banerjee, A., & Puppala, A. J. (2020). Field performance of geocell reinforced reclaimed asphalt pavement base layer. *Transportation Research Record: Journal of the Transportation Research Board*, *2674*(3), 69–80. https://doi.org/10.1177/0361198120908861

Khan, M. A. Nripojyoti, B., Banerjee, A., & Puppala, A. J. (2020). Performance of Geocell-Reinforced Reclaimed Asphalt Pavement (RAP) Bases in Flexible Pavements Built on Expansive Soils. *In Geo-Congress 2020: Geotechnical Earthquake Engineering and Special Topics* (pp 488–497). https://doi.org/10.1061/9780784482810.051

Kief, O., Schary, Y., & Pokharel, S. K. (2015). High-modulus geocells for sustainable highway infrastructure. *Indian Geotechnical Journal*, *45*(4), 389–400. https://doi.org/10.1007/s40098-014-0129-z

Kief, O. (2015). Structural Pavement Design with Geocells made of Novel Polymeric

Alloy. In *Proc., 2015 Geosynthetics Conference, Portland, Oregon* (pp. 1-10).

Kief, O., & Rajagopal, K. (2008). Three dimensional cellular confinement system contribution to structural pavement reinforcement. *Geosynthetics India*, *January*, 1–12.

Kim, W., & Labuz, J. (2007). *Resilient Modulus And Strength Of Base Course With Reclaimed Bituminous Material* (No. Mn/DOT 2007-05). Minnesota Department of Transportation. https://conservancy.umn.edu/handle/11299/5567

Kumar, V., & Saride, S. (2016). Rutting Behavior of Geocell Reinforced Base Layer Overlying Weak Sand Subgrades. *Advances in Transportation Geotechnics*, *143*, 1409–1416. https://doi.org/10.1016/j.proeng.2016.06.166

Li, C., Ashlock, J. C., Lin, S., & Vennapusa, P. K. R. (2018). In situ modulus reduction characteristics of stabilized pavement foundations by multichannel analysis of surface waves and falling weight deflectometer tests. *Construction and Building Materials*, *188*, 809–819. https://doi.org/10.1016/j.conbuildmat.2018.08.163

Little, D. N., Allen, D. H., & Bhasin, A. (2018). *Modeling and Design of Flexible Pavements and Materials*. Berlin: Springer. https://doi.org/10.1007/978-3-319-58443-0

Lowry, G., & Costello, T. J. (2016). *Texas Road Finance (Part I)*. https://comptroller.texas.gov/economy/fiscal-notes/2016/may/road-finance.php

Luo, X., Gu, F., Zhang, Y., Lytton, R. L., & Zollinger, D. (2017). Transportation Geotechnics Mechanistic-empirical models for better consideration of subgrade and unbound layers influence on pavement performance. *Transportation Geotechnics*, *13*, 52–68. https://doi.org/10.1016/j.trgeo.2017.06.002

Lytton, R., Luo, X., Saha, S., Chen, Y., Deng, Y., Gu, F., & Ling, M. (2019). *Proposed Enhancements to Pavement ME Design: Improved Consideration of the Influence of Subgrade and Unbound Layers on Pavement Performance* (No. NCHRP Project 01-53). https://doi.org/10.17226/25583

Lytton, R. (1989). Backcalculation of Pavement Layer Properties. In *Nondestructive Testing of Pavements and Backcalculation of Moduli*. ASTM International. https://doi.org/10.1520/stp19797s

Lytton, R., Aubeny, C., & Bulut, R. (2004). Design Procedure for Pavements on Expansive Soils: Volume 2 (FHWA Report No. 0-4518-1 Vol. 2). *Texas Deparment of Transportation*.

M. Pierce, L., Bruinsma, J. E., Smith, K. D., Wade, M. J., Chatti, K., & Vandenbossche,

J. M. (2009). *Using falling weight deflectometer data with mechanistic-empirical design and analysis, volume III: Guidelines for deflection testing, analysis, and interpretation (No. FHWA-HRT-16-011).* United States. Federal Highway Administration.

Machan, G., & Bennett, V. G. (2008). Use of Inclinometers for Geotechnical Instrumentation on Transportation Projects. In *Transportation Research Circular* (E-C129). https://doi.org/10.17226/23074

Mamatha, K. H., & Dinesh, S. V. (2017). Performance evaluation of geocell-reinforced pavements. *International Journal of Geotechnical Engineering*, *13*(3), 277–286. https://doi.org/10.1080/19386362.2017.1343988

Mandal, J. N., & Gupta, P. (1994). Stability of geocell-reinforced soil. *Construction and Building Materials*, *8*(1), 55–62. https://doi.org/10.1016/0950-0618(94)90009-4

Mengelt, M. J., Edil, T. B., & Benson, C. H. (2000). Reinforcement of flexible pavements using geocells. In *Geotechnical Engineering Report 00-04*, *Department of Civil and Environmental Engineering, University of Wisconsin-Madison, Madison, Wisconsin*. https://doi.org/10.1109/ROBOT.2009.5152690

Mhaiskar, S. Y., & Mandal, J. N. (1996). Investigations on soft clay subgrade strengthening using geocells. *Construction and Building Materials*, *10*(4), 281–286. https://doi.org/10.1016/0950-0618(95)00083-6

Michalak, C. H., & Scullion, T. (1995). *MODULUS 5.0: User's Manual*.

Nazzal, M., & Mohammad, L. (2011). Estimation of Resilient Modulus of Subgrade Soils Using Falling Weight Deflectometer. *Transportation Research Record: Journal of the Transportation Research Board*, *2186(1)*, 1–10. https://doi.org/10.3141/2186-01

Nelson, J. D., & Miller, D. J. (1997). *Expansive soils : problems and practice in foundation and pavement engineering*. John Wiley & Sons.

Norouzi, M., Pokharel, S. K., & Breault, M. (2019). Geocell-Reinforced Pavement Structure State of Practice in Canada. *AC-ITS Canada Joint Conference*, 1–19.

Paterson, W. D. O. (1986). International Roughness Index: Relationship To Other Measures of Roughness and Riding Quality. *Transportation Research Record*, *8*, 49–59.

Pedarla, A., Puppala, A. J., Savigamin, C., & Yu, X. (2015). Performance of Sand-Treated Clay Subgrade Supporting a Low-Volume Flexible Pavement. *Transportation Research Record: Journal of the Transportation Research Board*, *2473*(1), 91–97. https://doi.org/10.3141/2473-11

Pokharel, S. K., Han, J., Leshchinsky, D., & Parsons, R. L. (2018). Experimental evaluation of geocell-reinforced bases under repeated loading. *International Journal of Pavement Research and Technology*, *11*(2), 114–127. https://doi.org/10.1016/j.ijprt.2017.03.007

Pokharel, S. K., Han, J., Leshchinsky, D., Parsons, R. L., & Halahmi, I. (2010). Investigation of factors influencing behavior of single geocell-reinforced bases under static loading. *Geotextiles and Geomembranes*, *28*(6), 570–578. https://doi.org/10.1016/j.geotexmem.2010.06.002

Pokharel, S. K., Norouzi, M., Martin, I., & Breault, M. (2016). Sustainable Road Construction for Heavy Traffic Using High Strength Polymeric Geocells. *Resilient Infrastructure*.

Pokharel, S. K. (2010). *Experimental Study on Geocell-Reinforced Bases under Static and Dynamic Loading*. University of Kansas.

Pokharel, S. K., Martin, I., Norouzi, M., & Breault, M. (2015). Validation of geocell design for unpaved roads. *In Proceedings of Geosynthetics*.

Punthutaecha, K., Puppala, A. J., Vanapalli, S. K., & Inyang, H. (2006). Volume Change Behaviors of Expansive Soils Stabilized with Reclaimed Ashes and Fibers. *Journal of Materials in Civil Engineering*, *18*(2), 295–306. https://doi.org/10.1061/(asce)0899-1561(2006)18:2(295)

Puppala, A. J., Hoyos, L., Viyanant, C., & Musenda, C. (2008). Fiber and Fly Ash Stabilization Methods to Treat Soft Expansive Soils. *In Soft ground technology (pp. 136-145).* https://doi.org/10.1061/40552(301)11

Puppala, A. J., Pedarla, A., Chittoori, B., Ganne, V. K., & Nazarian, S. (2017). Long-Term Durability Studies on Chemically Treated Reclaimed Asphalt Pavement Material as a Base Layer for Pavements. *Transportation Research Record: Journal of the Transportation Research*, *2657*, 1–9. https://doi.org/10.3141/2657-01

Puppala, A. J., Congress, S. S. C., Talluri, N., & Wattanasanthicharoen, E. (2019). Sulfate-Heaving Studies on Chemically Treated Sulfate-Rich Geomaterials. *Journal of Materials in Civil Engineering*, *31*(6), 04019076. https://doi.org/10.1061/(asce)mt.1943-5533.0002729

Puppala, A. J., Hoyos, L. R., & Potturi, A. K. (2011). Resilient moduli response of moderately cement-treated reclaimed asphalt pavement aggregates. *Journal of Materials in Civil Engineering*, *23*(7), 990–998. https://doi.org/10.1061/(asce)mt.1943-5533.0000268

Puppala, A. J., & Musenda, C. (2000a). Effects of fiber reinforcement on strength and volume change in expansive soils. *Transportation Research Record*, *1736*(1), 134–140. https://doi.org/10.3141/1736-17

Puppala, A. J., Punthutaecha, K., & Vanapalli, S. K. (2006). Soil-Water Characteristic Curves of Stabilized Expansive Soils. *Journal of Geotechnical and Geoenvironmental Engineering*, *132*(6), 736–751. https://doi.org/10.1061/(asce)1090-0241(2006)132:6(736)

Puppala, A. J., Ramakrishna, A. M., & Hoyos, L. R. (2003). Resilient Moduli of Treated Clays from Repeated Load Triaxial Test. *Transportation Research Record*, *1821(1)*, 68–74. https://doi.org/10.3141/1821-08

Puppala, A. J., Saride, S., Sirigiripet, S. K., Willammee, R., & Dronamraju, V. S. (2008). Evaluation of Cemented Quarry Fines as a Pavement Base Material. In *GeoCongress 2008: Geotechnics of Waste Management and Remediation* (pp. 312-319).

Puppala, A. J., Saride, S., & Williammee, R. (2012). Sustainable Reuse of Limestone Quarry Fines and RAP in Pavement Base/Subbase Layers. *Journal of Materials in Civil Engineering*, *24*(4), 418–429. https://doi.org/10.1061/(ASCE)MT.1943-5533.0000404

Rajagopal, K., Chandramouli, S., Parayil, A., & Iniyan, K. (2014). Studies on geosynthetic-reinforced road pavement structures. *International Journal of Geotechnical Engineering*, *8*(3), 287–298. https://doi.org/10.1179/1939787914Y.0000000042

Rajagopal, K., Krishnaswamy, N. R., & Latha, G. M. (1999). Behaviour of sand confined with single and multiple geocells. *Geotextiles and Geomembranes*, *17*(3), 171–184. https://doi.org/10.1016/S0266-1144(98)00034-X

Saha, D. C., & Mandal, J. N. (2018). Performance of reclaimed asphalt pavement reinforced with Bamboo geogrid and Bamboo geocell. *International Journal of Pavement Engineering*, *21*(5), 571–582. https://doi.org/10.1080/10298436.2018.1502432

Sambodh, A. (2017). *Mechanical Properties of Soil-RAP-Geopolymer for the Stabilization of Road Base / Subbase*. University of Louisiana at Lafayette.

Saride, S., Gowrisetti, S., Sitharam, T. G., & Puppala, A. J. (2009). Numerical simulation of geocell-reinforced sand and clay. *Ground Improvement*, *162*(4), 185–198. https://doi.org/10.1680/grim.2009.162.4.185

Schaefer, V., & Berg, R. (2012). Compaction “Roadeo” Field Demonstration: Roller-

Integrated Compaction Monitoring and Subgrade Geosynthetic Reinforcement. *Geotechnical Solutions for Soil Improvement, Rapid Embankment Construction, and Stabilization of the Pavement Working Platform*, *December*. https://doi.org/10.17226/22683

Setiawan, A., Suparma, L. B., & Mulyono, A. T. (2017). Developing the elastic modulus measurement of asphalt concrete using the compressive strength test. *AIP Conference Proceedings*, *1903*, 05002(1–11). https://doi.org/10.1063/1.5011541

ShapeArray — *Geotechnical Observations*. (2021, August 2)). Retrieved from http://www.geo-observations.com/shape-arrays

Sherin, K. S., Chandrakaran, S., & Sankar, N. (2017). Effect of Geocell Geometry and Multi-layer System on the Performance of Geocell Reinforced Sand Under a Square Footing. *International Journal of Geosynthetics and Ground Engineering*, *20*(3), 1-11. https://doi.org/10.1007/s40891-017-0097-3

Shukla, S. K. (2002). *Geosynthetics and their applications*. Thomas Telford. https://doi.org/10.1680/GATA.31173.FM

Simpson, A. (2001). *Measurement of rutting in asphalt pavements*. The University of Texas at Austin, Texas https://repositories.lib.utexas.edu/bitstream/handle/2152/1660/simpsonal13317.pdf?sequence=2

Sitharam, T. G., Hegde, A. M., & Kolathayar, S. (2019). *Geocells*. Springer Singapore. https://link.springer.com/book/10.1007%2F978-981-15-6095-8

Smith, K. D., Bruinsma, J. E., Wade, M. J., Chatti, K., Vandenbossche, J. M., & Yu, H. T. (2017). *Using Falling Weight Deflectometer Data with Mechanistic-Empirical Design and Analysis, Volume 1* (No. FHWA-HRT-16-009). United States. Federal Highway Administration.

Sullivan, D. E. (2006). Materials in Use in U.S. Interstate Highways. *USGS: Science for a Changing World*. https://pubs.usgs.gov/fs/2006/3127/2006-3127.pdf

Sun, X., Guo, J., Han, J., & Guo, K. (2021). Stress analysis of geosynthetic access mat systems over weak subgrade. In *Computers and Geotechnics* 134, 104071. https://doi.org/10.1016/j.compgeo.2021.104071

Tabatabaee, N., & Sebaaly, P. (1990). State-of-the-Art Pavement Instrumentation. *Transportation Research Record*, 1260, 246–256. http://onlinepubs.trb.org/Onlinepubs/trr/1990/1260/1260-022.pdf

Tafreshi, S. N. M., Khalaj, O., & Dawson, A. R. (2014). Repeated loading of soil containing granulated rubber and multiple geocell layers. *Geotextiles and Geomembranes*, *42*(1), 25–38. https://doi.org/10.1016/j.geotexmem.2013.12.003

Taha, R., Al-Harthy, A., Al-Shamsi, K., and Al-Zubeidi, M. (2002). Cement stabilization of reclaimed asphalt pavement aggregate for road bases and subbases. *Journal of materials in civil engineering, 14*(3), 239–245. https://doi.org/10.1061/(ASCE)0899-1561(2002)14:3(239)

Taha, R., Ali, G., Basma, A., & Al-Turk, O. (1999). Evaluation of reclaimed asphalt pavement aggregate in road bases and subbases. *Transportation Research Record: Journal of the Transportation Research Board*, *1652*(1), 264–269. https://doi.org/10.3141/1652-33

Tamim, M. M. (2017). *Evaluating the effectiveness of a hybrid geosynthetic reinforcement system to mitigate differential heave on flexible pavement due to expansive subgrades*. Boise State University. Boise, Idaho.

Hu, S., Zhou, F., & Scullion, T. (2013). *Development of Texas mechanistic-empirical flexible pavement design system* (No. FHWA/TX-14/0-6622-2). Texas. Dept. of Transportation. Research and Technology Implementation Office.

Thakur, J. K. (2011). *Geocell-Reinforced Unpaved and Paved Roads with Reclaimed Asphalt Pavement ( RAP ) Bases : Experimental Study and Damage Model Development*. University of Kansas, Lawrence, KS.

Thakur, J. K., Asce, M., Han, J., Asce, F., Parsons, R. L., & Asce, M. (2017). Factors Influencing Deformations of Geocell-Reinforced Reclaimed Asphalt Pavement Bases under Cyclic Loading. *Journal of Materials in Civil Engineering*, *29*(3), 04016240(1–12). https://doi.org/10.1061/(ASCE)MT.1943-5533.0001760.

Thakur, J. K., & Han, J. (2015). Recent development of reclaimed asphalt pavement (rap) bases treated for roadway applications. *Transportation Infrastructure Geotechnology*, *2*(2), 68–86. https://doi.org/10.1007/s40515-015-0018-7

Thakur, J. K., Han, J., Pokharel, S. K., & Parsons, R. L. (2012). Performance of geocell-reinforced reclaimed asphalt pavement (RAP) bases over weak subgrade under cyclic plate loading. *Geotextiles and Geomembranes*, *35*, 14–24. https://doi.org/10.1016/j.geotexmem.2012.06.004

Thallak, S. G., Saride, S., & Dash, S. K. (2007). Performance of surface footing on geocell-reinforced soft clay beds. *Geotechnical and Geological Engineering*, *25*(5), 509–524. https://doi.org/10.1007/s10706-007-9125-8

Treenate, P., Limphitakphong, N., & Chavalparit, O. (2017). A complete life cycle assessment of high density polyethylene plastic bottle. *IOP Conference Series:*

*Materials Science and Engineering*, *222*(1). https://doi.org/10.1088/1757-899X/222/1/012010

Tseng, K.-H., & Lytton, R. L. (1989). Prediction of Permanent Deformation in Flexible Pavement Materials. *ASTM International*, 154–172.

TxDOT (2021). *Road User Costs*. Retrieved September 18, 2021, from https://www.txdot.gov/inside-txdot/division/construction/road-user-costs.html

TxDOT Pavement Manual. (2019). *Pavement Manual*.

Vennapusa, P. K. R., White, D. J., Wayne, M. H., Kwon, J., Galindo, A., & García, L. (2018). In situ performance verification of geogrid-stabilized aggregate layer: Route-39 El Carbón–Bonito Oriental, Honduras case study. *International Journal of Pavement Engineering*, *21(1)*, 100–111. https://doi.org/10.1080/10298436.2018.1442576

White, D. J., & Vennapusa, P. K. R. (2017). In situ resilient modulus for geogrid-stabilized aggregate layer : A case study using automated plate load testing. *Transportation Geotechnics*, *11*, 120–132. https://doi.org/10.1016/j.trgeo.2017.06.001

Williams, B. A., Willis, J. R., & Shacat, J. (2020). *Asphalt Pavement Industry Survey on Reclaimed Materials and Warm-Mix Asphalt Usage: 2019* (No. IS 138 (10e).

Yang, X. (2010). *Numerical Analyses of Geocell-Reinforced Granular Soils under Static and Repeated Loads Numerical Analyses of Geocell-Reinforced Granular Soils under Static and Repeated Loads*. University of Kansas, Lawrence, KS.

Yang, X., Asce, M., & Han, J. (2013). Analytical Model for Resilient Modulus and Permanent Deformation of Geosynthetic-Reinforced Unbound Granular Material. *Journal of Geotechnical and Geoenviromental Engineering*, *139*(9), 1443–1453. https://doi.org/10.1061/(ASCE)GT.1943-5606.0000879

Yang, X., Han, J., Leshchinsky, D., & Parsons, R. L. (2013). A three-dimensional mechanistic-empirical model for geocell-reinforced unpaved roads. *Acta Geotechnica*, 8(2), 201–213. https://doi.org/10.1007/s11440-012-0183-6

Zhou, H., & Wen, X. (2008). Model studies on geogrid- or geocell-reinforced sand cushion on soft soil. *Geotextiles and Geomembranes*, *26*(3), 231–238. https://doi.org/10.1016/j.geotexmem.2007.10.002

Zornberg, J. G., & Gupta, R. (2009). Reinforcement of pavements over expansive clay subgrades. *Proceedings of the 17th International Conference on Soil Mechanics and Geotechnical Engineering: The Academia and Practice of Geotechnical*

*Engineering*. https://doi.org/10.3233/978-1-60750-031-5-765

Zornberg, J. G., & Gupta, R. (2010). Geosynthetics in pavements: North American contributions. *In Theme Speaker Lecture, Proceedings of the 9th International Conference on Geosynthetics, Guarujá, Brazil, May* (Vol. 1, pp. 379-400).